Study of Electromagnetic and Thermal Transients in a High-temperature Superconducting Transformer during a Short Circuit

Manusov V.Z., Ivanov D.M.
Novosibirsk State Technical University
Novosibirsk, Russian Federation

***Abstract*.** Today, high-temperature superconducting (HTS) current limiters and transformers allow to limit the surge short circuit current during failure without negatively affecting on the power grid complex at the normal operation mode. However, the transition of a superconductor to a resistive state at the moment of current limitation can cause significant heat generation, which can destroy the transformer windings. The research goal is to provide optimal technical characteristics of the HTS transformer to achieve effective short circuit current limitation and prevent thermal breakdown of its windings. To achieve this goal, a mathematical model of a HTS transformer was developed. The presented method considers the material type and geometry of the superconducting tape, the critical parameters of the superconductor (current and temperature), the parameters of the cryogenic liquid, dependence of the resistance and heat capacity of the HTS tape layers on temperature. The simulation model was created in the Matlab/Simulink software. The most important result is the possibility of obtaining optimal electrical and thermal parameters of the HTS transformer windings during the short circuit current limitation, as well as ensuring the thermal stability of the superconducting tape at the quench moment. The obtained results are significant in the design and operation of HTS transformers. For efficient and safe operation in the current-limiting mode, it is necessary to take into account heat generation on the transformer windings. It is important for the superconductor returning to the superconducting state without causing significant overheating of the windings.
***Keywords*:** HTS transformer, high-temperature superconductivity, short-circuit current limitation, transient process, mathematical modeling, Matlab/Simulink, energy efficiency, liquid nitrogen.

DOI: https://doi.org/10.52254/1857-0070.2023.2-58.01
UDC: 621.314

Cercetarea proceselor tranzitorii electromagnetice și termice într-un transformator supraconductor la temperaturi ridicate în timpul unui scurtcircuit

Manusov V.Z., Ivanov D.M.
Universitatea Tehnică de Stat din Novosibirsk, Federația Rusă

Rezumat. Benzile supraconductoare la temperatură ridicată (SCTR) bazate pe ceramică de ytriu YBa2Cu3O7 sunt capabile să mențină supraconductivitatea la o temperatură de 77 K. Aceste mașini sunt capabile să limiteze curentul de supratensiune al unui scurtcircuit (SC) în caz de accidente, fără a afecta negativ complexul rețelei electrice în funcționare normală. Cu toate acestea, trecerea unui supraconductor la o stare rezistivă în momentul limitării curentului poate provoca fluxuri de căldură semnificative care pot perturba integritatea înfășurărilor transformatorului. Scopul lucrării este de a oferi caracteristici tehnice optime ale transformatorului SCTR pentru a obține o limitare eficientă a curentului de scurtcircuit și pentru a preveni defalcarea termică a înfășurărilor sale. Pentru a atinge acest obiectiv, a fost elaborat un model matematic al unui transformator SCTR, implementat în software-ul și sistemul de calcul Matlab/Simulink. Modelul ia în considerare materialul și geometria benzii supraconductoare, parametrii critici ai supraconductorului (curent și temperatură), caracteristicile lichidului criogenic și dependențele de temperatură ale rezistențelor specifice și capacităților termice ale straturilor de bandă SCTR. Cel mai important rezultat este posibilitatea de a obține parametrii electrici și termici optimi ai înfășurărilor transformatorului SCTR în momentul limitării curentului de scurtcircuit, precum și asigurarea stabilității termice a benzii supraconductoare în cazul pierderii și revenirii supraconductivității. S-a realizat modelarea numerică a pornirii unui transformator SCTR cu o înfășurare secundară scurtcircuitată pentru un interval de tensiune de la 40 V la 120 V. Ca rezultat al lucrării, se obțin oscilograme ale curenților și temperaturilor în înfășurările SCTR în timpul unui scurtcircuit, care descriu procesul tranzitoriu cu suficientă acuratețe. Rezultatele obținute sunt semnificative în proiectarea și funcționarea transformatoarelor SCTR.
Cuvinte-cheie: transformator SCTR, supraconductivitate la temperatură ridicată, limitarea curentului de scurtcircuit, tranzitoriu, modelare matematică, Matlab/Simulink, eficiență energetică, azot lichid.

Исследование электромагнитных и тепловых переходных процессов в высокотемпературном сверхпроводящем трансформаторе при коротком замыкании

Манусов В.З., Иванов Д.М.

Новосибирский государственный технический университет, г. Новосибирск, Российская Федерация

Аннотация. Высокотемпературные сверхпроводящие (ВТСП) ленты, созданные на основе иттриевой керамики $YBa_2Cu_3O_7$, способны сохранять сверхпроводимость при температуре 77 К. Благодаря свойству этого материала резко повышать свое активное сопротивление при потере сверхпроводимости, создаются ВТСП токоограничители и трансформаторы. Эти машины способны ограничивать ударный ток короткого замыкания (КЗ) при авариях, не оказывая негативного влияния на электросетевой комплекс в нормальном режиме работы. Однако, переход сверхпроводника в резистивное состояние в момент токоограничения может вызвать существенные тепловые потоки, способные нарушить целостность обмоток трансформатора. Целью работы является обеспечение оптимальных технических характеристик ВТСП трансформатора для достижения эффективного ограничения тока КЗ и предотвращения теплового срыва его обмоток. Для достижения поставленной цели была разработана математическая модель ВТСП трансформатора, реализованная в программно-вычислительном комплексе Matlab/Simulink. Модель учитывает материал и геометрию сверхпроводящей ленты, критические параметры сверхпроводника (ток и температуру), особенности криогенной жидкости, зависимости удельных сопротивлений и теплоемкостей слоев ВТСП ленты от температуры. Наиболее важным результатом является возможность получения оптимальных электрических и тепловых параметров обмоток ВТСП трансформатора в момент ограничения тока КЗ, а также обеспечение тепловой устойчивости сверхпроводящей ленты при потере и возврате сверхпроводимости. Проведено численное моделирование включения ВТСП трансформатора с закороченной вторичной обмоткой на диапазон напряжений от 40 В до 120 В. В результате работы получены осциллограммы токов и температур в ВТСП обмотках при коротком замыкании, с достаточной точностью описывающие переходный процесс. Полученные результаты являются значимыми при проектировании и эксплуатации ВТСП трансформаторов. Для эффективной и безопасной работы в режиме токоограничения необходимо учитывать тепловыделения на обмотках трансформатора, чтобы сверхпроводник успел вернуться в сверхпроводящее состояние, не вызывая значительный перегрев обмоток.

Ключевые слова: ВТСП трансформатор, высокотемпературная сверхпроводимость, ограничение токов короткого замыкания, переходный процесс, математическое моделирование, Matlab/Simulink, энергоэффективность, жидкий азот.

ВВЕДЕНИЕ

Развитие электросетевого комплекса, обусловленное постоянно растущим спросом на электроэнергию, приводит к повышению ожидаемых уровней токов КЗ в электрических сетях классов напряжений 35 – 220 кВ. В будущем уровни расчетных токов КЗ могут превысить предельную отключающую способность коммутационного электрооборудования, что может привести к разрушению обмоток генераторов, трансформаторов, синхронных компенсаторов и других электрических машин. За последнее десятилетие учеными ведущих мировых институтов создаются сверхпроводящие токоограничители следующих видов: резистивные, индуктивные (трансформаторного типа, выпрямительный и т.д.) [1-5]. Однако, процесс ограничения тока происходит благодаря уникальному свойству высокотемпературных сверхпроводников скачкообразно увеличивать свое активное сопротивление при потере сверхпроводимости [1, 2, 5-7]. Применение сверхпроводников в качестве материала для обмоток позволяет с совместить функцию ограничения токов КЗ и трансформацию напряжения в одном устройстве - ВТСП трансформаторе. Токоограничивающая функция снижает температурное и электродинамическое воздействие тока КЗ непосредственно на трансформатор, что говорит о пользе применения этого эффекта непосредственно в этих электрических машинах [6-9].

Следует отметить огромный интерес научного сообщества к разработке и исследованию ВТСП трансформаторов. Были разработаны как имитационные математические модели, так и физические прототипы ВТСП трансформаторов в диапазоне мощностей от 8 до 5000 кВА [10-14]. В работах [15-17] проведено исследование природы потерь в ВТСП трансформаторах и кабелях на переменном токе методом конечных элементов. Разработаны модели, позволяющие оценить переходный процесс при включении ВТСП трансформатора [18, 19]. Однако, научным сообществом мало

внимания уделяется исследованию электротепловых переходных процессов и времени возврата сверхпроводимости после ограничения тока КЗ.

В настоящей работе представлена электротермическая модель поведения ВТСП обмоток в момент КЗ, позволяющая адекватно моделировать электромагнитный и тепловой переходный процесс при потере сверхпроводимости. Модель позволяет выявить основные критерии и требования к обмоткам ВТСП трансформаторов с учетом критических и геометрических параметров сверхпроводника, параметров криогенной жидкости и условий возврата сверхпроводящего состояния обмоток после устранения КЗ.

МАТЕМАТИЧЕСКАЯ МОДЕЛЬ ОДНОФАЗНОГО ВЫСОКОТЕМПЕРАТУРНОГО СВЕРХПРОВОДЯЩЕГО ТРАНСФОРМТОРА

Чтобы успешно внедрить ВТСП трансформаторы в электрическую сеть, необходим способ удобного прогнозирования токоограничивающих характеристик. На поведение сверхпроводящих обмоток в момент КЗ влияет ряд параметров, таких как полное сопротивление смежной линии электропередачи, сопротивление КЗ, продолжительность КЗ. Ключевым моментом, является поведение ВТСП обмотки при потере сверхпроводимости (при превышении одного из критических параметров) и ее беспрепятственном возврате после устранения аварии.

Для построения адекватной модели поведения ВТСП обмоток необходимо учитывать слоистую структуру сверхпроводника. В модели будет рассматриваться трансформатор с обмотками из $YBa_2Cu_3O_7$ (YBCO). Структура ВТСП ленты второго поколения производства компании «SuperOx» представлена на рис. 4 [20, 21].

До начала переходного процесса ток течет по сверхпроводнику с нулевым сопротивлением (рис. 2а). После начала КЗ величина тока, текущего по ВТСП обмоткам, превышает критическую величину тока св [1, 2] Appendix 1 что вызывает потерю св и скачкообразное повышение активного сопротивления. В этот момент аварийный ток протекает сразу по всем слоям ВТСП провода (рис. 2б).

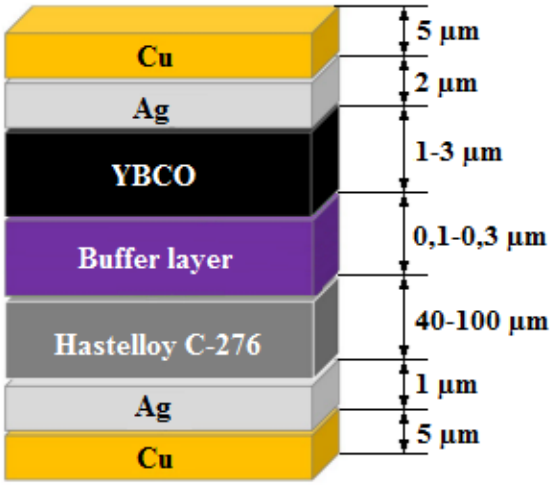

Рис.1. Структура ВТСП лент второго поколения компании «SuperOx».[1]

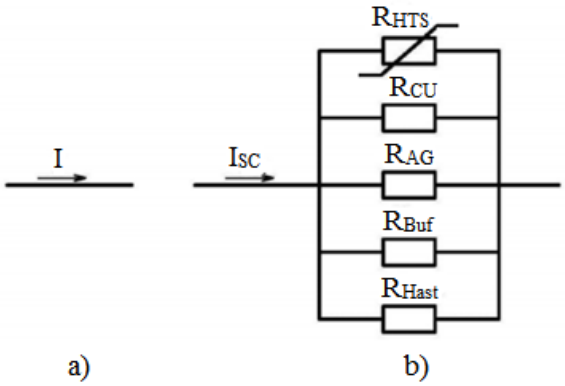

Рис.2. Схема замещения ВТСП провода.[2]

Отметим, что для корректного исследования теплового поведения ВТСП обмоток стоит учитывать зависимости активных сопротивлений несверхпроводящих слоев ВТСП ленты от температуры:

$$R_{NS}(T) = \frac{1}{\frac{1}{R_{cu}(T)} + \frac{1}{R_{ag}(T)} + \frac{1}{R_{buf}(T)} + \frac{1}{R_{hast}(T)}}, \quad (1)$$

где T – температура ВТСП ленты, R_{cu} – активное сопротивление меди, R_{ag} – активное сопротивление серебра, R_{buf} – активное сопротивление буферного слоя, R_{hast} – активное сопротивление хастеллоя.

Активное сопротивление ВТСП провода можно оценить по вольт-амперной

характеристике сверхпроводника YBCO, использованного в модели (рис. 3).

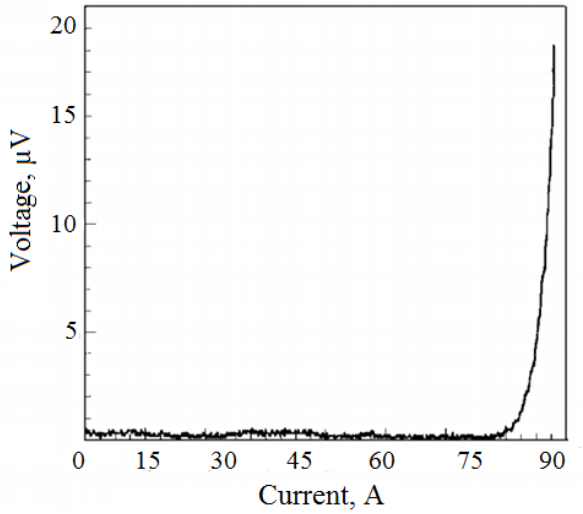

Рис.3. Вольт-амперная характеристика сверхпроводника YBCO.[3]

Аппроксимируя вольт-амперную характеристику, можно с достаточной степенью точности выразить нелинейное сопротивление ВТСП ленты, в зависимости от тока, протекающего по сверхпроводнику и температуры ленты. В качестве допущения примем однородность свойств ВТСП ленты на всей обмотке.

$$R_{HTS}(I,T) = \frac{E_0}{I}\left(\frac{I}{I_K(T)}\right)^n \cdot l, \qquad (2)$$

где I – ток протекающий по обмотке, $I_K(T)$ – критический ток сверхпроводника в зависимости от температуры; E_0 – напряженность электрического поля; n – степень вольтамперной характеристики, зависит от параметров ВТСП ленты; l – длина ВТСП ленты в обмотке.

Критический ток сверхпроводника $I_K(T)$ найдем из выражения, подробно описанного в [22]:

$$I_K(T) = -\frac{I_{K0}}{0{,}1848}\ln\left(\frac{T}{93}\right), \qquad (3)$$

где I_{K0} – критический ток при температуре 77 К, зависит от типа ВТСП пр рических параметров.

[3] Appendix 1

Эквивалентное активное сопротивление ВТСП обмотки для сверхпроводящего и резистивного состояния представим следующим выражением:

$$R_E(I,T) = \frac{R_{NS}(T)\cdot R_{HTS}(I,T)}{R_{NS}(T)+R_{HTS}(I,T)}. \qquad (4)$$

Для анализа времени возврата ВТСП обмотки трансформатора в сверхпроводящее состояние после устранения КЗ необходимо учитывать тепловой процесс, происходящий в ВТСП проводе. Принимая что температура по всей длине обмотки равномерна, найдем количество теплоты, выделяющееся на обмотке во время переходного процесса:

$$Q(I,T) = \int_0^t I^2 R_E(I,T)dt. \qquad (5)$$

Составим уравнение теплового баланса, которое позволяет оценить изменение температуры обмотки при переходном процессе, в зависимости от тока протекающего по обмотке тока и времени:

$$\frac{dT}{dt} = \frac{Q(I,T) - Aq(\Delta T)}{C_\Sigma(T)}, \qquad (6)$$

где $Q(I,T)$ – количество теплоты, выделяющееся на обмотке, A – площадь поверхности ВТСП ленты, $C_\Sigma(T)$ – общая теплоемкость ВТСП обмотки, $q(\Delta T)$ - плотность теплового потока в зависимости от разности температур (рис. 4).

Стоит пояснить, что используемая в уравнении (6) величина теплового потока q зависит от разницы температур между поверхностью ВТСП ленты и охлаждающей ее жидким азотом (рис. 4).

При существенном повышении температуры обмотки (при ΔT>30 K) режим охлаждения перейдет в стадию пленочного кипения жидкого азота, которая вызовет неэффективное охлаждение обмотки. Рассмотренный режим вызовет дальнейшее повышение температуры ВТСП ленты, что может привести к термическому разрушению обмотки.

Поэтому во избежание нарушения работы ВТСП трансформатора при ограничении тока КЗ следует не допускать больших тепловыделений, способных перегреть обмотки свыше температуры кризиса кипения жидкого азота ≈ 107 К [23-25].

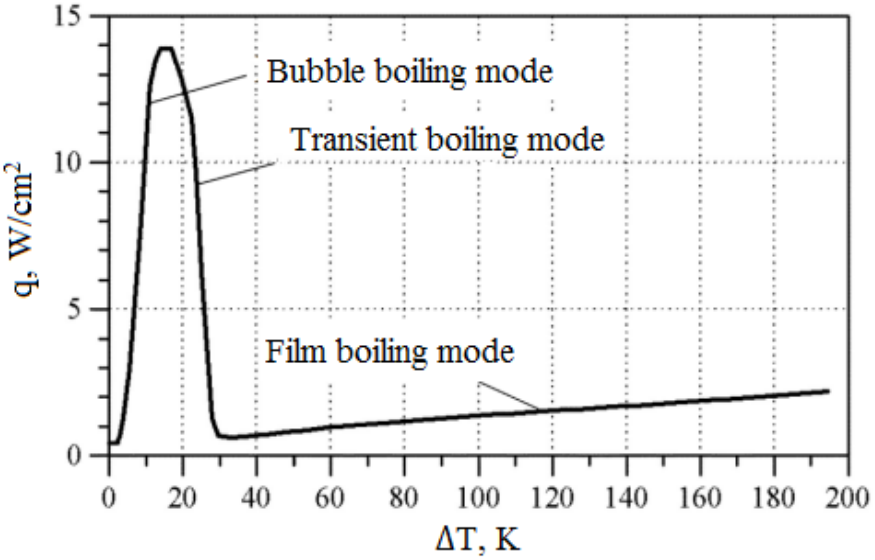

Рис. 4. Зависимость плотности теплового потока от разности температур.[4]

Для анализа переходных процессов составим схему замещения моделируемого ВТСП трансформатора с закороченной вторичной обмоткой (рис 5.).

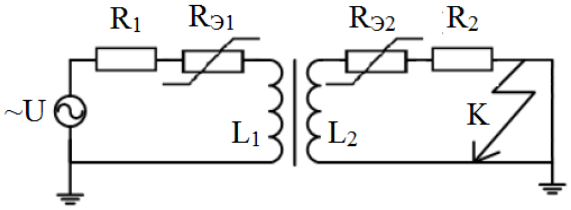

Рис. 5. Схема замещения моделируемого ВТСП трансформатора.[5]

Согласно схеме замещения трансформатора, составим дифференциальные уравнения, которые позволят описать электромагнитный переходный процесс. За допущения принимается отсутствие потерь и насыщения в магнитопроводе трансформатора.

$$U_m \sin(\omega t + \alpha) = L_1 \frac{di_1}{dt} + i_1(R_{E1}(i,T) + \\ + R_1) + M \frac{di_2}{dt}, \quad (7)$$

$$0 = L_2 \frac{di_2}{dt} + i_2(R_{E2}(i,T) + R_2) + M \frac{di_1}{dt}, \quad (8)$$

где L_1, L_2 – индуктивности первичной и вторичной обмоток ВТСП трансформатора; i_1, i_2 – токи в первичной и вторичной обмотках; M – взаимная индуктивность обмоток ВТСП трансформатора; R_1, R_2 – активные сопротивления токовводов и отходящих от них внешних цепей; U_m – амплитудное значение питающего напряжения; ω – циклическая частота; R_{E1}, R_{E2} – эквивалентное нелинейное активное сопротивление обмоток ВТСП трансформатора.

ЧИСЛЕННОЕ МОДЕЛИРОВАНИЕ ЭЛЕКТРОМАГНИТНЫХ И ТЕПЛОВЫХ ПЕРЕХОДНЫХ ПРОЦЕССОВ В ОДНОФАЗНОМ ВТСП ТРАНСФОРМАТОРЕ И ОБСУЖДЕНИЕ РЕЗУЛЬТАТОВ

Объектом моделирования является разработанная экспериментальная модель однофазного ВТСП трансформатора мощностью 2,5 кВА с закороченной вторичной обмоткой (рис. 6).

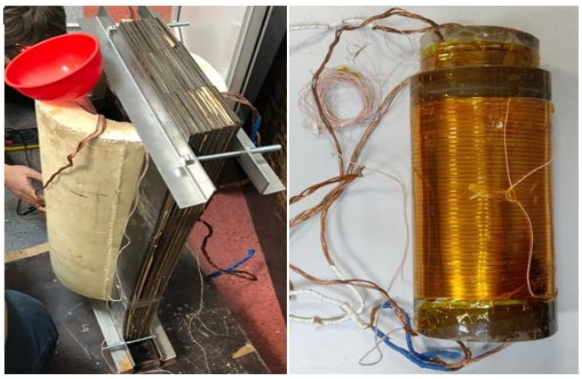

Рис. 6. Однофазный ВТСП трансформатор и его обмотки.[6]

[4, 5] Appendix 1

Численное решение представленной выше математической модели (уравнения (1-8)) было реализовано в программно-вычислительном комплексе Matlab/Simulink (рис. 7). Основные параметры обмоток моделируемого трансформатора представлены в таблице 1. На рис. 8 и рис. 9 представлена зависимость удельного активного сопротивления и теплоемкости от температуры для каждого слоя ВТСП ленты.

Для анализа электротеплового поведения ВТСП обмоток был смоделирован ряд экспериментов с включением ВТСП трансформатора с закороченной обмоткой низкого напряжения НН (трансформатор понижающий, 100/50 В) на питающее напряжение сети в диапазоне от 20 до 120 В (рис. 10-13).

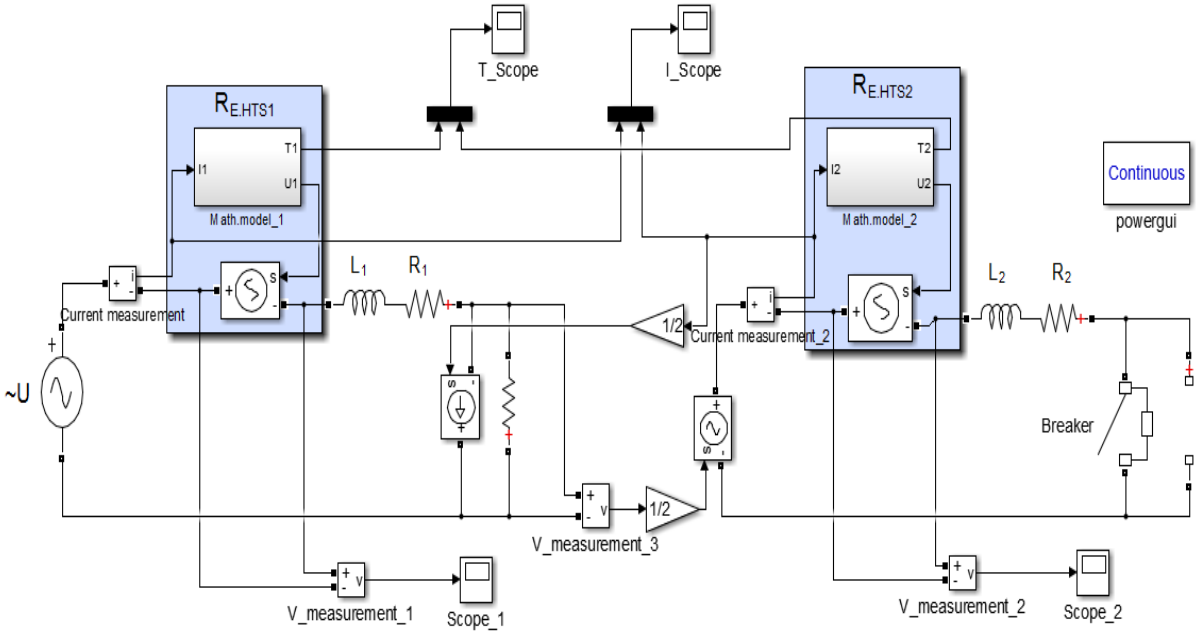

Рис. 7. Модель ВТСП трансформатора при КЗ в Matlab/Simulink.[7]

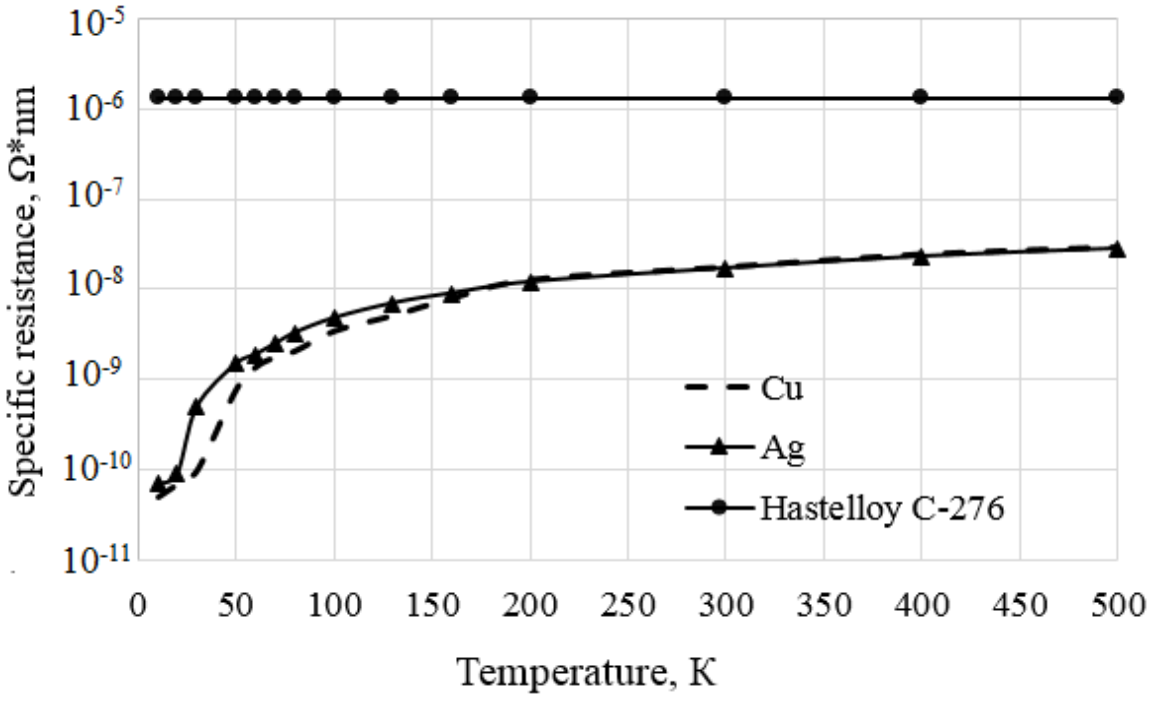

Рис. 8. Зависимость удельного сопротивления металлов от температуры.[8]

[6,7,8] Appendix 1

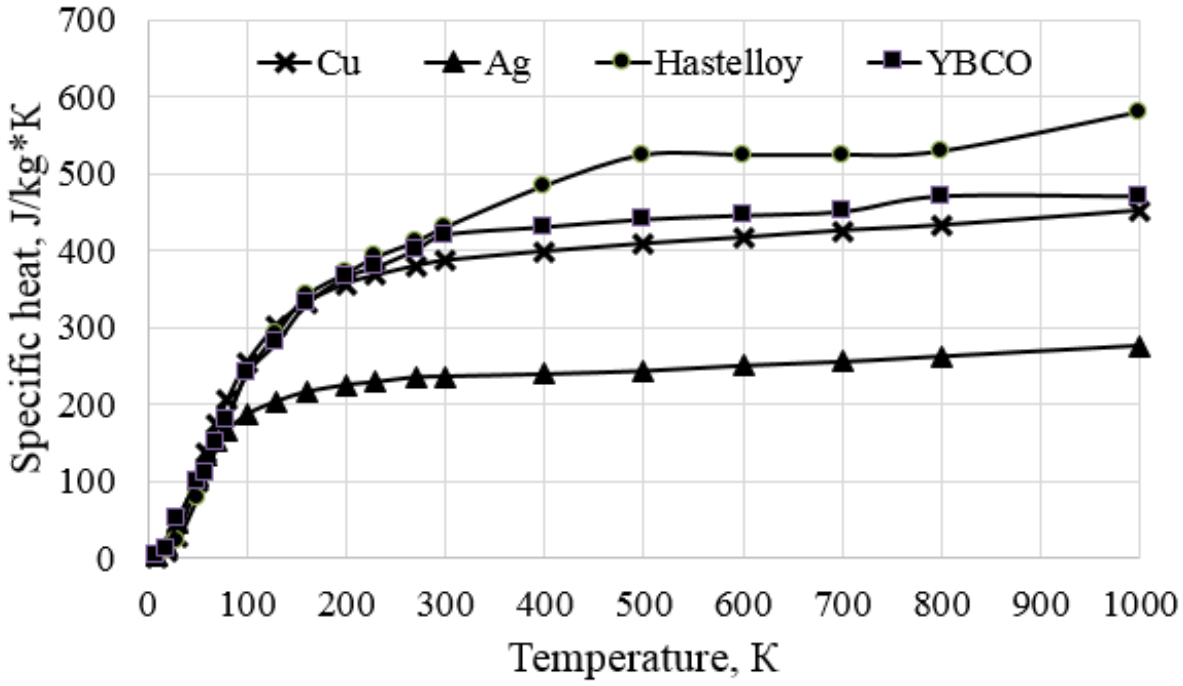

Рис. 9. Зависимость удельной теплоемкости металлов от температуры.[9]

Таблица 1[10].

Параметры обмоток опытного образца однофазного ВТСП трансформатора мощностью 2,5 кВА[11].

Параметр (Parameter)	Первичная обмотка (Primary winding)	Вторичная обмотка (Secondary winding)
Материал ВТСП ленты (HTS tape material)	$Y_1Ba_2Cu_3O_7$	
Ширина ВТСП ленты (HTS tape width), mm	4	
Критическая температура ленты (Critical temperature of tape), K	93	
Предел прочности ленты (Tensile strength of tape), MPa	500	
Критический ток ленты (Critical current), A	80	
Показатель степени вольт-амперной характеристики (Current-voltage characteristic exponent)	15	
Рабочая температура (Operating temperature), K	77	
Длина ВТСП ленты YBCO (HTS tape length), m	16,5	8,1
Напряжение (Voltage), V	100	50
Номинальный ток (Rated current), A	25	50
Число витков (Number of turns)	46	23
Индуктивность (Inductance), μH	162,09	34,4
Высота обмоток (Winding height), mm	210	135
Диаметр обмоток (Winding diameter), mm	130	110
Изоляция (Insulation)	Каптон (Kapton)	
Диэлектрическая среда (Dielectric medium)	Жидкий азот (Liquid nitrogen)	

[9,10,11] Appendix 1

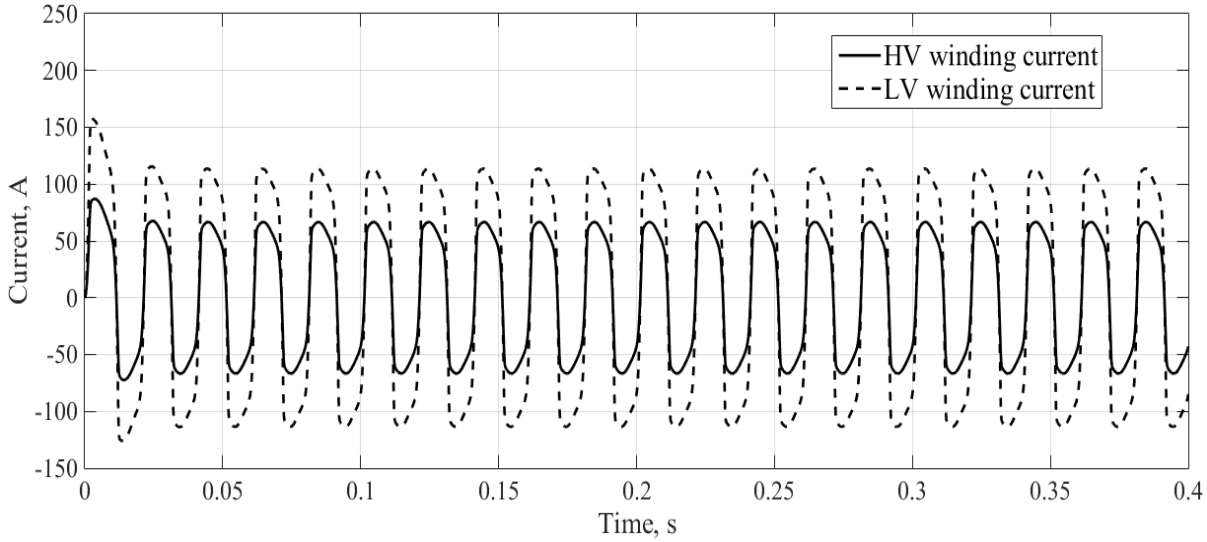

Рис. 10. Токи в ВТСП обмотках при питающем напряжении 40 В.[12]

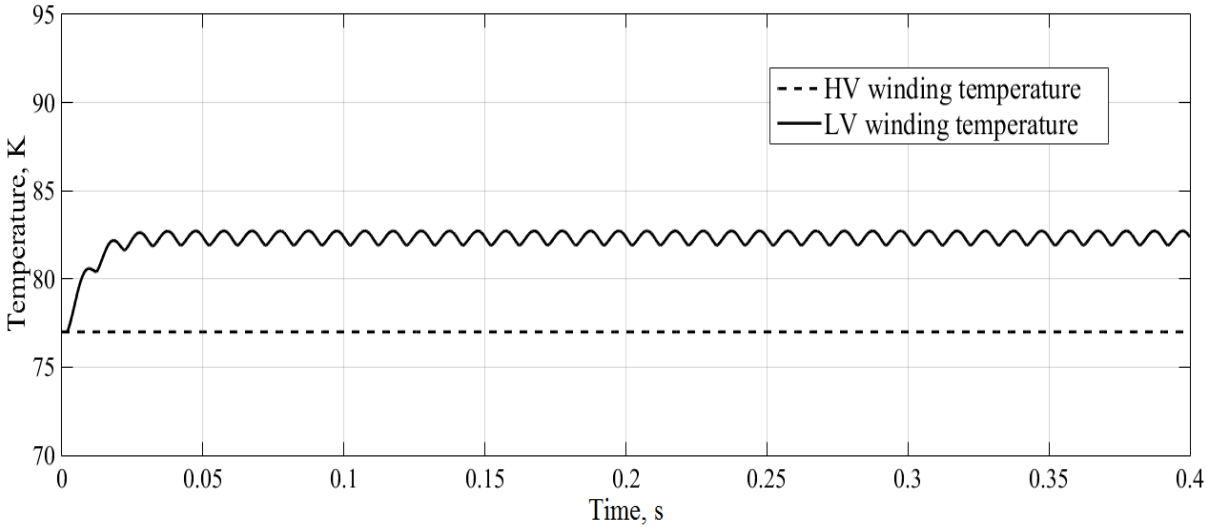

Рис. 11. Температура ВТСП обмоток при питающем напряжении 40 В.[13]

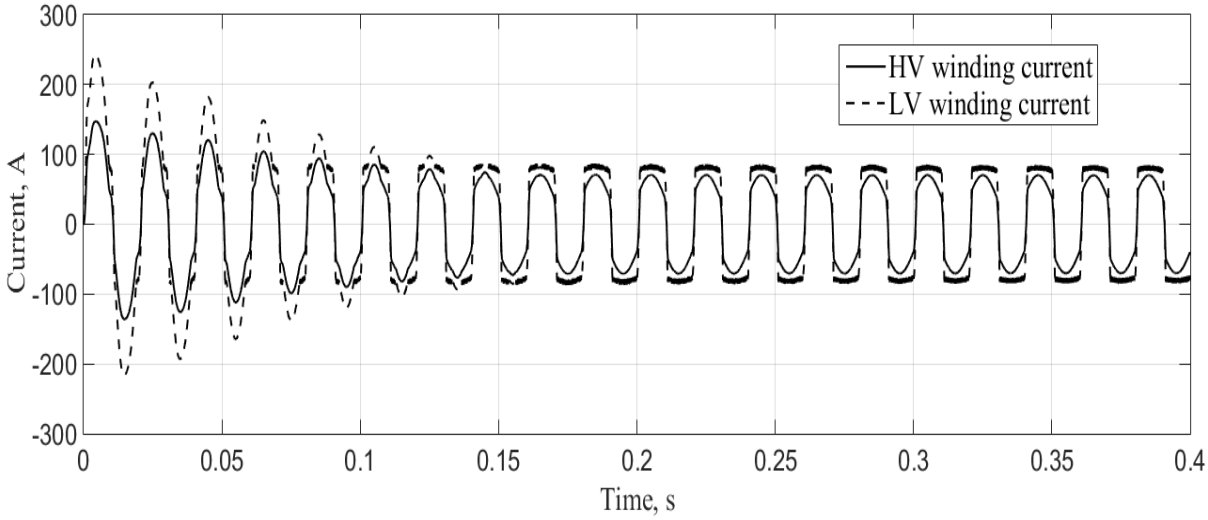

Рис. 12. Токи в ВТСП обмотках при питающем напряжении 120 В.[14]

[12,13,14] Appendix 1

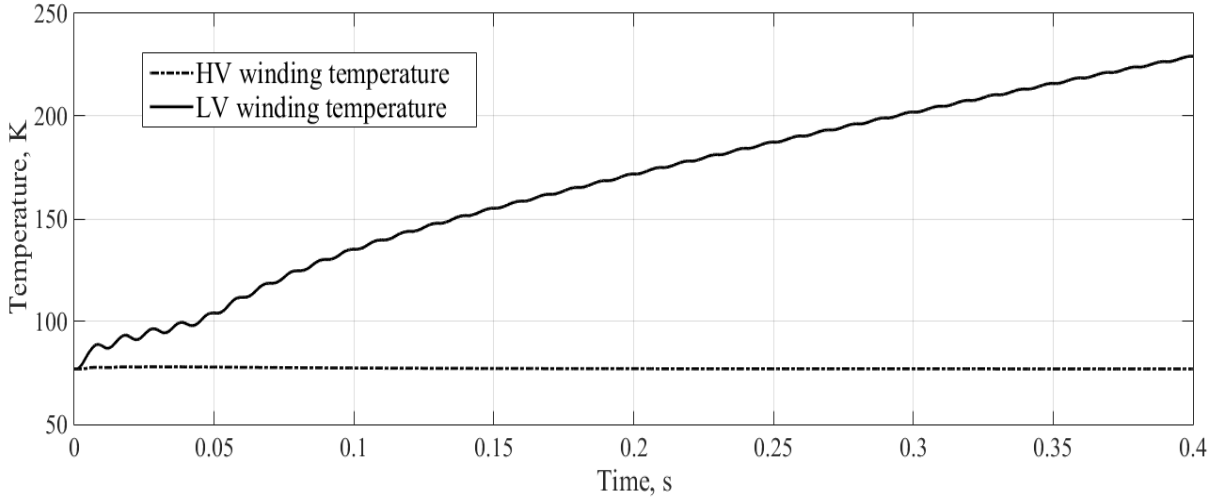

Рис. 13. Температура ВТСП обмоток при питающем напряжении 120 В.[15]

Форма кривых тока при подаче на трансформатор 40 В (рис. 10) и 120 В (рис. 12) свидетельствует об успешном ограничении тока в момент КЗ и хорошо коррелируется с результатами других авторов [26, 27] и проведенными натурными экспериментами авторами настоящей работы. Анализируя температурную зависимость, отметим что в первом случае (рис. 11) в обмотке ВН наблюдается незначительное изменение температуры, тогда как в обмотке НН происходит тепловая стабилизация (охлаждение провода происходит эффективно, так как система охлаждения находится в режиме пузырькового кипения жидкого азота), которая является безопасной для ВТСП обмотки. Однако во втором случае (рис. 13) наблюдается тепловой срыв, что часто приводит к необратимому перегреву провода и его дальнейшему повреждению.

Для оценки возврата сверхпроводимости обмотки был смоделирован эксперимент, при котором ВТСП трансформатор включается на питающее напряжение 120 В в режиме холостого хода и через 0.05 с происходит КЗ на вторичной обмотке НН, которое отключается через 0.1 с. Полученные осциллограммы токов и температур в обмотках (рис. 14, 15) свидетельствуют, что в момент КЗ происходит резкое повышение температуры, которое может вызвать тепловой срыв и термическое повреждение обмоток.

Как показал эксперимент, при быстром отключении КЗ, обмотки способны вернуться в сверхпроводящее состояние достаточно быстро (меньше 1 сек), не вызывая тепловой срыв и принудительное отключение трансформатора.

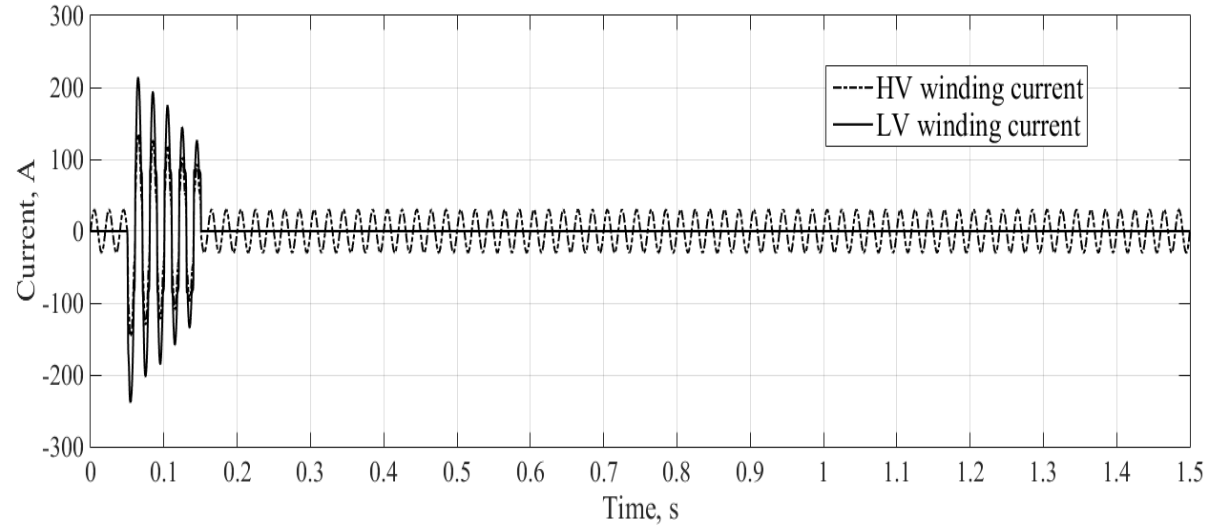

Рисунок 14. Токи в ВТСП обмотках при отключении КЗ при питающем напряжении 120 В.[16]

[15,16] Appendix 1

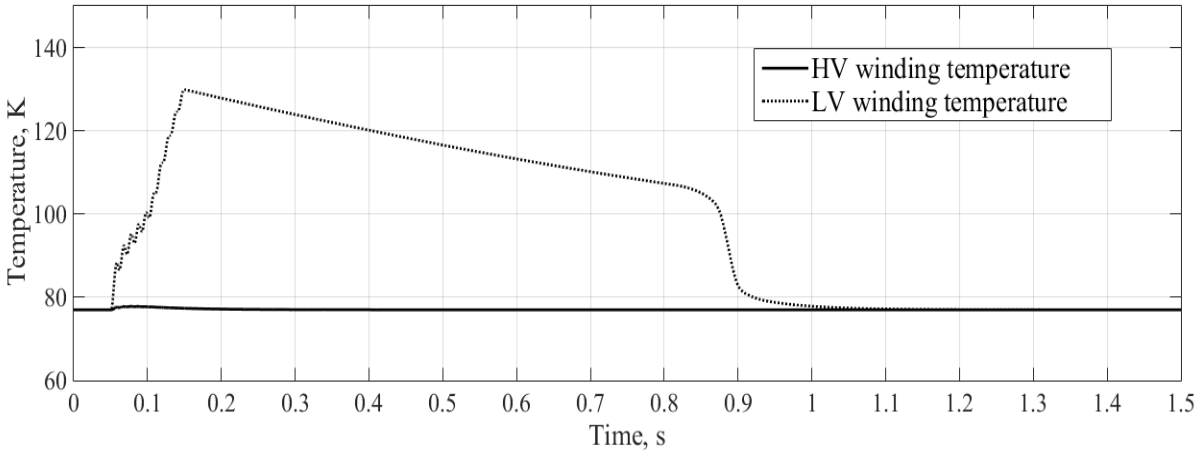

Рисунок 15. Температура ВТСП обмоток при отключении КЗ при питающем напряжении 120 В.[17]

Для стабилизации работы ВТСП трансформатора в момент КЗ предлагается использование ВТСП лент с большим сечением и критическим током в обмотке НН, так как по результатам экспериментов видно, что главную роль в ограничении тока играет именно обмотка НН. Сегодня ВТСП ленты изготавливают шириной 12 мм, с критическим током 500-600 А. Использование этих лент позволит существенно повысить токоограничивающую способность ВТСП трансформатора и тепловой запас его обмоток.

ЗАКЛЮЧЕНИЕ

Разработана математическая модель ВТСП трансформатора, позволяющая оценить переходные электромагнитный и тепловой процессы в его обмотках при КЗ. Проведено численное моделирование включения ВТСП трансформатора с закороченной вторичной обмоткой на диапазон напряжений от 40 до 120 В. Полученные осциллограммы тока показывают, что ВТСП трансформатор способен эффективно ограничивать ток КЗ. Однако, тепловыделения, возникающие при токоограничении, способны вызвать значительный перегрев обмоток, что приведет к тепловому срыву сверхпроводника и дальнейшему превышению температуры кризиса кипения жидкого азота. Рассмотренный режим может привести к термическому повреждению обмоток и их невозврату в сверхпроводящее состояние. Поэтому следует повышать термическую стойкость обмоток трансформатора путем использования ВТСП лент с большим сечением и большим критическим током во вторичной обмотке. Также возможно покрытие ВТСП лент дополнительным материалом-сопротивлением.

Разработанная модель может быть использована при проектировании ВТСП трансформаторов для определения оптимальных геометрических параметров его обмоток. Также модель позволяет оценить время возврата ВТСП провода в сверхпроводящее состояние после устранения КЗ. Численные эксперименты показали, что следует проектировать обмотки таким образом, чтобы за время бестоковой паузы (например, во время действия автоматического повторного включения) ВТСП провод успевал вернуться в сверхпроводящее состояние, не вызывая тепловой срыв обмоток.

APPENDIX 1 (ПРИЛОЖЕНИЕ 1)

[1]**Fig. 1.** Structure of the second-generation HTS tapes by «SuperOx» company

[2]**Fig. 2.** Equivalent circuit of HTS wire

[3]**Fig. 3.** Current-voltage curve of YBCO superconductor

[4]**Fig. 4.** Dependence of heat flux density on temperature

[5]**Fig. 5.** Equivalent circuit of a simulated HTS transformer

[6]**Fig. 6.** Single-phase HTS transformer and its windings

[7]**Fig. 7.** Matlab/Simulink model of HTS transformer during short circuit

[8]**Fig. 8.** The dependence of the specific resistance of metals on temperature

[9]**Fig. 9.** The dependence of the specific heat capacity of metals on temperature

[10,11]**Table 1.** Parameters of the windings of a single-phase HTS transformer prototype with a rated power of 2.5 kVA

[12]**Fig. 10.** Currents in HTS windings at a supply voltage of 40 V

[17] Appendix 1

[13]**Fig. 11.** Temperature of HTS windings at a supply voltage of 40 V
[14]**Fig. 12.** Currents in HTS windings at a supply voltage of 120 V
[15]**Fig. 13.** Temperature of HTS windings at a supply voltage of 40 V
[16]**Fig. 14.** Currents in HTS windings when a short circuit is switched off, supply voltage is 120 V
[17]**Fig. 15.** Temperature of HTS windings when a short circuit is switched off, supply voltage is 120 V

Литература (References)

[1] Moyzykh M., Gorbunova D., Ustyuzhanin P., Sotnikov D., Baburin K. First Russian 220 kV Superconducting Fault Current Limiter (SFCL) For Application in City Grid. *IEEE Transactions on Applied Superconductivity*, 2021, vol. 31, no. 5, pp. 1-7, Art no. 5601707

[2] Chen X., Gou H., Chen Y., Jiang C., Zhang M., Pang Z., Shen B. Superconducting fault current limiter (SFCL) for a power electronic circuit: experiment and numerical modelling. *Superconductor Science and Technology*, 2022, vol. 35, no. 4, Art no. 045010.

[3] Koziel J., Gnat D., Majka M., Turgynbekov Y. The latest superconducting short current limiters - review of selected solutions. *Przegląd Elektrotechniczny*, 2022 vol. 98, no. 2, pp. 156-159.

[4] Fisher L.M., Alferov D.F., Akhmetgareev M.R., Budovskii A.I., Evsin D.V., Voloshin I.F., Kalinov A.V. Superconducting fault current limiter for railway transport. *Physics of Atomic Nuclei*, 2015, vol. 78, no. 14, pp. 1654-1657.

[5] Ruiz H.S., Zhang X., Coombs T.A. Resistive-type superconducting fault current limiters: concepts, materials, and numerical modeling. *IEEE transactions on applied superconductivity*, 2015, vol. 25, no. 3, pp. 1-5.

[6] Berger A., Noe M., Kudymow A. Test results of 60 kVA current limiting transformer with full recovery under load. *IEEE transactions on applied superconductivity*, 2011, vol. 21, no. 3, pp. 1384-1387.

[7] Kondratowicz-Kucewicz B., Wojtasiewicz G. The Proposal of a Transformer Model With Winding Made of Parallel 2G HTS Tapes With Transpositioners and its Contact Cooling System. *IEEE Transactions Applied Superconductivity*, 2018, vol. 28, no. 4., Art. no. 5500405.

[8] Moradnouri A., Ardeshiri A., Vakilian M., Hekmati A., Fardmanesh M. Survey on High-Temperature Superconducting Transformer Windings Design. *Journal of Superconductivity and Novel Magnetism*, 2020, vol. 33, no. 9, pp. 2581-2599.

[9] Hellmann S., Abplanalp M., Elschner S., Noe M. Current Limitation Experiments on a 1 MVA-Class Superconducting Current Limiting Transformer. *IEEE Transactions on Applied Superconductivity*, 2019, vol. 29, no. 5, pp. 1-7, Art. no. 5501706.

[10] Dai S., Ma T., Qiu Q., Zhu Z., Teng Y., Hu L. Development of a 1250-kVA Superconducting Transformer and Its Demonstration at the Superconducting Substation. *IEEE Transactions on Applied Superconductivity*, 2017, vol. 26, no. 1, pp. 1-7, Art. no. 5500107.

[11] Hellmann S., Abplanalp M., Hofstetter L., Noe M. Manufacturing of a 1-MVA-Class superconducting fault current limiting transformer with recovery-under-load capabilities. *IEEE Transactions on Applied Superconductivity*, 2017, vol. 27, no. 4, pp.1-6, Art. no. 5500305.

[12] Hu D., Li Z., Hong Z., Jin Z. Development of a single-phase 330kVA HTS transformer using GdBCO tapes. *Physica C: Superconductivity and its applications*, 2017, vol. 539, pp. 8-12.

[13] Liu G., Zhang G., Liu G., Wang H., Jing L. Experimental and numerical study of high frequency superconducting air-core transformer. *Superconducting Science Technology*,2021, vol. 34, no. 8, Art. no. 85011.

[14] Vysotsky V.S., Fetisov S.S., Zubko V.V., Zanegin S., Nosov A.A., Ryabov S.M., Bykovsky N.V. Development and test results of HTS windings for superconducting transformer with 1 MVA rated power. *IEEE Transactions on Applied Superconductivity*, 2017, vol. 27, no. 4, pp. 1-5., Art. no. 5500105.

[15] Shen B., Grilli F., Coombs T. Review of the AC loss computation for HTS using H formulation. *Superconductor Science and Technology*, 2020 vol. 33, no. 3, Art. no. 033002.

[16] Song W., Jiang Z., Zhang X., Staines M., Fang J., Sogabe Y., Amemiya N. AC loss simulation in a HTS 3-Phase 1 MVA transformer using H formulation. *Cryogenics*, 2018, vol. 94, pp. 14-21.

[17] Grilli F., Ashworth S. Measuring transport AC losses in YBCO-coated conductor coils. *Superconductor Science and Technology*, 2007, vol. 20, pp. 794-799.

[18] Surdacki P., Wozniak Ł. Influence of the HTS Winding Tape on Limiting the Transient Currents in Superconducting Transformers. *Energies*, 2022, vol. 15., no. 5., pp. 1-16., Art no. 1688.

[19] Nemdili S., Belkhiat S. Electrothermal Modeling of Coated Conductor for a Resistive Superconducting Fault-Current Limiter. *Journal of Superconductivity and Novel Magnetism*, 2013, vol. 26, no. 8., pp. 2713–2720.

[20] Samoilenkov S., Molodyk A., Lee S., Petrykin V., Kalitka V., Martynova I., Makarevich A., Markelov A., Moyzykh M., Blednov A. Customised 2G HTS wire for applications. *Superconductor Science and Technology*, 2016, vol. 29, pp. 1-10.

[21] Molodyk A., Samoilenkov S., Markelov A., Lee S., Petrykin V., Gaifullin M., Kesler L., Vasiliev A. Development and large volume production of extremely high current density $YBa_2Cu_3O_7$ superconducting wires for fusion. *Scientific Reports*, 2021, vol. 11, pp. 1-11., Art. no. 2084.

[22] Lee S., Petrykin V., Molodyk A., Samoilenkov S., Kaul A., Vavilov A., Vysotsky V., Fetisov S. Development and production of second generation high Tc superconducting tapes at SuperOx and first tests of model cables. *Superconductor Science and Technology*, 2014, vol. 27, no. 4, Art. no. 044022.

[23] Lei W., Jiaojiao W., Tian Y., Xiaoning H., Fushou X., Yanzhong L. Film boiling heat transfer prediction of liquid nitrogen from different geometry heaters. *International Journal of Multiphase Flow*, 2020, vol. 129, Art. no. 103294.

[24] Hu M., Zhou Q.B., Wang X., Tang F.P., Sheng J., Bian X.Y., Jin Z.J. Study of Liquid Nitrogen Insulation Characteristics for Superconducting Transformers. *IEEE Transactions on Applied Superconductivity*, 2022, vol. 32, no. 4, pp. 1-5, Art. no. 5500305.

[25] Zhou J., Chan W., Schwartz J. Quench Detection Criteria for $YBa_2Cu_3O_{7-\delta}$ Coils Monitored via a Distributed Temperature Sensor for 77 K Cases. *IEEE Transactions on Applied Superconductivity*, 2018, vol. 28, no. 5, Art. no. 4703012.

[26] Elshiekh M., Zhang M., Ravindra H., Chen X., Venuturumilli S., Huang X., Schoder K., Steurer M., Yuan W. Effectiveness of Superconducting Fault Current Limiting Transformers in Power Systems. *IEEE Transactions on Applied Superconductivity*, 2018, vol. 28, no. 3, Art. no. 5601607.

[27] Wojtasiewicz G. Fault current limitation by 2G HTS superconducting transformer - experimental investigation. *Acta Physica Polonica A*, 2016, vol. 130, no. 2, pp. 516–520.

Сведения об авторах.

Манусов Вадим Зиновьевич
д.т.н., профессор кафедры «СЭСП» Новосибирский государственный технический университет.
Область научных интересов: применение методов искусственного интеллекта для планирования и оптимизации режимов электроэнергетических систем
E-mail: manusov36@mail.ru

Иванов Дмитрий Михайлович
Аспирант кафедры «СЭСП» Новосибирский государственный технический университет.
Исследование и разработка высокотемпературных сверхпроводящих трансформаторов
E-mail: mrdemasi123@gmail.com

The Dynamic Sliding Mode Controller with Observer of Coincident Perturbations and States for Buck Converter of Fuel Cell Source

Darvish Falehi Ali

Department of Electrical Engineering, Shadegan Branch, Islamic Azad University, Shadegan, Iran

***Abstract*.** Buck converter has been widely used in the DC renewable energy system application. The Fuel Cell (FC) based DC renewable energy is offered as a high-performance and low-emission power supply, which replaces conventional DC sources. Its relevant control system has regulated the output voltage under input voltage and load resistance variations to track the desired reference signal. To control the current sensorless-based buck converter with matched and mismatched uncertainties, the system must be modeled in such a way that by measuring the output voltage, both the inductor current and system perturbations can be estimated. The purpose of the work is suggestion of a novel dynamic sliding mode controller (DSMC) based on observer of coincident perturbations and states (CSPO) to enhance its controllability and tracking performance. The significance of the work lies in low cost and reduced losses due to the inductor current measurement. Lacking an exact value for inductor current, it is not possible to estimate and compensate the perturbations caused by parametric uncertainties in the buck converter. These objectives were achieved by modeling in the canonical form. The canonical model somehow converts both the matched and mismatched perturbations into the matched perturbation, in which the system states and perturbations can be merely estimated using only an output voltage value and a CSPO. The most important results are the fastness and robustness of the DSMC to control the buck converter and compensate the effect of mismatched uncertainties and nonlinear disturbances and chattering phenomenon.

***Keywords*:** fuel cell, buck converter, canonical model, dynamic sliding mode controller, observer of coincident perturbations and states.

UDC: 621.039.533.6
DOI: https://doi.org/10.52254/1857-0070.2023.2-58.02

Controlerul modului de alunecare dinamic cu observator al perturbațiilor și stărilor coincidente pentru convertizorului buck al sursei de celule de combustibil

Darvish Falehi Ali,

Departmentul de Electrotehnică, secția Shadegan, Universitatea Islamică Azad, Shadegan, Iran.

Rezumat. Energia regenerabilă de curent continuu bazată pe celule de combustie (FC) este oferită ca sursă de energie de înaltă performanță și cu emisii reduse de energie care înlocuiește surse de curent continuu convenționale. Sistemul său de control relevant a reglat tensiunea de ieșire sub variațiile tensiunii de intrare și rezistenței la sarcină pentru a urmări semnalul de referință dorit. Pentru a controla convertizorul buck fără senzori de curent cu incertitudini corelate și nepotrivite, sistemul trebuie modelat în așa fel încât, prin măsurarea tensiunii de ieșire, să poată fi estimate atât curentul inductorului, cât și perturbațiile sistemului. Scopul lucrării este propunerea unui nou controler cu mod de alunecare dinamic (DSMC) bazat pe observatorul de perturbare și stării coincidente (CSPO) pentru a-și îmbunătăți controlabilitatea și performanța de urmărire. Semnificația lucrării constă în costuri reduse și pierderi reduse datorate măsurării curentului inductorului. În lipsa unei valori exacte pentru curentul inductor, nu este posibil să se estimeze și să se compenseze perturbațiile cauzate de incertitudinile parametrice în convertorul buck. Aceste obiective au fost atinse prin modelare în formă canonică. Modelul canonic convertește într-un fel atât perturbațiile potrivite, cât și cele nepotrivite în perturbație potrivită, în care stările și perturbațiile sistemului pot fi doar estimate folosind doar o valoare a tensiunii de ieșire și un CSPO. Cele mai importante rezultate sunt rezistența și robustețea DSMC pentru a controla convertorul buck și pentru a compensa efectul incertitudinilor nepotrivite și al perturbărilor neliniare și al fenomenului de vibrație.

Cuvinte-cheie: celule de combustie, convertorul buck, model canonic, controler al modului de alunecare dinamic, observator al perturbațiilor și stărilor coincidente.

Динамический регулятор скользящего режима с наблюдателем совпадающих возмущений и состояний для понижающего преобразователя топливного элемента

Дарвиш Фалехи Али
Кафедра электротехники, Шадеганский филиал, Исламский университет Азад, Шадеган, Иран

***Аннотация*.** Понижающий преобразователь широко используется в системах возобновляемых источников энергии постоянного тока. Возобновляемая энергия постоянного тока на основе топливных элементов (ТЭ) предлагается в качестве высокопроизводительного источника питания с низким уровнем выбросов, который заменяет традиционные источники постоянного тока. Его соответствующая система управления регулирует выходное напряжение в соответствии с входным напряжением и изменениями сопротивления нагрузки, чтобы отслеживать желаемый опорный сигнал. Для управления бездатчиковым понижающим преобразователем тока с согласованными и несогласованными неопределенностями система должна быть смоделирована таким образом, чтобы путем измерения выходного напряжения можно было оценить, как ток катушки индуктивности, так и системные возмущения. Целью работы является предложение нового контроллера динамического скользящего режима (DSMC), основанного на наблюдателе совпадающих состояний-возмущений (CSPO), для повышения его управляемости и эффективности отслеживания. Значимость работы заключается в дешевизне и снижении потерь за счет измерения тока индуктора. В отсутствие точного значения тока дросселя невозможно оценить и компенсировать возмущения, вызванные параметрическими неопределенностями в понижающем преобразователе. Эти цели были достигнуты путем моделирования в канонической форме. Каноническая модель каким-то образом преобразует как согласованные, так и несогласованные возмущения в согласованные возмущения, в которых состояния системы и возмущения можно просто оценить, используя только значение выходного напряжения и CSPO. Наиболее важными результатами являются быстродействие и надежность DSMC для управления понижающим преобразователем и компенсации влияния несогласованных неопределенностей, нелинейных возмущений и явления дребезга.

Ключевые слова: топливный элемент, понижающий преобразователь, каноническая модель, динамический регулятор скользящего режима, наблюдатель совпадающих переменных состояния и возмущений.

I. INTRODUCTION

DC power sources have been extensively used in various industrial applications, so an interface device is required to provide a variable output DC voltage with respect to a constant input DC voltage. The DC-DC converters like an AC transformers can provide the desired DC voltage by tuning the duty cycle. Their various applications are commonly based on voltage regulator to convert unregulated DC voltage to optimum regulated DC voltage [1]. DC-DC converters have satisfactorily seen positions in electric vehicles, carrying systems, lifting forks and some mechanisms like that. They are characterized by precise acceleration control, high efficiency and fast dynamic response. Other applications of DC-DC converters are in compensation of reactive power, dynamic braking of DC motors and optimization of AC power networks [2-4]. There are two advanced DC-DC converter types called two-quadrant and four-quadrant. The first type is used in automatic control systems of renewable sources such as solar cells and wind turbines [5]. The second type is also used in systems with electric braking of DC motors such as transport systems and hybrid cars [6].

Buck converter as an inductor-based switch mode converter is used for step-down voltage conversion. The main purpose of buck converters is to regulate the output voltage by adjusting the input voltage and load resistance, and track different values of the reference voltage. Hence, a number of strategies have been proposed to regulate the output voltage of buck converters under input voltage and load resistance variations [7-9]. The stepping-based non-linear control is proposed for buck converter with uncertainty in load resistance [10], the integral sliding surface is proposed in [11] to control the power supply integrated with buck converter. An adaptive-neural backstepping control strategy is proposed for the buck converter to track the angular speed of the permanent magnet DC motor [12]. In [13], a cascade control structure based on hybrid Sliding mode Control (SMC) and PID is proposed to soft start the DC motor.

One of the effective control strategies to control such these systems is sliding mode controller due to its robustness against the uncertainties and perturbations [14]. The conventional sliding mode controllers are only robust against the matched uncertainties and perturbations, while the uncertainties expressed in the buck converter are mismatched. Some works have been performed to deal with the mismatched uncertainty in which the sign function is considered in the system's input signal, which causes the chattering phenomenon [15-17].

Another major sliding mode control problem is the chattering phenomenon, which has been alleviated using four common methods: boundary layer [18], adaptive boundary layer [19], high-order sliding mode controller [20] and dynamic sliding mode controller (DSMC) [21]. In the adaptive boundary layer method, the system immutability is lost. In the high-order method, the chattering phenomenon is eliminated by transferring the switching to the high derivative of the sliding surface in case of existence of the system model derivative. But then, high frequency fluctuations and chattering phenomenon caused by the sign function have been alleviated in the dynamic method via considering an integrator before the system. In paper [22], a chattering elimination method is proposed for adaptive sliding mode controller in the form of the multi-input-output systems with matched and mismatched uncertainties with assuming the bounded uncertainty derivatives. Multilevel sliding control is also a robust approach against the mismatched uncertainties, whereas it depends on the input derivatives [23]. Other strategies such as the perturbation observer and inertial delay control have also been proposed to solve this problem [24]. Likewise, a robust dynamic surface control is proposed with an approximation of the sign function avoid the implementation difficulty of multiple-surface sliding control [25]

To design the sliding mode controller for buck converter, all modes are required which can be worked out by measuring the inductor current. Shunt resistance is usually used to measure the current with a current measuring amplifier. The power losses would be increased in the converters with high inductor current. Therefore, this problem creates a great interest to develop the sensorless control techniques for DC-DC converters. An adaptive current sensorless control is proposed for buck converter to improve the transmit behaviour, controllability, and fault tolerability [26]. The inductor current can be estimated by the input current and the output voltage along with a first-order filter [27]. The common drawback of such these methods is measuring the all inputs and output voltage which can be solved by observer of coincident perturbations and states (CSPO) so that the inductor current to be estimated to reduce the costs and losses due to the inductor current measurement.

Based on the proposed observer, the output voltage of the buck converter is measured to estimate the inductor current. Likewise, the designed DSMC based on CSPO is robust and invariant against the mismatched uncertainties that exist in the buck converter due to the input voltage and load resistance. As for the dynamic design of this controller, its chattering-free feature is proven due to eliminating the sign function of the sliding mode controller. Lacking an exact value for inductor current, it is not possible to estimate and compensate the perturbations caused by parametric uncertainties in the buck converter. To solve this problem, this converter has been essentially modeled in the canonical form. The canonical model somehow converts both the matched and mismatched perturbations into the matched perturbation, in which the system states and perturbations can be merely estimated using only an output voltage value and a CSPO. The simulation results demonstrate the fastness and robustness of the DSMC to control the buck converter and compensate the effect of mismatched uncertainties and nonlinear disturbances and chattering phenomenon.

II. FUEL CELL FEATURES AND FUNCTIONS

FC source actually operates as a battery albeit oxygen and hydrogen or methane are used as its fuels, indeed, some important kinds are: Proton Exchange Membrane Fuel Cell (PEMFC), Solid Oxide Fuel Cell (SOFC) [28]. The fuels have been electrolytically attained using a single system which operates in either electrolyzer state or fuel cell state [29]. Given the low operating temperature, high energy density and quick starting feature, the PEMFC has found significant attraction among different FC types [30]. Likewise, it has been being successfully advanced as a reliable and portable power source to meet the power demands of various domestic applications. Analogous response of anode and cathode in the Membrane Electrode Assembly (MEA) for can be expressed by [31]:

The anode response: $H_2 \rightarrow 2H^+ + 2e^-$

The cathode response: $1/2O_2 + 2H^+ + 2e^- \rightarrow H_2O$

MEA can be seen in the single PEMFC schematic presented in Fig. 1. MEA is commonly put into two metal platters, which are mutually correlated to provide a bipolar platter when cells are stacked for higher voltages.

The FC performance has been practically distinguished according to the polarization curve, which depicts the FC output voltage in terms of the load current. Based on the Tafel equation

[32], the stack voltage can be presented as follows:

$$V_{stack} = V_{open} - V_{o\_mic} - V_{activation} - V_{concentraton} \quad (1)$$

Where

$$V_{open} = N_0 \cdot \left(E^0 + E^1\right) = N_0 \cdot \left(-\frac{\Delta \bar{g}_f^0}{2F} + \frac{RT}{2F} ln\left(\frac{p_{H_2} \cdot \sqrt{p_{o_2}}}{p_{H_2 o}} \right) \right) \quad (2)$$

$$V_{o\_mic} = R_{FC} \cdot (i + i_n) = R_{FC} \cdot I_{dc} \quad (3)$$

$$V_{activation} = N_0 \cdot \frac{RT}{2\alpha F} ln\left(\frac{I_{dc}}{I_0} \right) \quad (4)$$

$$V_{concenteration} = -c\, ln\left(1 - \frac{I_{dc}}{I_{lim}}\right) \quad (5)$$

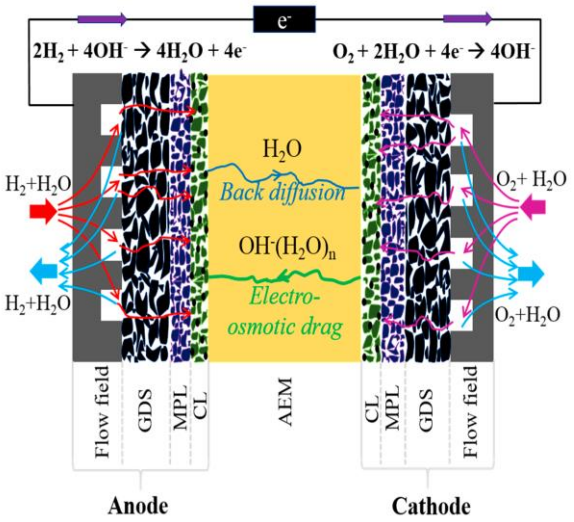

Fig. 1. Schematic of a single conventional PEMFC.

Where, N_0 indicates the number of cells, V_0 indicates the open cell voltage, R is the ideal gas constant, T is the stack temperature, F is the Faraday constant, P_{H2O}, P_{H2} and P_{O2} respectively are the water, hydrogen and oxygen partial pressures, P_O indicates the reference pressure, α indicates the charge transfer constant, I_{dc} represents the stack current, I_{Lim} represents the limited stack current, I_0 represents the stack total current density and c is the experimental constant for concentrate voltage.

The steady-state voltage considering one cell along with the power in terms of current density according to Eq. 1 can be attained as presented in Fig. 2.

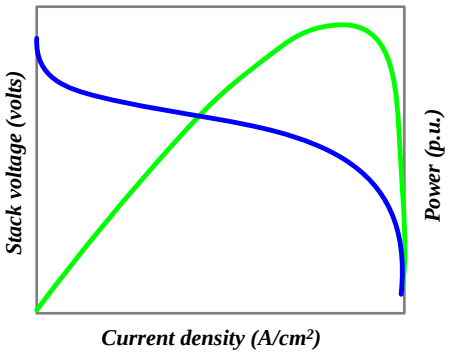

Fig. 2. Stack voltage along with power in terms of current density.

III. State Space Modeling of Buck Converter

The main operation and concept of the buck converter related to the continuous conduction, output voltage ripple and duty cycle have been here explained. Then, the state space of the buck converter is calculated and its controllability and observability are investigated. The effect of parametric uncertainties is considered as an external perturbation for the test system which is due to the mismatched perturbation.

A. Design and Operation of Buck Converter

This converter operates like a step-down transformer that reduces the input DC voltage to the required output DC voltage. This converter has been commonly used to regulate the output voltage of DC power supplies regulator and speed control of DC motors. The buck converter structure is presented in in Fig. 3. In this circuit, i_L is the inductor current, V_O is the output voltage and u is the control input. This converter can operate in both modes of continuous and discontinuous conduction modes which are determined by the inductor current. In the case of continuous inductor current, the values of the embedded elements in the converter along with the duty cycle are designed so that the inductor current is not zero at discharge period. In the case of discontinuous inductor current, the inductor current becomes zero at each discharge period.

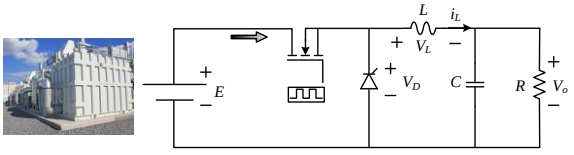

Fig. 3. Buck converter structure.

The buck converter's has been triggered with the period of T_s, ON-time of t_{on} and OFF-time of t_{off}. The duty cycle of this converter can be defined by:

$$D = t_{on}/T \tag{6}$$

The average value of the diode voltage $\bar{V}_d$, can be calculated by averaging its waveform over a switching period. The diode voltage in a switching period with assumption of its ideality is shown in Fig. 4. The average value of the diode voltage is also attained by the following equation.

$$\bar{V}_d = \frac{1}{T_s}\int_0^{T_s} V_d(t)dt = DE \tag{7}$$

It is obvious that, the average value of the diode voltage depends on the duty cycle.

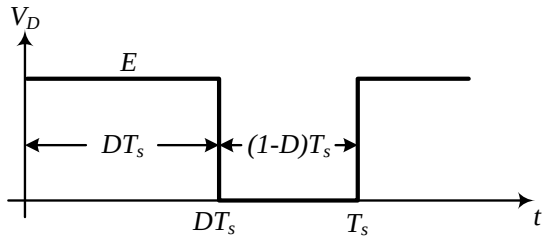

Fig. 4. Diode voltage in a switching period.

Buck converter has two operating modes. The first case is to conduct the switch and flow the current from the input source as shown in Fig. 5. Discarding the transient condition of the buck converter, the inductor voltage is calculated as follows [33].

$$V_L = E - V_o \tag{8}$$

The inductor currents during ON and OFF times can be respectively presented as follows:

$$V_L = L\frac{di_l}{dt} = E - V_o \rightarrow \frac{di_l}{dt} = \frac{E - V_o}{L} \tag{9}$$

$$V_L = -V_o \rightarrow \frac{di_l}{dt} = \frac{-V_o}{L} \tag{10}$$

According to the continuous mode of the inductor current which is presented in Fig. 5, it reaches a maximum value with a fixed slope when the switch is on, and then decreases with a constant negative slope when the switch is off. Note that, the initial and final values of the current are the same in each period. Thus, the net change of the inductor current, and consequently its voltage average in each period is zero. Hence, the output voltage can be calculated as follows:

$$\frac{E - V_o}{L}DT_s = \frac{V_o}{L}(1-D)T_s \rightarrow \frac{V_o}{E} = D \tag{11}$$

Likewise, the maximum and minimum inductor current as well as the output voltage ripple can be formulated as follows:

$$i_l^{max} = \frac{DE}{2RL}\left(2L + (1-D)RT_s\right) \tag{12}$$

$$i_l^{min} = \frac{DE}{2RL}\left(2L - (1-D)RT_s\right) \tag{13}$$

$$V_o^{ripple} = \frac{RT_s\bar{V}_o}{L}(1-D) \tag{14}$$

The output voltage of the buck converter can be considered as a sum of two terms. That is to say, the average value of the output voltage V_0 and its ripple V_o^{ripple}:

$$V_o(t) = \bar{V}_o + V_o^{ripple} \tag{15}$$

Providing well design of the circuit elements and correct operation of the circuit, the output voltage ripple is small and negligible as compared to its average value, i.e. the output voltage is approximately equal to the average value of the output voltage.

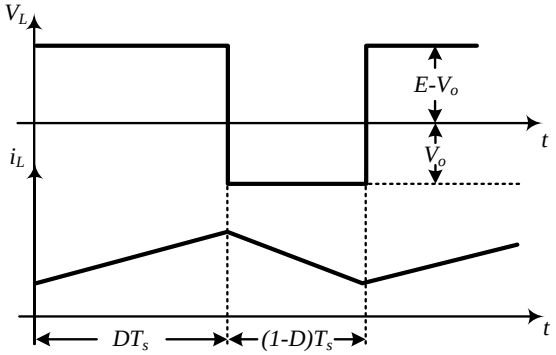

Fig. 5. Current and voltage of inductor in continuous mode.

B. State Space Modeling of Buck Converter

As to the presence of an inductor and a capacitor in the buck converter circuit, it is second order differential equation. To calculate its relevant

equations, the system is evaluated under two states, i.e. ON and OFF switch conditions. At first, the switch is considered to be ON. The state equations related to the inductor current and the capacitor voltage are presented as follows:

$$L\frac{di_l}{dt} = E - V_o \tag{16}$$

$$C\frac{dV_o}{dt} = i_l - \frac{V_o}{R} \tag{17}$$

And second, the switch becomes OFF.
The state equations related to the inductor current and the capacitor voltage are presented as follows:

$$L\frac{di_l}{dt} = -V_o \tag{18}$$

$$C\frac{dV_o}{dt} = i_l - \frac{V_o}{R} \tag{19}$$

Substituting the abovementioned equations, the buck converter state space are obtained as follows:

$$\frac{di_l}{dt} = -\frac{V_o}{L} + \frac{E}{L}u \tag{20}$$

$$\frac{dV_o}{dt} = \frac{i_l}{C} - \frac{V_o}{RC} \tag{21}$$

Where, u ∈ {0 1}.
Also, the buck converter equations can be represented by the following linear state space equations:

$$\dot{x} = Ax + Bu \tag{22}$$

Where:

$$A = \begin{pmatrix} -\frac{1}{RC} & \frac{1}{C} \\ -\frac{1}{L} & 0 \end{pmatrix}, \quad B = \begin{pmatrix} 0 \\ \frac{E}{L} \end{pmatrix} \tag{23}$$

Where, the system is both controllable and observable.

$$y = V_o \tag{24}$$

C. Buck Converter Modelling with Parametric Uncertainties

In fact, there are no exact values for the buck converter's components. This difference from the exact values can be due to the piece fabrication, physical and environmental conditions. Therefore, these conditions must be considered to design a robust and accurate controller.
Assuming the nominal elements' values are R_n, C_n, L_n, and E_n, the system model is obtained as follows.

$$\frac{dV_o}{dt} = \frac{i_l}{C_n} - \frac{V_o}{R_nC_n} + \left(\frac{i_l}{C} - \frac{i_l}{C_n}\right) + \left(\frac{V_o}{R_nC_n} - \frac{V_o}{RC}\right) \tag{25}$$

$$\frac{di_l}{dt} = -\frac{V_o}{L_n} + \frac{E_n}{L_n}u + \left(\frac{V_o}{L_n} - \frac{V_o}{L}\right) + \left(\frac{E}{L} - \frac{E_n}{L_n}\right)u \tag{26}$$

Where, $i_1 / C_n - V_o / R_nC_n$ *and* $E / L_n u - V_o / L_n$ are related to the nominal model of the system with the determinate values. But,

$$\left(i_1 / C - i_1 / C_n\right) + \left(V_o / R_nC_n - V_o / RC\right) \textit{ and } \ldots$$
$$+\left(V_o / L_n - V_o / L\right) + \ ) + \left(E / L - E / L_n\right)$$

due to the difference between the actual value and the nominal value of the parameters are indeterminate. Therefore, they are considered as external disturbances to the system.

$$\frac{dV_o}{dt} = \frac{i_l}{C_n} - \frac{V_o}{R_nC_n} + d_1 \tag{27}$$

$$\frac{di_l}{dt} = -\frac{V_o}{L_n} + \frac{E_n}{L_n}u + d_2 \tag{28}$$

Where,

$$d_1 = \left(\frac{i_l}{C} - \frac{i_l}{C_n}\right) + \left(\frac{V_o}{R_nC_n} - \frac{V_o}{RC}\right) \tag{29}$$

$$d_2 = \left(\frac{V_o}{L_n} - \frac{V_o}{L}\right) + \left(\frac{E}{L} - \frac{E_n}{L_n}\right)u \tag{30}$$

If the actual values are exactly equal to the nominal values, the perturbations d_1 and d_2 become zero.
Due to the limited difference between the nominal values and the actual values of the parameters, the perturbation values are also limited. In addition, according to the definitions of matched and mismatched perturbations, d_1 and d_2 are respectively mismatched and matched perturbations.
The conventional sliding mode controllers are only robust against the matched uncertainties and

perturbations, while the uncertainties expressed in the buck converter are mismatched. Since, one of the paper aims is to remove the inductor current sensor. This problem makes the controller unable to remove the disturbance effect. Hence, the buck converter's state space equations have been represented in the canonical form to overcome this problem.

D. Buck Converter Modeling in Canonical Form

The buck converter uncertainties can be considered as matched and mismatched disturbances in the system. Due to indeterminate values of these perturbations, these perturbations can be estimated using an accurate observer. Providing existence of the output voltage and the inductor current, the perturbations can be estimated. But, the main challenge is related to the inductor current which is not measured. To control the current sensorless-based buck converter with matched and mismatched uncertainties, the system must be modeled in such a way that by measuring the output voltage, both the inductor current and system perturbations can be estimated. In the canonical model, state variables are considered in such a way that the effect of matched and mismatched perturbations to be appeared in the form of a matched perturbation. Therefore, the proposed canonical model of the buck converter can be presented as follows:

$$\dot{q}_1 = q_2 \tag{31}$$

$$\dot{q}_2 = -\frac{q_1}{L_n C_n} - \frac{q_2}{R_n C_n} + \frac{E_n}{L_n C_n}(u + d) \tag{32}$$

Hence, both the matched and mismatched perturbations can be considered as a matched perturbation. Considering q_2 as the output of this model which is the output voltage of the buck converter, both the q_1 and d can be estimated.

E. Canonical Coincident State-Perturbation Observer Design

A CSPO is modeled to estimate the states and perturbations of the buck converter model. The equations for this observer are given in as follows:

$$\dot{\hat{q}}_1 = \hat{q}_2 + l_{11}(q_1 - \hat{q}_1) \tag{33}$$

$$\dot{\hat{q}}_2 = -\frac{\hat{q}_1}{L_n C_n} - \frac{\hat{q}_2}{R_n C_n} + \frac{E_n}{L_n C_n}\left(u + \hat{d}\right) + l_{11}(q_1 - \hat{q}_1) \tag{34}$$

$$\dot{\hat{d}} = l_{33}(q_1 - \hat{q}_1) \tag{35}$$

In this regard, $\hat{q}_1$, $\hat{q}_2$ and $\hat{d}$ are respectively the estimation of q_1, q_2 and d. l_{11}, l_{22} and l_{33} are the observer gains. Let consider the estimation error of each variable by $\tilde{q}_1 = q_1 - \hat{q}_1$, $\tilde{q}_1 = q_1 - \hat{q}_1$ and $\tilde{d} = d - \hat{d}$. Hence, the estimation error can be obtained as follows:

$$\dot{\tilde{q}}_1 = \tilde{q}_2 - l_{11}\tilde{q}_1 \tag{36}$$

$$\dot{\tilde{q}}_2 = -\frac{\tilde{q}_1}{L_n C_n} - \frac{\tilde{q}_2}{R_n C_n} + \frac{E_n}{L_n C_n}\tilde{d} - l_{22}\tilde{q}_1 \tag{37}$$

$$\dot{\tilde{d}} = \dot{d} - l_{33}\tilde{q}_1 \tag{38}$$

It can be generally represented by:

$$\dot{\tilde{q}} = A_o\tilde{q} + B_o\dot{d} \tag{39}$$

Where:

$$\tilde{q} = \begin{bmatrix}\tilde{q}_1 & \tilde{q}_2 & \tilde{d}\end{bmatrix}^T \tag{40}$$

$$A_o = \begin{pmatrix} -l_{11} & 1 & 0 \\ -\left(\frac{1}{L_n C_n} + l_{22}\right) & -\frac{1}{R_n C_n} & \frac{E_n}{L_n C_n} \\ -l_{33} & 0 & 0 \end{pmatrix}, \tag{41}$$

$$B_o = \begin{pmatrix} 0 \\ 0 \\ 1 \end{pmatrix}$$

The characteristic equation of the matrix A_0 is given as follows:

$$s^3 + \left(l_{11} + \frac{1}{R_n C_n}\right)s^2 + \left(l_{22} + \frac{1}{L_n C_n} + \frac{l_{11}}{R_n C_n}\right)s + \ldots \\ \ldots \frac{l_{33}E_n}{L_n C_n} = 0 \tag{42}$$

The values of observer gains along with l_{11}, l_{22} *and* l_{33} are determined somehow the eigenvalues of the A_0 matrix to be located at the left side of the imaginary axis.

IV. DYNAMIC SLIDING MODE CONTROLLER BASED ON COINCIDENT STATE-PERTURBATION OBSERVER

Unlike conventional sliding mode controllers, the dynamical sliding mode controller engages an integrator in the control law to diminish the

effect of the chattering phenomenon. This control method can give different characteristics to the control structure by selecting different sliding surfaces. The uncertainties in the buck converter can be considered as matched and mismatched perturbations in the system. Since these perturbations are not determinate, they must be estimated using an accurate observer. Given that both the output voltage and the inductor current are measured in the existing system, it is easy to estimate these perturbations using observers. But, the main challenge is related to the inductor current which is not measured. To control the current sensorless-based buck converter with matched and mismatched uncertainties, the system must be modeled in such a way that by measuring the output voltage, both the inductor current and system perturbations can be estimated. Therefore, the canonical model of the buck converter is provided in in the previous section.

As mentioned before, dynamic sliding mode controller is essentially presented to reduce the chattering effect. Also, due to being current sensorless, the sliding surface is selected so that there is no need for the inductor current and reference current, and only the output voltage and reference input voltage along with its derivatives are available. Having the estimated values of the variables q_1 and q_2, the sliding surface is considered as follows:

$$e = \hat{q}_1 - q_1^* \tag{43}$$

$$s = \dot{e} + \lambda e = \left(\dot{\hat{q}}_1 - \dot{q}_1^*\right) + \lambda\left(\hat{q}_1 - q_1^*\right) = \left(\hat{q}_2 + l_{11}(q_1 - \hat{q}_1) - \dot{q}_1^*\right) + \lambda\left(\hat{q}_1 - q_1^*\right) \tag{44}$$

$$\dot{s} = \left(\dot{\hat{q}}_2 + l_{11}\left(\dot{q}_1 - \dot{\hat{q}}_1\right) - \ddot{q}_1^*\right) + \lambda\left(\hat{q}_2 + l_{11}(q_1 - \hat{q}_1) - \dot{q}_1^*\right) = \left(-\frac{\hat{q}_1}{L_n C_n} - \frac{\hat{q}_2}{R_n C_n} + \frac{E_n}{L_n C_n}\left(u + \hat{d}\right) + l_{22}(q_1 - \hat{q}_1) + l_{11}\left(\dot{q}_1 - \dot{\hat{q}}_1\right) - \ddot{q}_1^*\right) + \lambda\left(\hat{q}_2 + l_{11}(q_1 - \hat{q}_1) - \dot{q}_1^*\right) \tag{45}$$

$$\ddot{s} = \left(\begin{array}{l} -\frac{\dot{\hat{q}}_1}{L_n C_n} - \frac{\dot{\hat{q}}_2}{R_n C_n} + \frac{E_n}{L_n C_n}\left(\dot{u} + \dot{\hat{d}}\right) + l_{22}\left(\hat{q}_2 - \dot{\hat{q}}_1\right) + \\ l_{11}\left(\dot{\hat{q}}_2 - \left(\dot{\hat{q}}_2 + l_{11}\left(q_2 - \dot{\hat{q}}_1\right)\right)\right) - \dddot{q}_1^* \end{array}\right) + \lambda\left(\dot{\hat{q}}_2 + l_{11}\left(q_2 - \dot{\hat{q}}_1\right) - \ddot{q}_1^*\right) \tag{46}$$

According to the sliding surface derivative, which is presented as follows:

$$\dot{s} = -k \cdot \mathrm{sign}(s) \tag{47}$$

The control law can be represented formulated as follows:

$$\dot{u} = \dot{u}_{eq} - k \cdot sign(s) = \frac{L_n C_n}{E_n}\left(\begin{array}{l} \frac{\dot{\hat{q}}_1}{L_n C_n} + \frac{\dot{\hat{q}}_2}{R_n C_n} - l_{22}\left(\hat{q}_2 - \dot{\hat{q}}_1\right) - l_{11}\left(\dot{\hat{q}}_2 - \left(\dot{\hat{q}}_2 + l_{11}\left(q_2 - \dot{\hat{q}}_1\right)\right)\right) + \\ \dddot{q}_1^* - \lambda\left(\dot{\hat{q}}_2 + l_{11}\left(q_2 - \dot{\hat{q}}_1\right) - \ddot{q}_1^*\right) - \frac{E_n}{L_n C_n}\dot{\hat{d}} \end{array}\right) - \ldots - ksign(s) \tag{48}$$

As can be seen from the control law, there is no need to measure the values of output voltage and inductor current, while the controller has tracked the reference voltage without dependence on the values of output voltage and current. The existence of the integrator in this control law eliminates the chattering phenomenon, and also increasing the value of the parameter k cannot exacerbate this phenomenon. One of the great advantages of this method is the lack of need to measure the inductor current and output voltage, which can significantly reduce production costs in practical applications.

V. SIMULATION RESULTS AND VALIDATION

This section has essentially focused on the designed control scheme results, and then analysis and validation. For better understanding the difference between the proposed control scheme and others, the results of each of the controllers were taken into account for the buck converter system. The buck converter circuit consists of components whose nominal values are given in Table 1. In this circuit, it is assumed that the diode and the switch are ideal.

Table 1. Nominal values of buck converter parameters

Components	Parameters	Nominal values	Unit
Resistance	R	15	Ω
Capacitor	C	125	μF
Inductor	L	200	mH
Voltage source	E	20	V
Switching frequency	f_s	10	kHz

A. Buck converter control under certain parameters and nominal condition

To design and analyze the sliding mode controller, the gain value is considered k=1. The output voltage and inductor current in which the actual values of the parameters are exactly equal to the nominal values are presented in Fig. 6 and Fig. 7. As to Fig. 8, the chattering phenomenon is enormous in duty-cycle despite no consideration of uncertainty in the system that must be inevitably passed through a limiter. This method can deteriorate the system controllability

and stability. In some cases, instead of the sign function, the saturation and tangent functions are used to reduce the chattering phenomenon, but the system controllability and stability fall into the deleterious condition.

B. Buck converter control under parametric uncertainty

In this section, it is considered that the value of the resistance changes from 15 to 10Ω in 0.2s which remains for 0.5s, whereas its value instantly reaches to 20Ω which stays for 1s.

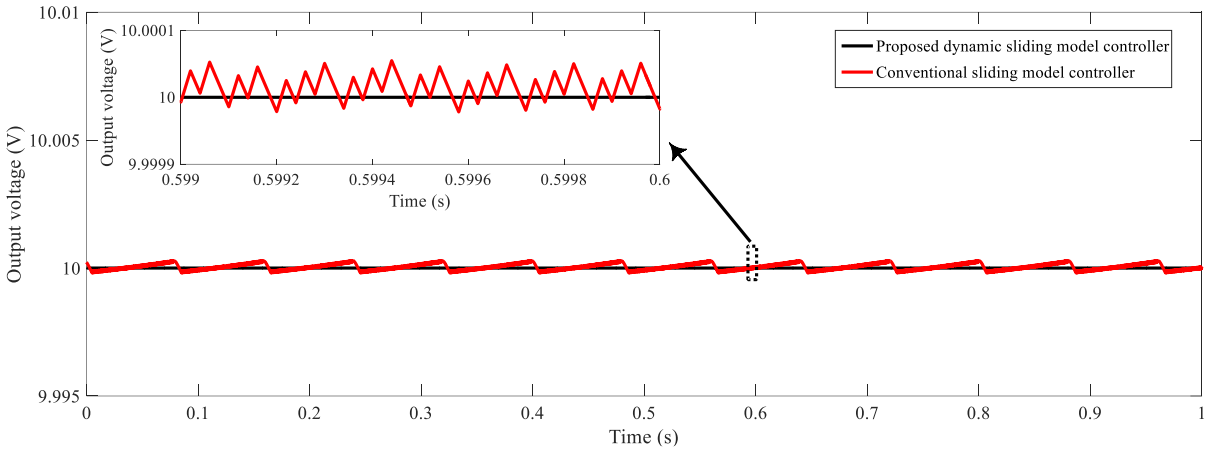

Fig. 6. Output voltage with conventional sliding mode controller under certain parameters.

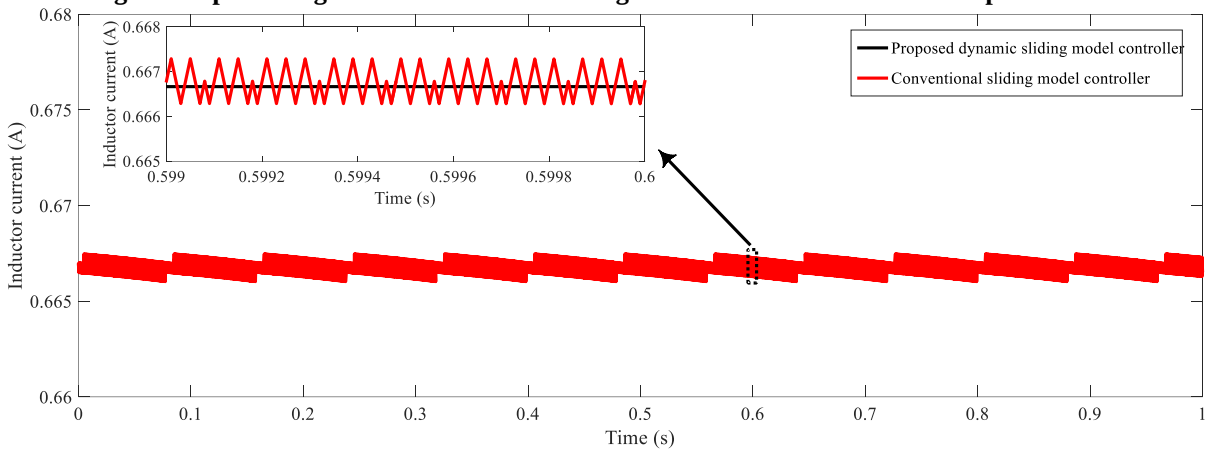

Fig. 7. Inductor current with conventional sliding mode controller under certain parameters.

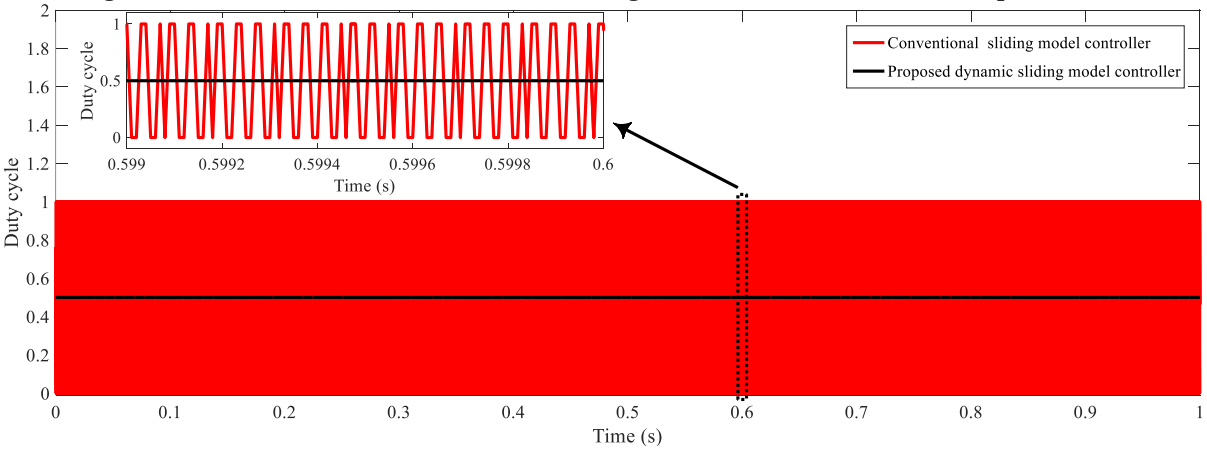

Fig. 8. Duty cycle with conventional sliding mode controller under certain parameters.

The output voltage and inductor current in which the actual values of the parameters are exactly equal to the nominal values are presented in Fig. 9 and Fig. 10. Also, the chattering phenomenon of the duty-cycle according to Fig. 11 has been significantly reduced as compared to discarding the system uncertainty. This uncertainty affects the performance of the closed-loop system, and

the output voltage and inductor current have relatively deviated from the nominal value.

The simulation results validate the robust performance of the proposed dynamic sliding mode controller as compared to the conventional sliding mode controller under this parametric uncertainty. The ability to reduce chatting of this controller was also confirmed.

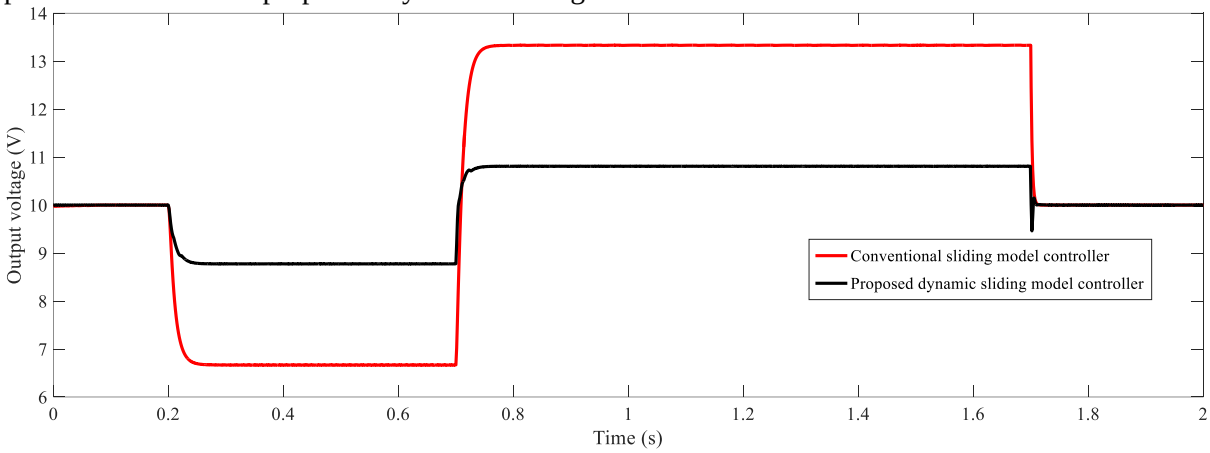

Fig. 9. Output voltage with conventional sliding mode controller under certain parameters.

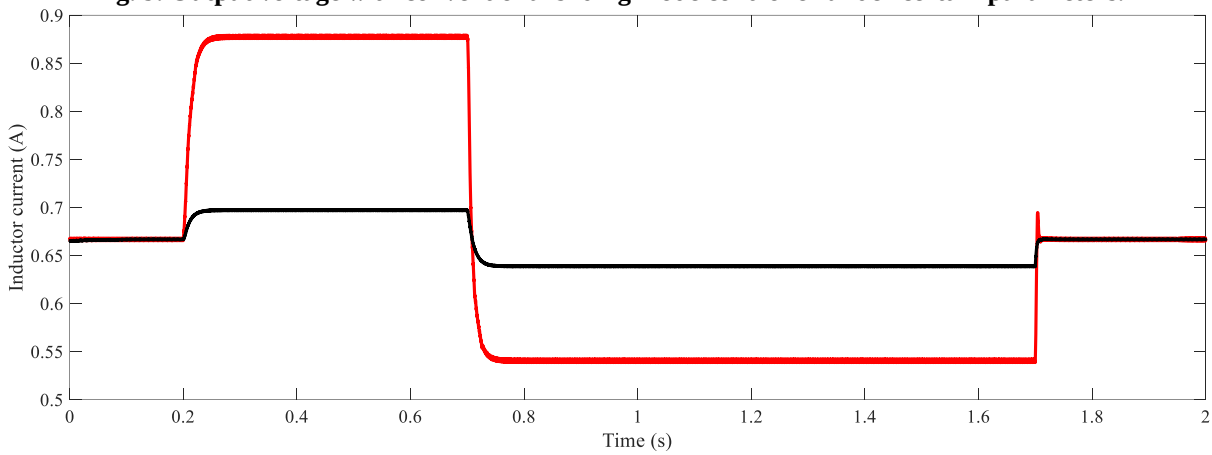

Fig. 10. Inductor current with conventional sliding mode controller under certain parameters.

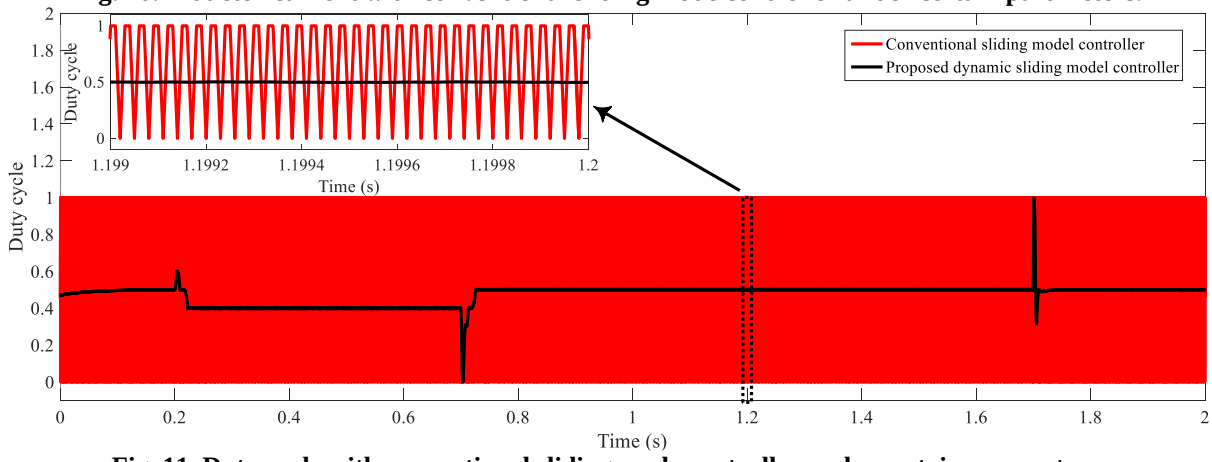

Fig. 11. Duty cycle with conventional sliding mode controller under certain parameters.

C. Buck converter control results with CSPO-based DSMC under parametric uncertainty

The previous uncertainty is considered for this section. Fig. 12 and Fig. 13 have respectively the output voltage and inductor current in which the actual values of the parameters are accurately equal to the nominal values. The duty-cycle curve presented in Fig. 14 has transparently validated the significant diminishing the chattering phenomenon. The CSPO-based

DSMC even with presence of parametric uncertainty is capable and efficient to reduce the effect of uncertainty and promptly retrieve the voltage to its nominal value. In fact, the proposed controller reduces the effect of perturbations due to parametric uncertainty by measuring the shortcomings of conventional sliding mode controllers without measuring the inductor current. The results validate the robust performance of the proposed controller.

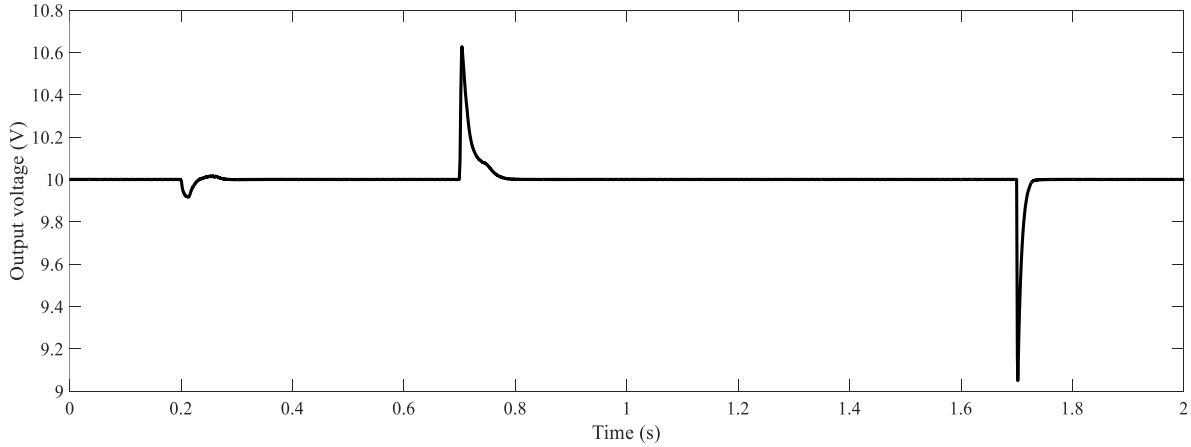

Fig. 12. Output voltage with conventional sliding mode controller under certain parameters.

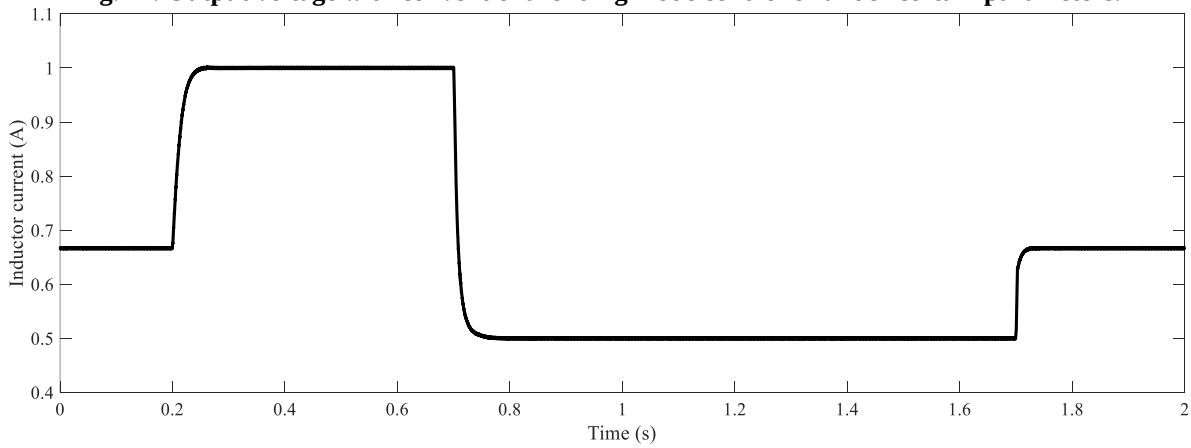

Fig. 13. Inductor current with conventional sliding mode controller under certain parameters.

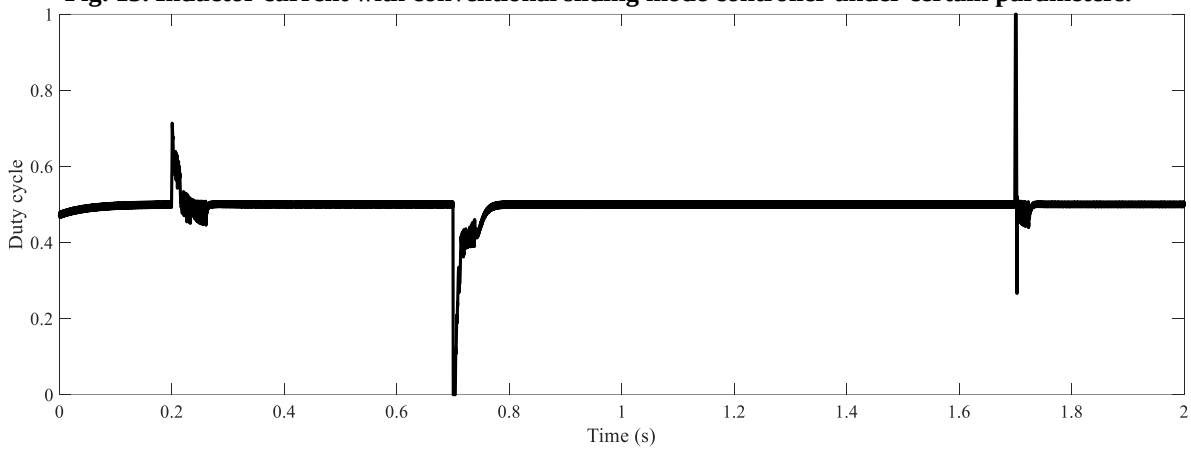

Fig. 14. Duty cycle with conventional sliding mode controller under certain parameters.

VI. CONCLUSION

The system control of buck converter is functionally designed to adjust the output voltage of fuel cell during the input voltage and load resistance variation, and also track different reference voltages. One effectual strategy to control such these systems is to implement the sliding mode controller. Conventional sliding controllers are only robust against matched uncertainties and perturbations, while the uncertainties expressed in the buck converter are mismatched and the sliding mode controllers are mismatched against these perturbations. Therefore, this paper proposes a novel dynamic

sliding mode controller based on coincident state-perturbation observer to reduce the impacts of mismatched perturbation and enhance controllability and tracking performance of the buck converter. Another salient problem related to the sliding mode controllers is the chattering phenomenon which is effectively solved by the proposed controller.

Due to matched and mismatched nature of this system, the inductor current must be essentially measured to estimate them. To overcome this problem, the buck converter has been modeled in canonical form that both perturbation types are appeared in matched perturbation to easily estimate the perturbations by observer, and also there is no need to measure the inductor current. To sum up, the results can be presented as follows:

1- Elimination of chattering phenomenon using proposed sliding mode controller

2- Elimination of inductor current sensor to estimate the perturbation using canonical model of buck converter

3- Reduction of the perturbation impacts caused by parametric uncertainties to enhance controllability and tracking performance of the buck converter

REFERENCES

[1] Ismail A. A. A., Elnady A., "Advanced Drive System for DC Motor Using Multilevel DC/DC Buck Converter Circuit," *IEEE Access*, 2019, vol. 7, pp. 54167–54178.

[2] Turksoy A., Teke A., Alkaya A., "A comprehensive overview of the dc-dc converter-based battery charge balancing methods in electric vehicles," *Renewable and Sustainable Energy Reviews*, 2020, vol. 133, pp. 110274

[3] Patel R., Chudamani R., "Stability analysis of the main converter supplying a constant power load in a multi-converter system considering various parasitic elements," *Engineering Science and Technology, an International Journal*, 2020, vol. 23, no. 5, pp. 1118-1125

[4] Faessler B., Kepplinger P., Petrasch J., "Field testing of repurposed electric vehicle batteries for price-driven grid balancing," *Journal of Energy Storage*, 2019, vol. 21, pp. 40-47.

[5] Alajmi B. N., Marei M. I., Abdelsalam I., "A Multiport DC–DC Converter Based on Two-Quadrant Inverter Topology for PV Systems," *IEEE Transactions on Power Electronics*, 2021, vol. 36, no. 1, pp. 522–532.

[6] Chaoui H., Alzayed M., Okoye O., Khayamy M., "Adaptive Control of Four-Quadrant DC-DC Converters in both Discontinuous and Continuous Conduction Modes," *Energies*, 2020, vol. 13, no. 16, pp. 4187.

[7] Durán E., Litrán S. P., Ferrera M. B., "Configurations of DC–DC converters of one input and multiple outputs without transformer," *IET Power Electronics*, 2020, vol. 13, no. 12, pp. 2658-2670.

[8] Alarcón O. G., Valenzuela J. M., "Analysis and Design of a Controller for an Input-Saturated DC–DC Buck Power Converter," *IEEE Access*, 2019, vol. 7, pp. 54261–54272.

[9] Mary A. H., Miry A. H., Miry M. H., "System uncertainties estimation based adaptive robust backstepping control for DC buck converter," *International Journal of Electrical and Computer Engineering*, 2021, vol. 11, , no. 1, pp.347-355.

[10] Rocha E. M., Barra W., Lucas K. E., Medeiros R. L. P., Benavides D. A. V., "Design and Experimental Assessment of a Robust Voltage Control for DC-DC Converters Considering Components Parametric Uncertainties," *IEEE Access*, 2020, vol. 8, pp. 109217-109231.

[11] Naik B. B., Mehta A. J., "Sliding mode controller with modified sliding function for DC-DC Buck Converter," *ISA transactions*, 2017, vol. 70, pp. 279-287.

[12] Nizami T. K., Chakravarty A., Mahanta C., "Design and implementation of a neuro-adaptive backstepping controller for buck converter fed PMDC-motor," *Control Engineering Practice*, 2017, vol. 58, pp. 78-87.

[13] Ortigoza R. S., Guzmán V. M. H., Cruz M. A., Carrillo D. M., "DC/DC Buck Power Converter as a Smooth Starter for a DC Motor Based on a Hierarchical Control," *IEEE Transactions on Power Electronics*, 2015, vol. 30, no. 2, pp. 1076–1084.

[14] Pandey S. K., Patil S. K. L., Phadke S. B., "Regulation of Nonminimum Phase DC–DC Converters Using Integral Sliding Mode Control Combined With a Disturbance Observer," *IEEE Transactions on Circuits and Systems II: Express Briefs*, 2017, vol. 65, no. 11, pp. 1649-1653.

[15] Mobayen S., Tchier F., "A novel robust adaptive second-order sliding mode tracking control technique for uncertain dynamical systems with matched and unmatched disturbances," *International Journal of Control, Automation and Systems*, 2017, vol. 15, pp. 1097–1106.

[16] Qian R., Luo M., Sun P., "Improved nonlinear sliding mode control based on load disturbance observer for permanent magnet synchronous motor servo system," *Advances in Mechanical Engineering*, 2016, vol. 8, no. 4, pp.295–300.

[17] Nagarale, R. M. Patre B. M., "Composite fuzzy sliding mode control of nonlinear singularly perturbed systems," *ISA Transactions*, 2014, vol. 53, no. 3, pp. 679-689.

[18] Suryawanshi P. V., Shendge P. D., Phadke S. B., "A boundary layer sliding mode control design for chatter reduction using uncertainty and disturbance estimator," International Journal of Dynamics and Control, 2016, vol. 4, no. 4, pp. 456-465.

[19] Chen M. S., Hwang Y. R., Tomizuka M., "A state-dependent boundary layer design for sliding mode control," *IEEE transactions on automatic control*, 2002, vol. 47, no. 10, pp. 1677-1681.

[20] Shi S., Xu S., Gu J., Min H., "Global High-Order Sliding Mode Controller Design Subject to Mismatched Terms: Application to Buck Converter," *IEEE Transactions on Circuits and Systems I: Regular Papers*, 2019, vol. 66, no. 12, pp. 4840–4849.

[21] Wang Z., Bao W., Li H., "Second-order dynamic sliding-mode control for nonminimum phase underactuated hypersonic vehicles," *IEEE Transactions on Industrial Electronics*, 2016, vol. 64, no. 4, pp. 3105-3112.

[22] Wang W., Ji Y., Lin D., Shi X., Zhao J., "Velocity-Free Fault-Tolerant Rendezvous Law Based on Dual-Layer Adaptive Algorithm," *IEEE Access*, 2020, vol. 8, pp. 135706-135721.

[23] Jeong S., Chwa D., "Coupled multiple sliding-mode control for robust trajectory tracking of hovercraft with external disturbances," *IEEE Transactions on Industrial Electronics*, 2017, vol. 65, no. 5, pp. 4103-4113.

[24] Falehi A. D., "Optimal robust disturbance observer based sliding mode controller using multi-objective grasshopper optimization algorithm to enhance power system stability," *Journal of Ambient Intelligence and Humanized Computing*, 2020, vol. 11, no. 11, pp. 5045–5063.

[25] Pan Y., Joo Y. H., Yu H., "On performance recovery of robust dynamic surface control," *International Journal of Robust and Nonlinear Control*, 2020, vol. 30, no.8, pp. 3094-3109.

[26] Wang Z., Li S., Yang J., Li Q., "Current sensorless finite-time control for buck converters with time-varying disturbances," *Control Engineering Practice*, 2018, vol. 77, pp. 127-137.

[27] Ling R., Shu Z., Hu Q., Song Y. D., "Second-order sliding-mode controlled three-level buck DC–DC converters," *IEEE Transactions on Industrial Electronics*, 2017, vol. 65, no. 1, pp. 898-906.

[28] Bizon N., "Hybrid power sources (HPSs) for space applications: Analysis of PEMFC/Battery/SMES HPS under unknown load containing pulses," *Renewable and Sustainable Energy Reviews*, 2019, vol. 105, pp. 14-37.

[29] A. K. Doddathimmaiah, J. Andrews, "Theory, modelling and performance measurement of unitised regenerative fuel cells," *International Journal* of *Hydrogen Energy*, vol. 34, 2009, pp. 8157-8170

[30] Gao Z., Mogni L., Miller E. C., Railsback J., "A Perspective on Low-Temperature Solid Oxide Fuel Cells," *Energy & Environmental Science*, 2016, vol. 9, no. 5, pp. 1602-1644.

[31] Bratsch S. G., "Standard electrode potentials and temperature coefficients in water at 298.15 K American Institute of Physics," *Journal of Physical and Chemical Reference Data*, 1989, vol. 18, no. 1, pp. 1-21.

[32] Thirumalai D., White R. E., "Mathematical modeling of proton-exchange-membrane fuel-cell stacks," Journal of The Electrochemical Society, 1997, vol. 144, pp. 1717-1723.

[33] Wang Z., Li S., Wang J., Li Q., "Robust control for disturbed buck converters based on two GPI observers," *Control Engineering Practice*, 2017, Vol. 66, pp. 13-22.

Information about author.

Ali Darvish Falehi received his Ph.D. and Post-Ph.D. degrees in Electrical Engineering from Shahid Beheshti University, Tehran, Iran. He ranked between the world's top 2% scientists listed by prestigious Stanford University in 2019 and 2020. He has also acted as chairman of R&D board of HICOBI Company. He has published more than 30 ISI papers like Elsevier, IET, Springer and Wiley. He has also recorded three national patent inventions. His interests include Power Electronics, Power Quality, Power System Stability and FACTS Devices.
E-mail: a_darvishfalehi@sbu.ac.ir

Comprehensive Management of Electricity Demand Distribution in Time

Serebrennikov B.[1], Petrova K.[2], and Serebrennikov S.[2],
[1]Institute of Economics and Forecasting of Ukraine's National Academy of Sciences, Kyiv, Ukraine
[2]Central Ukrainian National Technical University, Kropyvnytskyi, Ukraine

Abstract. The paper is aimed to strengthen the controllability of electricity consumption mode at all structural layers of the country's energy system (ES) to establish the optimal load curve in the PS. Following this goal, the energy system was broken down into seven structural layers - from the technological operation to the ES. For each layer, an expert assessment of the effectiveness of six institutional and operational methods of electricity demand-side management (DSM) was done. The integrated application of the suggested methods was tested in two industrial consumers, which proved the effectiveness of this approach for leveling their aggregated load curve. To ensure an appropriate economic impact on the electricity demand, given the influence of individual consumers on the load curve fluctuation in the ES, a particular price function considering the cross-correlation coefficient of the load curves was developed. It was proved that the complex DSM methods application significantly improved the controllability of the electricity consumption mode. To incentivize consumers to adjust their electricity consumption, a special price system functionally related to the cross-correlation coefficient of the consumer and the ES load curves was developed. The marginal price values depending on the cross-correlation coefficient were defined, while the intermediate price values were calculated by the functional transformation of the ES load curve into the price scale. The significance of the research results lies in the fact that ranking the DSM methods by the priority of application for various structural layers of ES and their integrated application almost doubled the DSM effectiveness.
Keywords: structural layers of power system, electricity load curve, regulation of electricity consumption mode, cross-correlation coefficient, price function.

DOI: https://doi.org/10.52254/1857-0070.2023.2-58.03
UDC: 621.311:351.824.11

Controlul distribuirii complexe cererii de energie electrică în timp

Serebrennikov B. S.[1], Petrova E. G.[2], Serebrennikov S. V.[2]
[1]Institutul de Economie și Prognoză al Academiei Naționale de Științe din Ucraina, Kiev, Ucraina
[2]Universitatea Națională Tehnică Centrală din Ucraina, Kropyvnytskyi, Ucraina

Rezumat. Scopul lucrării este de a consolida controlul modului de consum a energiei la toate nivelurile structurale ale sistemului unificat de energie electrică (UEES) al statului pentru a forma programul optim de încărcare pentru UEES. Pentru atingerea acestui scop s-a realizat structurarea sistemului de energie electrică pe 7 niveluri - de la funcționarea tehnologică până la UEES. Pentru fiecare nivel structural s-a efectuat evaluarea eficacității aplicării principalelor 6 metode instituționale și instrumentale de gestionare a regimului consumului de energie. Aprobarea utilizării complexe a metodelor de management a fost implementată pe exemplul a doi consumatori industriali, ceea ce a dovedit eficacitatea acestei abordări la nivelarea programului de sarcină electrică totală (LEG). Pentru impactul economic asupra formării cererii de energie electrică, ținând cont de influența consumatorului asupra neuniformității LEG al UOEES, a fost elaborată o funcție de preț din coeficientul de corelație încrucișată al LEG. Cele mai importante rezultate: metodele de control al consumului de energie se diferențiază în principale și auxiliare în funcție de gradul de impact al acestora asupra LEG al fiecărui nivel structural al UEES. Este dovedit că utilizarea complexă a metodelor a îmbunătățit semnificativ controlabilitatea modului de consum de energie. Semnificația rezultatelor cercetării constă în faptul că diferențierea metodelor de reglare a regimului de consum de energie prin prioritatea de aplicare pentru nivelurile structurale ale sistemului de energie electrică și utilizarea lor integrată a aproape dublat eficiența controlului modului.
***Cuvinte-cheie*:** nivelurile structurale ale sistemului de energie electrică, programul de sarcină electrică, reglarea modului de consum de energie, coeficientul de corelație încrucișată, funcție de preț.

Комплексное управление распределением спроса на электрическую энергию во времени

Серебренников Б. С.[1], Петрова Е. Г.[2], Серебренников С. В[.2]

[1]Институт экономики и прогнозирования Национальной академии наук Украины, Киев, Украина

[2]Центральноукраинский национальный технический университет, Кропивницкий, Украина

Аннотация. Целью работы является усиление управляемости режима электропотребления на всех структурных уровнях объединенной электроэнергетической системы (ОЭЭС) государства для формирования оптимального графика нагрузки ОЭЭС. Для достижения поставленной цели произведено структурирование электроэнергетической системы на 7 уровней – от технологической операции до ОЭЭС. Для каждого структурного уровня проведено экспертное рейтинговое оценивание эффективности применения основных 6 институциональных и инструментальных методов управления режимом электропотребления. Апробация комплексного использования методов управления реализована на примере двух промышленных потребителей, что доказало эффективность такого подхода при выравнивании их суммарного графика электрической нагрузки (ГЭН). Для экономического воздействия на формирование спроса на электрическую энергию, учитывающего влияние потребителя на неравномерность ГЭН ОЭЭС, разработана ценовая функция от коэффициента взаимной корреляции ГЭН. Наиболее существенные результаты: методы управления электропотреблением дифференцированы на основные и вспомогательные по степени их воздействия на ГЭН каждого структурного уровня ОЭЭС. Доказано, что комплексное использование методов существенно улучшило управляемость режима электропотребления. Для стимулирования потребителей к управлению электропотреблением разработана система цен на электроэнергию, функционально связанных с корреляцией суточных ГЭН потребителя и ОЭЭС. Установлены экстремальные значения ценового диапазона в зависимости от коэффициента корреляции, а промежуточные значения цены вычислены функциональным преобразованием ГЭН ОЭЭС в ценовую шкалу. Значимость результатов исследований заключается в том, что дифференцирование методов регулирования режима электропотребления по приоритетности применения для структурных уровней электроэнергетической системы и комплексное их использование повысило результативность управления режимом практически вдвое. Разработанная ценовая система, основанная на использовании коэффициента корреляции ГЭН, усилила мотивацию потребителей к выравниванию суммарного графика нагрузки ОЭЭС.

***Ключевые слова*:** структурные уровни электроэнергетической системы, график электрической нагрузки, регулирование режима электропотребления, коэффициент взаимной корреляции, ценовая функция.

LIST OF ABBREVIATIONS

UES - unified energy system; ELS - electrical load schedule; IC - industrial consumer; TP - technological process; CRM - correlation-resonance method; TTM - technical-technological method; OM - organizational method; DM - directive methods; EM - economic method; NM - normalization methods; ACM - agitation and communicative methods; DSO - distribution system operator; NPM - network planning and management; CRM - correlation-resonance method.

INTRODUCTION

Trends in the development of distributed generation, taking into account regional features of resource potential [1], the creation of small energy systems, and the implementation of new flexible forms of participation in the energy market, as well as the intergovernmental association of energy systems [2, 3], are the modern

European paradigm for transforming energy in order to decarbonize, enhance energy security and resilience of energy systems [4-7]. In addition, to a key process of such transformation the demand-side management of electricity [8-9]

should be added which, within national and macro-regional energy systems, allows for multiple positive effects: technical, economic, ecological-climatic, and others.

Unified energy systems of Moldova and Ukraine starting since 16.03.22 has been synchronized with the European Union (EU) energy system for parallel operation [2].

The transformation of Ukraine's electricity market into a competitive one, through the implementation of "bilateral contracts" and a "balancing market", highlights the need for mechanisms to maintain a permanent energy balance. The proper quality of electric power and high reliability of power supply are the easiest to ensure with a uniform electric load schedule (ELS). However, the characteristic feature of the daily schedules of electric loads of the Unified Energy System of most countries is the presence of two peaks - morning and evening - as well as a significant decrease in the load during night hours, with fluctuations between maximum and minimum values of consumed power reaching

25...30% [10]. Such a configuration of the electric load schedules is due to the fact that the total demand for most goods and services, exhibited by end consumers throughout the day, is characterized by significant non-uniformity, determined by the biological cycle of humans. Thus, in the morning and evening there is a surge in demand for electricity, gas, water, transport, communication, while these goods and services are hardly in demand at night. This can lead to a deficit or deterioration in quality during peak periods, and to the loss of such goods during the "night gap".

Aligning the load curves of the United Energy System will contribute not only to achieving the balance of the electrical energy [11], but also to saving fuel and energy resources, reducing losses of electrical energy in the electric networks, decreasing the wear and tear of network infrastructure, improving the quality and reliability of energy supply to consumers, as well as the environmental friendliness of the power industry.

Therefore, the UES and electricity producers are striving to align the load of electrical consumption over time, while consumers are primarily interested in saving on electricity bills. To achieve these goals, a range of institutional and instrumental methods are used to manage the regime of electricity consumption, among which economic ones should prevail, although they are not dominant in the energy sector of Ukraine. The time-differentiated pricing system currently functions only for the population and does not take into account the individual technical and economic characteristics of other segments of the electric energy market. At the same time, as experience shows, the use of only pricing levers is insufficient to solve this problem, especially in the short term.

In these conditions, the task of maintaining the balance of consumption with supply (generation) through alignment of the demand curve for electric power over time remains extremely relevant.

I. PROBLEM STATEMENT

Effective operation of the unified energy system is possible only with harmonious balancing of supply and demand in the electric energy market in real time through targeted management of the electricity consumption at all levels of the integrated power system. At the same time, the selectivity and degree of influence of each management method for each structural unit requires investigation.

To intensify the process of aligning the electricity load curve over time to an acceptable level for the European Union, it is necessary to provide an objective rating assessment of the priority of management methods and improve the methodology for calculating differentiated prices that encourage the increase of uniformity in daily electricity demand.

II. ANALYSIS OF RECENT RESEARCH

Studies aimed at aligning daily and annual electricity load curves are primarily focused on a specific industry or an individual management method, and as a result, do not provide tools for comprehensive impact on all segments of the electricity market consumers.

The authors [12] have improved the multi-level approach to managing hourly electricity consumption modes by industrial consumers using the technological process resource. However, the approaches proposed in [12] are complex and can only be applied to a limited range of technological processes.

In [13], administrative regulation of a company's electricity load with multiple levels of management is considered, which is necessary to balance the load and eliminate technical and economic consequences of imbalances. Demand management is limited to forming economic dispatch schedules for switching on and off the electric power consumers.

In the article [14], a mixed nonlinear programming model is developed taking into account electricity consumption and tariffs for managing the electricity load. However, to simultaneously reduce deviations and lower electricity costs, it is necessary to coordinate the load curve in advance.

The contribution [15] to the literature on energy consumption management consists of implementing a three-stage management structure to improve the energy stability of industrial consumers, differentiating them into large, medium and small ones. However, the optimality of energy consumption based on the results of reducing production costs and CO_2 emissions was tested on the example of two completely different industrial consumers - foundry and textile, without considering the specifics of their technological process.

Authors of [16] consider optimization tasks for the electricity consumption, including normalizing electricity consumption, demand management, by load shifting, and correction electricity consumption mode.

In [17], electricity consumption mode management is carried out using technical, organizational, and economic methods to reduce electricity consumption during peak energy system hours, but management is only considered at the level of individual enterprises.

In [18], the effectiveness of energy savings through administrative correction of time measurement is discussed. However, the specifics of electricity consumption distribution across regions of the country are not taken into account in the study.

The optimization task of the power supply mode is solved in [19] based on criteria of minimum losses in networks, as well as taking into account the constraints on the schedules of electrical loads corresponding to the maximum reduction of consumer costs and minimizing changes in operations that make up the technological process.

In [20], a methodology for calculating load losses of electrical energy in consumer networks is described; theoretical expressions for calculating losses are given, taking into account the shape of the consumer's electrical load schedule and the volume of transferred energy.

One organizational method of energy consumption management [21] is aimed at improving the consumer demand profile during peak hours through a compensatory photovoltaic system programmed to operate in parallel with the electrical grid. The methodology includes an analysis of the shape of the electrical load schedule, energy prices, and the profile of photovoltaic generation.

The Smart Energy Grid provides for direct or indirect energy consumption management [22]. Direct control programs include demand shaping, load shifting, peak limiting, filling gaps, strategic load growth, or its preservation. It is claimed that the load shifting is the best among the direct control methods.

Thus, the analysis of researches and publications indicates the relevance of further searching for effective methods for managing the electric load curve and incentives for reducing the unevenness of the daily electricity consumption. The examined methods could have given a much greater effect when used in combination.

Therefore, the aim of this work is to investigate the possibilities of the integrated application of economic, technological, organizational, and other methods of influence to form an optimal electricity consumption mode at all structural levels of the unified energy system, as well as to improve market levers for increasing the evenness of the electrical load schedules.

III. RESEARCH METHOD

The research was conducted using the following methods: expert evaluation of the priority of methods for managing the electricity consumption regime; graph-analytical method using graph theory to regulate the electricity load curve of an industrial consumer using technological resources; complete enumeration method to search for the optimal version of uniformity of the total electricity load curve; methods of mathematical statistics and probability theory to study the electricity load curve and determine the consistency of expert opinions; theory of functions and mathematical modeling in calculating the differentiated price system for electricity.

IV. RESULTS AND DISCUSSION

To maintain a permanent balance between energy production and import with energy consumption and export, let us consider the application of a complex of control measures directed simultaneously at all structural levels of the unified electric energy system (UES) (Fig. 1).

The UES is divided into the following levels:

- The simplest technological operation that sums up the power of the electrical equipment involved during the investigated time interval can be taken as the 1st basic level;
- The entire technological process should be taken as the 2nd level, as it integrates the powers consumed by the set of technological operations used in the considered section of the electrical load schedule;
- The 3rd level consists of consumers with commercial accounting of electrical energy as an autonomous market unit.
- The 4th level is occupied by electricity supply companies, which have a license for independent economic activity in supplying electrical energy to the end consumers of the electricity energy market (in Ukraine, these are suppliers at free prices, universal service providers, and the "last hope" supplier);
- The 5th level consists of regional distribution system operators (DSO), allocated by administrative-territorial features and engaged in the transmission and distribution of electrical energy. DSOs ensure the reliability and quality of power supply;

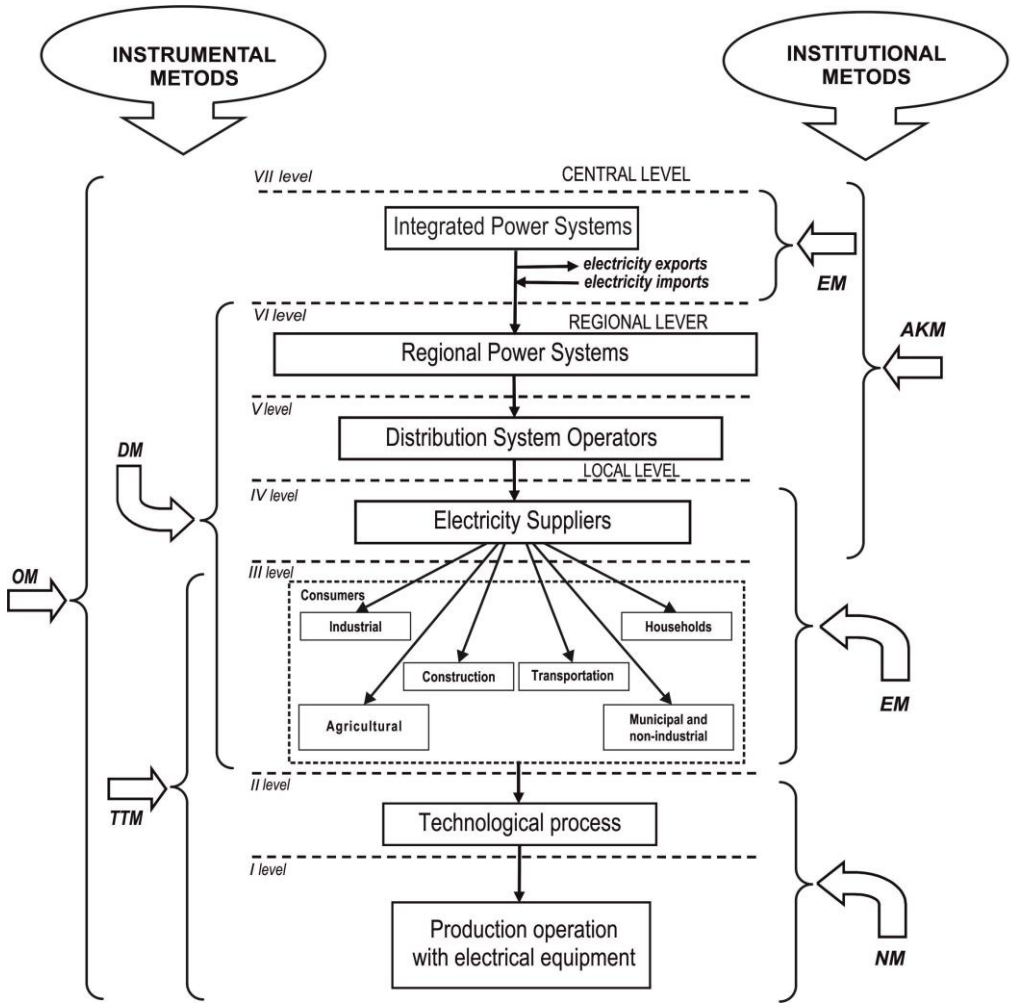

Fig. 1. Application of methods for managing the schedule of electrical load for the structural levels of the UES (EM - economic methods, NM - normalization methods, DM - directive methods, TTM - technical and technological methods, OM - organizational methods, AKM - agitative and communicative methods IC - information campaigns).

- The highest 7th level is formed by the unified energy system of the state - the totality of power plants, power grids, and other elements of the electric power industry under centralized management of a unified technological process of production, transfer and EE distribution.

For each level of the unified energy system, it is necessary to choose the most effective levers of influence and ensure their objective rating assessment for their comprehensive use. Rational management of power consumption mode is achieved through instrumental methods of direct impact (technical and technological, organizational, command-compulsory) and indirect institutional methods that stimulate demand regulation (economic, normative, agitation-communicative) and others.

From Fig 1, it can be seen that according to expert conclusions, technical and technological methods (TTM) that utilize technological resources are most applicable at levels 1-3.

Normalization methods (NM) justify the amount of specific energy costs and implement control over their compliance. NM are effective at levels 1-2; in this case, electricity consumption regulation mainly serves the purposes of energy conservation.

Organizational methods (OM), in particular, load curve alignment as a result of mutual displacement of its components, can be implemented at any structural level of the unified energy system – from 1 to 7, but its application is most accessible at lower levels. At the same time, organizing energy exchanges with other countries, transitioning to distributed power systems with an emphasis on using regional fuel and energy resources, and other similar policies are the prerogative of higher levels.

Agitative and communicative methods (ACM) are aimed at raising consumer awareness of the need to regulate demand with consideration of electricity payment based on the system of differentiated prices, use of individual renewable energy sources, energy labeling of products, etc.

Economic methods (EM) are based on financial and economic instruments that affect the volume and modes of energy consumption, with the price of electricity playing the role of the main regulator.

If market methods of demand regulation are inefficient or act too slowly, it is advisable to use directive methods (DM); for example, at levels 3-6, mandatory disconnection of category II and III consumers, limitation of daily electricity consumption, seasonal time counting correction, and so on.

In order to establish the selective responsiveness of levels of the unified energy system to a specific management method and to rank methods of influence, 12 experts, specialists in electricity consumption management, were surveyed. Experts assessed the priority of applying a particular method at each level of the unified energy system on a 6-point scale, where 1 corresponds to the least impact, and 6 corresponds to the most significant impact.

Statistical processing of the results allowed to calculate the coefficients of concordance W and Pearson's correlation coefficient using the $\chi_R^2 = W \cdot m \cdot (k-1)$, where $m = 12$ - the number of experts, $k = 6$ - the number of methods considered, and the tabular (critical) value $\chi_{KR}^2 =$ 11,07 for a 5% level of significance, the number of degrees of freedom $\gamma = k - 1 = 5$, and also to determine the degree of agreement among the experts (Table 1). The results indicate that differentiating methods into main (1, 2, 3) and auxiliary (4, 5, 6) based on their significant impact on the graph of the electric load at a certain level, and applying them in combination, will facilitate the formation of an optimal energy balance.

The effectiveness of complex management will be tested on two industrial consumers, starting with the implementation of technical and technological methods to balance the graph of the electric load in the most energy-intensive technological processes and workshops, using the identified time reserves in the technological processes and applying the network planning and management method (NPM) [23], and in the next stage, implementing the algorithm of the organizational correlation-resonance method (CRM) [24], by shifting the aligned graphs of the electric load of the industrial consumers relative to each other in time.

Figure 2 shows the initial winter electric load graphs of two machine-building industrial consumers (graph 1 in Fig. 2a and graph 3 in Fig. 2b). To align these graphs, reserves of production time R_t were identified through the analysis of the discrete technological process (TP) [23]. These reserves represented the possible displacement of parallel operations along the TPs and the corresponding movement of electric loads without violating the completion time and quality of the TPs.

The synthesis of new graphs was carried out by the purposeful redistribution of the starts and finishes of TP operations within R_t, using the exhaustive search method and guided by the criterion of reducing the unevenness of the graphs.

After redistributing the loads of most power-intensive operations along the technological process (up to 80% of the controllable power) within the calculated R_t, the configurations of the electrical load graphs of both industrial consumers acquired the shape of curves 2 and 4 on Fig. 2, respectively.

It can be seen that the redistribution of consumed power by operations led to a significant reduction in the unevenness of the electrical load graph, which is evidenced by the comparison of the calculated indicators of graph alignment (Table 2).

The following commonly used indicators were analyzed. The unevenness indicator K_{NR}, which characterizes the range of the electrical load graph, can be determined from the mathematical relationship:

Table 1

Results of ranking management methods by levels of the unified energy system

№	Naming of level of Unified Energy Systems of Ukraine	W	χ_R^2	Alternating management methods in order of their priority
1	Operation with electrical equipment	0,6356	38,14	1. TTM; 2. NM; 3. OM; 4. EM; 5. DM; 6. ACM

2	Technological process	0,4152	24,91	1. TTM;	2. OM;	3. NM;
				4. DM;	5. EM;	6. ACM
3	Consumer with commercial metering	0,8025	48,15	1. EM;	2. TTM;	3. DM;
				4. OM;	5. NM;	6. ACM
4	Electricity Suppliers	0,6982	41,89	1. EM;	2.ACM;	3. OM;
				4. NM;	5.TTM	6. DM
5	Distribution System Operators	0,8154	48,92	1. DM;	2. OM;	3. TTM;
				4. NM;	5. EM;	6. ACM
6	Regional Power System	0,9170	55,02	1. OM;	2.ACM;	3. DM;
				4. NM;	5. TTM;	6. EM
7	Unified Energy Systems of Ukraine	0,8264	48,59	1. EM;	2. OM;	3. ACM;
				4. DM;	5. TTM;	6. NM

$$K_{NR} = \frac{P_{MIN}}{P_{MAX}} \qquad (1)$$

where P_{MIN}, P_{MAX} are respectively the minimum and maximum power values.

Since the values of P_{MIN}, P_{MAX} can theoretically vary in the interval [0; +∞), the unevenness indicator takes values within the range [0; 1]. When $K_{NR} = 1$, the electrical load graph is perfectly uniform.

To investigate the relationship between the maximum power value P_{MAX} and its mean value P_{SR}, the maximum indicator K_M is used:

$$K_M = \frac{P_{MAX}}{P_{SR}}. \qquad (2)$$

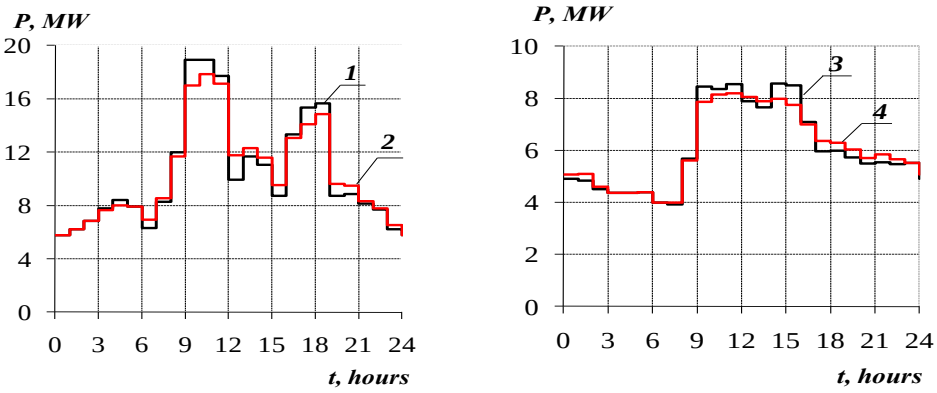

a b

Fig. 2. Electric load graph: a - industrial consumer IC-1 (1 - initial, 2 - after alignment by network planning and management method); b - industrial consumer IC-2 (3 - initial, 4 - after alignment by network planning and management method).

Theoretically, K_M can take values $K_M \geq 1$. An increase in K_M corresponds to an increase in the non-uniformity of the electric load graph.

The graph filling indicator K_{ZG} is inversely proportional to K_M:

$$K_{ZG} = \frac{1}{K_M} = \frac{P_{SR}}{P_{MAX}}. \qquad (3)$$

The limits of K_{ZG} correspond to the interval (0; 1].

From a statistical point of view, the shape indicator K_F provides a more detailed

assessment of the shape of the electric load graph than K_{NR}, K_M, and K_{ZG}, because K_F is defined as:

$$K_F = \frac{P_{SRKV}}{P_{SR}}, \quad (4)$$

where P_{SRKV} is the root mean square value of the power:

$$P_{SRKV} = \sqrt{\frac{1}{T}\int_0^T P^2(t)\,dt}, \quad (5)$$

where T is the duration of the selected period for calculations.

The daily electric load curve is usually presented as a histogram with hourly averaged power (Fig. 2), in which case P_{SRKV} is found using the formula:

$$P_{SRKV} = \sqrt{\sum_{i=1}^{n}\left(P_i^2 \cdot t_i\right) \Big/ \sum_{i=1}^{n} t_i}, \quad (6)$$

where P_i is the power on the *i*-th section with a duration of t_i; n is the number of sections in the electric load curve (for the daily electric load curve $n = 24$).

According to (4), K_F takes on the minimum value of $K_F = 1$ when $P_{SRKV} = P_{SR}$ at $P(t) = const$, which corresponds to the most preferable mode for the unified energy system.

The variance D_P is a measure of the deviation of the current power values P_i from their average value P_{SR}:

$$D_P = P_{SRKV}^2 - P_{SR}^2 = P_{SR}^2\left(K_F^2 - 1\right) \quad (7)$$

The indicators of non-uniformity of the electric load curves for two industrial consumers shown in Fig. 2, calculated from expressions (1)-(7), are presented in Table 2.

Table 2

Indicators of non-uniformity of ELS for two industrial consumers (IC) in Fig. 2.

ELS options of two IC	Indicators of non-uniformity of the ELS of IC				
	K_{ZG}	K_M	K_{NR}	K_F	D_P
ELS of IC-1 before regulation	0,5516	1,8127	0,3044	1,0723	17,027
ELS of IC-1 after regulation by network planning methods	0,5843	1,7114	0,3225	1,0574	13,415
ELS of IC-2 before regulation	0,7078	1,4128	0,4576	1,0335	2,6229
ELS of IC-1 after regulation by network planning methods	0,7418	1,3481	0,4877	1,0272	2,1208

The analysis of the indicators of non-uniformity presented in Table 2 shows that as a result of transforming graph 1 into graph 2, the indicator of the ELS filling K_{ZG} increased by 5.93%, indicating an overall increase in uniformity (for a perfectly uniform ELS $K_{ZG} \to 1$); the non-uniformity indicator K_{NR} increased by 5.95%, i.e., the difference between P_{MIN} and P_{MAX} decreased; the form factor indicator K_F decreased by 1.41% (indicating an approach of P_{SRKV} to P_{SR}); the peak indicator K_M decreased by 5.92%, and the variance D_P decreased by 26.9%.

The non-uniformity indicators also improved as a result of transforming graph 3 into graph 4: K_{ZG} increased by 4.8 %, K_{NR} increased by 6.58 %; K_F decreased by 2.3 %, K_M decreased by 4.8 %, and D_P decreased by 23.7 %.

The achieved alignment of the ELS of industrial consumers contributes to electricity savings due to a reduction in electrical energy losses in power grids; the electricity savings δW_{C1} will be calculated according to [20] as a result of changing the K_F indicator before and after aligning the ELS.

At an average level of losses in the industrial consumer networks of 13.6% of the total

consumed electrical energy, for industrial consumer IC-1 δW_{C1} during the day:

$$\delta W_{C1} = \Delta W_N \cdot \left(1 - \frac{K_{F2}^2}{K_{F1}^2}\right) = \\ = \frac{13{,}6\,\% \cdot 250{,}5}{100\,\%}\left(1 - \frac{1{,}0574}{1{,}0723}\right) = 0{,}47\ MW \cdot h$$

where ΔW_N - the losses of electrical energy in the IC networks before leveling the electrical load graph; K_{F1}, K_{F2} - indicators of the form before and after leveling the ELS, respectively (Table 1).

For industrial consumer IC-2, the savings δW_{C2} = 0.12 MW·h are achieved.

Of course, the achieved leveling of the ELS due to the energy-saving effect will lead to a proportional reduction in the payment for electrical energy.

Since the graph of the aggregated electrical power system load is a superposition of its load graphs, it is rational to apply the correlation-resonance method [25] in the next stage of leveling, which is based on leveling the resulting graph by shifting two electrical load graphs with a step of τ relative to each other. The variant with the minimum value of the cross-correlation function is preferred.

$$k(p_{RS}(\tau)) = \left[\frac{1}{t_C}\left(\begin{array}{l}\int\limits_{0}^{t_C-\tau} p_R(t)\,p_S(t+\tau)dt\ + \\ + \int\limits_{t_C-\tau}^{t_C} p_R(t)\,p_S(t-t_C+\tau)dt\end{array}\right)\right] - \\ - P_R P_S \ \rightarrow \min \qquad (8)$$

where $\tau = t_{RS}$ – is the time shift between graphs, hours;

t_C – cycle duration (period), for a daily electrical load graph, $t_C = 24$ hours;

$p_R(t)$, $p_S(t)$ - normalized to the maximum power value of the first and second electrical load graphs at time t, respectively, relative units;

P_R, P_S – average power of both electrical load graphs, relative unit.

The nature of the change in the cross-correlation function with an hourly shift of the electric load curve within τ = 1…24 hours is shown in Fig. 3: curve "k_1" represents the original ELS 1 relative to the ELS 3, curve "k_2" represents the adjusted load graphs ELS 2 and the ELS 4.

From (8), it can be seen that the cross-correlation function depends on the level of electricity consumption and can take any absolute values (on Fig. 3, $k(p_{RS}(\tau))$ varies from -0.062 to +0.07 relative units).

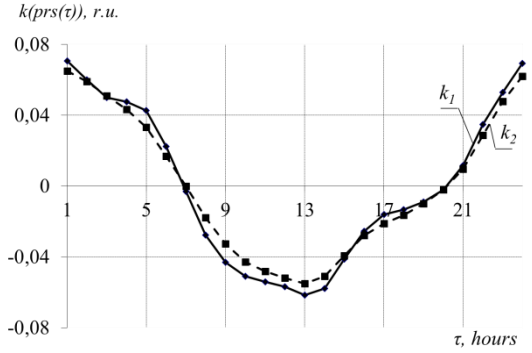

Fig. 3. Cross-correlation function as a function of shift τ: k_1 - for the electric load graph before regulation, k_2 - after applying network planning and management.

After applying network planning and management, the cross-correlation function decreased, and the minimum value of both $k(p_{RS}(\tau))$ corresponds to the optimal shift at $\tau = 13$ hours. However, implementing a shift of $\tau = 13$ hours in practice is extremely problematic. Therefore, it is appropriate to analyze the result of mutual shifting of electric load curves within realistically achievable limits of $\tau_P = \pm|1\ldots2|$ hours, which can be realized, for example, by shifting the start of work by τ_P.

The relationship of the cross-correlation function at four real shift options - 1, 2, 22, and 23 hours - showed (see Fig. 3) that for the load graphs ELS 1 and ELS 3, $k(p_{13}(1)) > k(p_{13}(2)) > k(p_{13}(23)) > > k(p_{13}(22))$ and for the adjusted load graphs ELS 2 and 4, $k(p_{24}(1)) > k(p_{24}(2)) > k(p_{24}(23)) > k(p_{24}(22))$ applies.

Therefore, the best result for aligning the resulting graph from the four options is achieved by shifting the load graph ELS 2 relative to the load graph ELS 4 by $\tau_P = 22$ hours ($\tau_P = -2$ hours).

Figure 4a shows the cumulative ELS of two industrial consumers: graph 5 is obtained by adding the original load graphs of ELS 1 and ELS 3 from Fig. 2; graph 6 - ELS 2 and ELS 4 after regulation by the method of network planning and management. It can be seen that the regulated

cumulative ELS 6 is smoother than the original graph ELS 5.

Figure 4b shows the cumulative ELS of the two industrial consumers: graph 7 - with the use of only the correlation-resonance method (by shifting the original ELS 1 relative to the ELS 3 by $\tau_P = -2$ hours); graph 8 - with the use of complex regulation: first with the method of network planning and management, and then with the correlation-resonance method. The best result of the 4 options was obtained using complex regulation (graph 8).

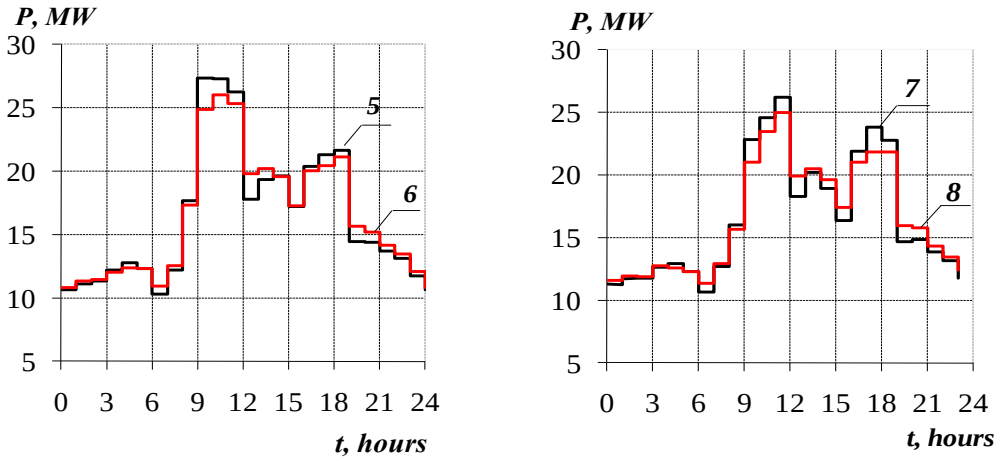

a b

Fig. 4. Cumulative ELS of both industrial consumers under different management approaches: a - curve 5 is the initial cumulative ELS, curve 6 is after management with only NPM; b - curve 7 is after applying only the correlation resonance method (shifted by $\tau_P = -2$ hours), curve 8 is after combined management using both methods - NPM and CRM.

Comparison of the indicators of unevenness of the cumulative load graphs (Table 3) confirms that as a result of complex control, the indicators have significantly improved: thus, after the method of network planning and management, the filling coefficient of the total ELS K_{ZG} increased by 5.47 %, and after the sequential use of NPM and CRM - already by 9.6 %.

Table 3

Indicators of non-uniformity of the cumulative ELS of two industrial consumers

Options for regulating	Indicators of the total ELS				
	K_{ZG}	K_M	K_{NR}	K_F	D_P
Before regulation	0,6031	1,6581	0,3755	1,0495	28,827
After regulation by network planning methods only	0,6347	1,5756	0,4161	1,0411	23,731
After regulation by correlation resonance method only	0,6305	1,586	0,4072	1,0418	24,264
With complex regulation by network planning methods and correlation resonance method	0,6607	1,5134	0,4514	1,0335	19,353

It is noteworthy that there are some peculiarities of the considered indicators: thus, K_{NR}, K_M, K_{ZG} describe the ELS graph only at certain points and depend only on its extremes, which does not allow for an unambiguous assessment of the degree of load unevenness, since different ELS graphs of different configurations can have the same values of the calculated indicators.

Indicator K_F does not always respond to regulation, for example, $K_F = const$ in the case of an additive shift of the ELS graph over time. Moreover, it should be noted that the K_F of two ELS graphs that are different in shape but

mirror-symmetric with respect to the vertical axis can have the same values.

The variance $D_P \geq 0$, but its upper limit is not determined, which makes it difficult to compare several different ELS graphs; in particular, the D_P indicator proves to be unsuitable for comparing ELS graphs that differ by orders of consumed power.

It should be noted that the tested methods of managing ELS graphs are quite universal and applicable to most levels of the unified energy system. Further alignment of ELS graphs can be achieved through additional use of other methods of influence.

Based on the fact that the economic method of control is one of the main ones for most structural levels of the unified energy system (Table 1), and the potential for saving on payments for electricity consumption represents a major incentive for electricity consumers, we consider the possibility of improving the system of differentiated prices with the aim of increasing the flexibility of pricing.

Considering that the unevenness of consumers' schedules is not as important as the degree of personal influence of each consumer on the configuration of the resulting energy system schedule ELS UES, we believe that the pricing function should primarily include the coefficient of mutual correlation - the indicator K_{COR}^{C}, which characterizes the degree of coincidence of the forms of two ELS (consumer and UES):

$$K_{COR}^{C} = \frac{\sum_{i=1}^{n} (p_{1i} - P_{SR1}) \cdot (p_{2i} - P_{SR2})}{(n-1) \cdot \sigma_{P1} \cdot \sigma_{P2}},$$

where p_{1i}, p_{2i} – the average hourly power of the 1st and 2nd ELS, respectively;

σ_{P1}, σ_{P2} – the standard deviation of power;

n – the number of ELS steps (for daily schedules $n = 24$);

P_{SR1}, P_{SR2} – the average values of the power of the compared ELS.

For any ELS K_{COR}^{C} varies within the range of [-1; 1], therefore, the coefficient of mutual correlation is more convenient when comparing numerically incomparable ELS, for example, in the case of a joint analysis of the graph of the machine-building industrial consumer and the total graph of the UES.

Most consumers operate in a "hard" technological mode with $K_{COR}^{C} \to 1$ relative to the UES graph, collectively determining its shape. In this case, it is possible to propose a pricing system in which the limiting values of prices C_{MAX} and C_{MIN} are calculated individually for each consumer based on the functional accounting of its K_{COR}^{C}. Since the price of electric energy is deterministic in the range $[C_{MIN}; C_{MAX}]$, it is advisable to choose a classifier for the pricing scale $C \in [C_{MIN}; C_{MAX}]$ when the maximum value of the price rate during peak demand is calculated as:

$$\begin{aligned} C_{MAX} &= \left(1 + K_{COR}^{C}\right) \cdot C_{MID} \quad \text{or} \\ C_{MAX}^{R} &= \left(1 + K_{COR}^{C}\right) \end{aligned} \tag{9}$$

and the minimum price C_{MIN} for the night drop in electricity consumption, symmetric to C_{MAX} with respect to C_{MID}, is calculated as:

$$\begin{aligned} C_{MIN} &= \left(1 - K_{COR}^{C}\right) \cdot C_{MID} \quad \text{or} \\ C_{MIN}^{R} &= \left(1 - K_{COR}^{C}\right), \end{aligned} \tag{10}$$

where $C_{MID} = const$ - the average price accepted for all industrial consumers at the level of the current single-stage value.

Intermediate price values within the range of $C_{MIN}^{R} \ldots C_{MAX}^{R}$ are calculated by transforming (normalizing) the price scale into an algebraically defined functional dependence on the relative price $C_i^{R} = C_i / C_{MID}$, based on the deviation of the relative power $\Delta P_i^{R} = (P_i - P_{MID}) / P_{MID}$ in the power system UES in the *i*-th time zone, for example, linearly [25]:

$$C_i^{R} = 1 + \alpha \Delta P_i^{R} \quad , \tag{11}$$

where α - is the price coefficient, unitless;

i - is the number of time intervals in a day;

P_i - is the power consumed in the *i*-th interval;

P_{MID} - is the daily average value of the power system's capacity.

Function (11) takes into account the sign of the deviation ΔP_i^{R} from P_{MID}: on segments with $+\Delta P_i^{R}$ surcharges are applied, and with negative increments $-\Delta P_i^{R}$ (during nighttime

demand drops) - discounts, the greater $\left|\Delta P_i^R\right|$, the greater the discount.

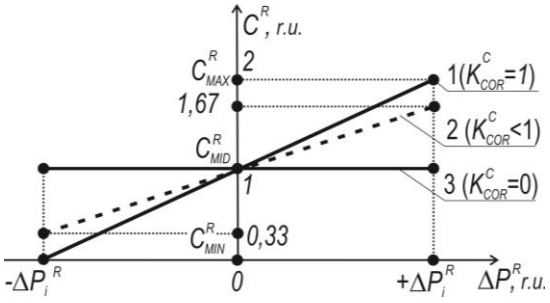

Fig. 5. Price function as a function of power deviation (in relative units).

From Fig. 5, it can be seen that when the demand for electric power is equal to the average daily value $(P_i = P_{MID})$, then $\Delta P_i = 0$ and payment for electric power is made according to C_{MID}. When $P_i > P_{MID}$, the price increases according to (11), and vice versa, when $P_i < P_{MID}$ - the price decreases.

Consumers with $K_{COR}^C \to 1$ (curve 1 in Fig. 5), who form the graph ELS of the energy system, will be most interested in shifting their graph of the power system, seeking to minimize payment for electric energy.

Since the coefficient of mutual correlation can vary within: $-1 \le K_{COR}^C \le 1$, then we focus on the expediency of considering only those graphs of the power system that increase the non-uniformity of the graph of UES, i.e., with a coefficient of mutual correlation within the range of $0 < K_{COR}^C < 1$ (on Fig. 5, the boundary curve 1 corresponds to $K_{COR}^C = 1$, curve 3 - $K_{COR}^C = 0$). In addition, values of C_i^R outside the limits of $0 < C_i^R < 2$ lose their economic meaning, since electric energy cannot be sold at a price of $C_i \le 0$.

Then for the industrial consumer IC-1, which has $K_{COR}^C = 0{,}67$, we obtain from (9) $C_{MAX}^R = 1{,}67$ and from (10) $C_{MIN}^R = 0{,}33$. Curve 2 in Fig. 5 shows the differentiated price system for the industrial consumer IC-1. For industrial consumer IC-1, the price coefficient $\alpha_1 = 4{,}786$, and for industrial consumer IC-2, which has $K_{COR}^C = 0{,}58$, the corresponding $\alpha_2 = 4{,}143$.

The proposed price system has no restrictions on the number of price levels N and responds to any violation of the uniformity of the regime. The flexibility of the price impact on industrial consumers is increased by increasing the daily price levels to $N \ge 24$, which provides a regularity of price distribution adequate to the configuration of the ELS UES. Thus, the price function (11) "tracks" the shape of the ELS UES (Fig. 6a) to encourage industrial consumers to shift their loads to the discount zone.

The daily payment X_E for electric power in relative units with hourly shift of the schedule within $i = 1 \ldots 24$ hours for the industrial consumer was calculated from the expression:

$$X_E = \sum_{i=1}^{N=1;24} C_i^R \cdot W_{E.i} / P_{E.MAX},$$

where $W_{E.i}$ - is the electric power consumed by industrial consumer in the *i*-th hour.

From Fig. 6b, it can be seen that the proposed 24-tariff system provides savings in the payment $\Delta X_E = X_{E.24} - X_{E.1}$ in the case of shifting the load curve of industrial consumer IC-1 by Δt =5.1...14.6 hours and the load curve of industrial consumer IC-2 by Δt =3.1...14.2 hours, where $X_{E.24} < X_{E.1}$. It should be noted that the energy consumption mode with $\Delta X_E \to \max$ is the most attractive for the consumer and the most desirable for the power grid. industrial consumer IC-2 is shifted by Δt =8 hours (Fig. 6b).

The minimum $X_{E.MIN}$ is achieved when the load curve of industrial consumer IC-1 is shifted by Δt =9.5 hours and the load curve of In this case, compared to the payment at the single tariff rate, the achieved savings $\Delta X_E = 200\% \left| X_{E.24} - X_{E.1} \right| / (X_{E.24} + X_{E.1})$ for industrial consumer IC-1 is 9.23% and for industrial consumer IC-2 is 8.7%.

With such a shift, industrial consumers IC-1 and IC-2 become consumer-regulators with a cross-correlation function of $K_{\text{COR.1}}^C$=-0.67 and $K_{\text{COR.2}}^C$=-0.58, respectively.

The criterion for the best option for load curve alignment is the following dynamics of the indicators discussed above:

$$\begin{cases} (D_P, K_F, K_M, K_{COR}^C, X_E) \downarrow; \\ (K_{ZG}, K_{NR}) \uparrow. \end{cases}$$

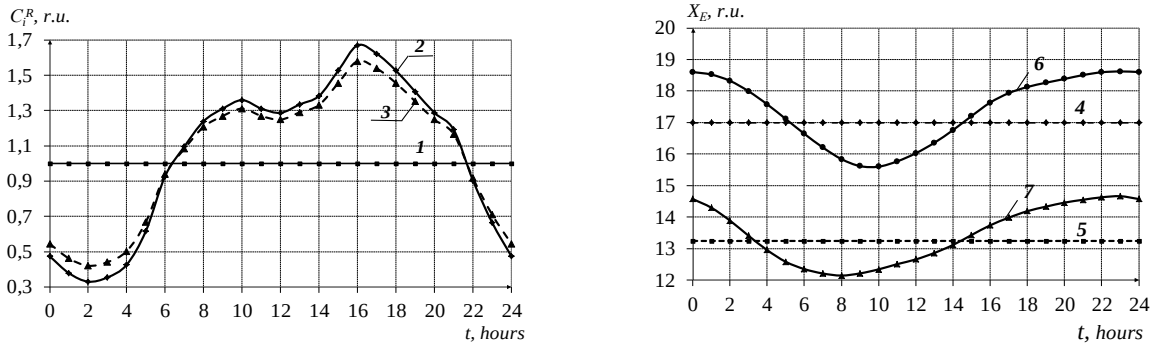

Fig. 6. Distribution graphs over time: a - retail price of electricity (1 - current single-rate price C_{MID}^R; 2 - 24-rate price for industrial consumer IC-1, 3 - for industrial consumer IC-2); b - daily payment for electricity with hourly shift of the industrial consumer power schedule (4 – payment $X_{E.1}$ for industrial consumer IC-1 and 5 $X_{E.2}$ - for industrial consumer IC-2 at a single rate; 6 - payment $X_{E.1–24}$ for industrial consumer IC-1 and 7 - $X_{E.2–24}$ for industrial consumer IC-2 at a 24-rate price).

V. CONCLUSIONS

1. Differentiation of the main methods of control by the degree of their influence on the ELS of each structural level of the energy system allowed identifying the main (primary) and auxiliary (secondary) methods, as well as an increase in the effectiveness of forming the energy-efficient power consumption regimes. The complex application of instrumental and institutional methods has increased the controllability of the power consumption regimes almost twofold.

2. For direct economic control of power consumption regimes taking into account the personal influence of the consumer on the unevenness of the ELS UES, it is expedient to include the K_{COR}^C indicator in the price function. Calculations of symmetric to C_{MID} maximum and minimum prices depending on K_{COR}^C and intermediate values of the price in the functional dependence on the power deviation relative to P_{MID} in the energy system, allowed the development of a flexible pricing system that enhances the motivation of consumers to align the total load curve of the power system.

3. The results of further scientific research in the field of energy complex management with consideration of more complex functional relationships of power consumption regimes with characteristics such as the ability of the consumer to regulate the technological process regime in time, the degree of interest in managing the demand for electricity, the quality of consumed electricity, the reliability of power supply, and others, are of practical interest.

References

[1] Hercher-Pasteur J., Loiseau E., Sinfort C., Hélias A. Energetic assessment of the agricultural production system. A review. Agronomy for Sustainable Development, 2020, vol. 29, pp. 29-40. doi: 10.1007/s13593-020-00627-2

[2] The Energy Community. Available at: https://www.entsoe.eu/news/2022/03/16/continental-europe-successful-synchronisation-with-ukraine-and-moldova-power-systems/ (accessed 12.02.2023)

[3] Olmos L., Pérez-Arriaga I. Evaluation of Three Methods Proposed for the Computation of Inter-TSO Payments in the Internal Electricity Market of the European Union. IEEE Transactions on Power Systems, 2007, vol. 22, no. 4, pp. 1507 – 1522 doi: 10.1109/TPWRS.2007.907118

[4] Building Resilient Energy Systems: Actions for Achieving Greater Energy Security, Affordability and Net-Zero in the UNECE Region [Ece energy series, №146, 2022]. Available at: https://unece.org/sites/default/files/2023-01/Resilient%20Energy%20Systems.pdf (accessed 12.02.2023)

[5] A Power System for a Carbon Neutral Europe [Report, 2022]. Available at: https://eepublicdownloads.entsoe.eu/clean-documents/tyndp-documents/entso-

e_Vision_2050_report _221006.pdf (accessed 12.02.2023)
[6] Aggregators: Innovation Landscape Brief [Report, 2022]. Available at: https://www.irena.org/-/media/Files/IRENA/Agency/Publication/2019/Feb/IRENA_Innovation_Aggregators_2019.PDF (accessed 12.02.2023
[7] Flexibility for Resilience How can Flexibility Support Power Grids Resilience? Available at: https://op.europa.eu/en/publication-detail/-/publication/54d9c702-dc9c-11ec-a534-01aa75ed71a1(accessed 12.02.2023)
[8] Samadi M., Fattahi J., Schriemer H., Erol-Kantarci M. Demand Management for Optimized Energy Usage and Consumer Comfort Using Sequential Optimization. Sensors, 2016, vol. 21 (1), pp. 130-138. doi: 10.3390/s21010130
[9] Amoasi Acquah M., Kodaira D., Han S. Real-Time Demand Side Management Algorithm Using Stochastic Optimization. Energies, 2018, vol. 11 (5), pp. 1166-1182. doi: 10.3390/en11051166
[10] Hu F., Qin J., Wang J. Electrical Load Schedule Optimization for Manufacturing Plants. Proceedings of the 11th IEEE International Conference on Networking, Sensing and Control, ICNSC 2014. Miami, FL, USA, 2019, pp. 7-12. doi: 10.1109/ICNSC.2014.6819591
[11] Komar V., Lezhniuk P., Lesko V., Malogulko Yu., Netrebskyi V., Sikorska O. Electricity Consumption and Renewable Energy Sources Generation Schedules Coordination in Electric Networks for Balance Reliability Increasing. Energy Facilities: Management and Design and Technological Innovations. Kharkiv: PC TECHNOLOGY CENTER, 2022, pp. 42–75. doi: 10.15587/978-617-7319-63-3.ch2
[12] Filimonova A. A., Zatsepin E. P., Zatsepina V. I. Multilevel Control of Power Consumption at Metallurgical Plants. Proc. IEEE Int. Russian Automation Conf., Sochi, Russia, 2018, pp. 1-4. doi: 10.1109/RUSAUTOCON.2018.8501746
[13] Jiang B., Muzhikyan A., Farid A. M., Youcef-Toumi K. Demand Side Management in Powergrid Enterprise Control: A Comparison of Industrial & Social Welfare Approaches. Applied Energy, 2017, vol. 187, pp. 833-846. doi: 10.1016/j.apenergy.2016.10.096
[14] Pan R., Li Z., Cao J., Zhang H., Xia X. Electrical Load Tracking Scheduling of Steel Plants Under Time-of-use Tariffs. Computers & Industrial Engineering, 2019, vol. 137, pp. 1-18. doi: 10.1016/j.cie.2019.106049
[15] Prashar, A. Towards Sustainable Development in Industrial Small and Medium-sized Enterprises: An Energy Sustainability approach. Journal of Cleaner Production, 2019, vol. 235, pp. 977-996. doi: 10.1016/j.jclepro.2019.07.045
[16] Sharda S., Singh M., Sharma K. Demand Side Management through Load Shifting in IoT Based HEMS: Overview, Challenges and Opportunities. Sustainable Cities and Society, 2021, vol. 65, pp. 1-22. doi: 10.1016/j.scs.2020.102517
[17] Parizy E., Bahrami H., Choi S. A Low Complexity and Secure Demand Response Technique for Peak Load Reduction. IEEE Transactions on Smart Grid, 2018, vol. 10(3), pp. 3259-3268. doi:10.1109/TSG.2018.2822729
[18] Rivera-Castro A., Fuentes-Velazquez J., Angeles-Camacho C. Energy Savings Due to Daylight Saving in Mexico; Case Study: Buildings and Facilities of CU-UNAM. 2019 IEEE 39th Central America and Panama Convention, CONCAPAN. Guatemala, 2019, pp. 1-7. doi: 10.1109/CONCAPANXXXIX47272.2019.8976996
[19] Alexandrov O., Dyagileva N. Optimization of Modes Electro-Power Engineering System at Interaction it with Consumer. 2018 Open Conference of Electrical, Electronic and Information Sciences, eStream, 2018. Vilnius, Lithuania, 2018, pp. 1-5. doi: 10.1109/eStream.2018.8394116
[20] Komlev Yu. Power Systems and Electric Networks: Calculation of the Transit Losses of Electric Power in the Radial Networks of Electric Supply Systems. Power Technology and Engineering, 2011, vol. 45 (4), pp. 309-314. doi: 10.1007/s10749-011-0267-8
[21] Mariano J., Urbanetz Jr. The Energy Storage System Integration Into Photovoltaic Systems: A Case Study of Energy Management at UTFPR. Frontiers in Energy Research, 2022, vol. 10, pp. 5431-5445. doi: 10.3389/fenrg.2022.831245
[22] Attia A. Simulation and Analytical Comparison between Load Management Techniques. 2020 8th International Conference on Smart Energy Grid Engineering, SEGE 2020. Oshawa, ON, Canada, 2022, pp. 128-132 doi: 10.1109/SEGE49949.2020.9182010
[23] Serebrennikov B.S., Petrova K.H. Upravlinnia Rezhymom Elektrospozhyvannia Promyslovykh Spozhyvachiv z Vykorystanniam Tekhnolohichnoho Resursu [The Control of the Electric Power Consumption of the Industrial Enterprises with the Use of the Technological Resource]. Elektrotekhnika ta elektroenerhetyka - Electrical and Power Engineering, 2013. no. 1, pp. 70-76. (In Ukrainian).
[24] Gordeev V. Regulirovanie Maksimuma Nagruzki Promyshlennykh Elektricheskikh Setei [Regulation of the Maximum Load of Industrial Electrical Networks. Moskva, 1981. 184 p. (In Russian).
[25] Serebrennikov B.S., Petrova K.H., Serebrennikov S.V., Savelenko I.V.

Ekonomicheskoe Stimulirovanie Operatorov Sistemyi Raspredeleniya Elektricheskoy Energii k Tehnicheskoy Modernizatsii Setevoy Infrastrukturyi [Economic Incentives for the Modernization of the Electricity Distribution System Operators' Network Infrastructure]. Problemele Energeticii Regionale, 2020, no. 3(47), pp. 101-115. doi: 10.5281/zenodo.4018972 (In Russian).

Information about the authors.

Serebrennikov Bohdan, Ph.D. in Economics, Senior Researcher at the Institute of Economics and Forecasting of the National Academy of Sciences of Ukraine, Kiev, Ukraine. His research interests include regulation of the electricity market, competition and pricing, market integration, energy and climate policy.
E-mail:
bs.serebrennikov@gmail.com

Petrova Kateryna, PhD in Engineering, Associate Professor at the Department of ETS and EM, CUNTU, Kropyvnytskyi, Ukraine. Research interests: management of electricity consumption modes over time, pricing in the electricity market, energy auditing.
E-mail:
Kateflash27@gmail.com

Serebrennikov Sergii, PhD in Technical Sciences, Professor at the Department of ETS and EM of CUNTU in Kropyvnytskyi, Ukraine. His research interests include vortex control in power engineering, regulation of electricity consumption modes over time, and pricing in the electricity market.
E-mail:
sv.serebrennikov@gmail.com

Generating a Set of Reference Images for Reliable Condition Monitoring of Critical Infrastructure using Mobile Robots

Sotnikov O.[1], Tymochko O.[2], Bondarchuk S.[2], Dzhuma L.[2], Rudenko V.[3], Mandryk Ya.[2], Surkov K.[2], Palonyi A.[2], Olizarenko S.[2]

[1]Kharkiv National Air Force University named after Ivan Kozhedub, Kharkiv, Ukraine

[2]Flying Academy of National Aviation University, Kropyvnytskyi, Ukraine

[3]Donbass State Engineering Academy, Kramatorsk, Ukraine

Abstract. The aim of this work is to reduce the amount of computational cost when monitoring the state of critical infrastructure objects using flying mobile robots equipped with correlation-extreme navigation system, based on minimizing the number of fragments of reference images. The goal is achieved by establishing a minimum permissible degree of correlation between the individual images, which form a set of reference images. The most essential result is substantiation of the approach to formation of a set of selective images based on scene correlation analysis and sufficiency of conservation of correlation connection of images in limits 0.6 ... 0.7. This reduces the amount of computation and extends the operating time of mobile robots while maintaining accuracy. The significance of the obtained results consists in the possibility of solving a complex task of forming a set of reference images, depending on the information content and stochastic conditions of sighting of critical infrastructure objects. The solution of this task will increase efficiency of critical infrastructure objects state control due to optimization of reference images number used in the monitoring process, increase operability, and provide high control reliability in stochastic sighting conditions. The novelty of the work lies in the fact that the method of process formalized description of forming a reference images set to ensure reliable monitoring of critical infrastructure facilities using flying mobile robots for various sectors of the economy, the practical application of which will ensure reliable control and their condition assessment.

Keywords: mobile robot, critical infrastructure object, reference images, navigation system, correlation coupling, optimization.

DOI: https://doi.org/10.52254/1857-0070.2023.2-58.04

UDC: 629.7.052:504.064.37

Formarea unui set de imagini de referință pentru monitorizarea fiabilă a stării obiectelor de infrastructură critică folosind roboți mobili

Sotnikov O.[1], Tymociko O.[2], Bondarciuk S.[2], Djuma L.[2], Rudenko V.[3], Mandrîk Ya.[2], Surkov K.[2], Palionnii A.[2], Olizarenko S.[2]

[1] Universitatea Națională a Forțelor Aeriene din Kharkiv, numită după Ivan Kozhedub, Kharkiv, Ucraina

[2]Academia de zbor a Universității Naționale de Aviație, Kropivnițkii, Ucraina

[3]Academia de Stat de Inginerie Donbass, Kramatorsk, Ucraina

Rezumat. Scopul acestei lucrări este de a reduce costurile de calcul la monitorizarea stărilor obiectelor de infrastructură critică folosind roboți mobili zburători echipați cu un sistem de navigație corelație-extremă bazat pe minimizarea numărului de fragmente de imagini de referință. Acest obiectiv este atins prin stabilirea gradului minim admis de corelare între imaginile individuale care formează un set de imagini de referință. Rezultatul cel mai semnificativ este fundamentarea abordării formării unui set de imagini selective pe baza analizei corelației scenelor și a suficienței menținerii corelației imaginilor în intervalul 0,6 ... 0,7. Acest lucru vă permite să reduceți semnificativ costurile de calcul și să creșteți durata de funcționare a roboților mobili, menținând în același timp precizia necesară. Semnificația rezultatelor obținute constă în posibilitatea rezolvării problemei complexe a formării unui set de imagini de referință în funcție de conținutul informațional și de condițiile stocastice de vizionare a obiectelor de infrastructură critică. Rezolvarea acestei probleme va îmbunătăți eficiența monitorizării stărilor obiectelor de infrastructură critică prin optimizarea numărului de imagini de referință utilizate în procesul de monitorizare, va crește eficiența și va asigura o fiabilitate ridicată a monitorizării în condiții de ochire stocastică. Noutatea lucrării constă în faptul că o descriere oficială a procesului de formare a unui set de imagini de referință a fost elaborate în continuare pentru a asigura monitorizarea fiabilă a obiectelor de infrastructură critică de la roboții mobili zburători.

Cuvinte-cheie: robot mobil, obiect de infrastructură critică, imagini de referință, sistem de navigație, corelare, optimizare.

Формирование совокупности эталонных изображений для осуществления надежного контроля состояний объектов критической инфраструктуры с помощью мобильных роботов

Сотников А.М.[1], Тимочко А.И.[2], Бондарчук С.В.[2], Джума Л.Н.[2], Мандрик Я.С.[2], Руденко В.[3], Сурков К.Ю.[2], Паленный А.С.[2], Олизаренко С.А.[2]

[1]Харьковский национальный университет Воздушных Сил имени Ивана Кожежуба, Харьков, Украина
[2]Летная академия Национального авиационного университета, Кропивницкий, Украина
[3]Донбасская государственная машиностроительная академия, Краматорск, Украина

Аннотация. Целью данной работы является снижение объема вычислительных затрат при осуществлении контроля состояний объектов критической инфраструктуры с помощью летающих мобильных роботов, оснащенных корреляционно-экстремальной системой навигации, на основе минимизации числа фрагментов эталонных изображений, используемых при формировании решающей функции, как результата сравнения изображений. Поставленная цель достигается путем установления минимально допустимой степени корреляционной связи между отдельными изображениями, которые образуют необходимую для мониторинга совокупность эталонных изображений в зависимости от объектового состава, геометрических условий формирования текущих изображений, яркостных, контрастных, структурных (геометрических) информативных параметров, распределение которых представляется в виде соответствующих информативных полей. Наиболее существенным результатом является обоснование подхода к формированию совокупности селективных изображений объектов критической инфраструктуры с использованием инвариантов, полученных на основе корреляционного анализа сцен, и достаточности сохранения корреляционной связи изображений в пределах 0.6… 0.7. Это позволяет существенно снизить объем вычислительных затрат и, соответственно, повысить быстродействие системы вторичной обработки, а также продолжительность функционирования мобильных роботов при сохранении требуемых точностных показателей. Значимость полученных результатов состоит в возможности решения сложной задачи формирования совокупности эталонных изображений, используемых на борту мобильных роботов, в зависимости от объема поступающей информации и стохастических условий визирования объектов критической инфраструктуры. Решение данной задачи позволит повысить эффективность контроля состояний объектов критической инфраструктуры за счет оптимизации числа эталонных изображений, используемых в процессе мониторинга, повысить оперативность и обеспечить высокую надежность контроля в стохастических условиях визирования. Новизна работы заключается в том, что усовершенствован способ формализованного описания процесса формирования совокупности эталонных изображений для обеспечения надежного мониторинга объектов критической инфраструктуры с помощью используемых в разных отраслях народного хозяйства летающих мобильных роботов, практическое применение которых обеспечит надежный контроль и оценку их состояния.

Ключевые слова: мобильный робот, объект критической инфраструктуры, эталонные изображения, система навигации, корреляционная связь, оптимизация.

INTRODUCTION

The task of monitoring the condition of critical infrastructure objects has always been an urgent issue. In conditions of increasing terrorist threat levels and military actions, the need to solve this problem has significantly increased. Critical infrastructure objects primarily include objects of the fuel and energy sector, including the electric power industry, oil and gas industries, nuclear energy, as well as water supply, medicine, transportation, defense, chemical industry, and other areas, whose disruption can lead to national security threats, severe ecological consequences, the population loss of life, destruction of buildings, structures, residential buildings, etc. The complexity of monitoring critical objects is caused by their territorial distribution, heterogeneity of the objects themselves according to geometric, structural, and other information parameters.

Currently, in addition to proactive monitoring methods of critical infrastructure objects, autonomous active methods using flying mobile robots (MR) based on the use of correlation-extreme navigation systems (CENS) are widely used. An essential feature of such MRs is their ability to operate without operator intervention over significant distances in remote and inaccessible areas, regardless of the season, time of day, and weather conditions. This is achieved by using multispectral sensors to extract information (to) obtain high-quality current images of controlled objects and their elements, as well as a set of reference images of critical infrastructure objects used on board for subsequent identification and assessment of their conditions.

It is evident that the diversity of monitoring perspectives and the influence of natural stochastic factors on the MR functioning will result in a mismatch between the current images produced and the reference images stored aboard. The desire to reduce this mismatch necessitates the use of a significant number of reference images aboard the MR that consider all possible conditions under

which current images can be obtained. However, this approach is technically impractical as it increases the volume of image comparison operations required to find the best match. As a result, such an approach leads to a decrease in the MR functional capabilities when monitoring critical infrastructure objects at the expense of a deterioration in the high-speed performance of the secondary processing system of CENS, increased energy consumption, which in turn slows down the process of making decisions about their condition.

One possible direction for the MR effective use in monitoring critical infrastructure objects is to form the minimum permissible set of reference images that ensure the required level of accuracy and reliability of the control system. In this context, the question arises as to which method should be used to form the required set of reference images that will provide the necessary performance indicators.

Several directions for improving the efficiency of using MR for monitoring tasks are known. However, this article will be focused on the formation of a set of reference images for reliable monitoring of critical infrastructure objects. This will be achieved by establishing the minimum permissible degree of correlation between individual images. Such images form the necessary set of reference images for monitoring, depending on the object composition, geometric conditions for forming current images, brightness, contrast, and structural (geometric) informative parameters.

Let us consider the known approaches to solving the problem of forming reference images for MR equipped with a CENS.

PUBLISHED LITERATURE ANALYSIS

Tarshin V.A. et al. (2015) proposed a method for forming a reference image based on constructing a fractal analysis field, which allows for operational assessment of the informativeness of the image. The method was developed for forming individual images without considering their possible use in forming a set of reference images.

J.C. Rodríguez-Quiñonez et al. (2017) proposed a method for improving the accuracy of 3D distance measurement in stereo vision systems using optimization methods and the optoelectronic channel for forming current images. The use of the brightest stationary objects ensures an increase in measurement accuracy in perspective and scale images. The interrelation between individual images was not considered.

M. Ivanov et al. (2019) improved the method for determining the coordinates of reference objects and mobile robots and calculating the resulting errors. They considered the directions and magnitudes of external influences on unmanned aerial vehicles that affect the deviation from the calculated trajectory of movement.

Yu Ishihara and Masaki Takahashi (2022) investigated the prediction of future images for mobile robot navigation based on alignment with the sighting surface with multiple bright objects. They selected a predictive image model using the alignment object selection on the high object saturation image. However, the authors did not pay sufficient attention to the study of the interdependence of object brightness on the behavior of the mobile robot.

Leonardo A.F. Fernandes and Manuel M. Oliveira (2008) reviewed approaches to object contour detection and localization on images using the Hough transform.

Fursov V. A., et al. (2013) studied the effect of scale distortions on the object localization process. However, the study was only performed on a single reference image.

S. Maji and J. Malik (2009) presented results of optimizing the object detection procedure on images.

Katulev A. N., et al. (2014) proposed an object detection method using optoelectronic systems without a priori information on the background-target scene.

V. V. Gnilitskii et al. (2010) solved the problem of localizing a given object on an aerial image of a complex three-dimensional ground scene.

R. Bogush and S. Maltsev (2007) proposed using a minimax similarity criterion between two images to form a unimodal decision function.

A.A. Potapov (2013) presented results of using fractal analysis theory for object localization on images of different types.

Trefilov P.M. (2019) showed the feasibility of using platform-less inertial navigation systems (PINS) in unmanned aerial vehicles (UAVs) for monitoring various territories. The physical and algorithmic methods for improving PINS were considered. It was shown that the physical method allows reducing the rate of error accumulation but is unable to eliminate it completely. The application of algorithmic methods based on integration with other measuring systems allows reducing PINS errors. It is noted that satellite navigation systems and technical vision systems can be used for integration with PINS, which can significantly

increase the accuracy of UAV navigation.

Scaramuzza D., et al. (2014) presented the results of an analysis of technical issues encountered during the development and testing of an autonomous navigation system. Experimental results demonstrating the autonomous navigation of three micro air vehicles (MAVs) in an unknown environment without GPS, but with the use of 3-D mapping and optimal coverage are presented. A limitation of the study is the complete absence of information on the potential use of the proposed approach for the object state monitoring and reference image formation tasks.

Kostyashkin L.N., et al. (2014) examine approaches to solving key tasks in the development of a combined vision system for aviation. It combines the best properties and functional characteristics of two systems: an enhanced vision system that forms an improved and combined image from several multispectral sensors of a technical vision system, and a synthesized vision system that forms an image of a virtual model of the terrain based on a digital map of the terrain, navigation, and piloting parameters of the UAV. The advantage of the work is the development of algorithmic methods for reducing the complexity of the task of image alignment based on geometric alignment, the necessity of which is associated with map and navigation errors, and the visualization of geometrically aligned images considering the stage of flight task execution and visibility conditions. The disadvantage of the work is the inability to use the developed methods without the participation of a pilot.

Loginov A.A., et al. (2015) considered the issue of reducing computational complexity of combining heterogeneous images in an aircraft's combined vision system. The strength of the work is the proposed solutions that allow reducing the computational complexity of correlation-extremal registration to enable real-time performance. To eliminate the course search, the authors proposed to create large-sized terrain reference images. To avoid pitch and roll search, they suggested using the horizon line or non-correlation registration for pitch. The main idea of non-correlation registration for pitch and roll is to find the real horizon line and combine it with the synthesized one. The limitation of the work is the practical application on unmanned aerial vehicles at low altitudes due to the impracticality of using large-sized reference images and the inability to determine the horizon line during steep trajectories.

Elesina S. and Lomteva O. (2014) presented the results of a study on a genetic algorithm aimed at obtaining optimal settings for its use in combined technical vision systems. The feasibility of using extended angles of reference images in the search for global extremes was shown. It was shown that using this approach, the system's performance increases by 5 times. However, the authors did not consider the possible influence of perspectives of reference and flowing images on real-time implementation, which is a disadvantage.

Yeromina N., et al. (2018a) proposed a method for generating a set of reference images for high-precision navigation of mobile robots. A disadvantage of the developed method in this work is its limited applicability to solving the navigation problem of mobile robots moving along trajectories without significant changes in altitude and viewing angles.

Yeromina, et al. (2021a) justified the need for a new approach to selecting a reference image from the set of images on board when performing localization of aircraft equipped with CENS. The results of developing a model for describing the process of forming the decision function because of comparing the current image formed by the secondary information processing system based on the available set of reference images are presented. Using this model, the task was formulated to develop a method and algorithm for rational selection of reference images in the secondary processing system of the CENS. For the selected initial data, the results of developing an iterative method and algorithm for selecting reference images from the available set based on modeling the brightness distribution of a typical image fragment of the viewing surface under various observation conditions and different resolution capabilities of CENS sensors are presented. The method involves using an iterative procedure for selecting reference images from the multidimensional matrix representation of the set of reference images based on the height parameter determined by the onboard radio electronic equipment of the UAV, and then refining based on angular parameters using the selected rule. An algorithm for implementing the reference image selection procedure based on the proposed method has been developed. However, the authors did not consider the issue of forming a minimal set of the reference images.

Yeromina N. et al. (2021b) proposed methods for synthesizing reference images for the UAV navigation in normal and hyperspectral modes.

Yeromina N. et al. (2018b), Yeromina N. et al. (2020a), Liashko O. et al. (2020), Yeromina N. et

al. (2020b), Yeromina N. et al. (2020c), and Vorobiov O. et al. (2020) presented research results on the synthesis of reference images with different levels of informational content and compared them with the current image. Methods for advance and real-time preparation of reference images were proposed based on the use of various invariants. When developing methods for constructing selective images, only the object composition of the viewing surface was considered. This approach made it possible to form reference images based on the most informative objects. It was assumed that the comparison of reference images with the current onboard image would be carried out using the "sliding window" method, and the formation of the comparison result for navigation object location correction would be based on one reference image. This means that these methods have limited applicability, which is a significant disadvantage. The reason for this is that they were not aimed at reducing the computational complexity of image comparison, did not consider the volume of image arrays and the need to form a set of images taking into account possible changes in the perspectives of current image formation on board the UAV.

Literature analysis suggests the prospects of using MR for monitoring ground objects and developing methods for generating reference images to reduce operational volume. At the same time, the problem of reducing computational costs for monitoring critical infrastructure objects using flying mobile robots equipped with a correlation-extreme navigation system remains unresolved. This can be achieved through minimizing the number of fragments of reference images while ensuring the required precision and reliability of monitoring critical infrastructure objects.

METHODS, RESULTS, AND DISCUSSION

To continue the approaches proposed by Tarshin V. A., et al., 2015, and Yeromina N., et al., 2018a for describing current images $\mathbf{S}_{CI}$ of critical infrastructure objects, we will use the brightness values of the corresponding objects and background surfaces in the resolution elements:

$$\mathbf{S}_{CI} = \mathbf{S}_{OI} = \left\| S(i,j) \right\|, \qquad (1)$$

where $\mathbf{S}_{OI}$ is the undistorted source image;

$$S(i,j) = \begin{cases} S_v(i,j), & \text{при } S(i,j) \in \mathbf{S}_v \\ S_w(i,j), & \text{при } S(i,j) \in \mathbf{S}_w \end{cases};$$

$S_v(i,j)$ – is the brightness of the v-th image element of the object $\mathbf{S}_v$;

$S_w(i,j)$ – is the brightness of the w-th image element of the background $\mathbf{S}_w$;

V and W are the number of critical infrastructure objects and backgrounds of different brightness and shapes in the source image, respectively.

We will take into account the following assumptions in the model of the current image:

1) The current and initial images have the same size of $N_1 \times N_2$ pixels;

2) Critical infrastructure objects have significantly higher brightness values compared to the background and are homogeneous in brightness within the resolution element;

3) Each i,j-th element of the current image represents a normally distributed variable with a variance of σ_{ij}^2 and a mean brightness value of $S(i,j)$, which, in the absence of interference, can take one of two values: $S_v(i,j)$ or $S_w(i,j)$;

4) The contrast of critical infrastructure objects relative to the surrounding background is determined as $\Delta S = S_v(i,j) - S_w(i,j)$;

5) The noise variance in the receiving channels of CENS is the same, i.e., $\sigma_{ij}^2 = \sigma^2$, where $i \in \overline{1, N_1},\ j \in \overline{1, N_2}$;

6) The number of background elements belonging to the set $\mathbf{S}_w$ and critical infrastructure objects belonging to the set $\boldsymbol{S_v}$, satisfies the relation $V << W$.

The probability density functions of the brightness S for the background elements and the critical infrastructure objects, considering the assumptions made, are determined by the following expressions:

$$w_w(S) = \frac{1}{\sqrt{2\pi}\sigma} \exp\left[-\left(S - S_w\right)^2 / 2\sigma^2 \right], \qquad (2)$$

$$w_v(S) = \frac{1}{\sqrt{2\pi}\sigma} \exp\left[-\left(S - S_v\right)^2 / 2\sigma^2 \right]. \qquad (3)$$

Description of a set of reference images.

The wide range of changes in the height of MR $h_i \in [h_{\min}, h_{\max}]$, viewing angles $\alpha_j \in [\alpha_{\min}, \alpha_{\max}]$, $\beta_k \in [\beta_{\min}, \beta_{\max}]$, differences in monitoring direction determined by vector $\mathbf{v}$, as well as

temporal changes t_p, necessitates the use of a set of reference images:

$$\begin{aligned} &\left\{\mathbf{S}_{RI}(2\theta_{0,5}, h_i, \alpha_j, \beta_k, \nu_l, \varphi_s, t_m)\right\}, \\ &i=\overline{1,I},\ j=\overline{1,J}, \\ &k=\overline{1,K},\ l=\overline{1,L}, \\ &p=\overline{1,P},\ s=\overline{1,S}. \end{aligned} \tag{4}$$

Each individual reference image corresponds to its own matrix of brightness values of the corresponding pixels:

$$\mathbf{S}_{RI}=\left\|S_{RI}(m,l)\right\|,\ m=\overline{1,M},\ l=\overline{1,L},$$

where M, L are the dimensions of the reference images.

Due to the instability both of the absolute brightness values of individual critical infrastructure objects and the contrast between control objects and the background, we will consider that the images are given by the contrast sign and the geometric shape of critical infrastructure objects, i.e. in the form of binary images formed for different heights and viewing angles. The values 1 correspond to the elements of critical infrastructure objects, and 0 to the background elements.

For these models of the current and reference images, we will represent the result of their comparison as follows:

$$\mathbf{R}(\mathbf{r},t)=\mathbf{F}_{SP}\begin{pmatrix}\mathbf{S}_{CI}(\mathbf{r},t), \\ \mathbf{S}_{RI}(2\theta_{0,5}, h_i, \alpha_j, \beta_k, \nu_l, \varphi_s, t_p)\end{pmatrix}, \tag{5}$$

where $\mathbf{F}_{SP}$ is the image comparison operator.

Problem statement.

For the considered image models, based on their comparison, it is necessary to solve the problem of minimizing the number of reference images that form the required set, the use of which will ensure the required accuracy and reliability of monitoring the states of critical infrastructure objects.

Solution.

The set of reference images $\{\bullet\}$ is a multidimensional matrix, the filling of which with individual images, without restrictions on the amount of computation, can be as large as desired, depending on the chosen discretization step, both in height and angles.

Obviously, the smaller the discretization step, the better the correspondence between the selected reference image for comparison and the current image. In other words, the higher the correlation coefficient of the compared images will be.

In addition, the degree of mutual correlation between individual neighboring reference images within the set itself will also be high. Based on this, the solution to the problem can be reduced to establishing the minimum permissible degree of correlation between individual images that make up the set of reference images. At the same time, the accuracy of monitoring the condition of critical infrastructure objects will actually be determined by the steepness of the $\mathbf{R}(\mathbf{r},t)$ function in the region of its maximum, according to the following relationship:

$$\sigma_{\mathbf{R}}=\sqrt{-\frac{1}{\frac{\partial^2\mathbf{R}(\mathbf{r},\mathrm{t})}{\partial\mathbf{r}^2}}}. \tag{6}$$

The reliability of monitoring the condition of critical infrastructure objects will be determined by the unimodality of the $\mathbf{R}(\mathbf{r},t)$, function, or, in other words, through the probability of occurrence of anomalous errors, which can be easily determined using the maximum likelihood method based on expressions (2), (3).

The diversity of critical infrastructure objects, differences in backgrounds, viewing conditions, and the influence of many random factors on the functioning of the MR require the presence of a large amount of statistical data, their generalization, classification, and a non-deterministic approach. Therefore, at this stage of the research, it is advisable to use the method of statistical modeling, since the problem being solved is stochastic. At the first stage of modeling, using various reference images of critical infrastructure objects for possible viewing conditions, it is necessary to construct selective images. The peculiarity of this stage is the obtaining of a set of selective images that will significantly differ in the number of objects in the images for different heights due to the spatial smoothing of objects in the images. This happens because some objects become small and comparable to, or smaller than, the resolution element of the antenna system channel for receiving information as the height increases. Another feature of this stage is the appearance of perspective distortions depending on the orientation of the antenna system (angle of inclination), which also leads to a decrease in correlation by geometric features. At the second stage, it is necessary to compare the reference image with the obtained

selective images.

The third stage involves determining the minimum permissible correlation between adjacent reference images forming the required minimum set for the chosen range of viewing parameters, satisfying condition (6) and the unimodality of the function $\mathbf{R}(\mathbf{r},t)$. In the final stage, the minimum number of reference images forming the desired set is determined based on the minimum permissible degree of correlation between individual images.

Modeling will be carried out using images of objects on the viewing surface with different object compositions and for different viewing angles at a height of 500 m. The influence of random factors on the formation of selective images will be considered by selecting the degree of correlation between the initial and selective reference images at a level ranging from 0.5 to 0.7.

Reference images of critical infrastructure monitoring areas, including energy infrastructure, are shown in Figs. 1, 4, 7, 10, 13; binary reference images obtained based on these reference images (Figs. 1, 4, 7, 10, 13) are shown in Figs. 2, 5, 8, 11, 14, and the results of their comparison based on the classical correlation algorithm are shown in Figs. 3, 6, 9, 12, 15.

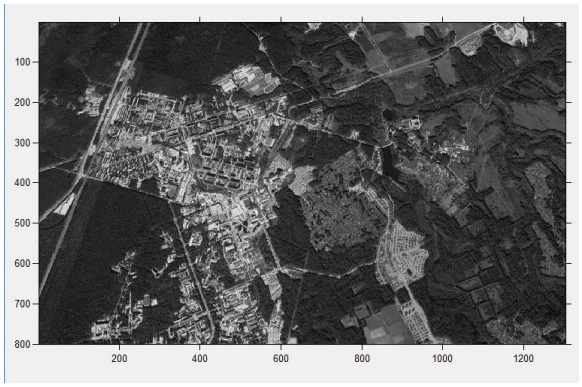

Fig. 1. Initial image of the monitoring area.

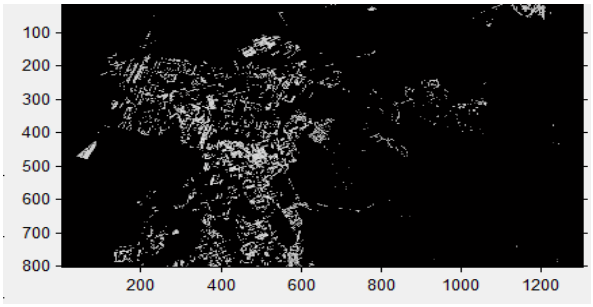

Fig. 2 Binary selective image at the cross-section level over the field of correlation analysis 0.7 to the original image.

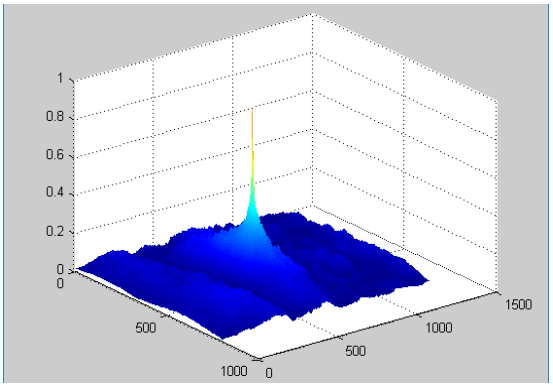

Fig. 3. The result of comparing the original image with its binary selective image.

Let's consider the case when the initial image was obtained at an angle of 30 degrees of viewing.

Fig. 4. The original image of the monitoring area at a viewing angle of 30 degrees.

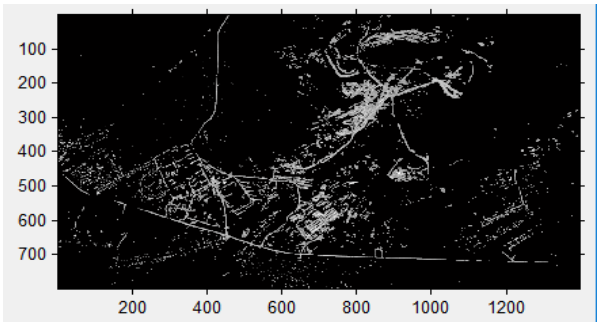

Fig.5. Binary selective image at the cross-section level over the field of correlation analysis 0.6 to the original image.

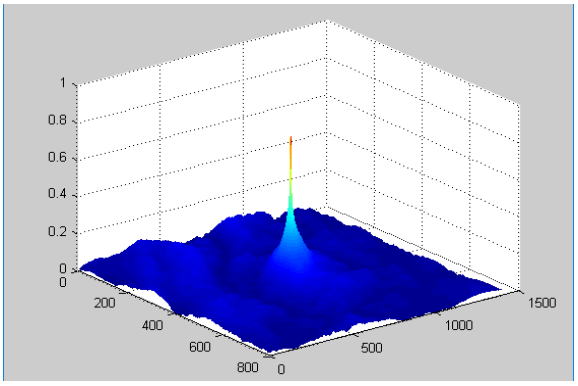

Fig. 6. The result of comparing the original image (Fig. 4) with its binary selective image.

Fig. 7. Initial image of the monitoring area with homogeneous objects of large sizes.

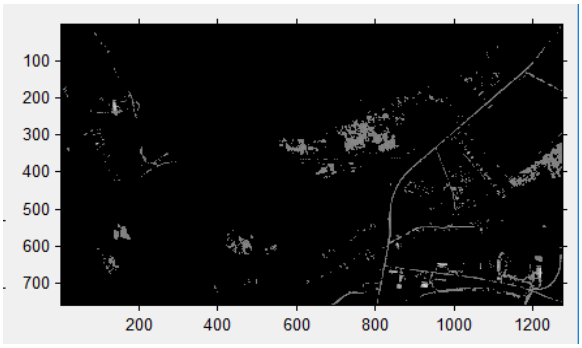

Fig. 8. Binary selective image at a cross-sectional level over the field of correlation analysis of 0.5 to the original image (Fig. 7).

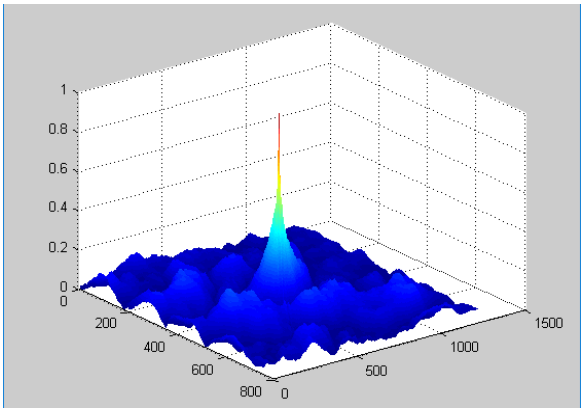

Fig. 9. The result of comparing the original image (Fig. 7) with its binary selective image.

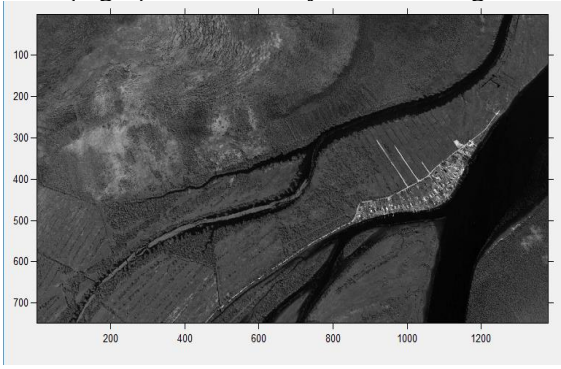

Fig. 10. Original image of a typical landscape.

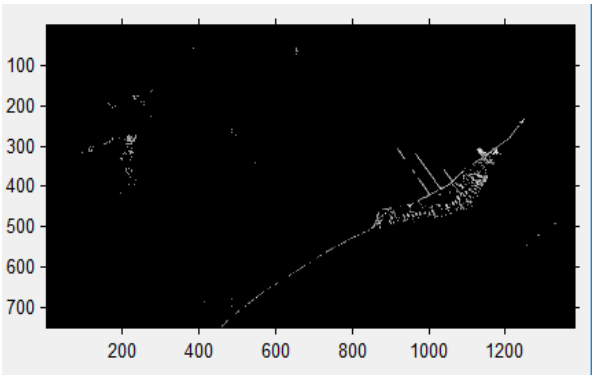

Fig. 11. Binary selective image at a cross-sectional level in the field of correlation analysis of 0.6 to the original image (Fig. 10).

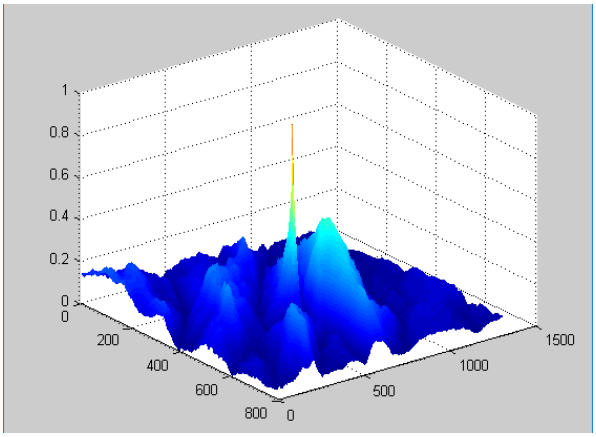

Fig. 12. The result of comparing the original image (Fig. 10) with its binary selective image.

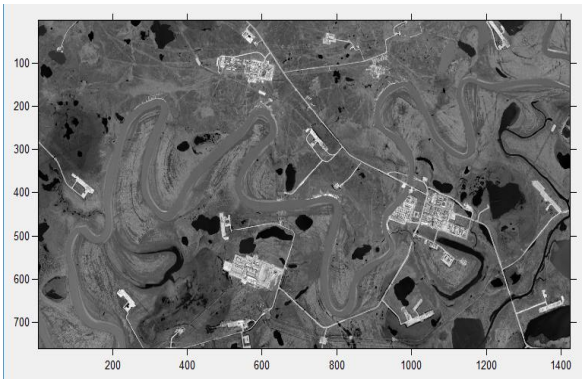

Fig. 13. Original image of a typical landscape with buildings.

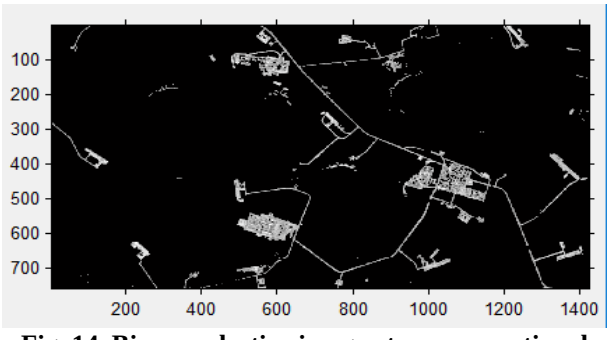

Fig. 14. Binary selective image at a cross-sectional level in the field of correlation analysis of 0.6 to the original image (Fig. 13).

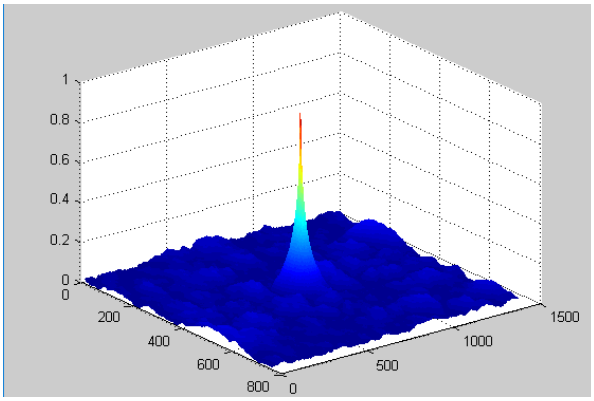

Fig. 15. The result of comparing the original image (Fig. 13) with its binary selective image.

The results of the modeling considering the influence of stochastic factors leading to a decrease in the correlation between images, presented in Figs. 1--15, show that when forming a minimal set of reference images that can ensure the required accuracy and reliability of monitoring the state of infrastructure objects, it is sufficient to maintain a correlation between adjacent images within 0.6. This correlation is ensured with a discretization step for angles within 30 degrees. These modeling results were obtained for a constant value of the height of MR.

The influence of changing in the height of the MR flight on the formation of the image comparison function is shown for the range of heights from 500 to 600 m in Fig. 16.

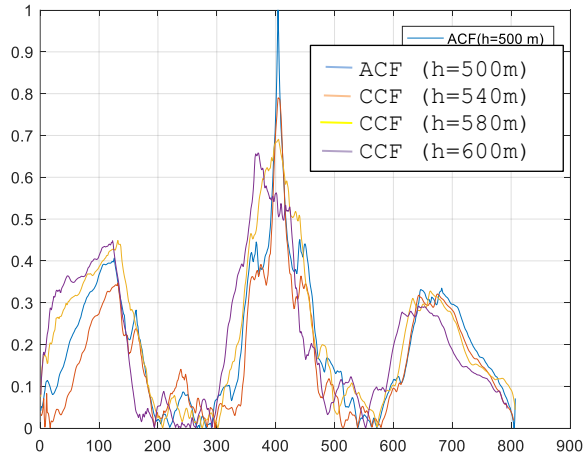

Fig. 16. The results of comparison of the original image with its binary selective image for the height range from 500 to 600 m.

The analysis of the comparison results between the initial image and its binary selective image for the altitude range from 500 to 600 meters, presented in Fig. 16, shows the possibility of using a height discretization step within the range of 80 to 100 meters, which maintains the unimodality of the image comparison function of $\mathbf{R}(\mathbf{r},t)$. At the same time, it is necessary to consider a significant deterioration in the accuracy of image comparison and, consequently, the accuracy of assessing the states of controlled objects.

For example, when the degree of correlation is at the level of 0.5, the accuracy will be in the order of tens of meters, which becomes unacceptable for monitoring the condition of small critical infrastructure objects. In this case, the reliability of monitoring the states of these objects is significantly reduced at a degree of correlation within the range of 0.5, when side outliers appear, comparable in magnitude to the main lobe of the image comparison function.

CONCLUSIONS

As a result of the conducted research, an approach to forming a set of selective images based on correlation analysis of scenes and the sufficient preservation of correlation between neighboring images within 0.6…0.7 has been justified. Such an approach allows for a significant reduction in computational costs by forming a set of reference images with a minimum permissible set of discretization parameters, which are about 30 degrees for angles and 80-100 meters for height. At the same time, high accuracy, and reliability of monitoring the state of critical infrastructure objects are ensured.

References

[1] Tarshin V. A. Podgotovka etalonnykh izobrazheniy dlya vysokotochnykh korrelyatsionno-ekstremal'nykh sistem navigatsii na osnove formirovaniya polya fraktal'nykh razmernostey [Tekst] / V. A. Tarshin, A. M. Sotnikov, R. G. Sidorenko, V. V. Megel'bey // Sistemi ozbroênnya í víys'kova tekhníka. – 2015. – № 2. – S. 142 -144.

[2] J.C. Rodríguez-Quiñonez, O. Sergiyenko, W. Flores-Fuentes, M. Rivas-lopez, D. Hernandez-Balbuena, R. Rascón, P. Mercorelli. Improve a 3D distance measurement accuracy in stereo vision systems using optimization methods' approach. Opto-Electronics Review by Elsevier, Volume 25, Issue 1, May 2017, P. 24–32.

[3] M. Ivanov, L. Lindner, O. Sergiyenko, J. C. Rodríguez-Quiñonez, W. Flores-Fuentes, and M. Rivas-López. "Mobile Robot Path Planning Using Continuous Laser Scanning." Optoelectronics in Machine Vision-Based Theories and Applications. IGI Global, 2019. Pp. 338-372. Web. 7 Dec. 2018. doi:10.4018/978-1-5225-5751-7.ch012

[4] Yu Ishihara, Masaki Takahashi. Empirical study of future image prediction for image-based mobile robot navigation. Robotics and Autonomous Systems. - 2022 - pp. 104018. DOI: 10.1016/j.robot.2021.104018.

[5] Pakhomov A.A. Obrabotka iskazhennykh atmosferoy izobrazheniy, poluchennykh aviatsionnymi kompleksami [Tekst] / A.A. Pakhomov, A.A. Potapov // Uspekhi sovremennoy radioelektroniki. – Radiotekhnika – 2015. – №5. – P. 144-145.

[6] Fernandes, L. Real-time line detection through an improved Hough transform voting scheme [Text] / Leonardo A.F. Fernandes, Manuel M. Oliveira // Pattern Recognition. – 2008. – V. 41, N 1. – P. 299-314. – ISSN 0031-3203.

[7] Fursov, V. A. Lokalizatsiya konturov ob'yektov na izobrazheniyakh pri variatsiyakh masshtaba s ispol'zovaniyem preobrazovaniya Khafa [Tekst] / V. A. Fursov, S. A. Bibikov, P. YU. Yakimov // Komp'yuternaya optika.– 2013. – T. 37, №4. – P. 496-502.

[8] Maji, S. A max-margin Hough transform for object detection [Text] / S. Maji, J. Malik. // Proc. of IEEE Computer Society Conference on Computer Vision and Pattern Recognition. – 2009.

[9] Katulev, A. N. Adaptivnyy metod i algoritm obnaruzheniya malokontrastnykh ob"yektov optiko-elektronnym sredstvom [Tekst] / A. N. Katulev, A. A. Kolonskov, A. A. Khramichev, S. V. Yagol'nikov // Opticheskiy zhurnal. – 2014. – № 2(81). – S. 29-39.

[10] Gnilitskii V.V. Decision making algorithms in the problem of object selection in images of ground scenes / V.V. Gnilitskii, V.V. Insarov, A.S.Chernyavskii //Journal of Computer and Systems Sciences International.–2010.–T.49. №6.–P.972-980. DOI: 10.1134/S1064230710060158.

[11] Bogush, R. Minimax Criterion of Similarity for Video Information Processing [Text] / R.Bogush, S. Maltsev // Control and Communications: Proc. of IEEE Int. Conf., Tomsk, April 20-21, 2007 / Tomsk Polytechnic University. - Tomsk, 2007. - P. 120-126.

[12] Potapov, A.A. Fractal paradigm and fractal-scaling methods in fundamentally new dynamic fractal signal detectors [Text] / A.A. Potapov // Proceedings – 2013 International Kharkov symposium on physics and engineering of millimeter and submillimeter waves, MSMW 2013. – 2013. – P. 644-647.

[13] Trefilov P.M. Comparative Analysis of Improving Accuracy of Inertial Navigation Systems. Trapeznikov Institute of Control Problems of the Russian Academy of Sciences. Proceedings of XIII All-Russian meeting on control problems VSPU-2019. Trapeznikov Institute of control problems. V.A. Trapeznikov RAS, Russia, 2019. pp. 470-474.

[14] Scaramuzza D., et al. ¨Vision-controlled micro flying robots: from system design to autonomous navigation and mapping in GPS-denied environments¨ in IEEE Robotics & Automation Magazine, Volume 21 , Issue: 3 , pp. 26-40, Sept. 2014.

[15] Kostyashkin L.N., Loginov A.A., Nikiforov M.B. Problem aspects of the combined vision system of flying vehicles // Izvestiya SFU. 2013. № 5. C. 61-65.

[16] Loginov A.A., Muratov E.R., Nikiforov M.B., Novikov A.I. Reducing the computational complexity of image matching in aviation vision systems // Dynamics of Complex Systems. 2015. T. 9, № 1. C. 33-40.

[17] Guide P-315 "On Minimum Aviation Systems Performance Standards (MASPS) for Enhanced Vision Systems, Artificial Vision Systems, Combined Artificial Vision Systems and Airborne Vision Enhancement Systems" of the Interstate Aviation Committee Aviation Register (IAC AR), 2008.

[18] Elesina S., Lomteva O. Increase of image combination performance in combined vision systems using genetic algorithm // Proceedings of the 3rd Mediterranean Conference on Embedded Computing. – Budva, Montenegro.– 2014. PP. 158-161.

[19] Yeromina N., Petrov S., Tantsiura A., Iasechko M., Larin V. Formation of reference images and decision function in radiometric correlation-extremal navigation systems, Eastern-European Journal of Enterprise Technologies. - 2018a. Vol.4, No.9 (94). - pp. 27-35. DOI: 10.15587/1729-4061.2018.139723.

[20] Yeromina, N., Tarshyn, V., Petrov, S., Salo, N., Chumak, O. Method of reference image selection to provide high-speed aircraft navigation under conditions of rapid change of flight trajectory. International Journal of Advanced Technology and Engineering Exploration, Vol 8(85), 2021 a. p.1621-1638. DOI:10.19101/IJATEE.2021.874814.

[21] Yeromina N., Kurban V., Mykus S., Peredrii O., Voloshchenko O., Kosenko V., Kuzavkov V., Babeliuk O., Derevianko M., Kovalov H. The creation of the database for mobile robots navigation under the conditions of flexible change of flight assignment. International Journal of Emerging Technology and Advanced Engineering, 2021 b, 11(5), pp. 37–44. doi.org/10.46338/ijetae0521_05.

[22] Yeromina N., Petrov S., Tantsiura A., Iasechko M., Larin V. Formation of reference images and decision function in radiometric correlation-extremal navigation systems, Eastern-European Journal of Enterprise Technologies. - 2018 b. Vol.4, No.9 (94). - pp. 27-35. DOI: 10.15587/1729-4061.2018.139723.

[23] Yeromina N., Petrov S., Antonenko N., Vlasov I., Kostrytsia V., Korshenko V. The Synthesis of the Optimal Reference Image Using Nominal and Hyperordinal Scales, IJETER, 8 (5), 2020 a, pp. 2080-2084, doi:10.30534/ijeter/2020/98852020.

[24] Liashko O., Klindukhova V., Yeromina N., Karadobrii T., Bairamova O., Dorosheva A. The Criterion and Evaluation of Effectiveness of Image Comparison in Correlation-Extreme Navigation Systems of Mobile Robots, IJETER, 8 (6), 2020, pp. 2841-2847, doi:10.30534/ijeter/2020/ 97862020.

[25] Yeromina N., Samoilenko V., Chukanivskyi D., Zadkova O., Brodova O., Levchenko O. The Method of Iterative Formation of Selective Reference Images, IJETER, 8 (7), 2020 b, pp. 3753-3759, doi:10.30534/ijeter/2020/ 138872020.

[26] Yeromina N., Petrov S., Samsonov Y., Pisarevskiy S., Kaplun S., Vlasenko I. The Simulation and Performance Evaluation of Adaptive Algorithm of Image Comparison in Correlation-Extreme Navigation

Systems, IJETER, 8 (8), 2020, pp. 4146-4151, doi:10.30534/ijeter/2020/19882020.
[27] Vorobiov O., Yeromina N., Petrov S., Ivashcuk O., Ivansky V., Pavlunko M., Nevhad S. The Study of Accuracy Characteristics of Information Extraction System Under Conditions of Change of State of the Working Signals Propagation Path and A-Priori Uncertainty About the Informative Parameters of Objects on the Sighting Surface, IJETER, 8 (9), 2020, pp. 5740-5745, doi:10.30534/ijeter /2020/134892020.

About authors.

Sotnikov Oleksandr, Doctor of Technical Sciences, Professor principal scientist, Kharkov National Air Force University; area of scientific interests: Navigation systems for mobile robots, image processing methods and algorithms, E-mail: alexsot@ukr.net

Tymochko Oleksandr, Doctor of Technical Sciences, Professor, Head of the Department Flight Academy of the National Aviation University, area of scientific interests: decision support systems, motion control, automation, E-mail: timochko.alex@gmail.com

Bondarchuk Svitlana, PhD, associate professor, Flight Academy of the National Aviation University, area of scientific interests: life safety E-mail: svitlanabon20@gmail.com

Dzhuma Liudmyla, Candidate of Technical Sciences (PhD in Engineering), associate professor, Flight Academy of the National Aviation University, area of scientific interests: database, E-mail: ldzhuma@sfa.org.ua

Rudenko Vladislav, Candidate of Technical Sciences (PhD in Engineering), Associate professor of the Department, Donbass State Engineering Academy (DSEA), area of scientific interests: modeling E-mail: vl_rudenko@ukr.net

Mandryk Yana, PhD, associate professor of department, Flight Academy of the National Aviation University, area of scientific interests: navigation, E-mail: yana.mandryk@gmail.com

Surkov Kostiantyn, Candidate of Technical Sciences (PhD in Engineering), senior lecturer of department, Flight Academy of the National Aviation University, area of scientific interests: navigation and motion control, E-mail: kskrua@gmail.com

Palonyi Andrii, Candidate of Technical Sciences (PhD in Engineering), associate professor of department, Flight Academy of the National Aviation University, area of scientific interests: mathematical modeling, E-mail: andreypalen@gmail.com

Olizarenko Serhij, Doctor of Technical Sciences, Senior Researcher, Professor of the Department, Flight Academy of the National Aviation University, area of scientific interests: mathematical modeling, E-mail: solizarenko71@gmail.com

Development of a Model and Experimental Study of Thermal Processes in a Ferrofluid Sealer

Nesterov S.A. and Baklanov V.D.
Ivanovo State Power Engineering University,
Ivanovo, Russian Federation

Abstract. The aim of the work is to create an interconnected numerical model of the magnetic, hydrodynamic and temperature fields of a ferrofluid sealer and to analyze thermal processes occurring in high-speed seals. This goal is achieved by selecting the necessary equations, boundary conditions, assumptions and physical properties of the magnetic fluid when building the numerical model of the sealer's working gap, verification of the developed model by the results of the physical experiment. The important results of the work are the obtained and analyzed data on the influence both of physical properties and the geometry of the working gap of the ferrofluid sealer on the heating of the ferrofluid. With a shaft radius of 140 mm and a linear velocity at the shaft surface of 25 m/s due to viscous heating the ferrofluid temperature exceeding the ambient temperature can reach values up to 80 degrees and higher, it has been shown. The use of the equation proposed by V.E. Fertman to determine the thermal conductivity of ferrofluid and the mixing rule to determine its heat capacity allows us to describe with sufficient accuracy for engineering calculations the thermophysical properties of concentrated ferrofluids, it was shown. The significance of the results consists in the possibility of using the developed numerical model in the study of interrelated physical processes in the working gap of the ferrofluid sealer of rotating shafts. The physical and concentration parameters of the synthetic oil-based magnetic fluid given in the paper and the results of its test operation as part of a ferrofluid seal can be used to verify the results of newly developed models of ferrofluid devices.
Keywords: ferrofluid, ferrofluid sealer, viscous heating, numerical simulation.

DOI: https://doi.org/10.52254/1857-0070.2023.2-58-05
UDC: 62-185.7

Elaborarea unui model și studiu experimental al proceselor termice într-un etanșant magnetofluidic
Nesterov S.A., Baklanov V.D.
Universitatea de Stat de Inginerie Energetică din Ivanovo, numită după V.I. Lenin, or. Ivanovo, Federația Rusă
Rezumat. Scopul lucrării este de a crea un model numeric interconectat magnetic, hidrodinamic și de temperatură ale cîmpurilor etanșantului fluidomagnetic și de a analiza procesele termice care au loc în etanșările de mare viteză. Scopul este atins prin alegerea ecuațiilor necesare, condițiilor la limită, ipotezelor și proprietăților fizice ale fluidului magnetic în construirea unui model numeric al golului de lucru al etanșării, verificând modelul elaborat pe baza rezultatelor unui experiment fizic. Rezultate importante ale lucrării sunt datele obținute și analizate privind efectul asupra vâscoasei, a încălzirii fluidului magnetic atât proprietățile sale fizice, cât și al geometriei spațiului de lucru al sigilantului cu fluid magnetic. Se arată că cu o rază a arborelui de 140 mm și o viteză liniară pe suprafața arborelui de 25 m/s, datorită încălzirii vâscoase, excesul de temperatură a fluidului magnetic față de temperatura ambiantă poate atinge valori de până la 80 de grade și mai mult. Se arată că utilizarea ecuației propuse de V.E. Fertman și pentru a determina capacitatea sa de căldură, regula de amestecare face posibilă descrierea proprietăților termofizice ale MF-urilor concentrate cu suficientă precizie pentru calculele de inginerie. Semnificația rezultatelor constă în posibilitatea utilizării modelului numeric elaborat în studiul proceselor fizice interconectate în spațiul de lucru al unei etanșări fluide magnetice a arborilor rotativi. Parametrii fizici și de concentrație ai unui fluid magnetic pe bază de ulei sintetic, indicați în lucrare, rezultatele testării acestuia în timpul funcționării ca parte a unui sigiliu de fluid magnetic pot fi utilizați pentru a verifica rezultatele modelelor nou elaborate a dispozitivelor cu fluid magnetic.
***Civinte-cheie*:** fluid magnetic, etanșant fluidomagnetic, încălzire vâscoasă, simulare numerică.

Разработка модели и экспериментальное исследование тепловых процессов в магнитожидкостном герметизаторе

Нестеров С.А., Бакланов В.Д.
ФГБОУ ВО Ивановский государственный энергетический университет имени В.И. Ленина,
г. Иваново, Российская Федерация

Аннотация. Целью работы является создание взаимосвязанной численной модели магнитного, гидродинамического и температурного полей магнитожидкостного герметизатора и анализ тепловых процессов, протекающих в высокоскоростных уплотнениях. Поставленная цель достигается за счёт выбора необходимых уравнений, граничных условий, допущений и физических свойств магнитной жидкости при построении численной модели рабочего зазора герметизатора, верификации разработанной модели по результатам физического эксперимента. Важными результатами работы являются полученные и проанализированные данные о влиянии на вязкостный разогрев магнитной жидкости как её физических свойств, так и геометрии рабочего зазора магнитожидкостного герметизатора. Показано, что при радиусе вала в 140 мм и линейной скорости на поверхности вала 25 м/с вследствие вязкостного разогрева превышение температуры магнитной жидкости над температурой окружающей среды может достигать значений до 80 градусов и выше. Показано, что использование для определения теплопроводности магнитной жидкости уравнения, предложенного В.Е. Фертманом, а для определения её теплоёмкости правила смешения позволяет с достаточной для инженерных расчётов точностью описать теплофизические свойства концентрированных жидкостей. Значимость результатов состоит в возможности использования разработанной численной модели при исследовании взаимосвязанных физических процессов в рабочем зазоре магнитожидкостного герметизатора вращающихся валов. Приведённые в работе физические и концентрационные параметры магнитной жидкости на основе синтетического масла, результаты её испытания при работе в составе магнитожидкостного уплотнения могут быть использованы для верификации результатов вновь разрабатываемых моделей магнитожидкостных устройств.

***Ключевые слова*:** магнитная жидкость, магнитожидкостный герметизатор, вязкостный разогрев, численное моделирование.

INTRODUCTION

Ferrofluids (FFs) are colloidal solutions of single-domain magnetic particles with typical sizes of about 10 nm, dispersed in a carrier liquid and stabilized by a surfactant that prevents irreversible agglomeration of particles under the influence of magnetic forces [1]. Since the 1960s of the twentieth century, when these materials were first synthesized, the areas of their technological application have continued to expand, thanks to the unique combination of fluidity and interaction with an external magnetic field.

The technology of ferrofluid sealing of rotating shafts of electric motors is a developing and promising area of application for FFs. Due to the relatively simple construction and the possibility of making it in small sizes, the installation of ferrofluid seals (FF seals) instead of bearing covers in electric motors ensures guaranteed separation of the internal volume of the electric motor from aggressive or explosive external environment with minimal friction and absence of mechanical wear of the surface of the shaft, which is typical for seals of traditional designs [2, 3, 4, 5, 6].

A typical structure of a rotary FF seal is shown in Fig. 1. A small volume of ferrofluid is retained in the annular area between the rotating shaft and the cylindrical magnetic pole surrounding it due to the additional volumetric magnetic force.

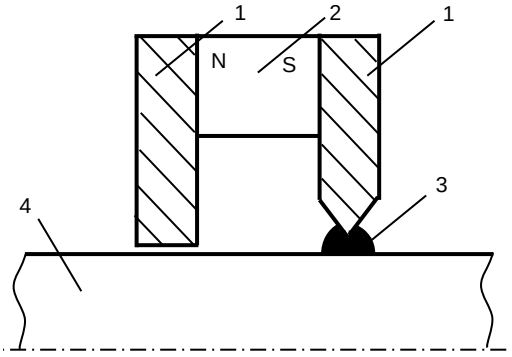

1 – pole, 2 – magnet, 3 – ferrofluid, 4 – shaft.

Fig. 1. FF seal of a typical design.

The main factor restraining the application of the FF seals on powerful machines with large diameter rotating shafts is the linear velocity increase on the surface of the shaft and the centrifugal forces and destructive effects associated with the viscous heating that occurs in the FF layer [7, 8].

With the development of numerical calculation systems for physical fields, the interest of researchers studying theoretical and practical aspects of ferrohydrodynamics is shifting towards creating models for a comprehensive assessment of the interrelated physical processes.

Among the series of works dedicated to the relationship between magnetic and hydrodynamic fields, it is worth noting the work of Kazakov Y.B. [9], which determines the shape of the ferrofluid in the gap of the FF seal using an optimization procedure, whereby the surface elements of the FF are ensured a magnetic induction value determined by pressure and temperature gradients. Rodionov A.V. with co-authors in [10, 11] define the boundaries of the ferrofluid plug in the gap of the FF seal based on the lines of equal induction obtained from numerical calculation of the magnetic field, and by using the method of finite volumes, they study the hydrodynamic processes in this volume of FF during the rotation of the shaft, assuming these boundaries are invariant. Yibiao Chen with co-authors in [12] find the initial boundaries of the FF plug in a similar way, and consider the deformation of the FF surface under the action of the applied pressure gradient and centrifugal forces when numerically calculating the hydrodynamic processes.

There are practically no works dedicated to the analysis of the thermal state and the creation of models for calculating the temperature field of the FF seals to date. The heterogeneity of the phase composition of the FF and the difference in the thermophysical properties of the magnetic phase and the liquid base (reaching two or more orders of magnitude) determine a significant dependence of the thermophysical properties of FF, such as heat capacity and thermal conductivity, on the concentration of the solid phase, and for concentrated liquids, on the intensity of the magnetic field if its vector is parallel to the heat flow [13, 14, 15, 16, 17].

Therefore, the creation of verified models for analyzing the thermal state of FF seals is an urgent scientific task.

METHODS FOR RESEARCH

The hydrodynamic calculation of the FF seal is based on the Navier-Stokes equation.

The effect of the magnetic field on the hydrodynamic processes is considered through an additional volume force acting on the FF in the gap and preset by the following equation:

$$\bar{F} = \mu_0 M \nabla \bar{H},$$

where M – is the magnetization of the FF; H – is the magnetic field intensity, and μ_0 – is the magnetic permeability of vacuum.

The magnetic field calculation is carried out according to the equations:

$$\nabla \times \overline{H} = \overline{J},\ \overline{B} = \nabla \times \overline{A},\ \overline{B} = \mu \overline{H},$$

where A – is the vector magnetic potential, B – is the magnetic induction vector, μ – is the magnetic permeability of the material.

The magnetic properties of steel and FF are specified by the corresponding magnetization curves. FF based on synthetic oil is chosen for the study, whose physical properties are summarized in Table 1.

Table 1

Physical properties of the FF and its components

Density at 293 K		1,301 g/cm^3	
Volume fraction of magnetic phase		8,89 %	
Volume fraction of surfactant		2 %	
Mass fraction of magnetic phase		35,19 %	
Mass fraction of surfactant		1,38 %	
Specific heat capacity of magnetic phase		603,5 J/(kg ·K)	
Specific heat capacity of surfactant		1848 J/(kg ·K)	
Thermal conductivity of magnetic phase		10 W/(m·K)	
Thermal conductivity of surfactant		0,231 W/(m·K)	
Plastic viscosity of FF		**Magnetization curve of the FF**	
T, K	η, Pa· s	H, A/m	M, A/m
253	36,7	0	0
263	13,7	13136	21014
273	5,78	49363	29625
283	2,59	78423	31896
293	1,3	110668	32962
303	0,724	143312	33673
313	0,457	236066	34226
323	0,302	355294	34365
Thermal conductivity of the base		**Specific heat capacity of the base**	
T, K	λ_0, W/(m· K)	T, K	C_O, J/(kg· K)
293	0,13	293	1930
313	0,128	313	1980
339	0,126	339	2030
373	0,123	373	2128
413	0,12		
433	0,118		

The problem of conjugate heat transfer is solved both in the area of the FF and in the surrounding elements of the FF seal. Heat transfer in

the FF occurs by convection and thermal conductivity, while in the solid bodies, heat transfer occurs only due to thermal conductivity. The temperature field is continuous when transitioning from the FF to the elements of the casing. Heat is generated due to the viscous heating of the FF during its shear flow following the rotating shaft. The temperature field is calculated based on the heat balance equation:

$$\rho C_p \frac{\partial T}{\partial t} + \nabla \cdot (-k \nabla T) + \rho C_p u \cdot \nabla T = \\ = \eta [\nabla u + (\nabla u)^T - \frac{2}{3} \cdot \eta \cdot (\nabla \cdot u) I)] : \nabla u \quad ,$$

where ρ – is the density, C – is the specific heat, T – is the temperature, k – is the thermal conductivity, η – is the viscosity, and u – is the velocity. The right-hand side of the equation represents the heat source due to the viscous dissipation of energy.

Given that the bases of the FF are usually operational at temperatures significantly different from the phase transition temperatures of its components, it is recommended to use the rule of mixtures when determining the heat capacity, according to which [18]:

$$C_{MK} = c_m^o \cdot C_p^o + c_m^c \cdot C_p^c + c_m^m \cdot C_p^m , \quad (1)$$

where c_m^o, c_m^c, c_m^m – are the mass fractions of the base, stabilizer, and magnetic phase, respectively; C_p^o, C_p^c, C_p^m – are the corresponding heat capacities.

To determine the thermal conductivity of concentrated FFs, formula [19] is recommended:

$$lg(\lambda) = (1 - c_V) \cdot lg(\lambda_O) + c_V \cdot lg(\lambda_m) , \quad (2)$$

where c_v – is the volume fraction of the magnetic phase, λ_O – is the thermal conductivity of the base, λ_m – is the thermal conductivity of the magnetic phase.

To verify the results obtained by numerical modeling, an experimental bench was developed, shown in Fig. 2. An asynchronous motor is rotated by the electromagnet shaft. The motor rotation frequency is regulated by a frequency converter within the range of 0 to 3500 rpm.

The power consumed by the asynchronous motor is displayed on a power meter. Based on the power meter readings, taking into account the losses in the electric motor and electromagnet, an estimation of the power liberated in the FF plug due to viscous friction is made.

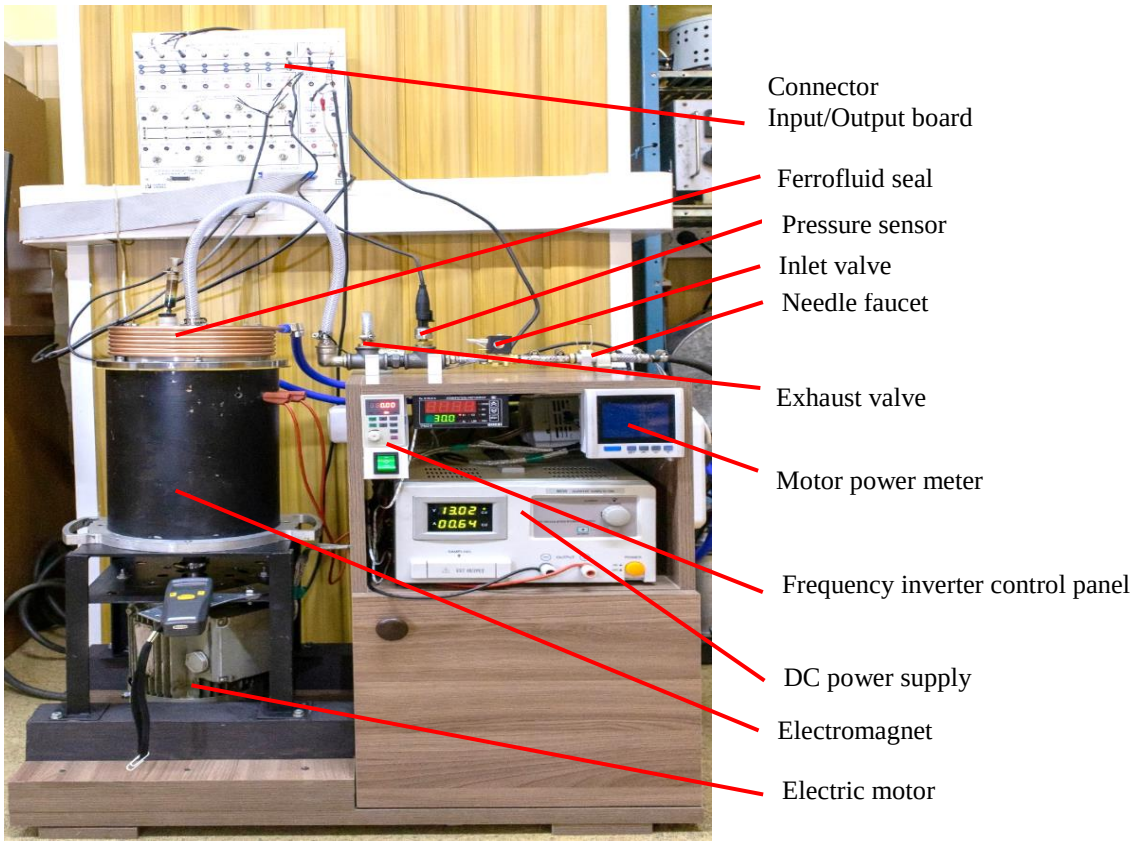

Fig. 2. Experimental bench.

The FF seal is installed on the top of the electromagnet (Fig. 3) via a 2-mm thick non-magnetic gasket, with a possibility of substitution the stationary pole attachment and the shaft for those required by the test program. The stationary pole attachment and the seal shaft form an FF seal working gap filled with FF.

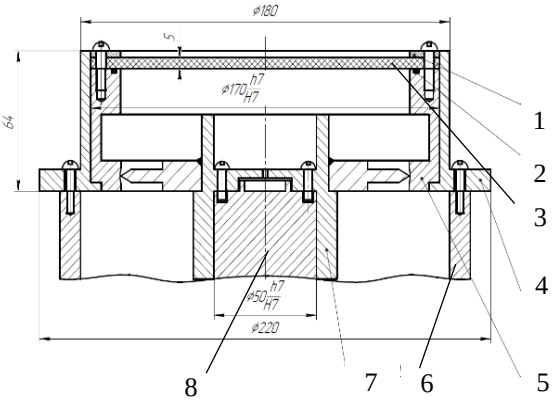

1 – pressure ring, 2 – sealing ring, 3 – polycarbonate cover, 4 – FF seal housing, 5 – fixed pole attachment, 6 – solenoid housing, 7 –FF seal shaft, 8 – solenoid shaft.

Fig. 3. Design of the ferrofluid sealer.

To directly monitor the FF temperature and experimental bench components, an infrared thermal imager UNI-T UTi260A was used. Since temperature measurement on shiny metallic surfaces is difficult, a black heat-resistant paint was applied onto them (Fig. 4).

1 – surface of the pole attachment, 2 – surface of the tooth on the FF seal shaft.

Fig.4. Heat-resistant paint application locations for thermal monitoring of the FF seal temperature.

RESULTS

The temperature distribution in the FF seal working gap after 10 seconds of rotation with a linear velocity of 5 m/s obtained from the numerical simulation is shown in Fig. 5. It can be seen that apart from small areas being in contact with cold metallic surfaces, the temperature distribution in the FF plug is sufficiently uniform, and thermal imaging temperature measurement on the surface of the FF allows a reliable estimation of the temperature inside it.

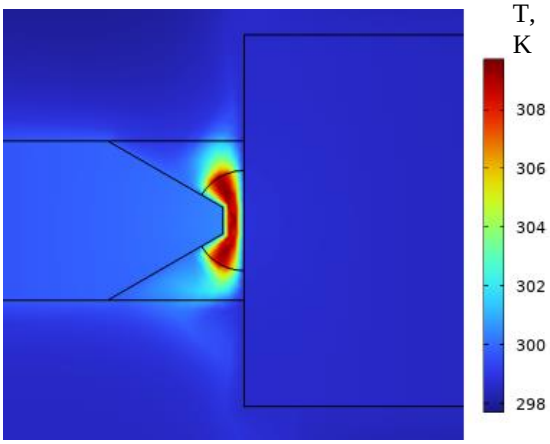

Fig. 5. Temperature distribution in the FF seal gap.

Comparison of the calculation results and the physical experiment presented in Fig. 6 shows their agreement with satisfactory accuracy for engineering calculations. The discrepancy of the curves at the initial stage is also related to the fact that in the physical experiment, unlike the mathematical one, the rotation frequency of the FF seal shaft increases not instantaneously, but gradually reaches the steady-state value over 5 seconds, and the heat release power in the FF is less than in the model.

The discrepancy in the dependencies shown in Fig. 6 after the 120th second is related to the complexity of accounting for the thermal state of technological gaps separating individual parts of the Ferrofluideal device from each other, which have a noticeable effect on its thermal conductivity.

Since such gaps are absent in the model, the thermal conductivity of the steel sections of the FF seal is higher than in the experimental device, and over time, this leads to a slowing down of the rate of temperature increase in the FF due to a more intensive heat dissipation to the metallic elements.

Figures 7 and 8 show the temperature distribution change in the FF seal when the shaft is rotated at speeds of 5 and 25 m/s, respectively, with a magnetic field induction of 1.2 T and a gap between the shaft and the pole piece of 0.5 mm.

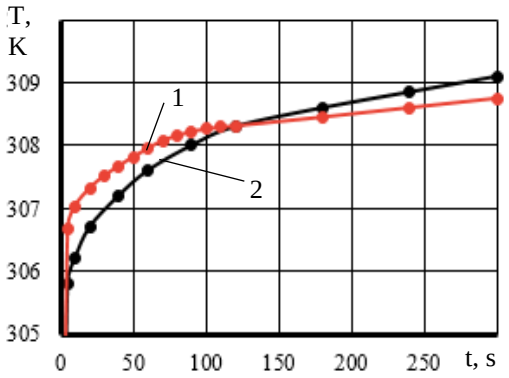

1–- simulation results,
2 – results of the physical experiment.

Fig. 6. Dynamics of ferrofluid heating. The linear velocity is 5 m/s.

Prior to the drive motor being turned on, the FF and FF seal had a room temperature of 296 K. The FF, as the main source of heat, has a maximum temperature equal to the upper limit of the thermal scale in these images. The temperature in the upper left corner of the image is equal to the temperature of the toothed shaft of the FF seal in close proximity to the FF plug. An analysis of the temperature distribution shows that in the first 10 seconds after the start of shaft rotation, the FF temperature in the gap sharply increases. For a speed of 5 m/s, the temperature increases by 10.2 K, and for 25 m/s - by 36.7 K. At the same time, the FF viscosity sharply decreases, fluid friction decreases, and the dynamics of heating significantly reduces.

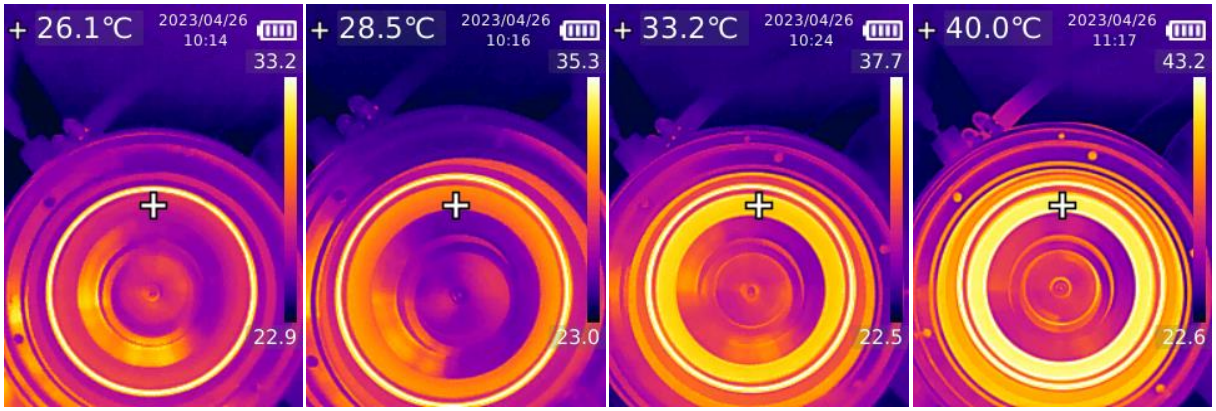

a) b) c) d)

a – 10 seconds, b – 2 minutes, c – 10 minutes, d – 60 minutes.

Fig. 7. Thermal state of the FF seal. The linear velocity is 5 m/s.

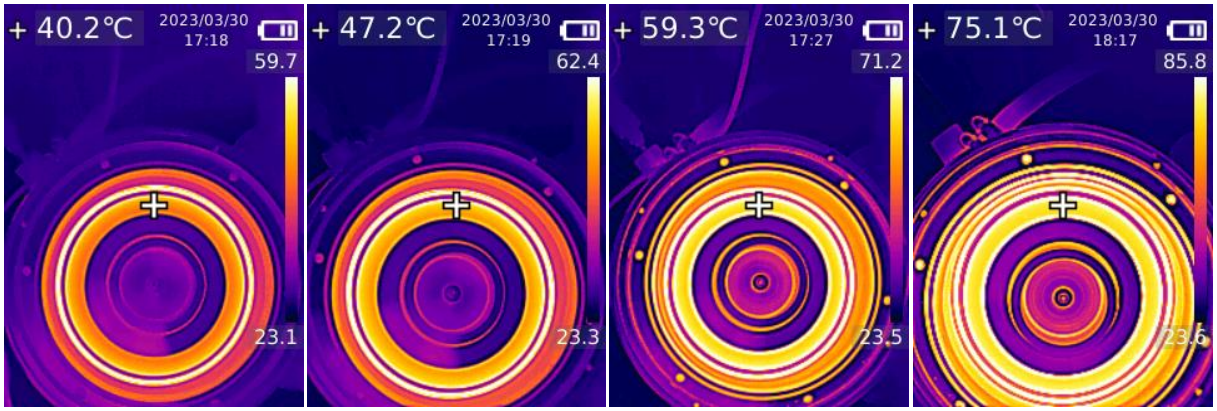

a) b) c) d)

a – 10 seconds, b – 2 minutes, c – 10 minutes, d – 60 minutes.

Fig. 8. Thermal state of the FF seal. The linear velocity is 25 m/s.

The viscous dissipation of energy in the FF plug of high-speed seals leads not only to a significant heating of the FF during operation, but also increases the overall losses in the electric motor. Figure 9 shows the change in dissipated power and temperature of the FF at a linear speed

on the surface of the single-toothed FF seal shaft of 25 m/s. The increase in the temperature of the FF in the first few seconds after the start of the rotation of the shaft leads to a sharp decrease in viscosity and, as a result, a decrease in the resistance torque of the FF seal and the dissipated power. The rate of change in temperature and power is determined by the temperature dependence of the viscosity of the FF.

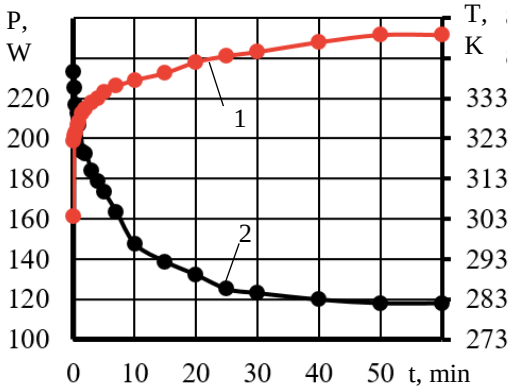

Fig. 9. Dependence of friction losses and temperature of FF in the seal.

The choice of the FF necessary volume for filling the FF seal can significantly affect the performance of high-speed seals. Fig. 10 shows the experimentally obtained change in the critical pressure of the FF seal and the steady-state temperature of the FF depending on the cross-sectional area of the ferrofluid plug, directly related to the volume of the filled fluid. It can be seen that the temperature increases almost linearly with an increase in the FF volume, while the pressure drop maintained by the FF seal significantly increases with an increase in the cross-sectional area of the FF plug from 2 to 4 mm. However, the FF further addition leads to a less significant increase in the pressure drop.

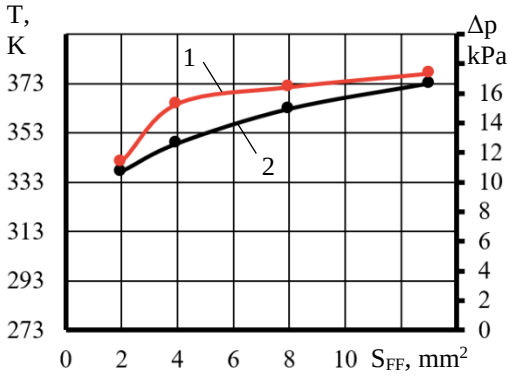

1 – critical pressure, 2 – temperature.

Fig. 10. Change of FF pressure and temperature depending on the seal filling volume.

Figure 11 shows the change in the FF temperature over time when using synthetic oil, polyethylsiloxane and polymethylsiloxane liquids, as the carrier fluid.

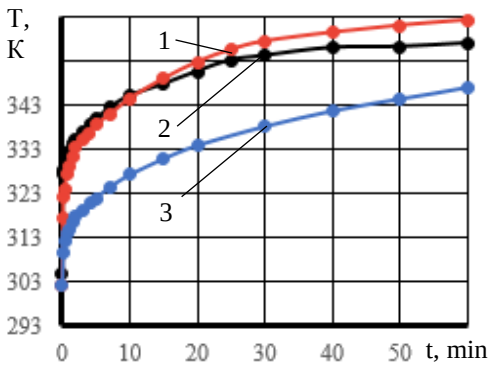

1 – FF based on polyethylsiloxane liquid, 2 – FF based on synthetic oil, 3 – FF based on polymethylsiloxane liquid.

Fig. 11. Change of the FF temperature on different carrier fluids.

Figure 12 demonstrates the temperature dependences of viscosity for each of these FFs. All fluids have a saturation magnetization of 40 kA/m. The surface velocity of the shaft is 25 m/s.

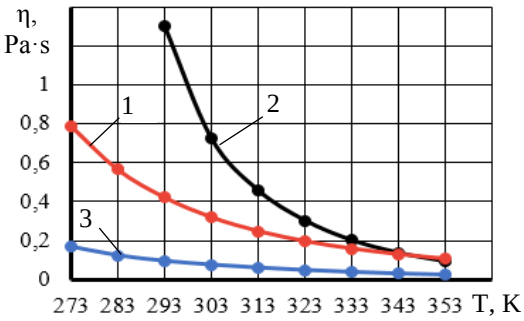

1 – FF based on polyethylsiloxane liquid, 2 – FF based on synthetic oil, 3 – FF based on polymethylsiloxane liquid.

Fig. 12. Change of FF viscosity on different carrier fluids.

Analyzing the dependencies shown in Fig. 11 and Fig. 12, it can be concluded that the viscosity of the FF at high temperatures has a determining effect on the heating of the FF during operation in high-speed FF seal. For example, the FF based on synthetic oil has a viscosity by 3.1 times higher than that of the FF based on polyethylsiloxane at room temperature, but due to a much more pronounced temperature dependence, after just 10 minutes of operation of the FF seal, the temperature of the polyethylsiloxane-based liquid starts to

exceed the temperature of the FF based on synthetic oil, and after 60 minutes of operation, this difference reaches 5.6 K. The use of a much less viscous FF based on polymethylsiloxane allows for a significant reduction in the heating of the FF seal, especially when operating in a repeat-short-term mode.

CONCLUSIONS

The developed numerical mathematical model for the integrated calculation of magnetic, hydrodynamic and thermal processes allows us to estimate the magnitude and rate of the viscosity heating of the FF by a rotating shaft in high-speed FF seals.

Comparison of the numerical calculation results with the physical experiment data shows that the use of equation (1) to determine the thermal conductivity of FF and expression (2) to determine the specific heat of FF allows describing the thermal properties of concentrated FFs with sufficient accuracy for the engineering calculations.

Experimental data show that the degree of viscosity decrease with increasing temperature has a significant influence on the magnitude of the viscosity heating of the FF plug during prolonged operation of the FF seal. The FF proper selection can significantly reduce overheating and increase the lifespan of the FF seal.

At a linear velocity of 25 m/s on the shaft surface, the temperature increase of the FF due to viscosity heating alone can reach values exceeding 80 degrees, which, in combination with the temperature increase from the operating equipment, can lead to the overheating and boiling of the FF.

Often, the FF seals are installed on industrial equipment, particularly electric motors, solely to ensure separation of the external explosive or fire hazardous environment from the internal volume. In this case, the seal only holds a small pressure differential, which is related to the heating of the air inside the operating device. In this case, reducing the volume fraction and, consequently, the viscosity and saturation magnetization of the FF appears to be an effective way to reduce the viscosity heating of the FF.

Developing a methodology for calculating the optimal volume of FF that satisfies conflicting requirements for maximum pressure differential and minimization of viscosity heating of the FF seal is a relevant scientific problem.

ACKNOWLEDGEMENT

This research was supported by the Russian Science Foundation grant No. 22-79-00156, https://rscf.ru/project/22-79-00156/ "Investigation of Thermal and Hydrodynamic Effects in Nanodisperse Ferrofluids for the Development of Models and Calculation Methods for High-Speed and High-Temperature Seals".

References

[[1] Rosensweig R. E. Magnetic Fluid Seals U.S. Patent no. 3,620,584, 1971.

[2] Orlov D.V., Mikhalev Yu.O., Myshkin N.K., Podgorkov, V.V., Sizov A.P. *Magnitnye Zhidkosti v Mashinostroenii* [Magnetic Fluids in Mechanical Engineering]. Moscow, 1993. 275 p.

[3] Morozov N.A., Kazakov Yu.B. *Nanodispersnye Magnitnye Zhidkosti v Tekhnike i Tekhnologiyakh* [Nanodisperse Magnetic Fluids in Machinery and Processes]. Ivanovo, 2011. 264 p.

[4] Ochofiski W. Dynamic Sealing with Magnetic Fluids. *Wear*, 1989, vol. 130, pp. 261–268.

[5] Vlasov A.V. *Elektrotekhnicheskaya sistema magnitozhidkostnoy germetizatsii valov reguliruemykh elektrodvigateley* [Electrotechnical system for ferrofluidic hermetization of controlled electric motor shafts]. PhD thesis. Ivanovo state power engineering university, the Russia, 2022. 150 p.

[6] Baart P., Lugt P.M., Prakash B. Review of the Lubrication, Sealing, and Pumping Mechanisms in Oil and Grease Lubricated Radial Lip Seals. *Proc. Inst. Mech. Eng. Part J: J. Eng. Tribol*, 2009, vol. 223, no. 3, pp. 347-358.

[7] Horak W., Szczęch M. Experimental and Numerical Determination of the Static Critical Pressure in Ferrofluid Seals. *Journal of Physics: Conference Series*, 2013, vol. 412, 012055. doi: 10.1088/1742-6596/412/1/012055

[8] Zoua J., Lib X., Lua Y., Hu J. Numerical Analysis on the Action of Centrifuge Force in Magnetic Fluid Rotating Shaft Seals. *Journal of Magnetism and Magnetic Materials*, 2002, vol. 252, pp.321-323.

[9] Kazakov Yu.B. *Chislennoe opredelenie polozheniya magnitnoy zhidkosti v magnitozhidkostnom germetizatore* [Numerical determination of the magnetic fluid position in the ferrofluid sealer]. *Elektrotekhnika*, 2002, no. 1, pp. 51-55.

[10] Radionov A., Podoltsev A., Zahorulkoc A. Finite-Element Analysis of Magnetic Field and the Flow of Magnetic Fluid in the Core of Magnetic-Fluid Seal for Rotational Shaft. *Procedia Engineering*, 2012, vol. 39, pp. 327-338. doi: 10.1016/j.proeng.2012.07.038

[11] Radionov A., Podoltsev A., Peczkis G. The Specific Features of High-Velocity Magnetic Fluid

Sealing Complexes. *Open Eng*, 2018, vol. 8, pp. 539-544. doi: 10.1515/eng-2018-0066

[12] Chen Y., Li D., Li Z., Zhang Y. Numerical Analysis on Boundary and Flow Regime of Magnetic Fluid in the Sealing Clearance With a Rotation Shaft. *IEEE Transactions on magnetics*, 2019, vol. 55, no. 2, 4600207. doi: 10.1109/TMAG.2018. 2882162

[13] Ghorbani B., Ebrahimi S., Vijayaraghavan K. CFD modeling and sensitivity analysis of heat transfer enhancement of a ferrofluid flow in the presence of a magnetic field. *International Journal of Heat and Mass Transfer*, 2018, vol. 127, pp. 544-552. doi: j.ijheatmasstransfer.2018.06.050

[14] Bahiraei M., Hangi M. Flow and heat transfer characteristics of magnetic nanofluids: A review, *Journal of Magnetism and Magnetic Materials*, 2015, vol. 374, pp. 125-138. doi: j.jmmm.2014.08.004

[15] Chernobay V.A. *Teplovye i gidrodinamicheskie protsessy v vysokoskorostnykh magnitozhidkostnykh uplotneniyakh, razrabotka ikh konstruktsiy* [Thermal and hydrodynamic processes in high-speed ferrofluid seals, development of their designs]. PhD thesis Belarusian order of the red banner of labor polytechnic institute, the Belorus, 1983. 175 p.

[16] Nkurikiyimfura I., Wang Y., Pan Z. Heat transfer enhancement by magnetic nanofluids – a review. *Renew. Sustain. Energy Rev,* 2013, vol. 21, pp. 548–561, doi: 10.1016/j.rser.2012.12.039.

[17] Zhenkun L., Decai L., Yibiao C., Yilong Y., Jie Y. Influence of Viscosity and Magnetoviscous Effect on the Performance of a Magnetic Fluid Seal in a Water Environment. *Tribology Transactions*, 2018, vol. 61, Issure 2, pp. 367-375. doi: 10.1080/10402004.2017.1324071

[18] Berkovskiy V.M., Medvedev V.F., Krakov M.S. *Magnitnye zhidkosti* [Magnetic Liquids]. Moscow, 1989, 240 p.

[19] Fertman V. E. *Magnitnye zhidkosti: Spravochnoe posobie* [Magnetic Liquids: Reference Manual]. Minsk, 1988, 184 p.

Information about the authors.

Sergey Alexandrovich Nesterov, Ph.D., head of the Electromechanics Department at the Ivanovo State Power Engineering University. Research interests: electric machines and apparatuses.
E-mail: elmash@em.ispu.ru

Vladislav Dmitrievich Baklanov, Bachelor of the Electromechanics Department at the Ivanovo State Power Engineering University. Research interests: electric apparatuses.
E-mail: elmash@em.ispu.ru

Recurrent Neural Network-Based Autoencoder for Problems of Automatic Time Series Analysis at Power Facilities

Matrenin P.V.[1], Khalyasmaa A.I.[1], Potachits Y.V.[2]

[1]Ural Federal University, Ekaterinburg, Russia
[2] Belarusian National Technical University, Minsk, Belarus

***Abstract*.** Digitalization of the energy sector leads to an increase in the volume and rate of data collection. A primary barrier to the proper management of the technological data is the lack of data labeling corresponding to emergency modes, power equipment technical state, etc. Thus, despite the large amount of data, there is a shortage of labeled data suitable for training, validating and testing the machine learning models. Labeling by an expert takes too much time, so there is an actual task to automatically identify data fragments that are potentially of interest. The aim of the work is to develop an algorithm for prioritizing the fragments of the time series using the compact recurrent autoencoder. To achieve the goal, a neural network architecture was developed based on recurrent encoding and decoding cells, capable of unsupervised learning. The model was tested on two data sets: a synthetic sinusoidal signal with missing values and electric current measurements with thermal limit deviations. The substantial results of the work are the compact architecture of the autocoding model and the high interpretability of the output. The most significant achievements of the study are both the autocoding neural network model, which does not require initial assumption about the type of deviations, and the proposed algorithm for prioritizing the data fragments. The significance of the results is prooved by the reduction of the time for analyzing and labeling large data arrays with technological parameters of the electrical networks, which allows using these data for training, validating and testing.
Keywords: autoencoder, time series processing, recurrent neural networks, operating parameters of electrical networks.

DOI: https://doi.org/10.52254/1857-0070.2023.2-58-06
UDC: 004.896

Autocodarea rețelei neuronale recurente pentru probleme de procesare automată a seriilor de timp la instalațiile energetice

Matrenin P.V.[1], Haliasmaa A.I.[1], Potaciț Ia.V.[2]

[1]Universitatea Federală Ural, Ekaterinburg, Federația Rusă
[2]Universitatea Națională Tehnică din Belarus, Minsk, Republica Belarus

Rezumat. Digitalizarea complexului de combustibil și energie duce la creșterea volumului de date colectate de la instalațiile de energie electrică și a vitezei de acumulare a acestora, dar un obstacol în calea utilizării datelor mari care conțin măsurători de putere, curent și tensiune este lipsa marcajului în datele care conțin informații despre modurile de funcționare de urgență, starea tehnică a echipamentului, anomalii. Scopul lucrării este de a elabora o metodă pentru îmbunătățirea eficienței marcajului seriilor de timp în problemele industriei energetice prin prioritizarea fragmentelor de serii temporale folosind modelul propus de autoencoder compact recurent. Pentru a atinge scopul, a fost elaborată o arhitectură de rețea neuronală bazată pe celule de codificare și decodare recurente, capabile să învețe fără profesor (fără date marcate) și testată pe două seturi de date: un semnal sinusoidal sintetic cu valori lipsă și măsurători curente în o secțiune a unei rețele electrice, care conține valori de exces de curent pe termen scurt. Deosebirea lucrării este arhitectura simplificată a modelului de autocodare recurentă și interpretabilitatea ridicată a valorilor de ieșire rezultate. Cele mai semnificative rezultate sunt modelul unei rețele neuronale cu autocodare pentru detectarea automată a abaterilor în serii de timp fără a se forma o ipoteză inițială despre tipul abaterilor, algoritmul propus pentru utilizarea modelului pentru prioritizarea analizei și etichetării fragmentelor de serie de timp în probleme. a industriei energiei electrice. Semnificația rezultatelor constă în faptul că metoda propusă face posibilă reducerea semnificativă a timpului de analiză și marcarea rețelelor mari de serii temporale care conțin date digitale ale parametrilor de funcționare ai rețelelor electrice.
Cuvinte-cheie: autoencoder, procesare serii de timp, rețele neuronale recurente, parametrii de regim ai rețelelor electrice.

Автокодирующая рекуррентная нейронная сеть для задач автоматизации анализа временных рядов на объектах энергетики

Матренин П.В.[1], Хальясмаа А.И.[1], Потачиц Я.В.[2]
[1]Уральский федеральный университет, Екатеринбург, Российская Федерация
[2]Белорусский национальный технический университет, Минск, Республика Беларусь

Аннотация. Цифровизация топливно-энергетического комплекса приводит к увеличению объема собираемых с объектов электроэнергетики цифровых данных и скорости их накопления, но препятствием для использования больших данных, содержащих измерения мощности, тока и напряжения, является отсутствие в данных разметки, содержащих сведения об аварийных режимах работы, техническом состоянии оборудования, аномалиях. Таким образом, несмотря на большой объем данных, сохраняется дефицит размеченных данных, пригодных для обучения, валидации и тестирования моделей на базе машинного обучения. Разметка таких объемов данных экспертом занимает слишком много времени, поэтому актуальной задачей является автоматическая идентификация в данных фрагментов, которые потенциально представляют наибольший интерес. Целью работы является разработка метода приоритезации фрагментов временных рядов с помощью предложенной модели компактного рекуррентного автокодировщика для автоматизации их анализа и разметки данных на объектах электроэнергетики. Для достижения цели была разработана архитектура нейронной сети на базе рекуррентных ячеек кодирования и декодирования, способная обучаться без учителя, и апробирована на двух наборах данных: синтетическом синусоидальном сигнале с пропущенными значениями и измерениях тока на участке электрической сети, содержащих кратковременные превышения значений тока. Отличием работы является компактная архитектура рекуррентной автокодирующей модели и высокая интерпретируемость получаемых выходных значений. Наиболее существенными результатами являются модель автокодирующей нейронной сети для автоматического выявления отклонений во временных рядах без формирования изначального предположения о виде отклонений и предложенный алгоритм использования разработанной модели для приоритезации анализа и разметки фрагментов временных рядов в задачах электроэнергетики. Значимость результатов заключается в том, что предложенный метод позволяет существенно сократить время на анализ и разметку больших массивов временных рядов, содержащих данные режимных параметров электрических сетей, что позволит использовать эти данные для обучения, валидации и тестирования моделей.

Ключевые слова: автокодировщик, обработка временных рядов, рекуррентные нейронные сети, режимные параметры электрических сетей.

ВВЕДЕНИЕ

A. Использование неразмеченных измерений мощности, тока и напряжения в электроэнергетических системах

Цифровизация топливно-энергетического комплекса приводит к увеличению объема собираемых с объектов энергетики данных. Внедрение цифровых счетчиков электроэнергии, устройств синхронизированных векторных измерений, Phasor Measurement Unit (PMU) [1-3] и цифровых подстанций [4, 5] приводят к формированию больших массивов цифровых данных, как и развитие возобновляемой энергетики и распределенной генерации [6, 7].

Данные, содержащие значения потребляемой и генерируемой мощности, тока и напряжения, могут быть использованы для решения различных задач: управление энергосистемами, диагностика состояния электрооборудования, обнаружение аварий.

Большой объем данных позволил применить методы машинного обучения для высокоэффективного решения задач во многих областях [8, 9], но существенным препятствием для использования больших данных в электроэнергетике является отсутствие в них разметки [3, 10]. Накапливается большой объем неразмеченных данных, которые не могут быть использованы для без решения проблемы анализа неразмеченных данных, поскольку для задач обнаружения неисправностей или оценки технического состояния высоковольтного оборудования наиболее эффективны алгоритмы машинного обучения с учителем, требующие размеченных данных [11].

Можно выделить следующие подходы к решению данной проблемы: методы обучения с частичным привлечением учителя (semi-supervised learning); кластерный анализ, автокодировщики и другие методы обучения без учителя (unsupervised learning); генерация синтетических данных.

Обучение с частичным привлечением учителя позволяет работать с данными, в которых размечена лишь небольшая часть. При наличии размеченной части выборки можно обучить модель на этих данных, затем использовать модель для получения авторазметки. В работе [12] такой метод используется для анализа графиков электропотребления, в работе

[13] частичное обучение применено для детектирования нетехнологических потерь электроэнергии. Применение частичного обучения для обнаружения неисправностей описано в статье [14]. Недостатком является необходимость иметь очень точную разметку для части данных. В задачах мониторинга электрооборудования и электрических сетей всегда присутствует сильный дисбаланс классов, примеров данных, относящихся к авариям, очень мало, поскольку это редкие события. Статистически они могут рассматриваться как отклонения от нормального состояния или выбросы. Поэтому формирование авторазметки для редких классов может иметь высокую погрешность, что не позволит применять полученные модели с достаточной степенью уверенности в их надежности.

Кластерный анализ относится к обучению без учителя и не требует разметки. В работах [15, 16] кластеризация применяется для обнаружения провалов напряжения. Использование кластеризации измерений тока и напряжения для анализа состояния и управления регуляторами распределенной киберфизической системы описано в статье [17]. Особенностью применения кластерного анализа является необходимость последующей интерпретации полученных результатов, так как нет гарантии, что ситуации, связанные с неисправностями, попадут в одни кластеры, а прочие ситуации в другие. В результате экономия трудозатрат за счет отказа от разметки данных частично компенсируется на этапе анализа результатов модели.

Генерация новых размеченных данных на основе имеющихся является подходом, успех которого в ряде областей обеспечен применением генеративно-состязательных нейронных сетей (ГСНС) [18, 19]. Подход заключается в обучении двух конкурирующих моделей, одна из которых стремится генерировать синтетические данные, статистически соответствующие заданной выборке данных, а вторая – отличать синтетические данные от реальных [20]. Применение глубоких ГСНС для заполнения пропущенных данных векторных измерений для обнаружения предварийных ситуаций в электрической сети описано в статье [21]. В статье [22] генеративно-состязательная модель использована для генерации большого массива данных PMU для исследовательских или образовательных целей. При этом следует особое внимание уделять сохранению в синтетических данных физического смысла, присущего процессам в электрических сетях [23, 24].

Хотя применением генеративно-состязательных нейронных сетей представляется наиболее перспективным направлением решения указанной проблемы, для каждого частного объекта требуется разметка достаточного объема данных для запуска процесса генеративно-состязательного процесса и обучение глубоких нейронных сетей. Несмотря на развитие инструментов для работы с нейронными сетями, создание такой модели является сложной исследовательской задачей. Кроме того, нерешенным остается вопрос надежности и безопасности применения моделей, обученных не на реальных данных.

B. Автокодирующие нейронные сети

Особым направлением обучения без учителя является использование автокодирощиков (autoencoder) – особой архитектуры нейронных сетей, которые обучаются так, чтобы результаты на выходе сети были как можно ближе к входным данным [25]. За счет того, что объем данных, который может быть передан между скрытыми слоями, намного меньше объема данных во входных экземплярах, автокодировщик стремится закодировать входные данные, сжимая их, чтобы затем декодировать (восстановить). Кодировщик стремится преобразовать пространство входных данных в пространство меньшей размерности с минимальной потерей информации. Если входной экземпляр является выбросом, то автокодировщик с высокой вероятностью восстановит его с высокой погрешностью [26-32].

Применению автокодировщика для выявления выбросов во временных рядах посвящено большое число работ. В настоящее время наибольшее внимание исследователей в данной области привлечено к обработке многомерных временных рядов, поэтому рассматриваются глубокие нейронные сети, в которых часть, отвечающая за автокодирование, не является наиболее важной и сложной.

Так, в статьях [26-30] используются модели на базе сверточных нейронных сетей CNN (Convolutional Neural Networks), ConvLSTM (Convolutional Long Short-Term Memory) для обнаружения выбросов в данных о работе киберфизических систем и систем на базе Интернета вещей [26, 27, 31], оптических данных [28], данных о работе промышленных роботов

[29] и показаний вибро- и акустических датчиков с вращающихся машин [32].

Применение автокодировщика для диагностики неисправностей электрооборудования по таким сигналам как вибрация, ток и углы поворота приведено в работах [30-35]. В них данные тока и напряжения используются как дополнительные или не используются, а более информативными оказываются данные, которые сильнее коррелируют с характеристиками физических процессов. Существенно меньше число исследований, направленных на анализ временных рядов тока, напряжения и мощности как основного источника данных [36-40].

В работе [36] автокодировщик применен для кластеризации потребления электроэнергии (без выделения выбросов). Автокодирощик для очищения данных от шума и последующей классификации данных, в том числе аномалий в графиках электропотребления, представлен в [37].

Векторные измерения тока и напряжения используются в работе [38] для обнаружения кибератак, связанных с подменой данных. При этом используется глубокая нейронная есть и переход от исходных сигналов тока и напряжения в специализированное пространство статистических признаков. Глубокий автокодировщик на базе нейронной сети временной свертки для классификации возмущений в сигналах PMU предложен в работе [39]. Представленные в данных работах модели специализированы под конкретные области применения и имеют высокую сложность.

В статье [40] проводится сравнение автокодировщика с моделью на базе метода главных компонент и метода опорных векторов в задаче обнаружения опасных событий в распределительной электрической сети. Хотя использование в качестве автокодировщика лишь одного нейрона свидетельствует о том, что метод не в полной мере учитывает особенности, присущие временным рядам.

Анализ существующих исследований показывают актуальность работ, направленных на применение автокодировщиков для анализа неразмеченных данных PMU. Во-первых, использование рекуррентных нейронных сетей в качестве автокодировщиков не в полной мере изучено для обработки измерений мощности, тока и напряжения. Во-вторых, не рассматривается изначальная проблема – каким образом можно повысить безопасность применения моделей машинного обучения, построенных на неразмеченных данных.

Наиболее важным вопросом, на который обращено недостаточное внимание, является вопрос доверия к результатам, полученным на неразмеченных данных. Автокодировщики демонстрируют относительно высокую эффективность, но они обучаются для каждого частного случая, а результаты успешных применений публикуют на порядок чаще, чем неудачных. В результате точность автокодировщика невозможно протестировать без разметки. Для действительно безопасного применения машинного обучения в задачах энергетики анализ данных специалистами и разметка данных являются необходимыми этапами. Поэтому в работе предложен новый метод для применения автокодировщка на базе рекуррентной нейронной сети для разметки больших объемов неразмеченных данных.

Целью работы является разработка метода приоритезации фрагментов временных рядов с помощью предложенной модели компактного рекуррентного автокодировщика для автоматизации их анализа и разметки данных на объектах электроэнергетики. Отличием работы является упрощенная архитектура рекуррентной автокодирующей сети, универсальность за счет применения к неразмеченным данным без необходимости без формирования изначального предположения о виде отклонений и интерпретируемость результатов модели, поскольку она расставляет приоритеты фрагментам временного ряда для анализа и позволяет затем визуально и численно сравнить отобранные фрагменты с результатами их кодирования-декодирования.

II. Методы исследования

A. Предложенный метод

Автокодировщик имеет следующую функцию потерь, которая используется при обучении:

$$L(\varphi,\theta)=\frac{1}{n}\sum_{i=1}^{n}\Delta X, \tag{1}$$

$$\Delta X=\frac{1}{l}\sum_{j=1}^{l}\left(f_\theta(g_\varphi(X_i)-X_i\right)_l^2, \tag{2}$$

где L – функция потерь, φ – обучаемые параметры кодирующей части модели, θ – обучаемые параметры декодирующей части, f_θ – декодировщик, g_φ – кодировщик, X – входной экземпляр (фрагмент), l – его длина.

Минимизация функции потерь в процессе обучения приводит к тому, что пара f_θ, g_φ образуют аппроксимацию $f_\theta(g_\varphi(X_i))$, которая для

каждого X_i дает его приближенное значение X'_i. Из-за того, что размерность $g_\varphi(X_i)$ меньше размерности X_i, отклонение ΔX является случайной величиной. Таким образом, приведенная в выражении (1) функция потерь является средним значением данной величины для всей обучающей выборки данных. Схема работы автокодировщика приведена на Рисунке 1.

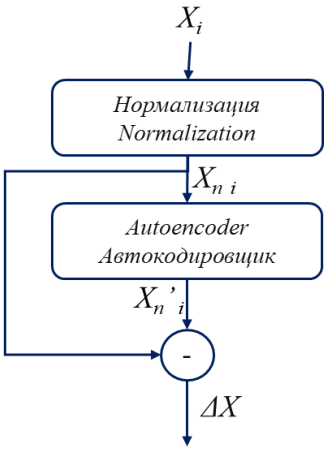

Рис.1. Принципиальная схема автокодировщика

X_i – входные данные, $X_{n,i}$ – нормализованные входные данные, $X'_{n,i}$ – нормализованные выходные данные, ΔX – отклонение.

Fig.1. An autoencoder schematic diagram:

X_i – input data, $X_{n,i}$ – normalized input data, $X'_{n,i}$ – normalized output data, ΔX – difference.

Использование автокодировщика для выявления выбросов в данных основано на том, что минимизация функции потерь $L(\varphi, \theta)$ выполняется на основе обработки всех фрагментов обучающей выборки с построением аппроксимации $f_\theta(g_\varphi(X))$, поэтому выбросы (редкие события во временном ряду) оказывают малое влияние на полученные параметры φ, θ. В то же время выбросы характеризуются отличным от остальных фрагментов закономерностями между элементами вектора признаков X. В результате отклонение ΔX для выбросов принимает большее значение, чем для остальных фрагментов.

B. Рекуррентный автокодировщик

В отличии от приведенные выше работ, использующих модели на базе глубокого обучения и сверточных рекуррентных нейронных сетей [26-30], в данном исследовании рассматриваются намного более простые рекуррентные модели, в которых кодирование g_θ и декодирование f_φ выполняется однослойными рекуррентными блоками. Архитектура модели приведена на Рисунке 2.

Гиперпараметры модели: вид рекуррентных ячеек, число слоев кодировщика, число слоев декодировщика, число признаков скрытого состояния (hidden state size). Последний гиперпараметр равен размерности закодированной последовательности $Z = g_\varphi(X)$ (скрытое состояние рекуррентной модели, которое передается от кодировщика и декодировщику), то есть числу элементов в векторе Z. В результате вычислительных экспериментов число признаков скрытого состояния было выбрано равным 16.

В настоящее время наиболее часто применяются обычные рекуррентные ячейки с одним блоком памяти, рекуррентные ячейки долговременной краткосрочной памяти LSTM [41] и управляемые рекуррентные ячейки GRU [42]. Результаты их сравнения приведены ниже.

Для обучения модели был использован алгоритм обучения Adam с шагом обучения $5*10^{-4}$, размером мини-пакета, равным четырем, и эвристикой “Teacher forcing” [43, 44]. В качестве функции потерь при обучении используется $L(\varphi, \theta)$ из выражения (1).

Программная реализация выполнена на основе фреймворка с открытым исходным кодом Pytorch. Код для формирования модели и реализации процесса обучения создан на основе репозитория [44].

III. Результаты

A. Метод приоритезации анализа и разметки фрагментов временных рядов

Используется следующая последовательность действий.

1. Выбор длительности временного окна (фрагмента временного ряда), кратной периодичности входного сигнала. Фрагмент может длиться m периодов.

2. Формирование матрицы D, содержащей фрагменты временного ряда. Временной ряд из s отсчетов с периодичностью c отсчетов, будет преобразован в k пересекающихся фрагментов (пересечение равно длительности периода):

$$k = \frac{s}{c} - m, \tag{3}$$

$$X_i = D[i \cdot c : (i + m) \cdot c],\ i = 0,1,...,k \tag{4}$$

3. Нормализация данных с помощью линейной Min-Max нормализации:

$$X^n = (X - \min(D)) / (\max(D) - \min(D)), \quad n = 1, 2, ..., s \tag{5}$$

4. Разделение X на две равные части случайным образом. Обучение автокодировщика на первой части и применение на второй с сохранением результатов для каждого фрагмента второй части.

5. Замена частей местами и выполнение той же процедуры, что описана в шаге 4. Это необходимо, чтобы получать оценки отклонений не на той части выборки, на которой обучилась модель.

6. Ранжирование фрагментов по убыванию отклонения ΔX.

7. Визуализация, анализ и разметка первых w фрагментов в ранжированной последовательности.

Описанная выше задача обучения автокодирощика с минимизацией функции $L(\varphi, \theta)$ направлена на решение задачи следующего вида:

$$\begin{aligned} &Y_{ab}(\varphi,\theta) : \Delta X_a(\varphi,\theta) > \Delta X_b(\varphi,\theta), \\ &V_{ab} : a - выброс, b - не\ выброс, \\ &\varphi^*, \theta^* = \arg\max(\mathrm{P}(Y_{ab} \mid V_{ab}), \end{aligned} \tag{6}$$

где Y_{ab}, V_{ab} – события; $P(Y_{ab}|V_{ab})$ – вероятность того, что если фрагмент a является выбросом, а фрагмент b нет, то отклонение ΔX_a окажется больше, чем отклонение ΔX_b; φ^*, θ^* – искомые обучаемые параметры модели.

Величину ΔX можно использовать как количественную оценку приоритета, который нужно отдать фрагменту при анализе и разметке. В результате потенциально аномальные ситуации будут проверены в первую очередь. Если они представляют собой ошибки или искажения при сборе данных, то они будут исключены из выборки. Если же это редкие ситуации, то они будут размечены, а среди прочих данных размечать можно будет лишь некоторую часть. После этого применять описанные выше подходы: обучение с частичным привлечением учителя или ГСНС.

B. Пример обнаружения пропусков

Первый рассмотренный пример представляет собой обнаружение пропусков в синтетическом сигнале, сгенерированном с помощью функции:

$$X(t) = \sin(2t) + \varepsilon(t), \tag{7}$$

где ε – шум, распределенный по нормальному закону распределения с математическим ожиданием 0 и среднеквадратическим отклонением 0,2.

Сигнал сгенерирован для 5 тысяч отсчетов с шагом 0,016π. В шести случайно выбранных интервалах длительностью 40 отсчетов внесена имитация потерь сигнала, $X(t) = 0$. Фрагмент полученного сигнала показан на Рисунке 3.

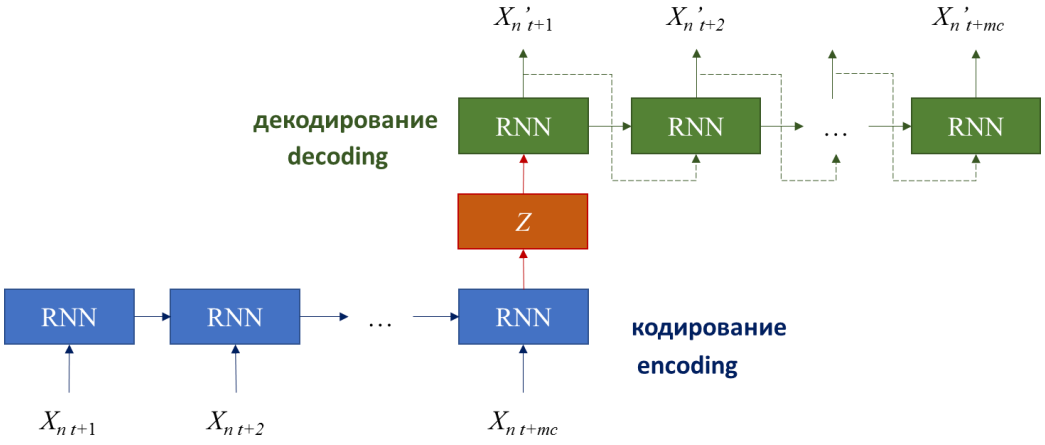

Рис.2. Архитектура рекуррентного автокодировщика
t – индекс начала фрагмента временного ряда, Z – закодированное представление данных,
RNN – рекуррентный слой нейронной сети (RNN, LSTM или GRU).

Fig.2. The architecture of the recurrent autoencoder:
t – start index of the time series fragment, Z – encoded data representation,
RNN – recurrent neural network layer (RNN, LSTM or GRU).

Ширина окна для анализа выбрана равной двум периодам синусоиды.

Независимо от выбора вида рекуррентных ячеек, все потери сигнала были определены – они получили наибольшие приоритеты для анализа, намного превышающие приоритеты фрагментов сигнала, не содержащих потери. Примеры выявленных фрагментов с потерями сигнала приведены на Рисунках 4 и 5, пример фрагмента сигнала без потерь – на Рисунке 6.

C. Пример обнаружения пиков тока на участке электрической сети

Во втором примере используется набор данных PMU, собранных с реальной подстанции 110/35/10 кВ. Особенность установленной системы измерения заключается в том, что она записывает в базу данных сигналы тока и напряжения с высокой частотой дискретизации по времени (128 значений за 0,02 секунды), но в течение только одного периода промышленной частоты 50 Гц каждые 3 минуты. Поэтому сигнал оказывается прерывистым, на стыках синусоид возникают искажения сигнала, препятствующие его анализу. В рассматриваемой выборке в сигнале присутствуют кратковременные превышения тока, которые и являются целевыми для детектирования. Общая длительность наблюдений составляет одни сутки.

Среднее время обучения для RNN, LSTM, GRU ячеек составило 203, 344 и 293 секунды, соответственно. В отличие от первого примера ячейкам RNN не удалось обучиться выявлению паттерна с достаточной точностью для выявления требующих анализа фрагментов данных. LSTM и GRU ячейки показали одинаковую точность, поставив наивысший приоритет фрагментам с повышенным значением тока.

В Таблице 1 приведены полученные значения ΔX для фрагментов с превышениями тока и без них. Для трех приведенных в Таблице 1 примеров фрагменты сигнала и результаты кодирования-декодирования представлены на Рисунках 7, 8 и 9. На Рисунках 7 и 8 показаны фрагменты с наибольшими отклонениями, на Рисунке 9 приведен фрагмент сигнала с низким значением приоритета, что означает что модель посчитала его типичным. Видно, что на Рисунке 9 выход модели близок к исходному сигналу.

Таблица 1

Значения ΔX для фрагментов временного ряда с превышением тока и без превышения.

Table 1

ΔX values for fragments of the time series with and without overcurrent.

№ фрагмента Fragment's ID	Превышение тока Overcurrent	ΔX
143	да yes	2822,24
45	да yes	2443,83
215	да yes	1851,26
83	да yes	1796,35
69	нет no	276,12
13	нет no	240,35
247	нет no	206,94
209	нет no	167,62

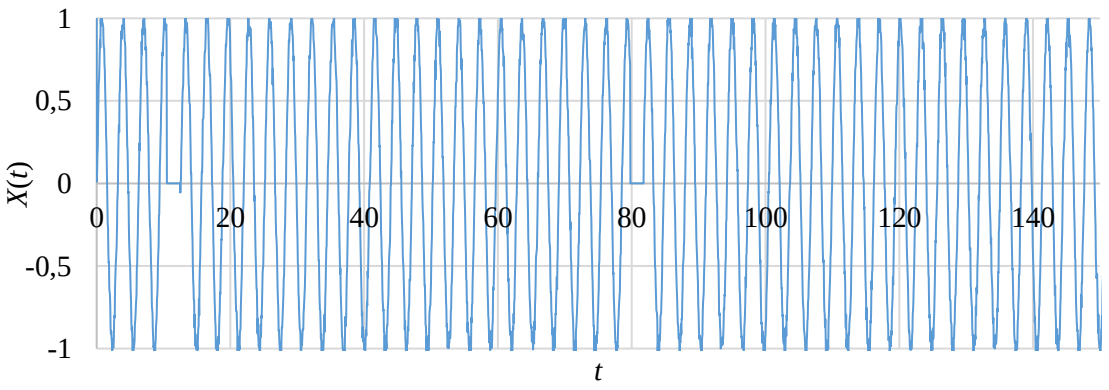

Рис.3. Фрагмент сигнала с потерями.
Fig.3. A signal fragment with losses.

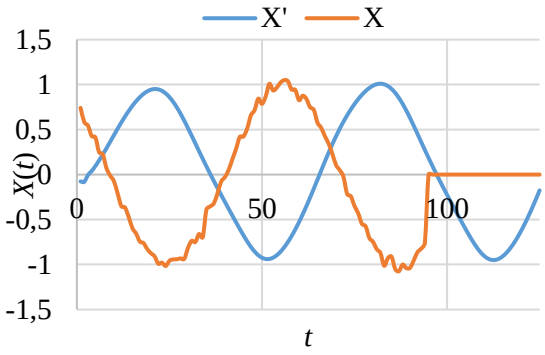

Рис.4. Пример выявленного фрагмента сигнала с потерями.
Fig.4. An example of signal fragment with losses.

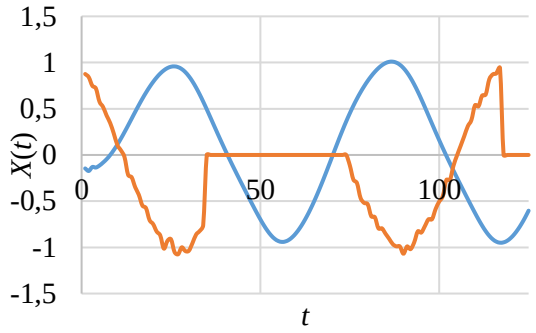

Рис.5. Фрагмент сигнала с потерями.
Fig.5. Signal fragment with losses.

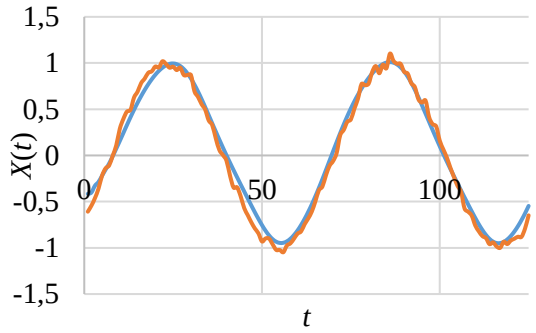

Рис.6. Фрагмент сигнала без потерь.
Fig.6. Signal fragment without losses.

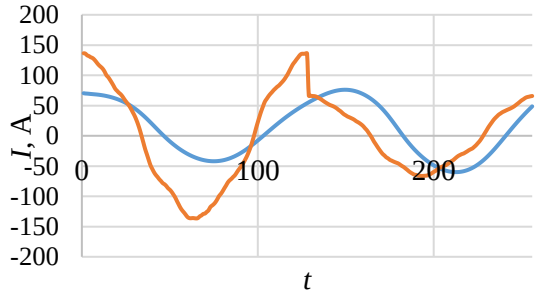

Рис.7. Фрагмент сигнала тока № 143.
Fig.7. Signal fragment of current ID 143.

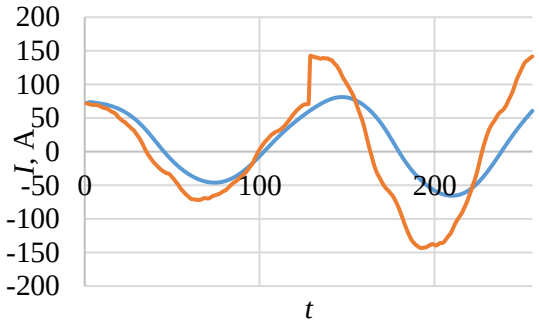

Рис.8. Фрагмент сигнала тока № 45.
Fig.8. Signal fragment of current ID 45.

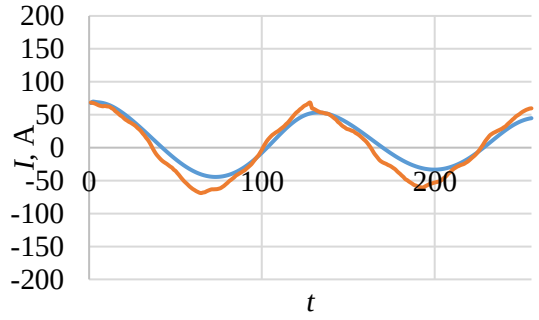

Рис.9. Фрагмент сигнала тока № 247.
Fig.9. Signal fragment of current ID 247.

IV. Обсуждение результатов

Проведенные вычислительные эксперименты как на реальных данных тока участка электрической сети, так и на синтетических данных с потерями показали, что предложенный метод позволяет приоритезировать фрагменты временного ряда с точки зрения необходимости их анализа экспертом для выявления отклонений, свидетельствующих об аварийных режимах, ошибках в данных, других отклонениях, представляющих интерес при анализе данных.

Метод может быть использованы для выявления выбросов различных видов: пропущенные значения, ошибки в данных, выбросы, редкие ситуации. Такое свойство достигается за счет небольшой размерности модели, что отличает ее от аналогов [26-31], и снижает риск переобучения. Кроме того, не требуется настраивать гиперпараметры модели, что повышает скорость получения результатов с ее использованием.

Исследование показано, что для решаемой задачи более точные результаты дают рекуррентные ячейки LSTM и GRU. Процесс обучения автокодировщика, использующего LSTM или GRU, занимает в 1,7 раз больше времени,

чем автокодировщика на ячейках RNN. Однако за счет простой архитектуры моделей обучение проходит за минуты без использования графических процессоров.

Необходимо подчеркнуть, что модели обучались на неразмеченных данных, то есть в процессе обучения им не ставилась задача детектировать определенные выбросы. Более того, в предложенном методе модель не стремятся решить задачу классификации и отделить определенные выбросы от всего остального сигнала, как в аналогичных работах по анализу сигналов тока и напряжения. Разработанная модель расставляет приоритеты всем фрагментами временного ряда, по которым затем необходимо выполнить анализ. При этом ситуации с искажениями получают наиболее высокий приоритет.

Для анализа сигнала разработанной моделью достаточно использовать временное окно, охватывающее два периода главной частоты сигнала.

Заключение

Проведено исследование применимости компактных двухслойных автокодирующих рекуррентных нейросетевых моделей для задачи анализа и разметки временных рядов, содержащих значения режимных параметров электрических сетей. Разработана модель, способная обучаться без размеченных данных, ее работа проанализирована на двух наборах данных: синтетическом синусоидальном сигнале с пропущенными значениями и измерениях тока на реальном участке электрической сети, содержащих кратковременные превышения значений тока.

Метод не требует формирования изначального предположения о виде отклонений и способен существенно сократить время на анализ и разметку больших массивов временных рядов.

ACKNOWLEDGEMENTS

Работа выполнена в рамках государственного задания при финансовой поддержке Министерства науки и высшего образования Российской Федерации (тема № FEUZ-2022-0030 Разработка интеллектуальной мультиагентной системы для моделирования глубоко интегрированных технологических систем в электроэнергетике).

Литература (References)

[1] Zhang L., et al. Voltage and Current Response Characteristics of PMU Device by PCI Simulation. *2022 IEEE International Conference on High Voltage Engineering and Applications (ICHVE)*, 2022, pp. 1-4. doi: 10.1109/ICHVE53725.2022.9961637

[2] Kummerow A., Monsalve C., Brosinsky C., Nicolai S., Westermann D. A Novel Framework for Synchrophasor Based Online Recognition and Efficient Post-Mortem Analysis of Disturbances in Power Systems. *Applied Science*, 2020, vol. 10, 5209. doi: 10.3390/app10155209

[3] Aligholian A., Shahsavari A., Stewart E. M., Cortez E., Mohsenian-Rad H. Unsupervised Event Detection, Clustering, and Use Case Exposition in Micro-PMU Measurements. *IEEE Transactions on Smart Grid*, 2021, vol. 12, no. 4, pp. 3624-3636. doi: 10.1109/TSG.2021.3063088

[4] Mathebula V. C., Saha A. K. Impact of Quality of Repairs and Common Cause Failures on the Reliability Performance of Intra-Bay IEC 61850 Substation Communication Network Architecture Based on Markov and Linear Dynamical Systems. *IEEE Access*, 2021, vol. 9, pp. 112805-112820. doi: 10.1109/ACCESS.2021.3104020

[5] Mathebula V. C., Saha A. K. Mission critical safety functions in IEC-61850 based substation automation system—A reliability review. *International Journal of Energy Research in Africa*, 2020, vol. 48, pp. 149-161. doi: 10.4028/www.scientific.net/JERA.48.149

[6] Li Z., Chen Z., Gao X., Wang S., Di F., Ye R. The Fast Simulation Architecture Construction for Integrated Electric Transmission and Distribution Power Grid Based On Big Data Platform. *2021 China International Conference on Electricity Distribution (CICED)*, 2021, pp. 484-489. doi: 10.1109/CICED50259.2021.9556785

[7] Ambia M.N., Al-Durra A., Caruana C., Muyeen S.M. Power management of hybrid micro-grid system by a generic centralized supervisory control scheme. *Sustainable Energy Technologies and Assessments*, 2014, vol. 8, pp. 57-65.

[8] Lv Z., Song H., Basanta-Val P., Steed A., Jo M. Next-Generation Big Data Analytics: State of the Art, Challenges, and Future Research Topics. *IEEE Transactions on Industrial Informatics*, 2017, vol. 13, no. 4, pp. 1891-1899. doi: 10.1109/TII.2017.2650204

[9] Singh N., Lai K.-H., Vejvar M., Cheng T.C.E. Big Data Technology: Challenges, Prospects, and Realities. *IEEE Engineering Management Review*, 2019, vol. 47, no. 1, pp. 58-66. doi: 10.1109/EMR.2019.2900208

[10] Zhao J., Ding Y., Zhai Y., Jiang Y., Zhai Y., Hu M. Explore unlabeled big data learning to online failure prediction in safety-aware cloud environment. *Journal of Parallel and Distributed Computing*, 2012, vol. 153, pp. 53-63. doi: 10.1016/j.jpdc.2021.02.025

[11] Mantach S., Lutfi A., Moradi Tavasani H., Ashraf A., El-Hag, A., Kordi B. Deep Learning in High

Voltage Engineering: A Literature Review. *Energies*, 2022, vol. 15, 5005. doi: 10.3390/en15145005

[12] Han Y., Li K., Feng H., Zhao Q. Non-intrusive load monitoring based on semi-supervised smooth teacher graph learning with voltage–current trajectory. *Neural Computing and Application*, 2022, vol. 34, pp. 19147–19160. doi: 10.1007/s00521-022-07508-7

[13] Lu X., Zhou Y., Wang Z., Yi Y., Feng L., Wang F. Knowledge Embedded Semi-Supervised Deep Learning for Detecting Non-Technical Losses in the Smart Grid. *Energies*, 2019, vol. 12, 3452. doi: 10.3390/en12183452

[14] Zhao Y., Ball R., Mosesian J., de Palma J. -F., Lehman B. Graph-Based Semi-supervised Learning for Fault Detection and Classification in Solar Photovoltaic Arrays. *IEEE Transactions on Power Electronics*, 2015, vol. 30, no. 5, pp. 2848-2858. doi: 10.1109/TPEL.2014.2364203

[15] Hao C., Jin J. Clustering Analysis of Voltage Sag Events Based on Waveform Matching. *Processes* 2022, vol. 10, 1337. doi: 10.3390/pr10071337

[16] Garcia-Sánchez T., Gómez-Lázaro E., Muljadi E., Kessler M., Muñoz-Benavente I., Molina-Garcia A. Identification of linearised RMS-voltage dip patterns based on clustering in renewable plants. *IET Generation Transmission Distribution*, 2018, vol. 12, pp. 1256-1262.

[17] Abegaz B., Kueber J. Smart Control of Automatic Voltage Regulators using K-means Clustering. *2019 14th Annual Conference System of Systems Engineering (SoSE)*, 2019, pp. 328-333. doi: 10.1109/SYSOSE.2019.8753873

[18] Creswell A, White T., Dumoulin V., Arulkumaran K., Sengupta B., Bharath A.A. Generative Adversarial Networks: An Overview. *IEEE Signal Processing Magazine*, 2018, vol. 35, no. 1, pp. 53-65. doi: 10.1109/MSP.2017.2765202

[19] Wang K., Gou C., Duan Y., Lin Y., Zheng X., Wang F. -Y. Generative adversarial networks: introduction and outlook. *IEEE/CAA Journal of Automatica Sinica*, 2017, vol. 4, no. 4, pp. 588-598, doi: 10.1109/JAS.2017.7510583

[20] Goodfellow I., et al., Generative Adversarial Nets. *Advances in Neural Information Processing Systems 27 (NIPS 2014)*, 2014, pp. 2672-2680.

[21] Ren C., Xu Y. A Fully Data-Driven Method Based on Generative Adversarial Networks for Power System Dynamic Security Assessment With Missing Data. *IEEE Transactions on Power Systems*, 2019, vol. 34, no. 6, pp. 5044-5052. doi: 10.1109/TPWRS.2019.2922671

[22] Zheng X., Wang B., Xie L. Synthetic Dynamic PMU Data Generation: A Generative Adversarial Network Approach. *2019 International Conference on Smart Grid Synchronized Measurements and Analytics (SGSMA)*, 2019, pp. 1-6, doi: 10.1109/SGSMA.2019.8784681

[23] Zheng X., Wang B., Kalathil D., Xie L., Generative Adversarial Networks-Based Synthetic PMU Data Creation for Improved Event Classification. *IEEE Open Access Journal of Power and Energy*, 2012, vol. 8, pp. 68-76. doi: 10.1109/OAJPE.2021.3061648

[24] Yang Y., McLaughlin K., Gao L., Sezer S., Yuan Y., Gong Y. Intrusion detection system for IEC 61850 based smart substations. *2016 IEEE Power and Energy Society General Meeting (PESGM)*, 2016, pp. 1-5. doi: 10.1109/PESGM.2016.7741668

[25] Kingma D.P., Welling M. Auto-Encoding Variational Bayes. Available at: https://arxiv.org/abs/1312.6114 (accessed 02.01.2023).

[26] Meng C. Jiang X.S., Wei X.M., Wei T. A Time Convolutional Network Based Outlier Detection for Multidimensional Time Series in Cyber-Physical-Social Systems. *IEEE Access*, 2020, vol. 8, pp. 74933-74942. doi: 10.1109/ACCESS.2020.2988797

[27] Nizam H., Zafar S., Lv Z., Wang F., Hu X. Real-Time Deep Anomaly Detection Framework for Multivariate Time-Series Data in Industrial IoT. *IEEE Sensors Journal*, 2022, vol. 22, no. 23, pp. 22836-22849. doi: 10.1109/JSEN.2022.3211874

[28] Yokkampon U., Mowshowitz A., Chumkamon S., Hayashi E. Robust Unsupervised Anomaly Detection with Variational Autoencoder in Multivariate Time Series Data. *IEEE Access*, 2022, vol. 10, pp. 57835-57849. doi: 10.1109/ACCESS.2022.3178592.

[29] Yu J., Liu X., Ye L. Convolutional Long Short-Term Memory Autoencoder-Based Feature Learning for Fault Detection in Industrial Processes. *IEEE Transactions on Instrumentation and Measurement*, 2012, vol. 70, 3505615. doi: 10.1109/TIM.2020.3039614

[30] Dewangan G., Maurya S. Fault Diagnosis of Machines Using Deep Convolutional Beta-Variational Autoencoder. *IEEE Transactions on Artificial Intelligence*, 2022, vol. 3, no. 2, pp. 287-296. doi: 10.1109/TAI.2021.3110835

[31] Yin C., Zhang S., Wang J., Xiong N.N. Anomaly Detection Based on Convolutional Recurrent Autoencoder for IoT Time Series. *IEEE Transactions on Systems, Man, and Cybernetics: Systems*, 2022, vol. 52, no. 1, pp. 112-122. doi: 10.1109/TSMC.2020.2968516

[32] Chen T., Liu X., Xia B., Wang W., Lai Y. Unsupervised Anomaly Detection of Industrial Robots Using Sliding-Window Convolutional Variational Autoencoder. *IEEE Access*, 2020, vol. 8, pp. 47072-47081. doi: 10.1109/ACCESS.2020.2977892

[33] Shimizu M., Perinpanayagam S., Namoano B. A Real-Time Fault Detection Framework Based on Unsupervised Deep Learning for Prognostics and

Health Management of Railway Assets. *IEEE Access*, 2022, vol. 10, pp. 96442-96458. doi: 10.1109/ACCESS.2022.3205352
[34] Huang Y., Chen C. -H., Huang C. -J. Motor Fault Detection and Feature Extraction Using RNN-Based Variational Autoencoder. *IEEE Access*, 2019, vol. 7, pp. 139086-139096. doi: 10.1109/ACCESS.2019.2940769
[35] Chadha G.S., Islam I., Schwung A., Ding S.X. Deep Convolutional Clustering-Based Time Series Anomaly Detection. *Sensors*, 2021, vol. 21, 5488. doi: 10.3390/s21165488
[36] Zheng K., Yang J., Gong Q., Zhou S., Zeng L., Li S. Multivariate Extreme Learning Machine Based AutoEncoder for Electricity Consumption Series Clustering. *IEEE Access*, 2021, vol. 9, pp. 148665-148675. doi: 10.1109/ACCESS.2021.3124009
[37] Zhao Q., Chang Z., Min G. Anomaly Detection and Classification of Household Electricity Data: A Time Window and Multilayer Hierarchical Network Approach. *IEEE Internet of Things Journal*, 2022, vol. 9, no. 5, pp. 3704-3716. doi: 10.1109/JIOT.2021.3098735
[38] Wang J., Shi D., Li Y., Chen J., Ding H., Duan X. Distributed Framework for Detecting PMU Data Manipulation Attacks With Deep Autoencoders. *IEEE Transactions on Smart Grid*, 2019, vol. 10, no. 4, pp. 4401-4410. doi: 10.1109/TSG.2018.2859339
[39] Niazazari I., Livani H. Disruptive Event Classification using PMU Data in Distribution Networks. Available at: https://arxiv.org/abs/1703.09800 (accessed 05.01.2023)
[40] Mishra A., de Callafon R.A. Voltage State Estimation using a Power Network Model driven Auto-Encoder Neural Network. *IFAC-PapersOnLine*, 2021, vol. 54, no. 7, pp. 517-522. doi: 10.1016/j.ifacol.2021.08.412
[41] Hochreiter S., Schmidhuber J. Long short-term memory. *Neural Computing*, 1997, vol. 9, pp. 1735-1780.
[42] Cho K., van Merriënboer B., Gulcehre C., Bahdanau D., Bougares F., Schwenk H., Bengio Y. Learning Phrase Representations using RNN Encoder-Decoder for Statistical Machine Translation. Available at: https://arxiv.org/abs/1406.1078 (accessed 04.01.2023)
[43] Lamb A., Goyal A., Zhang Y., Zhang S., Courville A., Bengio Y. Professor Forcing: A New Algorithm for Training Recurrent Networks. Available at: https://arxiv.org/abs/1610.09038 (accessed 04.01.2023)
[44] Kulowski L. Building a LSTM Encoder-Decoder using PyTorch to make Sequence-to-Sequence Predictions. Available at: https://github.com/lkulowski/LSTM_encoder_decoder (accessed 02.01.2023)

Сведения об авторах.

Матренин Павел Викторович, к.т.н., ведущий научный сотрудник научной лаборатории цифровых двойников Уральского федерального университета.
Область научных интересов: системный анализ, методы машинного обучения в электроэнергетике, обработка временных рядов.
E-mail: p.v.matrenin@urfu.ru

Хальясмаа Александра Ильмаровна, к.т.н., доцент, заведующий научной лаборатории цифровых двойников в электроэнергетике Уральского федерального университета.
Область научных интересов: диагностика состояния электрооборудования, системы поддержки принятия решений.
E-mail: a.i.khaliasmaa@urfu.ru

Потачиц Ярослав Владимирович, к.т.н., старший преподаватель кафедры электрических станций Белорусского национального технического университета.
Область научных интересов: электродинамическая стойкость, обработка временных рядов.
E-mail: potachits@bntu.by

Centrifugal Compressors Gas-Dynamic Characteristics Influence on the Refrigerating Machines Efficiency

Danilishin A.M., Kozhukhov Y. V.
ITMO University
Saint-Petersburg, Russian Federation

***Abstract*.** The article is devoted to the study R134a refrigerating machine efficiency and consisting of a centrifugal compressor, a condenser, a temperature-regulating valve and an evaporator. The main purpose of the work is to analyze the centrifugal compressor gas dynamic characteristics effect on the refrigeration machine vapor-compression cycle efficiency. This goal is achieved through the study by actual working process numerical experiment in the refrigeration machine centrifugal compressor with an idealized process for other elements. The object of the study are the refrigeration machine characteristics, expressed by the theoretical refrigeration coefficient COP_{Rt}. Single-stage centrifugal compressors with the design conditional flow coefficient in the range from 0.035 to 0.12 are considered. The design of centrifugal compressors was carried out according to a new calculation method to the flow part efficiency increase. The method comprehensively combines the inviscid and viscous flow calculations with the use of the single-criteria and multiparametric optimization. Previously, the method was tested and compared with experimental data. The most important result is the results of the refrigeration cycle efficiency evaluating through the centrifugal compressors highly efficient flow parts design methodology application. An increase in COP_{Rt} was obtained taking into account the centrifugal compressor actual process in the range from 2.6% to 7.2%. The significance of the results obtained lies in the possibility of using high-efficiency centrifugal compressors gas dynamic characteristics for the chillers refrigeration cycles analysis and calculation. The level of the compressors isentropic efficiency ranges from 0.80 to 0.85, depending on the design conditional flow coefficient.
***Keywords*:** chiller, refrigeration centrifugal compressor, vapor-compression cycle, CFD, flow part, R134a.

DOI: https://doi.org/10.52254/1857-0070.2023.2-58-07
UDC: 621.515

Danilișin A.M., Kojuhov Iu.V
Universitatea ITMO, Sankt-Petersburg, Federația Rusă

Rezumat. Articolul este dedicat studiului eficienței unei mașini frigorifice care funcționează pe freon R134a și constă dintr-un compresor centrifugal, condensator, supapă de expansiune și evaporator. Scopul principal al lucrării este de a analiza efectul caracteristicilor gaz-dinamice ale unui compresor centrifugal asupra eficienței ciclului unei mașini frigorifice cu compresie de vapori. Acest scop este atins prin studierea, printr-un experiment numeric, a procesului efectiv de lucru în compresorul centrifugal al unei mașini frigorifice cu un proces idealizat pentru alte elemente. Obiectul studiului îl constituie caracteristicile ciclului frigorific al unei mașini frigorifice, exprimate prin coeficientul teoretic de performanță $COP_{R}t$. Compresorul centrifugal al mașinii de refrigerare include o treaptă de tip final și constă dintr-un dispozitiv de admisie, un rotor axial, un difuzor fără palete și un dispozitiv de evacuare. Intervalul debitului condiționat calculat pentru gama principală de compresoare centrifuge este de la 0,035 la 0,12. Proiectarea compresoarelor centrifugale a fost realizată după o nouă metodă de calcul pentru creșterea eficienței căii de curgere. Tehnica combină în mod cuprinzător calculul fluxului inviscid și vâscos cu utilizarea optimizării multi-parametrice cu un singur criteriu. Anterior, tehnica a fost testată și comparată cu date experimentale. Experimentul numeric pentru partea de flux a fost efectuat folosind pachetul software *Ansys CFX v18.0*. S-a obținut o creștere a $COP_{R}t$, luând în considerare procesul efectiv într-un compresor centrifugal, în intervalul de la 2,6% la 7,2%, în funcție de debitul condiționat calculat. Semnificația rezultatelor obținute constă în posibilitatea analizei, calculării ciclurilor de refrigerare a chillerelor folosind caracteristicile gazodinamice ale compresoarelor centrifuge de înaltă eficiență.
***Cuvinte-cheie*:** chiller, compresor centrifugal frigorific, ciclu de compresie a vaporilor, CFD, parte de curgere, R134a.

Влияние газодинамических характеристик центробежных компрессоров на эффективность холодильных машин

Данилишин А.М., Кожухов Ю.В.
Университет ИТМО, Санкт-Петербург, Российская Федерация

***Аннотация*.** Статья посвящена исследованию эффективности холодильной машины, работающей на фреоне R134a, и состоящей из центробежного компрессора, конденсатора, терморегулирующего вентиля и испарителя. Основной целью работы является анализ влияния на эффективность цикла парокомпрессионной холодильной машины газодинамических характеристик центробежного компрессора. Поставленная цель достигается за счет исследования посредством численного эксперимента действительного рабочего процесса в центробежном компрессоре холодильной машины при идеализированном процессе для других элементов. Объектом исследования являются характеристики холодильного цикла холодильной машины, выражаемые теоретическим холодильным коэффициентом COP_{Rt}. Центробежный компрессор холодильной машины включает ступень концевого типа и состоит из входного устройства, осерадиального рабочего колеса, безлопаточного диффузора и выходного устройства. Диапазон расчетного условного коэффициента расхода для основного типового ряда центробежных компрессоров составляет от 0.035 до 0.12. Проектирование центробежных компрессоров осуществлено по новой расчетной методике повышения эффективности проточной части. Методика комплексно сочетает в себе проведение расчетов невязкого и вязкого потока с применением однокритериальной многопараметрической оптимизации. Ранее методика была апробирована и сопоставлена с экспериментальными данными. Численный эксперимент для проточной части осуществлен с помощью пакета программ *Ansys CFX v18.0*. Решение проверено на сеточную независимость и сходимость. Наиболее важным результатом являются результаты оценки эффективности холодильного цикла за счет применения методики проектирования высокоэффективных проточных частей центробежных компрессоров. Получено повышение COP_{Rt} с учетом действительного процесса в центробежном компрессоре в диапазоне от 2.6% до 7.2% в зависимости от расчетного условного коэффициента расхода. Значимость полученных результатов состоит в возможности анализа, расчета холодильных циклов чиллеров при использовании газодинамических характеристик высокоэффективных центробежных компрессоров. Уровень изоэнтропического коэффициента полезного действия компрессоров составляет от 0.80 до 0.85 в зависимости от расчетного условного коэффициента расхода.

Ключевые слова: чиллер, холодильный центробежный компрессор, парокомпрессионный цикл, CFD, проточная часть, R134a.

ВВЕДЕНИЕ

Холодильные установки с центробежным компрессором применяются для систем общего кондиционирования больших объемов. Типичная схема чиллера состоит из следующих основных элементов: центробежный компрессор, конденсатор, терморегулирующий вентиль (ТРВ), испаритель [1]. В большинстве установок в качестве хладагента используется фреон R134a [2]. На рисунке 1 показан рассматриваемый цикл парокомпрессионной холодильной машины — чиллера в *p*—*i* диаграмме. Здесь процесс 1—2s — изоэнтропическое сжатие в компрессоре, 1—2_{pol} — действительный (политропный) процесс сжатия в компрессоре с учетом потерь. Процесс 2—3 — охлаждение и конденсация хладагента в конденсаторе, 3—4 — изоэнтальпийное расширение в ТРВ, 4—1 — кипение и перегрев хладагента в испарителе. Конструкция центробежного компрессора может быть одноступенчатой или двухступенчатой.

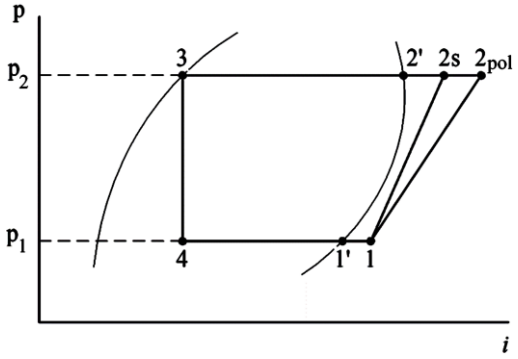

Рис.1. *p*—*i* диаграмма парокомпрессионного цикла. [1]

Часто используются две параллельно работающие одноступенчатые конструкции с двумя приводами. Существуют двухступенчатые конструкции с последовательным расположением двух ступеней (первая промежуточного типа с обратно-направляющим аппаратом, и вторая концевого типа) или оппозитным расположением двух концевых ступеней.

[1] Appendix 1

Приводом служит электродвигатель с переменным или постоянным числом оборотов [3], [4]. Асинхронный (индукционный) электродвигатель с частотой вращения 3000 об/мин или 3600 об/мин (без учета скольжения) в зависимости от частоты электрического тока в сети. Для увеличения оборотов ротора компрессора используется мультипликатор. Могут применятся высокоскоростные электродвигатели, с использованием частотного преобразователя. Для исключения использования масла применяются синхронные электродвигатели с постоянными магнитами и магнитным подвесом.

Отношение давлений в одноступенчатом центробежном компрессоре варьируется от 2.0 до 3.5. При таком отношении давлений значение условного числа Маха M_u составляет от 0.9 до 1.4. Холодопроизводительность чиллеров с центробежным компрессором в промышленности обычно варьируется от 700 до 7000 кВт и выше.

В ряде работ рассмотрено использование методов вычислительной газодинамики (*CFD*) [5]–[10] для проектирования, совершенствования, исследования проточной части центробежного компрессора.

Исследование входной неравномерности потока с применением входного направляющего аппарата в одноступенчатом центробежном компрессоре с отношением давлений П=1.97 и условным числом Маха M_u=1.011 чиллера рассмотрено в [11]. В работе [12] рассматривается цикл с использованием экономайзера с заменой двухступенчатого компрессора на одноступенчатый с отношением давлений П=3.0 и условным коэффициентом расхода Ф=0.083. Повышение энергоэффективности достигается впрыском пара из экономайзера в ступень компрессора. В [13]–[15] с помощью *CFD* выполнено моделирование проточной части двухступенчатого центробежного компрессора для оценки осевого усилия при использовании газовых подшипников. По результатам *CFD* моделирования характеристик в [16]–[18] рассмотрены различные хладагенты в концевой центробежной компрессорной ступени.

Проведенный обзор литературы показывает актуальность задач по совершенствованию проточной части центробежных компрессоров, применяющихся в холодильных установках — чиллерах. К сожалению, во многих исследованиях значение эффективности является приведенным и не может быть оценено в абсолютных значениях и быть применено в проектных расчетах, что также затрудняет определение текущего уровня развития техники. Основным методом исследования является моделирование при помощи вычислительной гидрогазодинамики. Это вполне обосновано, поскольку для натурного исследования требуется дорогостоящее стендовое оборудование с замкнутым контуром для циркуляции хладагента.

Учитывая вышесказанное, в данном исследовании поставлена задача анализа эффективности цикла чиллера при использовании разработанных высокоэффективных проточных частей центробежных компрессоров на основе их действительной эффективности.

МЕТОДЫ, РЕЗУЛЬТАТЫ И ОБСУЖДЕНИЕ

Для анализа влияния эффективности центробежного компрессора на работу чиллера выполняется расчет идеального парокомпрессионного холодильного цикла для чиллерной установки с центробежным компрессором. В данном расчете для оценки влияния компрессора принято, что все элементы, кроме компрессора работают без учета потерь. Расчет холодильного коэффициента выполнен по методике [19]. Проектирование компрессоров велось при помощи комплексной методики проектирования высокоэффективных центробежных компрессоров. Повышение эффективности проточной части центробежного компрессора достигается за счет сочетания подходов расчета невязкого квазитрехмерного потока и *CFD* моделирования с однокритериальной многопараметрической оптимизацией. Расчет невязкого потока используется для коррекции коэффициента теоретического напора при проведении газодинамического расчета, а также профилирования рабочего колеса с учетом определения рационального распределения относительных скоростей на лопатке. Обычно используется многокритериальная и многопараметрическая оптимизация формы проточной части, но такой подход требует значительных временных и вычислительных ресурсов.

Благодаря невязкому расчету существенно сокращается число вариантных расчетов при проведении многопараметрической и однокритериальной оптимизации. Оптимизация проводилась с использованием метода *ASO (adaptive single objective)* для параметризированной модели проточной части рабочего колеса и безлопаточного диффузора. Для каждого газодинамического проекта выполнено порядка 100 *CFD* расчетов для выполнения цели оптимизации — максимизации эффективности ступени.

Уравнение 1 представляет собой условный коэффициент расхода центробежного компрессора. В данной работе рассматриваются десять газодинамических проектов центробежных компрессоров с диапазоном условного коэффициента расхода на расчетном режиме $\Phi_р$ от 0.035 до 0.12. Диаметр рабочих колес одинаковый и составляет D_2=0.28 м. Номинальное число оборотов ротора для всех десяти компрессоров находится в диапазоне от 11850 об/мин до 12100 об/мин.

$$\Phi = \frac{4\bar{m}}{\rho_0^* \pi D_2^2 u_2}, \quad (1)$$

где $\bar{m}$ — массовый расход; ρ_0^* — плотность на входе, рассчитанная по полным параметрам; D_2 — диаметр рабочего колеса; u_2 — окружная скорость на диаметре D_2.

Уравнение 2 представляет собой теоретический холодильный коэффициент или COP_{Rt}.

$$\varepsilon_т(COP_{Rt}) = \frac{i_1 - i_4}{i_2 - i_1}, \quad (2)$$

где i — энтальпия (индексы см. рис. 1).

Действительный холодильный коэффициент реальной холодильной машины определяются с учетом всех затрат на привод компрессора и выражается уравнением 3.

$$COP_R = \frac{Q_0}{W_{input}}, \quad (3)$$

где Q_0 — холодопроизводительность, W_{input} — суммарная потребляемая мощность всех компонентов установки, включая вспомогательное питание и исключая встроенные насосы.

Таким образом, чтобы учесть действительный холодильный коэффициент, требуется знание эффективности следующих элементов: компрессора, механической части, передающей крутящий момент, опор и привода. В зависимости от выбора компоновки и типа привода, изменение действительного COP_R может быть весьма существенно. Сравнение должно быть произведено для одинаковых уровней температуры и давления в холодильном цикле, так как их различие вызывает изменение Q_0. Поэтому в данной работе оценка эффективности холодильного цикла производится посредством исследования действительного рабочего процесса в центробежном компрессоре холодильной машины с помощью численного эксперимента.

Для проектирования проточной части могут использоваться различные методики проектирования [20], [21]. В качестве исходных данных принимаются рекомендации стандарта [22] *Air-Conditioning Heating and Refrigeration Institute (AHRI)* для большинства центробежных чиллеров с водяным охлаждением. Согласно стандарту, температура воды на выходе из чиллера составляет 6.67 °C, а поступающей в конденсатор 29.44 °C. Разница температур воды на входе и выходе в испарителе и конденсаторе составляет 10 °C. Перегрев в испарителе принимаем равным 2°C. Переохлаждение в конденсаторе отсутствует. Обычно для расчета цикла принимается расчетный изоэнтропический коэффициент полезного действия, равный η_s=0.80.

Давление хладагента на входе в компрессор составляет $p_н$=0.356 МПа, на выходе $p_к$=0.919-0.935 МПа (конечное давление принималось по результатам численного моделирования каждого компрессора). Проектное отношение давлений в компрессоре составляет П=2.56.

Окончательное моделирование рабочего процесса осуществлялось с помощью вычислительного комплекса *Ansys CFX V18.0*. Расчетная область проточной части центробежного компрессора изображена на рисунке 2 и состоит из следующих элементов: входной осевой патрубок (1), осерадиальное рабочее колесо полуоткрытого типа (2), безлопаточный диффузор (3), выходная сборная камера постоянного сечения (4). Между корпусом и лопатками

рабочего колеса устанавливался зазор 0,4 мм. В качестве граничных условий на входе выбрано давление и температура по полным параметрам. На выходе из компрессора устанавливался массовый расход от границы помпажа до начала запирания (режима максимальной производительности). Между вращающейся и неподвижными областями устанавливался интерфейс *frozen rotor*. Модель турбулентности *SST (shear stress transport).* Размер расчетной сетки составлял порядка 5.6 млн. элементов для каждой расчетной модели.

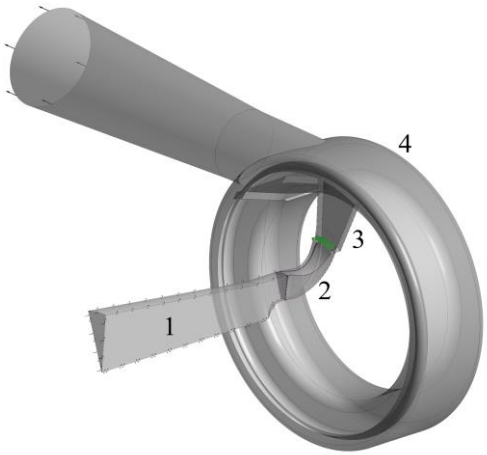

Рис.2. Расчетная область проточной части центробежного компрессора. [2]

Так как используется фреон R134a, то необходимо учитывать реальность газа при сжатии в центробежном компрессоре [23]. Использование термогазодинамических свойств рабочей среды в *Ansys CFX* выполнялось с помощью предварительно рассчитанных таблиц *RGP (Real Gas Property)*. Для расчета термогазодинамических свойств реального газа – фреона R134a использована методика *FES* [24]. Данный подход обеспечивает наибольшую точность в отличие от использования стандартных уравнений состояния в *CFX*.

Сходимость решения контролировалось падением уровня невязок, схождением небалансов и точек мониторинга. Все расчетные точки достигли сходимости решения.

На рисунке 3 представлены газодинамические характеристики десяти центробежных компрессоров на фреоне R134a, полученные с помощью численного моделирования. Газодинамические характеристики включают себя: изоэнтропический коэффициент полезного действия, отношение давлений компрессора, а также коэффициент теоретического напора, рассчитываемый по формуле 4.

$$\psi_т = \frac{c_{u2}}{u_2}, \qquad (4)$$

где c_{u2} — окружная составляющая абсолютной скорости потока на диаметре D_2.

Коэффициент внутреннего напора, рассчитываемый по формуле 5.

$$\psi_i = \frac{i^*_{0'—0'} - i^*_{0—0}}{u_2^2}, \qquad (5)$$

где $i^*_{0'—0'} - i^*_{0—0}$ — перепад полных энтальпий между выходом и входом в компрессор.

Представленные характеристики имеют достаточный запас по помпажу, около 30%. Коэффициент теоретического напора составляет порядка $\psi_T = 0.77$.

Максимальная производительность ограничена режимом запирания межлопаточного канала рабочего колеса, вследствие чего ограничивается зона работы компрессора. Проанализируем эффективность ступеней.

На рисунке 4 представлено распределение политропного КПД по сечениям компрессоров в зависимости от расчетного условного коэффициента расхода. Сечение 2’—2’ — сечение за рабочим колесом на диаметре $1.05D_2$, 4—4 — сечение за диффузором, 0’—0’ — сечение на выходе из компрессора.

Расчеты производились от сечения на входе 0—0 до указанного выше сечения за элементом ступени.

В диапазоне расчетного коэффициента расхода от 0.035 до 0.065 наблюдается монотонное увеличение эффективности компрессора.

Начиная с 0.065 эффективность компрессора находится примерно на одном уровне около 0.85.

Максимальный уровень расчетного политропного КПД концевой ступени достигнут на уровне 0.90 для $Ф_р$=0.12.

Рассмотрим подробнее структуру потока в рабочем колесе для этого компрессора.

[2] Appendix 1

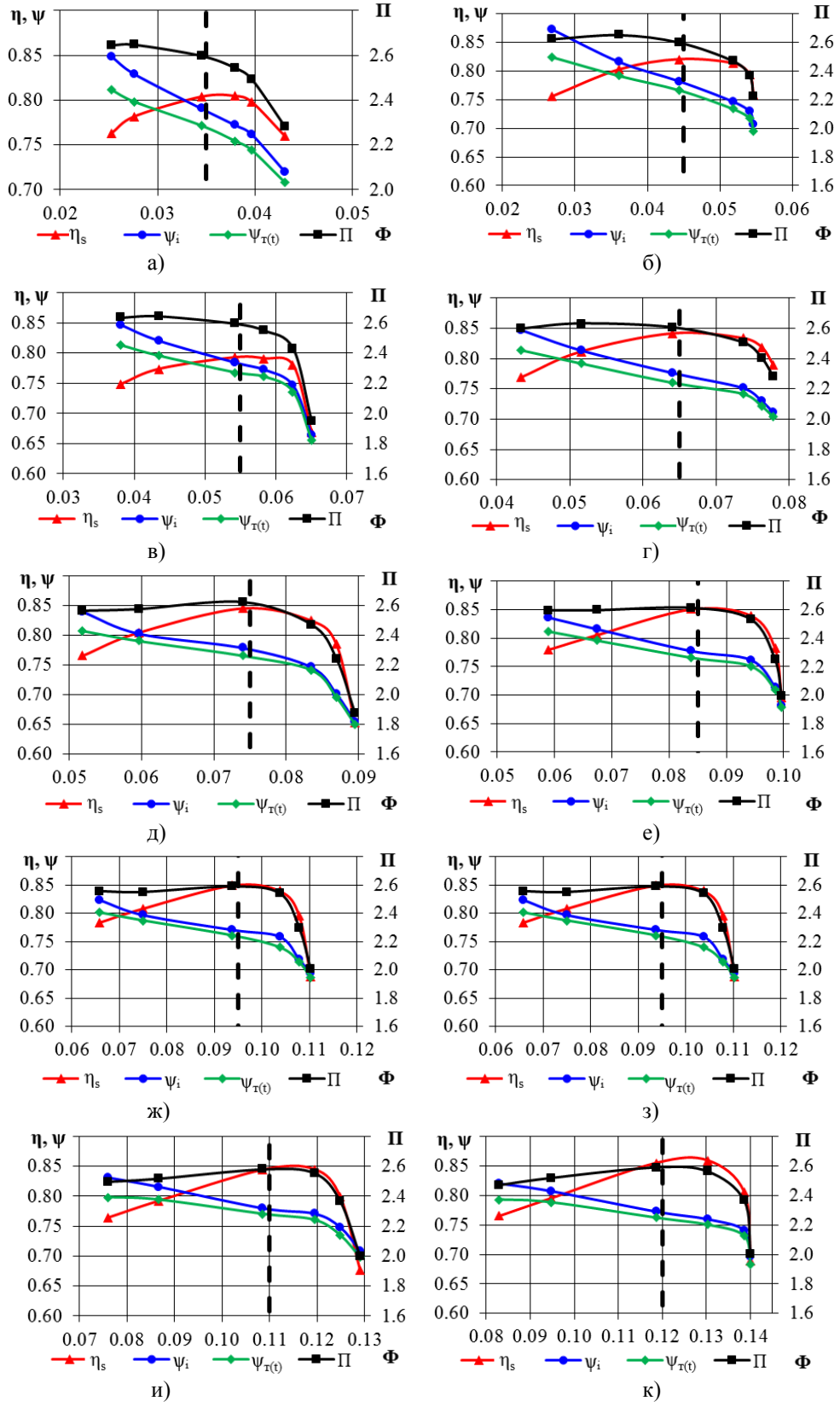

а-$Ф_{р1}$=0.035, б- $Ф_{р2}$=0.045, в- $Ф_{р3}$=0.055, г- $Ф_{р4}$=0.065, д- $Ф_{р5}$=0.075 е- $Ф_{р6}$=0.085 ж- $Ф_{р7}$=0.095 з- $Ф_{р8}$=0.10, и- $Ф_{р9}$=0.11, к- $Ф_{р10}$=0.12 .

Рис. 3. Характеристики холодильных центробежных компрессоров. [3]

[3] Appendix 1

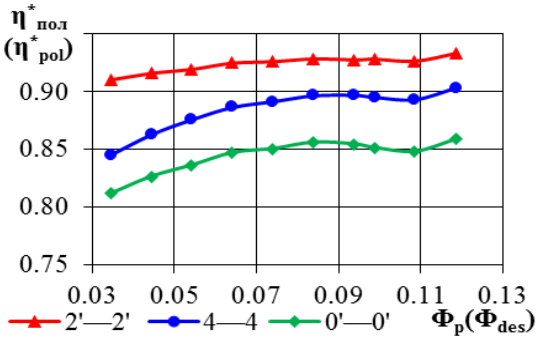

Рис.4. Распределение политропного КПД по сечениям компрессоров в зависимости от расчетного коэффициента расхода. [4]

На рисунке 5 представлено распределение числа Маха на средней по высоте лопатки поверхности на трех режимах от минимальной до максимальной производительности для центробежного компрессора №10.

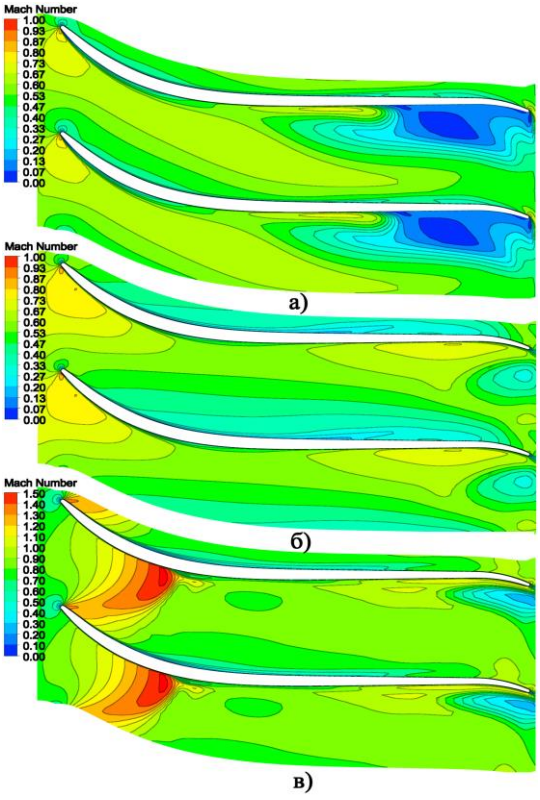

а-Ф$_{min}$, б- *Ф$_p$*, в- *Ф$_{max}$*

Рис. 5. Распределение числа Маха на средней по высоте лопатки поверхности в рабочем колесе центробежного компрессора №10. [5]

На режиме малой производительности (а) на задней поверхности лопатки у задней кромки находится крупная рециркуляционная зона — отрыв потока. На расчетном режиме (б) наблюдается безотрывный режим работы. На режиме максимальной производительности (в) наблюдается скачок уплотнения в межлопаточном канале.

Рассмотрим уровень потенциального влияния действительной эффективности центробежных компрессоров на эффективность холодильного цикла на примере разработанных компрессоров.

На рисунке 6 показано значение относительного повышения теоретического холодильного коэффициента COP_R парокомпрессионного цикла при применении высокоэффективных проточных частей центробежных компрессоров относительно базового компрессора с изоэнтропическим КПД η_s=0.80 в зависимости от холодопроизводительности.

По результатам расчета теоретический холодильный коэффициент с учетом действительного процесса в компрессоре $\varepsilon_т(COP_{Rt})$ повышается от 2.6% до 7.2%, при повышении изоэнтропического КПД компрессора от 2% до 5.5%, за исключением компрессора №1, где изоэнтропический КПД совпадает с базовым. Диапазон холодопроизводительности чиллеров с центробежным компрессором составляет от Q_0=990 кВт до Q_0=3317 кВт.

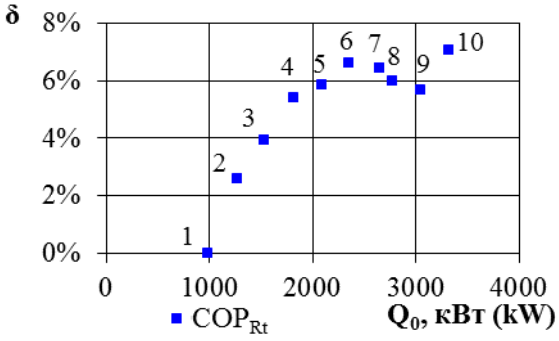

Рис.6. График относительного повышения COP_{Rt} цикла при применении высокоэффективных проточных частей центробежных компрессоров. [6]

ЗАКЛЮЧЕНИЕ

Разработан ряд из десяти газодинамических проектов проточных частей высокоэффективных центробежных компрессоров для чиллера. Полученные характеристики центробежных компрессоров могут быть применены для анализа влияния на эффективность холодильного цикла холодильных машин — чиллеров, работающих на фреоне R134a в

[4,5,6] Appendix 1

исследовательской и проектной деятельности.

Значение теоретического холодильного коэффициента ε_T (COP_{Rt}) чиллера составило от 6.1 до 6.52 в диапазоне расчетного условного коэффициента расхода компрессора Φ_p от 0.035 до 0.12 соответственно. Максимальное значение при идеальном цикле составляет 7.61.

Максимальное значение политропного КПД центробежного компрессора из всего ряда равно 0.86 для компрессора с условным коэффициентом расхода на расчетном режиме Φ_p=0.12.

В дальнейшем исследовании планируется увеличить значение КПД центробежного компрессора за счет внесения конструктивных изменений: установки лопаточного диффузора и замены выходного устройства улиткой переменного сечения.

APPENDIX 1 (ПРИЛОЖЕНИЕ 1)

Fig. 1. *p—i* diagram of the vapor compression cycle.

Fig. 2. The design area of the flow part of the centrifugal compressor.

Fig. 3. Characteristics of refrigeration centrifugal compressors

Fig. 4. Distribution of polytropic efficiency across compressor sections depending on the calculated flow coefficient.

Fig. 5. Distribution of the Mach number on the average height of the blade surface in the impeller of the centrifugal compressor No. 10.

Fig. 6. COP_R relative increase graph when using highly efficient centrifugal compressors flow parts.

Литература (References)

[1] ASHRAE Handbook— Refrigeration. Ashrae, 2022.

[2] Roytta P., Honkatukia J., and Turunen-Saaresti T. Centrifugal Compressor Working Fluids for Refrigeration Cycle', in Volume 4: Cycle Innovations; Industrial and Cogeneration; Manufacturing Materials and Metallurgy; Marine, Jan. 2009, pp. 89–97, doi: 10.1115/GT2009-59150.

[3] Hsu C.-N. and Wang S.-H. 'Evaluating the Performance of Water Chillers Equipped with Constant- or Variable-Frequency Centrifugal Compressors, Processes, vol. 9, no. 6, p. 1039, Jun. 2021, doi: 10.3390/pr9061039.

[4] Oliveira F., Ukil A., 'Comparative Performance Analysis of Induction and Synchronous Reluctance Motors in Chiller Systems for Energy Efficient Buildings', IEEE Trans. Ind. Informatics, vol. 15, no. 8, pp. 4384–4393, Aug. 2019, doi: 10.1109/TII.2018.2890270.

[5] Lee K.-Y., Choi Y.-S., and Park W.-J. Numerical Study on the Performance Characteristics of a Centrifugal Compressor for a R134a Turbo-Chiller, J. Fluid Mach., vol. 7, no. 2, pp. 14–20, Apr. 2004, doi: 10.5293/KFMA.2004.7.2.014.

[6] Park H.-Y., Oh H.-T., Shin Y.-H., Lee Y.-P., Kim K.-H., and Chung J.-T. Numerical Analysis Techniques and Flow Characteristics of Two-Stage Centrifugal Compressor for R134a Turbo-Chiller, KSFM J. Fluid Mach., vol. 10, no. 4, pp. 29–38, Aug. 2007, doi: 10.5293/KFMA.2007.10.4.029.

[7] Yu L., Cousins W. T., Shen F., Kalitzin G., Sishtla V., and Sharma O. Numerical Investigation of the Effect of Diffuser and Volute Design Parameters on the Performance of a Centrifugal Compressor Stage, in Volume 2D: Turbomachinery, Jun. 2016, doi: 10.1115/GT2016-57057.

[8] Hwang Y., Park H., Oh S., Lee H., Park Y., and Lee K. The evaluation of energy saving performance for the modular design centrifugal chiller, E3S Web Conf., vol. 111, p. 01018, Aug. 2019, doi: 10.1051/e3sconf/201911101018.

[9] Xu C., Fan C., Zhang Z., and Mao Y. Numerical study of wake and potential interactions in a two-stage centrifugal refrigeration compressor, Eng. Appl. Comput. Fluid Mech., vol. 15, no. 1, pp. 313–327, Jan. 2021, doi: 10.1080/19942060.2021.1875887.

[10] Kawaguchi D., Okada T., and Nakamura Y., Effect of pressure balance between multi-stages on part-load performance of centrifugal compressor for turbo chiller, J. Fluid Sci. Technol., vol. 10, no. 1, pp. JFST0010–JFST0010, 2015, doi: 10.1299/jfst.2015jfst0010.

[11] Shen F., Yu L., Cousins W. T., Sishtla V., and Sharma O. P. Numerical investigation of the flow distortion impact on a refrigeration centrifugal compressor, in Proceedings of the ASME Turbo Expo, 2016, doi: 10.1115/GT2016-57063.

[12] Cousins W. T., Sishtla V., Yu L., and Shen F. Analytical and experimental results of a novel single-stage centrifugal compressor with economizer injection, in Proceedings of the ASME Turbo Expo, 2018, doi: 10.1115/GT2018-76967.

[13] Yi K., Zhao Y., Yu G., Yang Q., Liu G., and Li L. Research on performance of refrigeration centrifugal compressor with gas bearings for water chillers, Energy Reports, vol. 8, pp. 5562–5569, Nov. 2022, doi: 10.1016/j.egyr.2022.04.031.

[14] Liu Y.,. Liu G, Yang Q., Zhao Y., and. Li L, Research on motor cooling process of centrifugal refrigeration compressor with gas bearings, Int. J. Refrig., vol. 145, pp. 68–77, Jan. 2023, doi: 10.1016/j.ijrefrig.2022.09.018.

[15] Yi K., Zhao Y., Liu G., Yang Q., Yu G., and Li L. Performance Evaluation of Centrifugal

Refrigeration Compressor Using R1234yf and R1234ze(E) as Drop-In Replacements for R134a Refrigerant, Energies, vol. 15, no. 7, p. 2552, Mar. 2022, doi: 10.3390/en15072552.

[16] Hung K.-S., Ho K.-Y., Hsiao W.-C., and Kuan Y.-D., The Characteristic of High-Speed Centrifugal Refrigeration Compressor with Different Refrigerants via CFD Simulation, Processes, vol. 10, no. 5, p. 928, May 2022, doi: 10.3390/pr10050928.

[17] Hung K.-S., Hsiao W.-C., Li Y.-C., and Kuan Y.-D. 150USRT Class R-513A Refrigerant Two-Stage Centrifugal Compressor Design Point and Separation Point Flow Field Simulation Analysis, Processes, vol. 11, no. 1, p. 253, Jan. 2023, doi: 10.3390/pr11010253.

[18] Park J., Shin Y., and Chung J. Performance Prediction of Centrifugal Compressor for Drop-In Testing Using Low Global Warming Potential Alternative Refrigerants and Performance Test Codes, Energies, vol. 10, no. 12, p. 2043, Dec. 2017, doi: 10.3390/en10122043.

[19] Teplovye i konstruktivnye raschety kholodilnykh mashin: Ucheb. posobie. [Thermal and structural calculations of refrigerating machines: Textbook. manua.] / Bambushek E. M., Bukharin N. N., Gerasimov E. D., Evstafev V.A., Ilin A.Ia., Koshkin N.N., Noskov A.N., Pekarev V.I., Sakun I.A., Stukalenko A.K., Suetinov V.P., Sysoev V.L., Timofeevskii L.S. ; Pod obshch, red. I. A. Sakuna.. — L.: Mashinostroenie, Leningr. otd-nie, 1987. — 423 p.

[20] Aungier, Ronald H.Centrifugal Compressors: A Strategy for Aerodynamic Design and Analysis, 2000.

[21] Simonov A.M. Issledovanie effektivnosti i optimalnoe proektirovanie vysokonapornykh tsentrobezhnykh kompressornykh stupenei. [Efficiency research and optimal design of high-pressure centrifugal compressor stages] p. 164 – 188. / Proceedings of the scientific school of compressor engineering of SPbGPU. Edited by prof. Galerkin Yu. B. – Publishing house of SPbGPU, St. Petersburg, 2010 - 670 p.

[22] ANSI/AHRI 550/590-2011: Performance Rating of Water-Chilling and Heat Pump Water-Heating Packages Using the Vapor Compression Cycle.

[23] Bukharin N.N., ‘Modelirovanie kharakteristik tsentrobezhnykh kompressorov [Centrifugal compressors characteristics simulation]. — L.: Mashinostroenie, Leningr. otd-nie, 1983.— 214 p.

[24] Span W., Wagner R. Equations of State for Technical Applications. I. Simultaneously Optimized Functional Forms for Nonpolar and Polar Fluids.’, Int. J. Thermophys., no. 24, pp. 1–39, 2003, doi: 10.1023/A:1022390430888.

Сведения об авторах.

Данилишин Алексей Михайлович, инженер, прикрепленное лицо для подготовки диссертации, Университет ИТМО. Область научных интересов: центробежные компрессоры, турбохолодильные машины, турбодетандеры, численное моделирование. E-mail: danilishin_am@mail.ru

Кожухов Юрий Владимирович, к.т.н., доцент, Университет ИТМО. Область научных интересов: компрессорная и холодильная техника, системы транспорта и переработки газа, декарбонизация топливно-энергетического комплекса. E-mail: kozhukhov_yv@mail.ru

Research of the Influence of the Combined Electromagnetic Field on Biogas Output

Zablodskiy M.[1], Klendiy P.[2], Dudar O.[3], Radko I. [1]
[1]National University of Life and Environmental Sciences of Ukraine,
Kyiv, Ukraine
[2] Separated subdivision "Berezhany Agrotechnical Institute" National University of Life and Environmental Sciences of Ukraine,
Berezhany, Ukraine
[3]Separated structural subdivision "Berezhany professional college of National University of Life and Environmental Sciences of Ukraine"
Berezhany, Ukraine

Abstract. The purpose of research is determining the conditions of stimulating effect of the combined influence of constant and variable electromagnetic fields on the substrate and microorganisms in the bioreactor. This goal is achieved by solving the following tasks: development of mathematical model, conducting numerical simulation to determine the distribution of magnetic field in active zones of the stator-bioreactor system; conducting experimental researches during the fermentation of pig's manure with litter from wheat straw in the mesophilic mode of fermentation. One category of bioreactors (control samples) was not exposed to influence of magnetic field, for the other, periodically were made treatment simultaneously with a low-frequency electromagnetic field and constant magnetic field synchronously with the process of mixing the substrate. The most significant results are: an experimental proof of effectiveness of the proposed method of intensification of the biogas output and increasing its quality, high accuracy of mathematical model of distribution the magnetic field in active zones of the stator-bioreactor system; assessment of the levels of consumption of nutrients by microorganisms from the substrate under the influence of the combined magnetic field and without influence of the magnetic field. The significance of obtained results lies in the fact that the proposed approach to intensification of the biogas output provides increase of the level production, the quality of biogas, and cumulative rate of methane output per unit of organic mass in the reactor.
***Keywords*:** biogas, combined electromagnetic field, microorganisms, mesophilic regime, methane, substrate, methanogenesis**.**

DOI: https://doi.org/10.52254/1857-0070.2023.2-58-08
UDC: 621.37:631.95

Studiul influenței câmpului electromagnetic combinat asupra randamentului de biogaz

Zablodskii N.[1]. Klendii P. [2], Dudar O.[3], Dadico I.[1]
[1]Universitatea Națională de Bioresurse și Managementul Naturii din Ucraina, Kiev, Ucraina,
[2]Subdiviziune separată „Institutul Agrotehnic Berezhany" a Universității Naționale de Bioresurse și Managementul Naturii din Ucraina, Berezhany, Ucraina,
[3]Subdiviziune structurală detașată „Colegiul Profesional Berezhany al Universității Naționale de Bioresurse și Managementul Naturii din Ucraina", Berezhany, Ucraina.

Abstract. Scopul studiului este de a determina condițiile pentru acțiunea stimulatoare al impactului combinat al câmpurilor electromagnetice constante și variabile asupra substratului și microorganismelor din bioreactor. Scopul se realizează prin rezolvarea următoarelor probleme: elaborarea unui model matematic, efectuarea simulării numerice pentru determinarea distribuției câmpului magnetic în zonele active ale sistemului stator - bioreactor; efectuarea studiilor experimentale în timpul fermentației gunoiului de porc cu așternut de paie de grâu în modul mezofil de fermentație. O categorie de bioreactoare (probe de control) nu a fost expusă unui câmp magnetic, în timp ce cealaltă categorie a fost tratată periodic simultan cu un câmp electromagnetic de joasă frecvență și un câmp magnetic constant sincron cu procesul de amestecare a substratului. Cele mai semnificative rezultate sunt: eficiența metodei propuse de intensificare a randamentului de biogaz și îmbunătățirea calității acestuia, precizia ridicată a modelului matematic de distribuție a câmpului magnetic în zonele active ale sistemului stator-bioreactor; evaluarea nivelurilor de consum a nutrienților de către microorganisme din substrat sub influența unui câmp magnetic combinat și fără influența unui câmp magnetic. Semnificația rezultatelor

obținute constă în faptul că abordarea propusă pentru intensificarea randamentului biogazului asigură o creștere a nivelului de producție, a calității biogazului și a ratei cumulate a randamentului de metan pe unitatea de masă organică din reactor.
Cuvinte-cheie: biogaz, câmp electromagnetic combinat, microorganisme, regim mezofil, metan, substrat, metanogeneză.

Исследование влияния комбинированного электромагнитного поля на выход биогаза

Заблодский Н.[1]. Клендий П. [2], Дудар О.[3], Радько И.[1]
[1]Национальный университет биоресурсов и природопользования Украины, Киев, Украина
[2]Отделенное подразделение «Бережанский агротехнический институт» Национального университета биоресурсов и природопользования Украины, Бережаны, Украина,
[3]Отделенное структурное подразделение «Бережанский профессиональный колледж Национального университета биоресурсов и природопользования Украины», Бережаны, Украина.

***Аннотация*.** Целью исследования является определение условий стимулирующего действия комбинированного воздействия постоянного и переменного электромагнитных полей на субстрат и микроорганизмы в биореакторе. Поставленная цель достигается путем решения следующих задач: разработки математической модели, проведения численного моделирования по определению распределения магнитного поля в активных зонах системы статор – биореактор; проведения экспериментальных исследований при ферментации навоза свиней с подстилкой из пшеничной соломы в мезофильном режиме сбраживания. Одна категория биореакторов (контрольные образцы) не подвергалась воздействию магнитного поля, для другой - периодически выполняли обработку одновременно низкочастотным электромагнитным полем и постоянным магнитным полем синхронно с процессом перемешивания субстрата. Наиболее существенными результатами являются: экспериментальное доказательство эффективности предложенного способа интенсификации выхода биогаза и повышения его качества, высокой точности математической модели распределения магнитного поля в активных зонах системы статор – биореактор; оценка уровней потребления микроорганизмами питательных веществ из субстрата при воздействии комбинированного магнитного поля и без влияния магнитного поля. Значимость полученных результатов состоит в том, что предложенный подход к интенсификации выхода биогаза обеспечивает повышение уровня производства, качества биогаза и кумулятивной скорости выхода метана на единицу органической массы в реакторе.
Ключевые-слова: биогаз, комбинированное электромагнитное поле, микроорганизмы, мезофильный режим, метан, субстрат, метаногенез.

INTRODUCTION

In connection with completeness of the Earth's minerals and pollution of the environment, humanity has been faced with the question of how to ensure energy production and improve ecology. The solution of this issue is in the use of non-traditional energy sources, in particular, obtaining energy from biomass. The production of biogas solves a multi-vector problem in the national and economic complex, namely: it improves the ecological situation, which allows the processing of waste from the food industry, agriculture, household and drain water treatment; possible production of heat, electricity and cold, as well as highly mineralized organic fertilizer that will allow to improve fertility of soils. The process of biogas production is based on the fermentation of biomass, that is, its decomposition by various groups of bacteria. On the vital activity of bacteria which take part in production of biogas, like most living organisms, significantly affects their environment. To increase the efficiency of biogas installations, the addition of special enzymes, maintenance of the appropriate thermal regime and mixing are used, but the last require significant energy consumption, which increases the cost of such production. Since the widely used methods of intensification of biomethanogenesis have practically exhausted themselves, the question of developing and improving new ones arises [1].

ANALYSIS OF LATEST RESEARCHES AND PUBLICATIONS

Numerous biological researches show that microorganisms are sensitive to constant magnetic fields, electromagnetic and acoustic fields of various frequency ranges[2,3]. These fields, as shown by the results of experiments, can have an inhibitory, stimulating or destructive effect on biological objects. The work [1] shows the application of the magnetic field with the frequency of 50 Hz and an induction of 0.28-12 mT, which is created inductively connected by Helmholtz’s coils. Observations of S.Cerevisiae

for 9 hours showed that their greatest growth by 17% occurs with magnetic induction of 0.5 mT. Researches [4] of impact of the combined electromagnetic field created by pair of Helmholtz's coils on samples of brew show that the level of stimulation can reach 30%. Conducted researches [5] of impact of the constant magnetic field on substrate at thermophilic and mesophilic temperature modes of operation showed that at the intensity of the last 15 mT it is possible to increase the amount of biogas mixture release by 12-14%, in comparing with experiment without using of such field. Conducted experiments of impact of the low-frequency electromagnetic field with an intensity of 3.5 mT on substrate made of pig's manure [6] show that the biogas output increases and its maximum value reaches on the 9-11th day of fermentation, and the pH value stabilizes at the neutral level. Also in [7-9] were studied the aspects of influence on microorganisms by the system with combination of constant and variable fields. It was established that the reaction of cells in this case depends from the spatial orientation of the last, and their perpendicularity provokes the greatest effect [9]. In addition, it was proved in [10] that there is a fundamental difference between the final effect from stimulation by impulse and constant magnetic field, and in some cases the direction of the total vector can have decisive importance for the flow of life processes, and therefore will be determine the intensity of biogas output and the efficiency of process in general.

Magnetic-field effects in the range of 2-10 mT, that are registered for all bacteria regardless of the magnesium-isotope enrichment of the environment, indicate about sensitivity of intracellular processes to weak magnetic fields.

Several physico-chemical mechanisms have been proposed to explain the effects of magnetism in biological systems [11–14]. One of the most likely is enzymatic spin-dependent ion-radical reactions [12–14]. They were for the first time described for enzymatic phosphorylation with the participation of the magnetic isotope ^{25}Mg [12,13]. The detected magnetic- isotope effect (MIE) during the enzymatic synthesis of ATP is explained by the magnetic interaction of the ^{25}Mg nucleus with the unpaired electron spin and induction of the singlet-triplet conversion of the ion-radical pair in the active site of the phosphorylating enzyme. When the probability of direct reaction of ATP synthesis increases, the output of product increases accordingly. Similar MIE were detected in the synthesis of ATP for the magnetic isotopes of zinc ^{67}Zn and calcium ^{43}Ca, as well as in the synthesis of DNA in vitro's experiments [12,13, 15,16].

The joint effect of the constant magnetic field and magnetic isotopes of magnesium and zinc allowed to change the growth and biochemical parameters of E. coli bacteria [17, 18]. Such effects open new opportunities for controlling enzymatic processes and, as a result, the main physiological properties of bacteria. One of such properties of particular interest is the formation of biofilms. Communities of microorganisms united in biofilms are a complex structure that consisting of the microbes themselves and the polymer matrix synthesized by them (proteins, polysaccharides, and nucleic acids). Biofilms protect bacteria from the influence of external physical and chemical factors: antibiotics, ultraviolet radiation, mechanical impact, etc. [19].

The theory of biological magnetosensitivity justifies the sensitivity of intracellular processes to the external magnetic field and to magnetic moments of atomic nuclei of isotopes [14]. The sequence of intracellular biochemical reactions, in which the process involving magnetic isotopes takes place, will lead to the physiological response of the organism available for experimental registration. Thus, the addition of the magnetic isotope of magnesium to the nutrient medium for the growth of E. coli bacteria contributed to increase in growth rate and colony-forming ability [14].

In 1975 R. Blackmore discovered strong natural intracellular nano-sized magnets (biogenic magnetic nanoparticles) in bacteria and their synthesis is carried out by the genetically programmed microorganisms themselves. Bacteria that synthesize chains of biogenic magnetic nanoparticles (BMN) were called magnetotaxis bacteria, of point of view on given possible functional appointment of such natural magnets — taxis, that is, orientation of bacterial movement in the direction of force lines of the geomagnetic field [20].

To date, BMN has been found in archaea [21], which include methanogenic bacteria.

At the same time, it is known that genes of the magnetosomal island of magnetotaxis bacteria are related with the metabolic ways of anaerobic respiration [22].

Own heterogeneity magnetic fields of BMN will significantly affect on the speed of

biochemical reactions, the slowest stage of which is the transport of reactants or reaction of products (diffusion or mixed kinetics) [23, 24, 25].

For magnetotaxis bacteria, depending on the magnitude and duration of application of an external magnetic field, the effects of change in the shape of chain and location of BMN due to the purely mechanical movement of magnetic nanoparticles under the influence of the external magnetic field [26], as well as a significant increase in the number of BMN, change in their shape, size, and location were found as a result of increased expression genes of magnetosomal island during long-term cultivation of magnetotaxis bacteria in the external magnetic field [27]. The duration of application of external magnetic fields is an important parameter during studying their effect on living organisms due to impact on the process of biomineralization of BMN.

1, 2 – measuring tube of biogas output from bioreactors, 3 – teslameter, 4 – laid stators with a substrate, 5 – the substrate is laid, 6 – a moving platform for mixing the substrate of test samples, 7 – container with lime water.

Fig. 1. Experimental installation.

Therefore, the external magnetic field can improve microbial activity and promote biodegradation of organic matter. However, little researches has been conducted due to use of the combined magnetic field to stimulate biogas production in anaerobic fermentation systems.

The purpose of research is experimental determine the stimulating action of the combined impact of constant and variable low-frequency electromagnetic fields on substrate and microorganisms to increase the output of biogas and methane.

RESEARCH METHODS

Determination of the intensity of biogas and biomethane output during liquid anaerobic fermentation (L-AD) of pig's manure mixed with wheat straw under influence of the variable and constant electromagnetic field was carried out on specially designed installation (Fig. 1). For conducting the experiment, containers (mini bioreactors) were taken, which were filled with 200 ml of seeding from the operating bioreactor

and 25 g of pig's manure was added together with the litter made of lignocellulosic raw material, namely wheat straw. Pigs from the private sector were fed with dry food. Three samples of bioreactors were exposed to impact of the low-frequency variable electromagnetic field with the magnetic induction of 3.5 mT and the constant one - 4.5 mT, and the other three similar samples of bioreactors were controls. To create magnetic fields, stators of single-phase electric engines were used, one of which was connected to the variable current source of industrial frequency of reduced voltage of 29 V, and the second one was powered by constant current with voltage of 12 V (Fig. 2). A 43205/1 teslameter was used to measure electromagnetic fields. The operating mode of bioreactors is mesophilic (t=38-40ºC). Before laying, the pH of substrate was measured with a pH 301 device, the initial value pH = 7.6. The fermentation process took place for 21 days, while stirring and treating of three samples with the combined electromagnetic field were carried out periodically (three times a day). The output of biogas was measured by amount of displaced water from the measuring tubes (Fig. 1). For measuring the amount of produced methane , the output from the bioreactors is connected to containers which are filled with lime water (450 ml) for removing carbon dioxide from the formed biogas. At the same time, a corresponding chemical reaction occurs:

$$CO_2 + Ca(OH)_2 \rightarrow CaCO_3 \downarrow + H_2O \qquad (1)$$

Containers with lime water are connected with measuring tubes, filled with water, and by amount of displaced water was determined the output of biomethane.

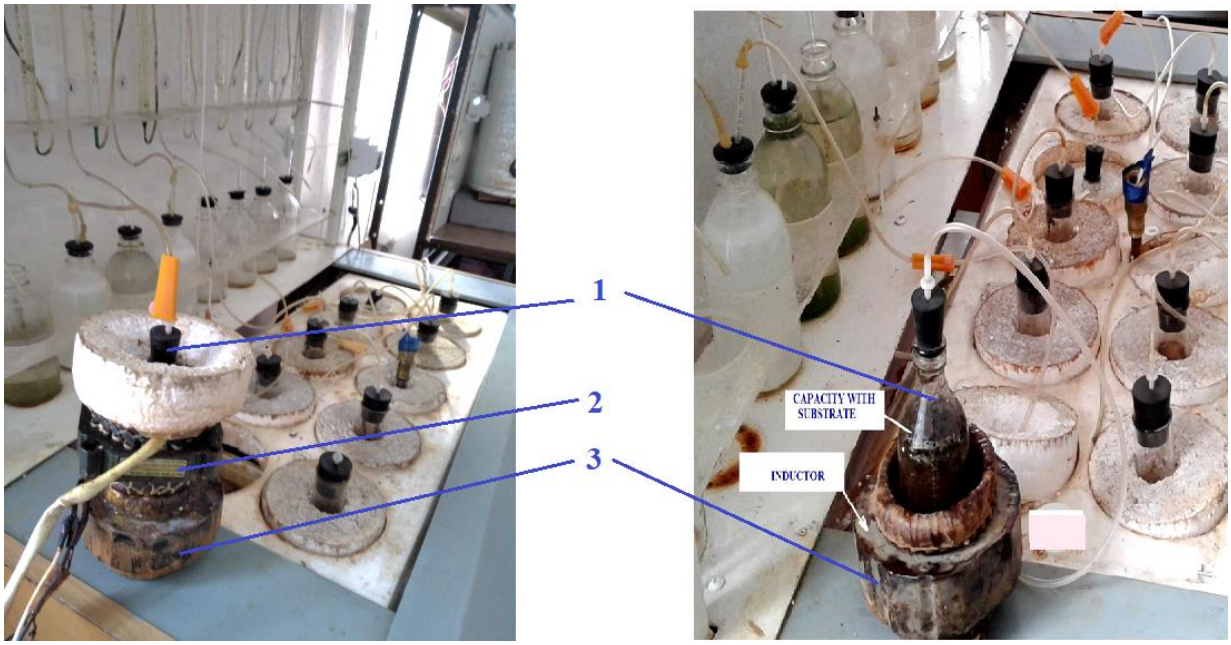

1 – bioreactor, 2- the stator of an electric engine that is powered by a constant current source, 3 – the stator of the electric engine, which is powered by variable current of industrial frequency.

Fig. 2. Bioreactor with devices of electromagnetic influence.

The installation was turned on for creating the combined electromagnetic field (Fig. 2) three times a day for 20 minutes. and at the same time mixing of substrate was carried out.

To determine the consumption of nutrients by microorganisms from the substrate under the influence of the combined magnetic field and without influence, the following experiment was conducted. Digestate was taken from two mini bioreactors, which were used in experiments with and without influence of the combined magnetic field, dried, and then the same weights

were burned to determine the inorganic residue according to the standard method.

RELATIONSHIP OF MAGNETIC AND ELECTRICAL PARAMETERS OF DEVICES THAT CREATE ELECTROMAGNETIC FIELDS

The equation that relating the magnetic induction B and the vector magnetic potential A for constant current is described by the expression:

$$B = \nabla A = \begin{pmatrix} i & j & k \\ \frac{\partial}{\partial x} & \frac{\partial}{\partial y} & \frac{\partial}{\partial z} \\ A_x & A_y & A_z \end{pmatrix} = \\ = i\left(\frac{\partial}{\partial y}A_z - \frac{\partial}{\partial z}A_y\right) - \\ - j\left(\frac{\partial}{\partial x}A_z - \frac{\partial}{\partial z}A_x\right) + \\ + k\left(\frac{\partial}{\partial x}A_y - \frac{\partial}{\partial y}A_x\right) \quad , \qquad (2)$$

The equation that connecting the magnetic field strength H and the current density vector J is described by the expression:

$$\nabla H = \begin{pmatrix} i & j & k \\ \frac{\partial}{\partial x} & \frac{\partial}{\partial y} & \frac{\partial}{\partial z} \\ H_x & H_y & H_z \end{pmatrix} = \\ = i\left(\frac{\partial}{\partial y}H_z - \frac{\partial}{\partial z}H_y\right) - \\ - j\left(\frac{\partial}{\partial x}H_z - \frac{\partial}{\partial z}H_x\right) + \\ + k\left(\frac{\partial}{\partial x}H_y - \frac{\partial}{\partial y}H_x\right) \quad , \qquad (3)$$

Combining expressions (2) and (3), we obtain the Poisson's equation for the vector potential A due to the current density J :

$$\Delta A = \frac{\partial^2}{\partial x^2}A + \frac{\partial^2}{\partial y^2}A + \frac{\partial^2}{\partial z^2}A = J \text{ , } (4)$$

For variable current, after solving the Helmholtz's equation according to expression (2), we obtain the following formula:

$$\left(j\omega\rho - \omega^2\varepsilon\varepsilon_0\right)A + \nabla H = j \text{ , } \qquad (5)$$

where, ω-is the angular frequency;

ρ – specific electrical conductivity of the conductor; ε – dielectric permeability of the substance;

ε_0 – dielectric permeability in vacuum.

Let's transform expression (5) into a compact form of notation that connecting the current density J and the vector magnetic potential A:

$$\left(j\omega\rho - \omega^2\varepsilon\varepsilon_0\right)A + \mu\Delta A = j \text{ , } \quad (6)$$

where μ -is the magnetic permeability.

When working with expression (6), you can use the following form of the equation:

$$\left(j\omega\rho - \omega^2\varepsilon\varepsilon_0\right)A + V(\mu^{-1}VA) = \frac{\rho V}{2\pi r} \text{ ,(7)}$$

where, V -is the voltage, that applied to the coil.

Magnetic energy is calculated according to the expression:

$$W = 2\pi\oint Ardr \text{ , } \qquad (8)$$

For creating an electromagnetic field, stators of the single-phase asynchronous engine were introduced, in the middle of which the container with substrate was placed (Fig. 2). The electromagnetic field at each point of the considered region is determined by the vectors of magnetic induction $\vec{B}$, magnetic field strength $\vec{H}$, electric displacement $\vec{D}$ and electric field strength $\vec{E}$. The mathematical model of a nonlinear magnetic system with distribution of current densities is the system of Maxwell's equations for electromagnetic field vectors in all areas of the engine, which contains: full current law

$$rot\vec{H} = \vec{j} \text{ , } \qquad (9)$$

the law of electromagnetic induction

$$rot\vec{E} = -\frac{d\vec{B}}{dt} \text{ , } \qquad (10)$$

the equation of the continuity of the magnetic field

$$div\vec{B} = 0 \text{ , } \qquad (11)$$

A quasi-stationary field is considered. Displacement currents are neglected.

The system of equations (1) – (11) is supplemented by the equation of the connection between the vectors of induction and magnetic field intensity

$$\vec{B} = \mu\vec{H} \text{ , } \qquad (12)$$

Where $\mu = \mu_0 + \mu_\upsilon$ is the absolute magnetic permeability of the substrate; μ_0 - magnetic

permeability of vacuum; μ_υ - relative magnetic permeability of the substrate.

Using the proposed mathematical model, numerical simulation was carried out in the computer program COMSOL Multiphysics using the finite element method.

RESEARCH RESULTS AND THEIR DISCUSSION

In Fig. 3 and Fig. 4 are shown graphical dependences of the volumes of produced biogas and methane for each day during 21 days of anaerobic fermentation in the mesophilic mode, respectively. The research results show that the output of biogas and methane under the influence of the combined electromagnetic field increases in comparing to the control samples.

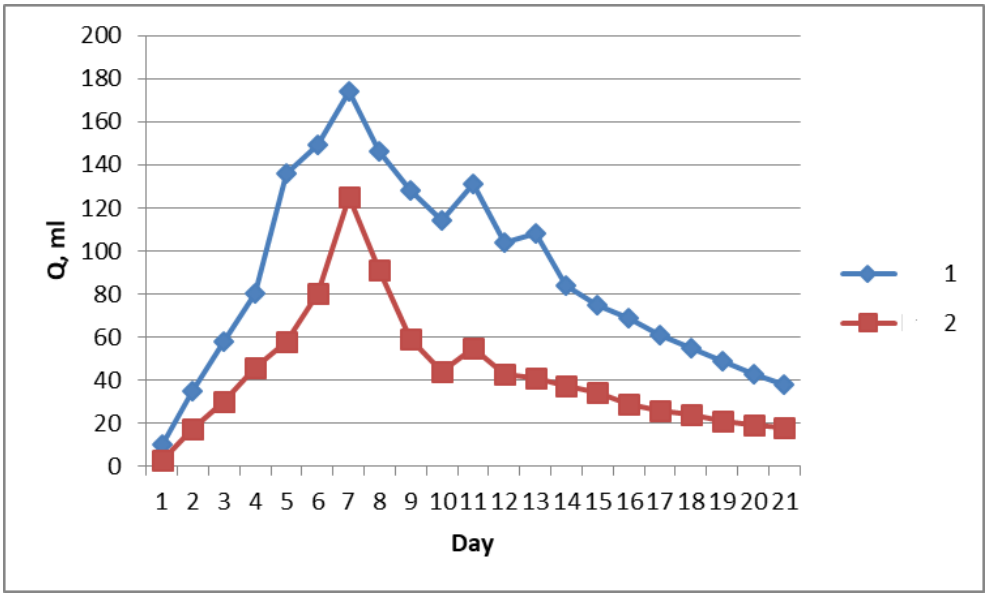

1– when the substrate is exposed by the combined magnetic field, 2-without exposure.

Fig. 3. Biogas output.

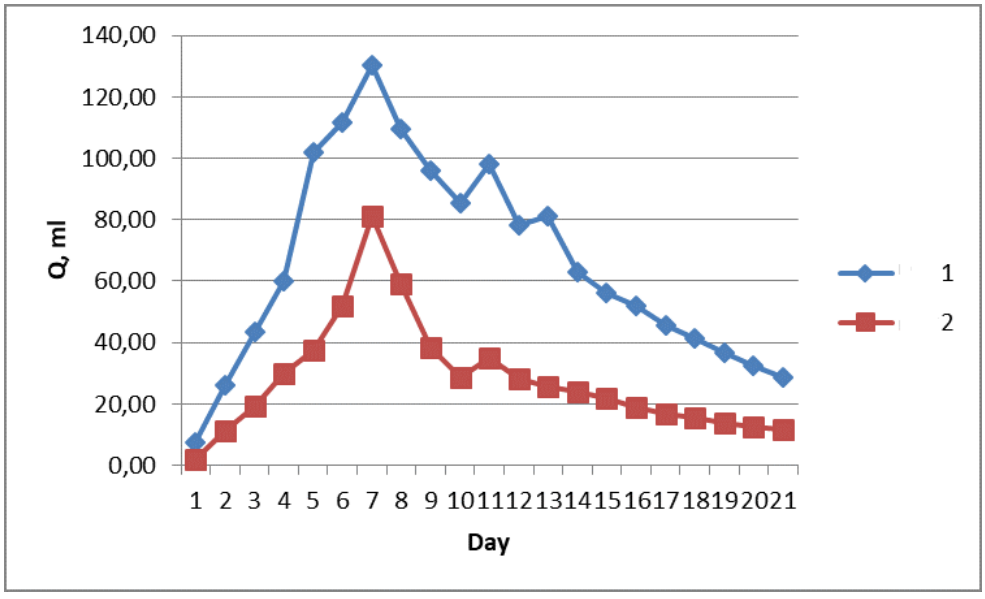

1– when the substrate is exposed by the combined magnetic field, 2– without exposure

Fig. 4. Output of methane.

The highest value of the achieved current rate of CH_4 production (average for repetitions) was: for bioreactors with influence of the combined magnetic field – 1.67 ml/kg/day; for reactors without exposure – 0.93 ml/kg/day. Therefore, the impact of the combined magnetic field increases the current production rate of CH_4 by almost in 1.8 times.

The cumulative specific rate of release of CH_4 from a unit mass of the experimental mixture in the reactor over the entire period of observation for bioreactors under the influence of the combined magnetic field was 2.11 ml/kg/day; for bioreactors without exposure – 0.92 ml/kg/day. The added mass of dry organic matter of the experimental mixture, including the inoculant, was used for calculations.

The average concentration of CH_4 in biogas based on research results is presented in Table 1. Under the influence of the combined magnetic field, is observed the significant (by 10%) increases in the concentration of CH_4 in biogas

.

Table 1

Average concentration of CH_4 in biogas

Conditions of anaerobic fermentation	Average concentration of CH_4 in biogas , %			
	5 day	7 day	10 day	21 day
Without influence of the magnetic field	66.1	64	64.4	65
Under the influence of the combined magnetic field	76,1	74	74	75

The kinetics of biogas and methane production, which is shown in Fig. 3 and Fig. 4, was modeled using linear[28] and exponential equations[29]. The kinetic researches was divided into two rate periods, namely the increasing period and the decreasing period of the methanogenesis rate. In Fig. 5 and Fig. 6 are shown the results of the approximation of methane production rate graphs, respectively, for periods of growth and decline in the rate of methanogenesis.

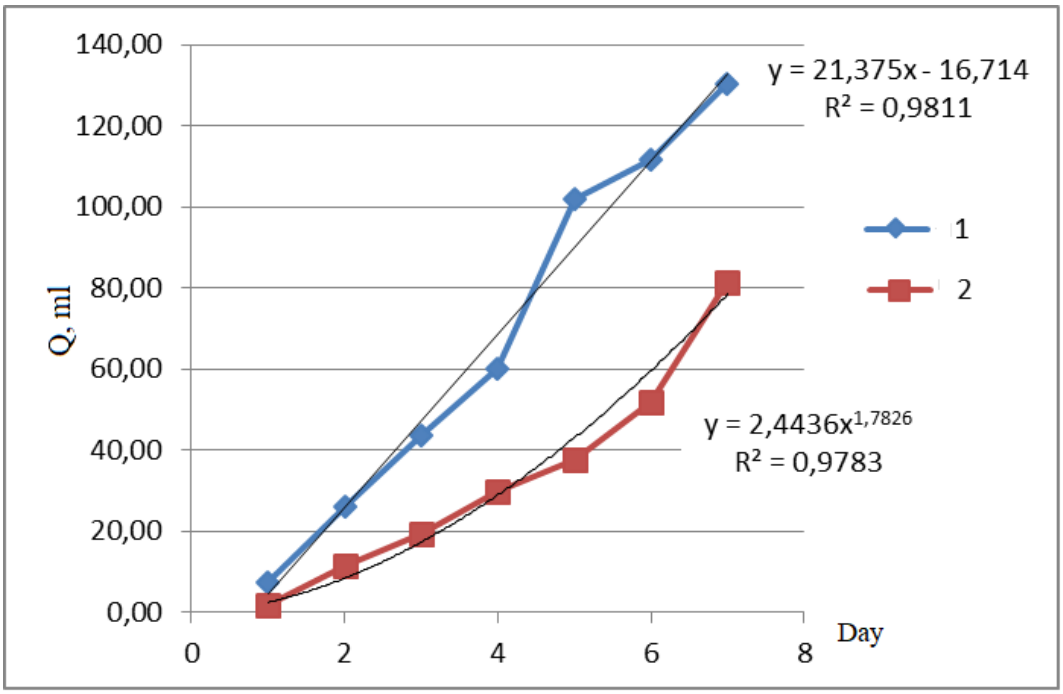

1– when the substrate is exposed by the combined magnetic field, 2– without exposure.

Fig. 5. Approximation equations of periods of growth in the rate of methane production.

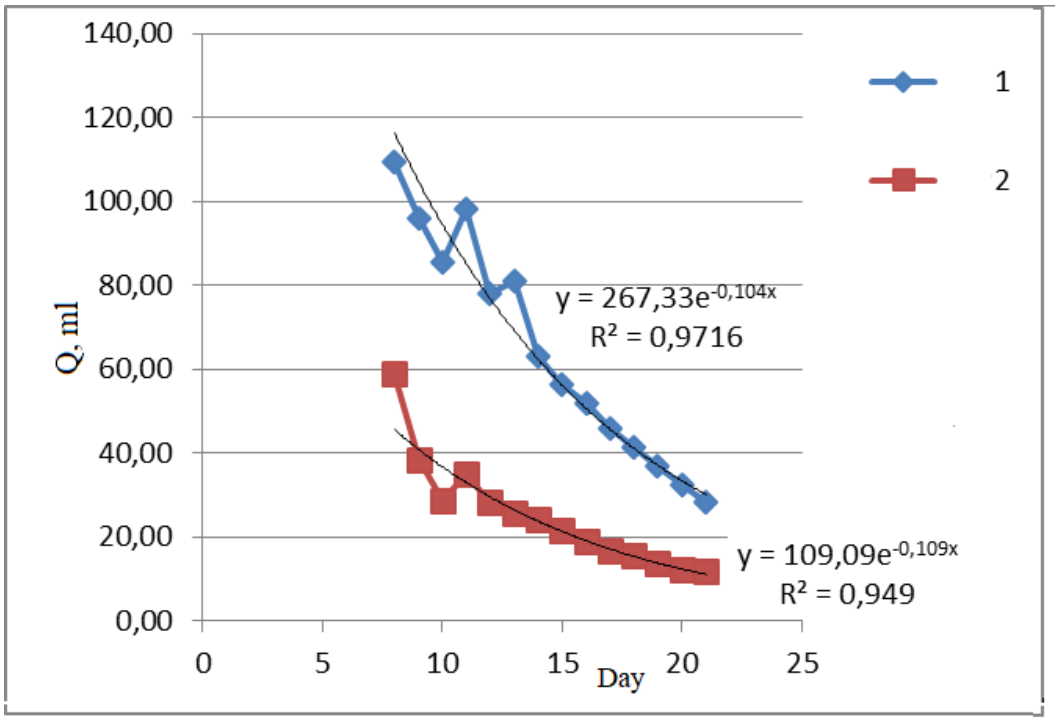

1– when the substrate is exposed by the combined magnetic field, 2– without exposure.

Fig. 6. Approximate equations of the periods of decline in the rate of methane production.

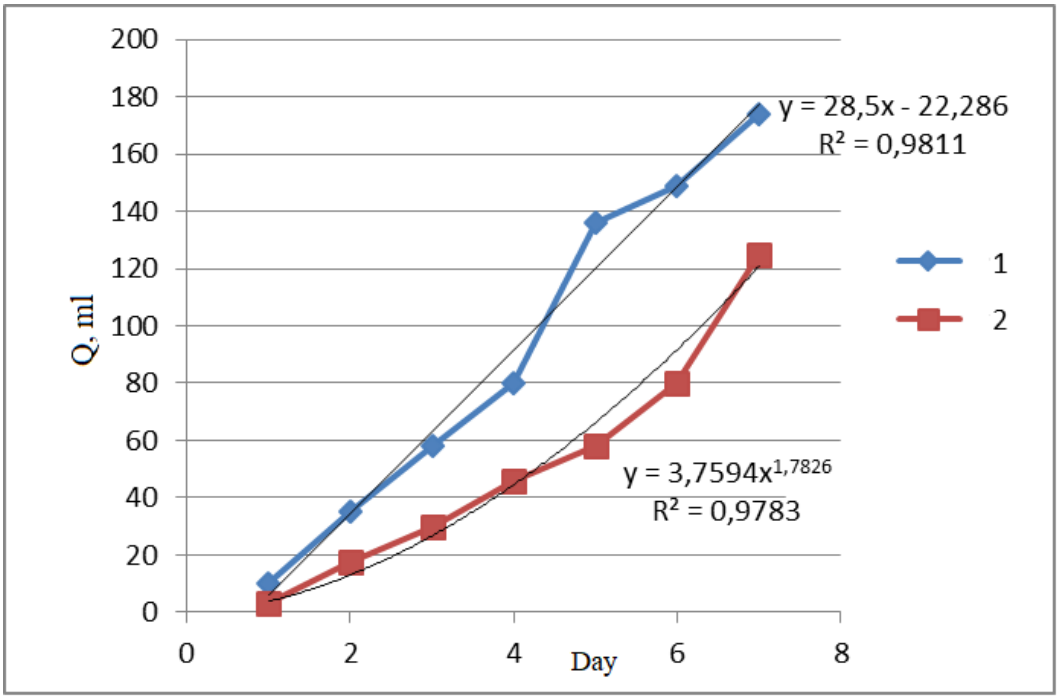

1– when the substrate is exposed by the combined magnetic field, 2– without exposure.

Fig. 7. Approximation equations of periods of growth in rate of biogas production.

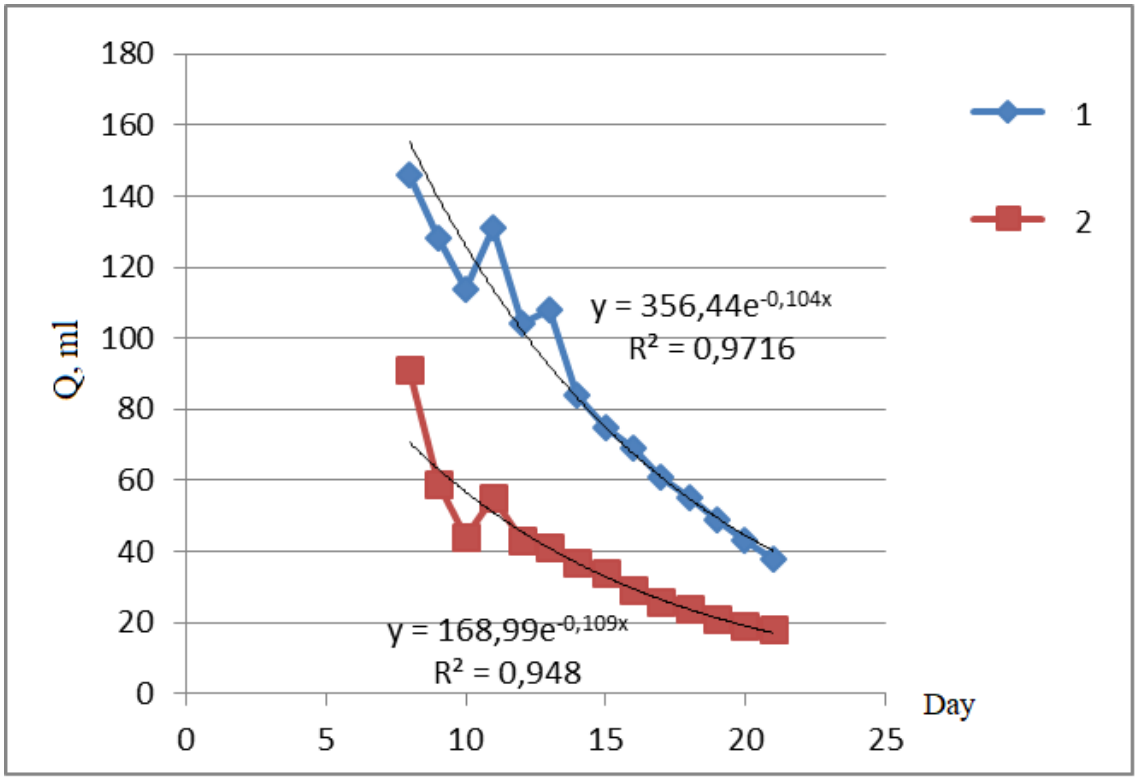

1– when the substrate is exposed by the combined magnetic field, 2– without exposure.

Fig. 8. Approximation equations of periods of decline in rate of biogas production.

With sufficiently high regression coefficient R^2= 0.9783, the generation of biogas and methane during the absence of influence of the combined magnetic field on substrate occurs according to an exponential dependence both during the period of growth and during the period of decrease in the rate of methane production. At the same time, a short lag- phase is observed at the initial stage. This agrees with results obtained in work [30] during recearch of methane production during liquid anaerobic digestion (L-AD) of the mixture of lignocellulosic biomass (wheat straw) with an inoculant. Methane production in this case can be explained by a simple first-order kinetic model.

It is necessary to pay attention to the difference in the nature of the approximation equations of periods of growth in the rate of biogas (methane) production under the influence of the combined magnetic field on substrate and without influence of the magnetic field.

The influence of different magnetic fields on the activity of anaerobic sludge was studied in laboratory reactors that containing two predominant strains - Bacillus sp. and Brevibacillus sp.[31]. A linear dependence of variation of the accumulated volume of methane with the reaction time during the growth period was observed for reactors with action of the magnetic heterogeneous field and, on the contrary, an exponential dependence for reactors without the impact of the magnetic field. The results showed that magnatic heterogeneous field of 0–4 mT most effectively improved the activity of this sludge, and the peak methane generation rate increased by 20.6%. But in our research, significantly higher results were obtained both as for the achieved current and cumulative specific rates of CH_4 production, so and of the level of methane concentration in biogas.

The average concentration of CH_4 in biogas based on research results is presented in Table 1. Under the influence of the combined magnetic field, there is the significant (by 10%) increase in the concentration of CH_4 in biogas.

Table 2

Average concentration of CH_4 in biogas.

Conditions of anaerobic fermentation	Average concentration CH_4 in biogas, %			
	5 day	7 day	10 day	21 day
Without influence of the magnetic field	66.1	64	64.4	65
Under influence of the combined magnetic field	76,1	74	74	75

The effect of increasing the concentration of CH_4 in biogas under the influence of the combined electromagnetic field was also observed in researches [32], in which a solenoid created the magnetic and an electric field at the same time. The average level of magnetic induction (4.1-6.2) mT, which has a positive effect on the process of anaerobic digestion, is also confirmed. According to research [32], the electromagnetic system, such as solenoid, generates both the electric field and the magnetic field, which form significant Lorentz forces in substrate. Therefore, increasing the intensity of the magnetic field above the level of 6.2 mT leads to decrease in productivity of the bioreactor. The effect of the electromagnetic field strengthens the clustering of colloidal particles of substrate and bacterial activity, but duration of this impact also has certain limits, if it is exceeded, depression of the bacterial community can be observed. In our researches, the impact of the combined magnetic field was carried out periodically synchronously with mixing, which ensured mass exchange of the volumes of substrate exposed to the magnetic field and the total exposure time of 60 min/day.

Obviously, there is an optimal exposure time for different substrates. For example, during anaerobic fermentation of municipal drain sludge, the extended time (432 min/day) significantly reduced the output of CH_4, as well as the population of methanogenic bacteria. At the same time, the highest content of methane in biogas (66.1% ± 1.9%) was found in the variant with the influence of the magnetic field of 144 min/day [33].

Since the two bioreactors have the same composition of substrate, as well as the fermenters are in the same temperature regime and mixing regime, the explanation of different rate of the fermentation process and biogas output should be sought in the mechanisms of influence of the magnetic field. According to research [6], the schemes of interaction between molecular and ionic structures of substrate during methane generation during two different processes of processing substrate fractions with methanogenic bacteria can be represented by the following equations:

$$4H_2 + CO_2 \rightarrow CH_4 + 2H_2O$$

$$\Delta G^o = -135kJ / mol.methane, \qquad (13)$$

$$CH_3COOH \rightarrow CH_4 + CO_2$$

$$\Delta G^o = -31kJ / mol.methane, \qquad (14)$$

Specified processes are carried out by two different types of methanogenic bacteria. Mandatory components of community are primary anaerobes of hydrolytic microflora (hydrolyze biopolymers), fermentative microflora (ferment monomer molecules), acetogenic microflora (transform various fermentation products into methanogenesis substrates) and secondary anaerobes - methane-forming archaea. The mechanism of interaction of charged particles (ions), polar molecules and the possibility of the influence of the magnetic field on the kinetics of chemical reactions in substrate is proposed in [6]. . The speed of chemical reactions in substrates and the interaction of charged particles (ions), polar molecules under the influence of the magnetic field increases and is determined by the square of the magnetic induction and the speed of movement of ions [6].

The growth of bacterial mass in the process of methane fermentation is relatively low and, according to [34], less than 5% of the carbon mass is converted into bacterial mass. When evaluating the degree of decomposition of the organic matter of substrate, according to the German standard [35], the total increase in the cell mass of the bacterial consortium at the level of 7% of the mass DOM of t substrate is taken into account. It is obviously that the existing norms should be specified during applying additional stimulating conditions regarding the bacterial consortium.

During conducting the experiment to determine the consumption of nutrients by microorganisms from substrate, the dry digestate was weighed on an electronic scale WPS

110/C/1 (RAGWAG) with 3.692 g of each sample. After incineration, the inorganic residue of each sample was weighed according to the standard method. The sample that was exposed to influence of the combined electromagnetic field weighed 1.221 g, and the sample that was not treated by the magnetic field weighed 0.856 g (Fig. 9).

1–with the influence of the magnetic field, 2– without the influence of the magnetic field

Fig. 9. The process of weighing digestate samples from bioreactors.

During biomass destruction, occurs the decrease of particle's size, which in turn leads to increase in the reaction of surface area. According to simple model of collisions, a chemical reaction between two starting substances can occur only in result of collision of the molecules of these substances. But not every collision leads to the chemical reaction. It is necessary to overcome the certain energy barrier so that the molecules start to react with each other. That is, molecules must have certain minimum activation energy to overcome this barrier

It can be concluded that microorganisms under the influence of the combined electromagnetic field processed more organic material and, accordingly, produced more biogas.

The obtained data regarding output of biogas and methane (Fig. 3 and Fig. 4) show that the maximum output of biogas and methane is observed on the 6-8th day of fermentation. But from the bioreactor, which contained substrate treated with electromagnetic fields, more biogas is released (curve 1) than from the control sample of the bioreactor (curve 2). This can be explained by the fact that under the influence of electromagnetic fields, the metabolism of microorganisms improves, the availability of microorganisms to food and, accordingly, the increase of their colonies. In substrate that is fermented, there is wheat straw, in which, in recalculation on dry matter, the concentration of Fe (with the content DM of 10%) will be 2360 mg/kg [36].The magnetized state of Fe, a food component, as well as the magnetization of biogenic magnetic nanoparticles [20] created conditions for the dynamic direction of microorganisms to nutrients. At the same time, the output of biogas increased by 35%.

The output of methane in the treated substrate increased by 56% in comparing to the untreated sample, that is, it can be assumed that the methane-forming bacteria are magnetotaxis archaea and the electromagnetic field has a stimulating effect. The decrease in the output of biogas and methane after the maximum on the 9th day of fermentation (Fig. 3, Fig. 4) can be explained by the gradual decrease of the food, and the fluctuations on the 10th - 12th days of fermentation - by the decrease of the food and periods of "rest-immobilization".

The results of modeling to determine the distribution of the magnetic field in the active zones of the stator - bioreactor system are presented in Fig. 10 and Fig. 11.

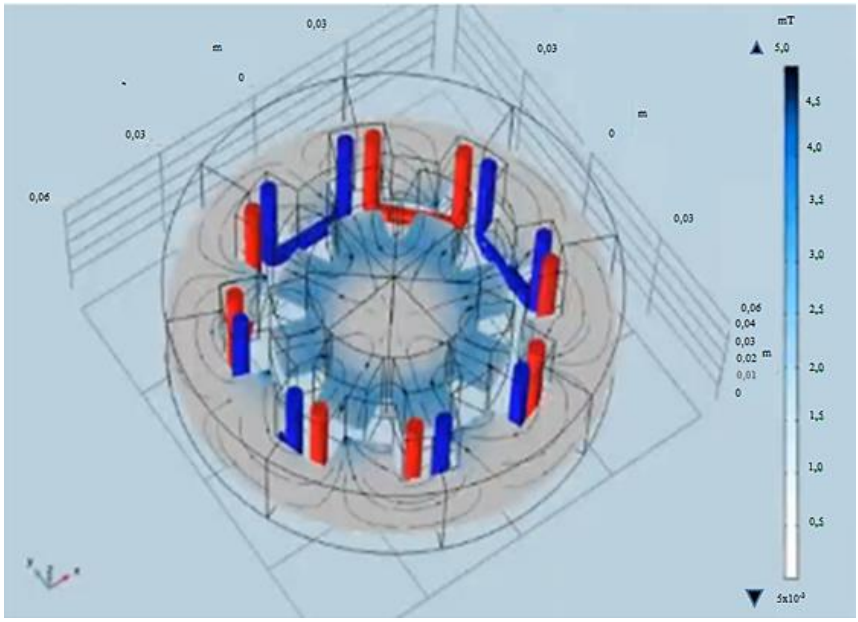

Fig. 10. Magnetic field in the cross-section of the stator of variable current electric engine.

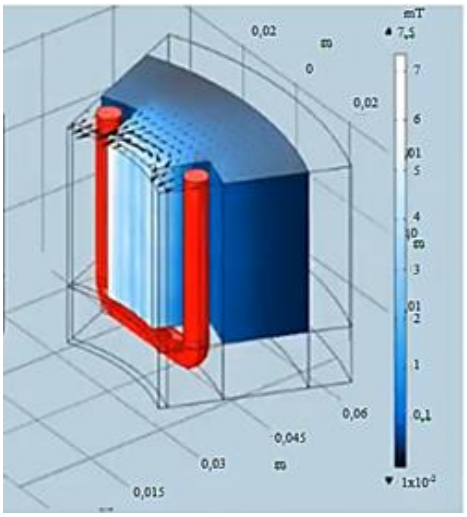

Fig. 11. The magnetic field in the pole zone of the stator fed by direct current.

Since the bioreactor was located in the inner cavity of the stators, the intensity of the magnetic fields throughout the volume of the bioreactor was different, i.e., a heterogeneous magnetic field was created not only in space, but also in time. The level of magnetic induction of the constant magnetic field in substrate near the walls of the bioreactor, directly tangential to the field source, is 5.5 mT, and in the middle, near the center, it is 0.4 mT. The level of magnetic induction of the low-frequency variable electromagnetic field in substrate near the walls of the bioreactor is 3.6 mT, and in the medium, near the center, it

0.5 mT. The difference between the average values of the magnetic induction in substrate, which were measured experimentally and obtained by simulation results, does not exceed 11.5%, which confirms the adequacy of the mathematical model of the stator-bioreactor system.

In comparison with [6], the level of magnetic induction was reduced through the combined impact of constant and variable low-frequency

electromagnetic fields during maintaining the achieved effect of increasing productivity and increasing the concentration of methane in biogas. The stimulatory action of impact of combined electromagnetic field, which reached 30% in researches of brew samples, was confirmed [4]. But in this research, this method was used to stimulate biogas production in anaerobic fermentation systems.

CONCLUSIONS

According to the research results, it was established that the combined impact of constant and variable magnetic fields on methanogenesis not only increases the output of biogas, but also improves its quality, and also allows to reduce the duration of methanogenesis and increase the productivity of the biogas installation.

The highest value of the achieved current rate of CH_4 production (average for repetitions) was: for bioreactors with the influence of the combined magnetic field – 1.67 nl/kg/day; for reactors without influence – 0.93 nl/kg/day. Therefore, the impact of the combined magnetic field increases the current production rate of CH_4 by almost in 1.8 times.

The cumulative specific rate of release of CH_4 from a unit mass of the experimental mixture in the reactor over the entire period of observation for bioreactors under the influence of the combined magnetic field was 2.11 nl/kg/day; for bioreactors without influence – 0.92 nl/kg/day.

The difference in the character of the approximation equations of periods of growth of the rate of biogas (methane) production under the influence of the combined magnetic field on substrate and without the influence of the magnetic field has been established.

According to the results of the experiment with digestate samples, the levels of consumption of nutrients by microorganisms from substrate under the influence of the combined magnetic field and without influence were determined. Microorganisms under the influence of the combined electromagnetic field processed more organic material and, accordingly, produced more biogas.

In this work, for the first time, the real distribution of the combined magnetic field in the working zones of anaerobic fermentation was determined. Using the proposed mathematical model by the finite elements method in the computer program COMSOL Multiphysics, numerical simulation was carried out to determine the level of induction of the magnetic field and its distribution in the system of the source of the magnetic field - the bioreactor . By volume of the bioreactor a non-uniform magnetic field is created not only in space but also in time with an intensity of no more than 5.5 mT.

REFERENCES

[1] Regarding to impact of magnetic fields on microorganisms involved in biomethanogenesis Y.G. Kachan, V.L. Kovalenko, O.I. Lapikova Renewable energy. [Shchodo vplyvu mahnitnykh poliv na zadiiani v biometanohenezi mikroorhanizmy Yu.H.Kachan, V.L.Kovalenko, O.I.Lapikova Vidnovliuvana enerhetyka]. 2017. №. 1P 87-92

[2] Alagöz, B. A., Yenigün, O., & Erdinçler, A. (2018). Ultrasound assisted biogas production from co-digestion of wastewater sludges and agricultural wastes: Comparison with microwave pre-treatment. *Ultrasonics Sonochemistry*, *40*, 193-200.

[3] Research of influence of electromagnetic, constant magnetic and acoustic fields on microorganisms Klap Y. A., Yaremkevich O. S., Chervetsova V. G., Zayarnyuk N. L., Novikov V. P., 2016 National University “Lviv Polytechnic” , B 846 Chemistry, technology of substances and their application. [Doslidzhennia vplyvu elektromahnitnykh, postiinykh mahnitnykh ta akustychnykh poliv na mikroorhanizmy Klap Ya. A., Yaremkevych O. S., Chervetsova V. H., Zaiarniuk N. L., Novikov V. P., 2016Natsionalnyi universytet “Lvivska politekhnika”,V 846 Khimiia tekhnolohiia rechovyn ta yikh zastosuvannia.] P. 168-173

[4] Perspectives ways of intensification of fermentation processes in biogas installations Ryzhkov A.O., Sydorenko A.O. Works of the Tavri State Agrotechnological University. - Issue 10. V 4 - Melitopol: TDATU. [Perspektyvni shliakhy intensyfikatsii fermentatsiinykh protsesiv u biohazovykh ustanovkakh Ryzhkov A.O., Sydorenko A.O. Pratsi Tavriiskyi derzhavnyi ahrotekhnolohichnyi universytet. - Vyp. 10. T.4 - Melitopol: TDATU], 2010. P.120-123

[5] Intensification of biogas release using magnetic and electromagnetic fields V.L. Kovalenko, E.V. Kuznetsova, V.V. Kuznetsov National TU "Dniprovska Polytechnic" MINING ELECTROMECHANICS and AUTOMATICS Energy saving and energy

efficiency. [Intensyfikatsiia vydilennia biohazu zastosuvanniam mahnitnykh ta elektromahnitnykh poliv V.L. Kovalenko, Ye.V. Kuznietsova, V.V. Kuznetsov Natsionalnyi TU «Dniprovska politekhnika» HIRNYChA ELEKTROMEKhANIKA ta AVTOMATYKA Enerhozberezhennia ta enerhoefektyvnist] №. 102 2019 P 84-90

[6] Electrochemical Characteristics of the Substrate based on Animal Excrement during Methanogenesis with the Influence of a Magnetic Field Zablodskiy, M., Kozyrskyi, V., Zhyltsov, A., Klendiy, P., Klendiy, G. 2020 IEEE 40th International Conference on Electronics and Nanotechnology, ELNANO 2020 - Proceedings, 2020, pp. 530–535, 9088763 (in Ukraine)

[7] Blackman, C.; Benane, S.G.; House, D.E.; Elliott, D.J. Importance of alignment between local DC magnetic field and an oscillating magnetic field in response to brain tissue in vitro and in vivo. Bioelectromagnetics 1990, 11, 159–167.

[8] Reese, J.; Frazier, M.E.; Morris, J.E.; Buschbom, R.L. Evaluation of changes in diatom mobility after exposure to 16 Hz electromagnetic fields. Bioelectromagnetics 1991, 12, 21–25.

[9] Blackman, C.; Blanchard, J.P.; Benane, S.G.; House, D.E. Effect of AC and DC magnetic field orientation on nerve cells. Biochem. Biophys. Res. Commun. 1996, 220, 807–811.

[10] Pilla, A.A.; Kaufman, J.J.; Ryaby, J.T. Electrochemical kinetics at the cell membrane: A physicochemical link for electromagnetic bioeffects. In Mechanistic Approaches to Interaction of Electric and Electromagnetic Fields with Living Systems; Blank, M, Findl, E., Ed.; 1987; pp. 39–61.

[11] Binhi V.N. Magnetobiology Underlying Physical Problems. Tokyo: Acad. Press, 2009. P. 473.

[12] Buchachenko A. // Bioelectromagnetics. 2016. V. 37. P. 1–13.

[13] Buchachenko A. Magneto-Biology and Medicine. N.Y.: Nova Sci. Publ., 2014. 144 p.

[14] Magnetic Fields and Magnetic Isotope 25Mg Effects on Biofilms Formation by Bacteria E. coli. U. G. Letuta, T. A. Tikhonova Dokl Biochem Biophys. 2019 May; 484(1): 85–87. Published online 2019 Apr 22. doi: 10.1134/S160767291901023X

[15] Buchachenko A.L., Chekhonin V.P., Orlov A.P., Kuznetsov D.A. // Int. J. Mol. Med. Adv. Sci. 2010. V. 6. P. 34–37.

[16] Buchachenko A.L., Orlov A.P., Kuznetsov D.A., Breslavskaya N.N. // Nucl. Acids Res. 2013. V. 41. P. 8300–8307.

[17] Letuta U.G., Berdinskiy V.L. // Bioelectromagnetics. 2017. V. 38. № 8. P. 581–591.

[18] Letuta U.G., Shailyna D.M. // DAN 2018. V. 479. №. 5. P. 585–588.

[19] Zhou G., Li L., Shi Q., Ouyang Y., Chen Y., Hu Can W. // J. Microbiol. 2014. V. 60. P. 5–14.

[20] Biomagnetism and biogenic magnetic nanoparticles O. Y. Gorobets. M. NAS of Ukraine. Biomahnetyzm i biohenni mahnitni nanochastynky Horobets O.Iu. Visn. NAN Ukrainy, 2015, №. 7 P 53-64

[21] Vainshtein M., Suzina N., Kudryashova E., Ariskina E. New magnet-sensitive structures in bacterial and archaeal cells. Biology of the Cell. 2002. 94: 29—35.

[22] Nakazawa H., Arakaki A., Narita-Yamada S. Whole genome sequence of Desulfovibrio magneticus strain RS-1 revealed common gene clusters in magnetotactic bacteria. Genome Res. 2009. 19: 1801—08.

[23] Gorobets O.Yu., Gorobets Yu.I., Bondar I.A. Quasi-stationary heterogeneous states of electrolyte at electrodeposition and etching process in a gradient magnetic field of a magnetized ferromagnetic ball. J. Magn. Magn. Mater. 2013. 330: 76—80.

[24] Gorobets O.Yu., Gorobets Yu.I., Rospotniuk V.P. Movement of electrolyte at metal etching and deposition under a non-uniform steady magnetic field. Magnetohydrodynamics. 2014. 50(3): 317—32.

[25] Gorobets O.Yu., Gorobets Yu.I., Rospotniuk V.P., Legenkiy Yu.A. Electric cell voltage at the etching and deposition of metals under an inhomogeneous constant magnetic field. Condensed Matter Physics. 2014. 17: 1—18.

[26] Kornig A., Dong J., Bennet M., Widdrat M., Andert J., Muller F.D., Schuler D., Klumpp S., Faivre D. Probing the Mechanical Properties of Magnetosome Chains in Living Magnetotactic Bacteria. Nano Letters. 2014. 14: 4653—59.

[27] Wang X., Liang L. Effects of Static Magnetic Field on Magnetosome Formation and Expression of mamA, mms13, mms6 and magA in Magnetospirillum magneticum AMB-1. Bioelectromagnetics. 2009. 30: 313—21.

[28] Ghatak, M. D., & Mahanta, P. (2014). Comparison of kinetic models for biogas production rate from saw dust. Carbon, 63, 35.

[29] Lo, H. M., Kurniawan, T. A., Sillanpää, M. E. T., Pai, T. Y., Chiang, C. F., Chao, K. P., Liu M. H., Chuang S. H., Banks C. J., Wang S. C., Lin K. C., Lin C. Y., Liu W. F., Cheng P. H., Chen C. K., Chiu H. Y., Wu H. Y.

(2010). Modeling biogas production from organic fraction of MSW co-digested with MSWI ashes in anaerobic bioreactors. Bioresource technology, 101(16), 6329-6335.

[30] Brown, D., Shi, J., & Li, Y. (2012). Comparison of solid-state to liquid anaerobic digestion of lignocellulosic feedstocks for biogas production. Bioresource technology, 124, 379-386.

[31] Xu, Y. B., Duan, X. J., Yan, J. N., Du, Y. Y., & Sun, S. Y. (2009). Influence of magnetic field on activity of given anaerobic sludge. Biodegradation, 20(6), 875.

[32] Madondo, N. I., Kweinor Tetteh, E., Rathilal, S., & Bakare, B. F. (2022). Effect of an electromagnetic field on anaerobic digestion: Comparing an electromagnetic system (ES), a microbial electrolysis system (MEC), and a control with No external force. Molecules, 27(11), 3372.

[33] Zieliński, M., Dębowski, M., & Kazimierowicz, J. (2021). The Effect of Static Magnetic Field on Methanogenesis in the Anaerobic Digestion of Municipal Sewage Sludge. Energies, 14(3), 590.

[34] Krich, K., Augenstein, D., Batmale, J. P., Benemann, J., Rutledge, B., & Salour, D. (2005). Biomethane from dairy waste. Report. Western United Dairymen. 74. VDI 4630:2006-04 “Fermentation of organic materials. Characterisation of the substrate, sampling, collection of material data, fermentation tests” (2006) / Verein Deutscher Ingenieure, Düsseldorf. – 92 p.

[35] VDI 4630:2006-04 “Fermentation of organic materials. Characterisation of the substrate, sampling, collection of material data, fermentation tests” (2006) / Verein Deutscher Ingenieure, Düsseldorf. – 92 p.

[36] Geletuha H.G. Scientific and technical principles of energy production from biological types of fuels: Dissertation for obtaining a PhD. Doctor of Science: 05.14.08. Kyiv.[Heletukha H.H. Naukovo-tekhnichni zasady vyrobnytstva enerhii z biolohichnykh vydiv palyva: Dysertatsiia na zdobuttia n.s. d.t.n].: 05.14.08. Kyiv, 2021.332p.

Information about authors.

Zablodskiy Mykola, professor of the department of electrical engineering, electromechanics and electrotechnologies, National university of life and environmental sciences of Ukraine, doctor of technical sciences, scientific interest is technologies conversion of biomass into high-quality bio-gas with a shortened fermentation period under the influence of electromagnetic field.
E-mail: zablodskiynn@gmail.com

Dudar Oksana, teacher of the cycle committee of special electrical engineering disciplines, SSS “Berezhany professional college of National university of life and environmental sciences of Ukraine”, scientific interest is renewable sources of energy.
E-mail: oksana-dydar@ukr.net

Klendiy Petro, associate professor of the department of power engineering and automation,SS "Berezhany agrotechnical institute" National university of life and environmental sciences of Ukraine, candidate of technical sciences, scientific interest is renewable sources of energy
E-mail: pklendii@gmail.com

Radko Ivan, associate professor of the department electrical engineering, electromechanics and electrotechnologies,
National university of life and environmental sciences of Ukraine, candidate of technical sciences, scientific interest is
development and research of properties of new composite contact materials
E-mail: ivan_radko@ukr.ne

Bivalent Carbon Dioxide Heat Pump for Heating Multi-Storey Buildings

Sit M.L., Juravleov A.A., Tirsu M.S., Timchenko D.V., Lupu M.L., Daud V.P.

Technical University of Moldova, Institute of Power Engineering,
Kishinau, Republic of Moldova

Abstract. The aim of the work is to analyze the operation of a hybrid heat pump that simultaneously uses the heat of the return network water and outdoor air for heating multi-storey buildings. To achieve this goal, the following tasks are solved: the influence of influences on the temperature of the return network water, air temperature and their compensation on the operation of the product is considered, intermediate circuits at the evaporator and gas cooler are considered for transferring a variable heat load to the heat pump and from the heat pump. The most significant results are the hydraulic-aerodynamic scheme of the heat pump, the schemes of the intermediate circuits before the evaporator and the gas cooler. The significance of the results obtained lies in the establishment of such technical solutions for the CHP - heat pumps system, which allow saving gas consumption at the CHP, the cost of heat consumers to pay bills. The use of a working fluid cooler before the gas cooler of the heat pump to control the temperature of the direct network water of the heating system of the building allows you to select such a compressor pressure at which the amount of heat given off by the heat pump to the building will correspond to the temperature curve. In this case, it is desirable to install an air-to-refrigerant heat exchanger after the compressor before the gas cooler. It has been established that a PI controller can be used to control the temperature at the outlet of the gas cooler through the inlet air channel.of various parameters, including solar radiation, ambient temperature, compressor speed and initial water temperature, have been simulated and analyzed on the thermal performance of the system.
Keywords: heat exchanger, variable heat transfer surface, control system, mathematic model, heat pump.

DOI: https://doi.org/10.52254/1857-0070.2023.2-58-09
UDC: 697.34; 621.577.42

Pompă de căldură bivalentă cu dioxid de carbon pentru încălzirea clădirilor cu mai multe etaje

Șit M.L., Juravliov A.A., Tîrșu M.S., Lupu M.L., Timcenko D.V., Daud V.P.
Institutul de Energetică al UTM, Republica Moldova

Rezumat. Scopul lucrării este de a analiza funcționarea pompei de căldură hibride care utilizează simultan căldura apei rețelei de retur și aerul exterior pentru încălzirea clădirilor cu mai multe etaje. Pentru atingerea acestui scop, se rezolvă următoarele probleme: se ia în considerare impactul influenței temparaturii apei rețelei de retur, temperaturii aerului și compensarea acestor influențe asupra funcționării produsului, se ia în considerare circuitul intermediar al evaporatorului și răcitorul de gaz pentru transfer, sarcină termică variabilă a pompei de căldură și de la pompa de căldură. Cele mai semnificative rezultate sunt schema hidraulico-aerodinamică a pompei de căldură, schemele circuitelor intermediare înainte de evaporator și răcitorul de gaz. Semnificația rezultatelor obținute constă în stabilirea unor astfel de soluții tehnice pentru sistemul CHP-Pompe de căldură, care să permită economisirea consumului de gaz la CET și a costului căldurii inclus în facturile de a plată petnru consumatori. Utilizarea unui răcitor de fluid de lucru in fața răcitorului de gaz al pompei de căldură pentru a controla temperatura apei din rețeaua directă a sistemului de încălzire a clădirii vă permite selectarea unei astfel de presiuni a compresorului la care cantitatea de căldură produsă de pompă căldură transmisă clădirii va corespunde curbei de temperatură. În acest caz, este de dorit să fie instalat un schimbător de căldură aer-refrigerant după compresor in fața răcitorului de gaz. Aerul încălzit în acest schimbător de căldură trebuie utilizat pentru a încălzi aerul înainte de evaporatizatorul al pompei de căldură. S-a stabilit că un regulator PI poate fi utilizat pentru a controla temperatura la ieșirea răcitorului de gaz prin canalul de admisie a aerului.
Cuvinte-cheie: pompă de căldură, schimbător de căldură, suprafață variabilă a schimbului de căldură, sistem de control, model matematic.

Бивалентный тепловой насос на диоксиде углерода для отопления многоэтажных зданий

Шит М.Л., Журавлев А.А., Тыршу М.С., Лупу М.Л., Тимченко Д.В., Дауд В.П.
Технический Университет Молдовы, Институт энергетики, Кишинев, Республика Молдова

Аннотация. Целью работы является анализ работы гибридного теплового насоса, использующего одновременно теплоту обратной сетевой воды и наружного воздуха для отопления многоэтажных зданий. Для достижения поставленной цели решаются следующие задачи: рассматривается влияние воздействий по температуре обратной сетевой воды, температуре воздуха и их компенсация на работу изделия, рассматриваются промежуточные контуры у испарителя и газоохладителя для передачи переменной тепловой нагрузки к тепловому насосу и от теплового насоса. Наиболее существенными результатами являются гидравлическо-аэродинамическая схема теплового насоса, схемы промежуточных контуров перед испарителем и газоохладителем. Значимость полученных результатов состоит в установлении таких технических решений для системы «ТЭЦ-тепловые насосы», которые позволяют экономить расход газа на ТЭЦ, затраты у потребителей теплоты на оплату счетов. Использование охладителя рабочего тела перед газоохладителем теплового насоса для регулирования температуры прямой сетевой воды системы отопления здания позволяет выбрать такое давление компрессора, при котором количество теплоты, отдаваемое тепловым насосом зданию будет соответствовать температурному графику. При этом желательна установка теплообменника «воздух-хладагент» после компрессора перед газоохладителем. Воздух подогретый в этом теплообменнике должен быть использован для подогрева воздуха перед испарителем теплового насоса. Установлено, что для управления температурой на выходе газоохладителя по каналу входного воздуха может быть использован ПИ-регулятор. Результаты моделирования показали, что САУ отрабатывает скачкообразные возмущения по входному сигналу с апериодическим процессом, а возмущения по температуре хладагента на входе газоохладителя с однократным перерегулированием. Разработан алгоритм расчета необходимого расхода воздуха при его заданной температуре для обеспечения доставки заданной тепловой мощности к испарителю теплового насоса для получения заданной тепловой мощности на газоохладителе.

Ключевые слова: теплообменник, переменная площадь поверхности теплообмена, математическая модель, тепловой насос.

ВВЕДЕНИЕ. Работа относится к области применения бивалентных (гибридных) тепловых насосов в системах теплоснабжения с ТЭЦ.

Состояние систем теплоснабжения в Республике Молдова.

Система теплоснабжения в крупных городах построена на базе ТЭЦ и использует, в основном, качественный закон регулирования теплового режима отапливаемых помещений. На автоматизированных тепловых пунктах отдельных зданий используются количественно-качественные законы регулирования теплового режима.

В небольших городах Республики Молдова отопление производится от котельных.

По поисковому запросу в google.com под названием *«modern heat pumps for district heating»* приведено 41 100 000 ссылок, что свидетельствует об огромном интересе к этой тематике. В Европейском Союзе предлагается ряд технических решений по использования ТН для систем теплоснабжения. Так, Ommen [24] предложил систему теплоснабжения, где тепловой насос «воздух-вода» *подогревает обратную сетевую воду* в трубопроводе обратной сетевой воды системы теплоснабжения. Предполагается, что тепловой насос получает электроэнергию от возобновляемых источников энергии. Источником теплоты для потребителей являются или ТЭЦ, или котельные. Авторами [22] было предложено использовать тепловые насосы для выработки теплоты и ТЭЦ для выработки электроэнергии для тепловых насосов. Целью работы являлось минимизация числа пусков тепловых насосов. Европейские директивы по энергоэффективности зданий продвигают высокоэффективные альтернативные системы, такие как: а) децентрализованные системы энергоснабжения, использующие энергию из возобновляемых источников энергии, б) комбинированное производство тепла и электроэнергии – когенерация, с) централизованное отопление или охлаждение, особенно если оно полностью или частично использует энергию из возобновляемых источников энергии, г) использование энергии окружающей среды с помощью тепловых насосов, насколько это технически, функционально и экономически целесообразно [3, 4, 5]. В [20] приведен обширный обзор по применению ТН для

систем теплоснабжения. Так, в нем отмечается, что в г. Сараево планируется установка в квартальных тепловых сетях тепловых насосов, использующих теплоту сточных вод. В известных авторам системах теплоснабжения с ТН и ТЭЦ, отсутствуют системы, которые используют *одновременно* теплоту ОСВ и теплоту воздуха в тепловом насосе. В данной работе рассмотрены:

- схема ТНУ, которое работает с качественно-количественным законом управления;
- работа испарителя при предлагаемых схемах, ввод второго газоохладителя типа «воздух-хладагент»;
- схема подачи воздуха через ТНУ;
- компенсация расходом воздуха отклонения температуры обратной сетевой воды от заданного значения;
- статическая и динамическая модель ТН в предлагаемой системе.

Целью исследования является разработка и обоснование структуры гибридного ТН в котором используется воздух и обратная сетевая вода, в качестве источников низкопотенциальной теплоты для испарителя ТН, предназначенного для отопления многоэтажного здания, и САУ этого ТН. Для реализации поставленной цели были решены следующие задачи: установление методики выбора оптимального давления газоохладителя в зависимости от давления испарителя [12], установление связи между давлением в испарителе и температурой антифриза в испарителе при заданном уровне теплового агента в испарителе и при заданном (или меняющемся расходе теплового агента через испаритель). Использование охладителя рабочего тела перед газоохладителем теплового насоса для регулирования температуры прямой сетевой воды системы отопления здания позволяет выбрать такое давление компрессора, при котором количество теплоты, отдаваемое тепловым насосом зданию будет соответствовать температурному графику. При этом желательна установка теплообменника «воздух-хладагент» после компрессора перед газоохладителем. Воздух подогретый в этом теплообменнике должен быть использован для подогрева воздуха перед испарителем теплового насоса. На рис.1 приведено техническое решение по передаче теплоты испарителю ТН при различных температурах наружного воздуха с использованием двух теплообменников – теплообменника отбора теплоты от трубопровода ОСВ и испарителя ТН.

На рис. 2 приведена схема встраивания теплового насоса в систему теплоснабжения здания. На рис.3 приведено техническое решение по отдаче теплоты зданию газоохладителем ТН с использованием теплового четырехполюсника – промежуточного контура, включающего в себя газоохладитель и систему отопления здания.

МЕТОДЫ, РЕЗУЛЬТАТЫ И ОБСУЖДЕНИЕ

Данная работа базируется на нашей работе, опубликованной в 2022 в этом же журнале и конкретизирует ряд вопросов, связанных с выполнением конструкции испарителя теплового насоса, газоохладителя теплового насоса и теплообменника отдачи теплоты от обратного трубопровода.

Для управления мощностью испарителя используется регулирование расхода воздуха, проходящего через теплообменник съема теплоты с трубопровода ОСВ, регулирование температуры воздуха, подаваемого на испаритель, а также площадь поверхности теплообмена теплообменников, входящих в промежуточный контур – тепловой четырехполюсник. Отметим, что отбор теплоты от ОСВ к испарителю необходимо производить только в случае, если при этом можно обеспечить равенство или гарантированное превышение тепловой мощности воздуха над заданной мощностью испарителя. Уравнение (1), связывающее расход воздуха через теплообменник и мощность снимаемой теплоты с трубопровода обратной сетевой воды и мощностью испарителя имеет вид:

$$G_{AER} = m_{RW} \cdot c_{RW} \cdot \left(t_{IN} - t_{OUT}\right) / \ldots \\ \left(c_{AER}\left(t_{AER\_OUT} - t_{AER\_IN}\right)\right). \quad (1)$$

$$m_H \cdot G_H \cdot \left(h_{OUT}^{EV} - h_{IN}^{EV}\right) = \ldots \\ \ldots G_{AER} c_{AER}\left(t_{AER\_OUT}^{RW} - t_{AER\_IN}^{RW}\right). \quad (2)$$

В уравнении (1) G_{AER} – расход воздуха через теплообменник съема теплоты с трубопровода ОСВ (ТОСВ), c_{AER} – теплоемкость воздуха,

t_{AER_OUT} – температура воздуха после ТОСВ, t_{AER_IN} – температура наружного воздуха, m_{RW} – массовый расход ОСВ через ТОСВ, c_{RW} – теплоемкость воды, t_{IN}, t_{OUT} – теплоемкость воды перед и после ТОСВ, соответственно. Расход воды в промежуточном контуре, G_{WI}, вычисляем из уравнения теплового баланса для вторичной цепи теплообменника SC теплового четырехполюсника (рис.1):

$$G_{AER} \cdot c_{AER} \cdot \left(t_{AER\_OUT} - t_{AER\_SC\_OUT}\right) = ... \\ ...G_{CI} \cdot c_{CI} \cdot \left(t_{W\_IN\_SC} - t_{W\_OUT\_SC}\right) = ... \\ ...G_{CI} \cdot c_{CI} \cdot \Delta t_{EV} \quad (3)$$

$t_{W\_IN\_SC}, t_{W\_OUT\_SC}$ – температура воды на входе и выходе вторичной цепи теплообменника SC, соответственно, G_{CI} – массовый расход воды в промежуточном контуре, Δt_{EV} – перепад температур воды на испарителе.

Из уравнений (2) и (3) можно определить расход воздуха на обдув испарителя с целью передачи через тепловой четырехполюсник заданной тепловой мощности испарителю теплового насоса.

Для того, чтобы обеспечить нормальную работу испарителя необходимо, чтобы температура теплоносителя в промежуточном контуре была на 5-10 градусов выше, чем температура хладагента в испарителе. Мощность теплообменника SC должна быть равна или больше тепловой мощности испарителя, что обеспечивается выбором необходимой площади поверхности теплообменника SC и расхода теплоносителя во промежуточном контуре.

Рассмотрим, как обеспечивается требуемое значение температуры теплового агента в промежуточном контуре.

Схема связи теплового насоса с линией обратной сетевой воды выходящей из группового теплового пункта или других низкопотенциальных источников теплоты имеет вид (рис.2).

Тепловой четырехполюсник, изображенный на рис.2, включает в себя теплообменник SC, установленный в линии ТОСВ, испаритель теплового насоса EV, два насоса, Р1 и Р2, промежуточный резервуар $VS1$.

Рассмотрим качественную сторону процесса изменения температуры на выходе нагреваемой в теплообменнике среды, например, при скачкообразном снижении уровня жидкости в кожухозмеевиковом (или кожухотрубном) теплообменнике.

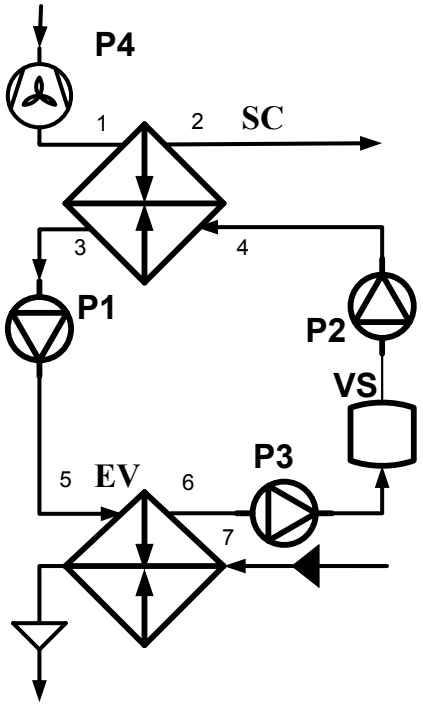

P4- напорный вентилятор, P1, P2, P3 – насосы, VS-промежуточный сосуд.

Рис. 1. Тепловой четырехполюсник для регулирования мощности испарителя.

P4- pressure fan, P1, P2, P3 – pumps, VS-intermediate vessel.

Fig. 1. Thermal quadripole for evaporator power control.

Роль основного резервуара играет теплообменник SC, уровень в котором регулируется в зависимости от требуемой передаваемой им тепловой мощности.

Расход воды через теплообменник SC изменяется регулирующим вентилем CV. Или синхронно работающими насосами Р1 и Р2.

Схема контура, рис.1 работает следующим образом:

- Р4 – является вентилятором, подающим воздух на теплообменник SC. Таким образом воздух нагревается теплотой обратной сетевой воды.
- насос Р2 является базовым (т.е. его производительность не изменяется).
- при необходимости изменить уровень теплоносителя в теплообменнике SC насос Р1

или уменьшает или увеличивает свою производительность, а насос P3 также уменьшает или увеличивает свою производительность, с тем, чтобы уровень теплоносителя в EV не изменился.
если необходимо изменить уровень в EV, то базовым является насос P1, а насос P3 или увеличивает или уменьшает свою производительность. При этом уровень в SC не изменяется, так как не изменяются производительности насосов P1 и P2. Красным цветом на рисунке 1 обозначены элементы, относящиеся к воздушному тракту.

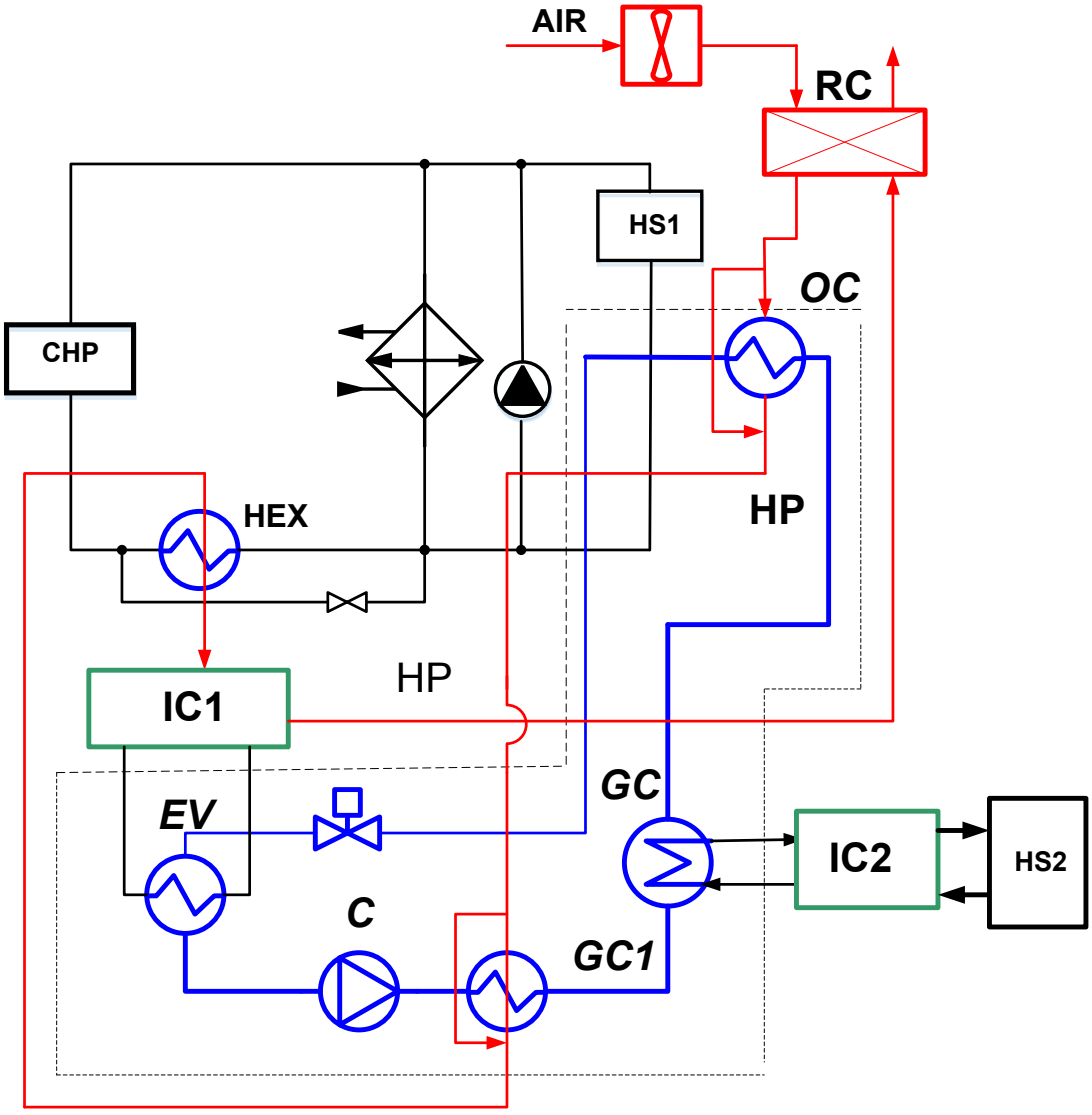

RC-рекуператор, GC- газоохладитель, HP-тепловой насос, EV-испаритель, HEX-теплообменник для съема теплоты от трубопровода обратной сетевой воды, CHP- ТЭЦ, OC- переохладитель рабочего тела, IC1 – промежуточный контур испарителя, IC2- промежуточный контур газоохладителя, HS1- система теплоснабжения базовая, HS2- система теплоснабжения здания, отапливаемого тепловым насосом, C- компрессор, GC1- теплообменник тонкой регулировки температуры первого газоохладителя.

Рис. 2. Схема системы теплоснабжения с ТЭЦ и тепловыми насосами (ТН).

RC-recuperator, GC- gas cooler, HP-heat pump, EV-evaporator, HEX- heat exchanger for removing heat from the return network water pipeline, CHP- ТЭЦ, OC- second gas cooler, IC1 – intermediate circuit of evaporator, IC2- intermediate circuit of the gas cooler, HS1- base heat supply system , HS2- heating system of a building heated by a heat pump, C- compressor, GC1- heat exchanger for fine adjustment of the temperature of the first gas cooler.

Fig. 2. Scheme of the heat supply system with CHP and heat pumps (HP).

Структурная схема САУ режимом работы переохладителем рабочего тела ТН

Уравнение статики задающего воздействия – зависимости расхода воздуха на выходе второго газоохладителя от параметров, входящих в (4) имеет вид:

$$G_{AER} = m_H \cdot \left(h_{IN} - h_{OUT}\right) / \ldots \left(c_{AER}\left(t_{AER\_OUT} - t_{AER\_IN}\right)\right). \quad (4)$$

В этом уравнении наиболее существенным возмущением является температура воздуха перед теплообменником (влажностью воздуха пренебрегаем). Расход и температуру хладагента считаем постоянными.

Вопросам построения передаточной функции теплообменника по каналу «скорость теплового агента в первичном контуре теплообменника» - «температура рабочего тела второго газоохладителя теплового насоса» посвящены работы [11]. Так, в диссертациии, опубликованной в 1962 г., в [10] приведена передаточная функция в виде:

$$\frac{T_{OUT}(p)}{G(p)} = \frac{\left(T_1 p + 1\right)e^{-p\tau}}{T_2 p^3 + T_3 p^2 + T_4 p + 1} \quad (5)$$

В работе [18], 1988 г., приведена передаточная функция в таком же виде. При выводе передаточных функций используют различные подходы, связанные с линеаризацией [11]. Мы, в данной задаче, пренебрегаем влажностью воздуха.

Уравнение теплового баланса для хладагента во втором газоохладителе.

$$M_R c_R \frac{dT_R}{dt} = G_R c_R \left(T_{R0} - T_R\right) - \alpha_0 F_0 \left(T_R - T_M\right) \quad (6)$$

Уравнение для теплового баланса поверхности теплообмена газоохладителя.

$$M_M c_M \frac{dT_M}{dt} = \alpha_0 F_0 \left(T_R - T_M\right) - \alpha_1 F_1 \left(T_M - T_A\right). \quad (7)$$

Тепловой баланс для воздуха (влажность воздуха не учитываем)

$$M_A c_A \frac{dT_A}{dt} = G_A c_A \left(T_{A0} - T_A\right) - \alpha_1 F_1 \left(T_A - T_M\right). \quad (8)$$

Линеаризуем уравнения (6)…(8).

В результате получаем:

$$T_R \frac{dT_R}{dt} + \Delta T_R = k_1 \Delta T_M + k_2 \Delta T_{R0} \quad (9)$$

$$T_M \frac{d\Delta T_M}{dt} + \Delta T_M = k_3 \Delta T_R + k_4 \Delta T_A; \quad (10)$$

$$T_A \frac{d\Delta T_A}{dt} + \Delta T_A = k_5 \Delta T_{A0} + k_6 \Delta G_A + k_7 \Delta T_M; \quad (11)$$

Мы используем для аппроксимации базовых уравнений, описывающих теплообменник, один из известных численных методов – метод прямого счета. В качестве базового был принят кожухотрубный теплообменник «вода-вода» с тепловой мощностью около 8 кВт.

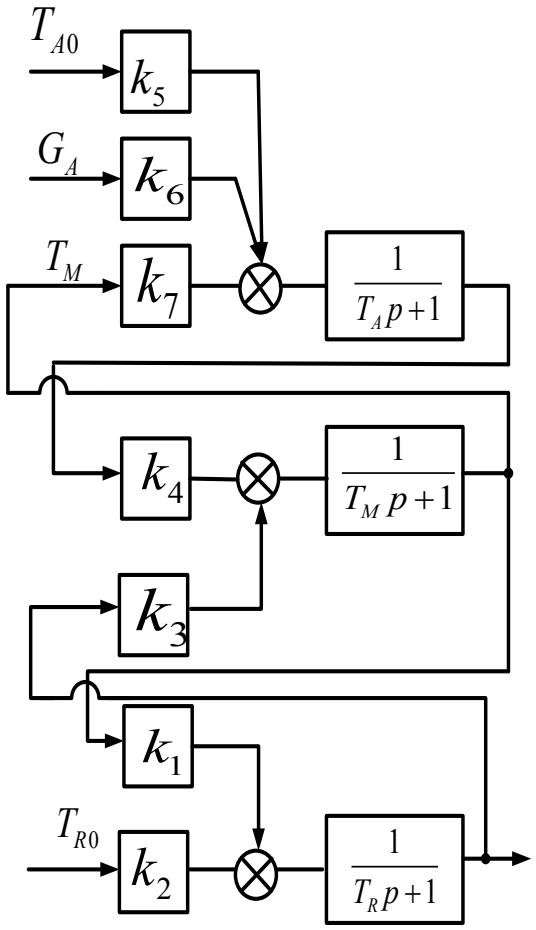

Рис.3. Структурная схема второго газоохладителя, как объекта регулирования температуры на его выходе.
Fig.3. Structural diagram of the second gas cooler as an object of temperature control at its outlet.

Из вида структурной схемы следует, что теплообменник, как объект управления в системе регулирования температуры на

выходе вторичной цепи представляет собой объект третьего порядка.

Такой вид структурной схемы (рис.3) позволяет оценить влияние каждого конструктивного элемента теплообменника на его динамику. На рис.3 показаны те воздействия или возмущения, которые рассматриваются, как существенные при работе теплового насоса.

Из вида передаточной функции второго теплообменника очевидно, что величина расхода воздуха, компенсирующая изменение его температуры рассчитывается по формуле:

$$\Delta G_A = \Delta T_A \cdot k_5 / k_6 . \quad (12)$$

Компенсация влияния температуры рабочего тела на входе во второй газоохладитель осуществляется посредством регулирования перегрева газа после испарителя и регулированием давления на выходе компрессора.

Структурная схема САУ стабилизации температуры хладагента на выходе второго газоохладителя имеет вид (рис.4).

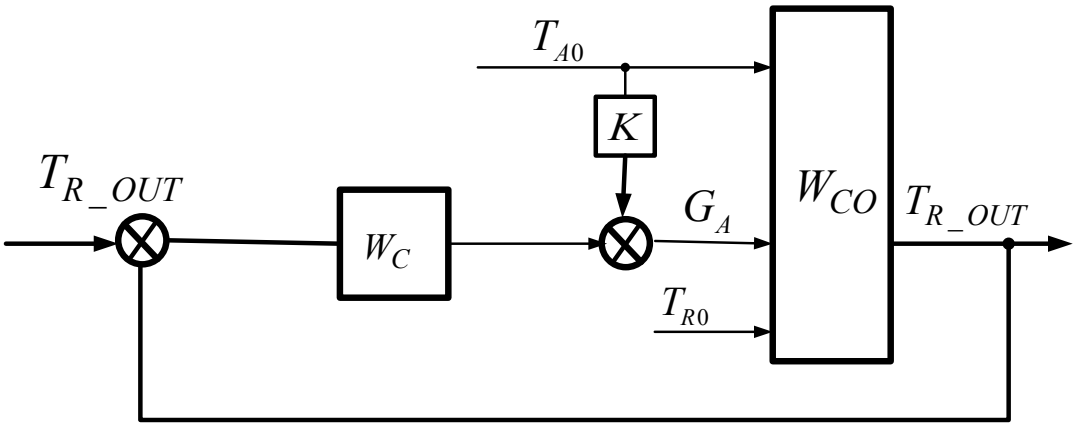

W_C, K – контроллер, W_{CO} -объект управления, T_{R_OUT} - температура на выходе газоохладителя.

Рис. 4. Структурная схема САУ температурой на выходе второго газоохладителя.

W_C, K – controller, W_{CO} -controlled object, T_{R_OUT} - temperature on gas cooler outelr.

Fig. 4. Structural diagram of ACS with temperature at the outlet of the second gas cooler.

Контроллер в данной САУ может быть выполнен в виде ПИ (ПИД) -регулятора. Результаты моделирования показали, что САУ отрабатывает скачкообразные возмущения по входному сигналу с апериодическим процессом, а возмущения по температуре хладагента на входе газоохладителя с перерегулированием.

Температура воздуха на выходе из теплообменника трубопровода ОСВ вычисляется по формуле

$$t_{AER\_OUT} = t_{AER\_IN} + \frac{G_{WAT} c_{WAT}}{G_{AER} c_{AER}} \left(t_{WIN} - t_{WOUT} \right) \quad (12)$$

Мощность потока теплоты, поступающего на испаритель, Q_{EV_IN} вычисляем по формуле

$$Q_{EV\_IN} = dt_{EV} G_{WAT} c_{WAT} , \quad (13)$$

dt_{EV} –разность температур на концах первичной цепи испарителя. dt_{EV} –разность температур на концах первичной цепи испарителя. Мощность потока теплоты, поступающего на испаритель, Q_{EV_IN} вычисляем по формуле

$$Q_{EV\_IN} = dt_{EV} G_{WAT} c_{WAT} , \quad (14)$$

dt_{EV} –разность температур на концах первичной цепи испарителя.

Заданный расход воздуха при его заданной температуре для обеспечения доставки заданной тепловой мощности Q_{EV} к *испарителю теплового насоса* для получения заданной тепловой мощности на газоохладителе вычисляется по следующему алгоритму:

- Сначала задаются расходом хладагента через газоохладитель G_H и тепловой

мощностью хладагента Q_{GC}, которая должна быть отдана газоохладителем (ГО) в соответствии с температурным графиком для заданных метеоусловий.

$$G_H = G_H(t_{EXT}); Q_{GC} = G_{GC}(t_{EXT}) \cdot \left(h_{GC}^{IN} - h_{GC}^{OUT}\right), \quad (13)$$

$$t_{GC}^{DIR} = t_{IN}^{DW} + \Delta t\,. \quad (14)$$

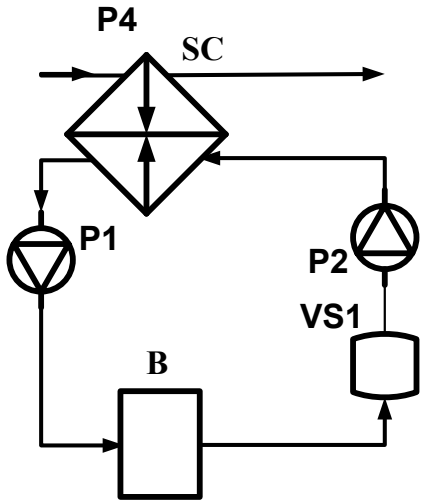

B- система отопления здания, VS1 – расширительная емкость.

Рис.5. Гидравлическая схема теплового четырехполюсника для регулирования режима первого (основного) газоохладителя.

B – building's heating system, VS1 - expansion tank. **Fig.5. Hydraulic diagram of a thermal quadrupole for regulating the mode of the first (main) gas cooler.**

- Задаются значением величины энтальпии хладагента на входе в испаритель, h_{IN}^{EV}, из условия выполнения требования к работе второго теплообменника, - обеспечить заданную температуру хладагента (ХА), t_{IN}^{EV}, на входе в испаритель.
- Вычисляют энтальпию ХА на выходе испарителя (И), h_{OUT}^{EV}, и, из расчета внутреннего теплообменника, задаются перегревом газа после И dt_{SH} .
- Параллельно с выполнением п.3, задаются давлением газа P_{EV} в испарителе, (с учетом характеристик компрессора) при температуре ХА в испарителе t_{IN}^{EV} .
- По предварительно идентифицированным величинам КПД компрессора и по заданной величине давления после компрессора по формулам Шпана и Вагнера (R.Span, W.Wagner) определяем температуру газа после компрессора и его энтальпию.

ЗАКЛЮЧЕНИЕ

1. Для применения гибридных тепловых насосов с высоким COP, необходимо, чтобы тепловая мощность, доставляемая к испарителю наружного воздуха, подогретого в калорифере, установленном на трубопроводе обратной сетевой воды, была достаточна для получения на выходе газоохладителя требуемой тепловой мощности.
2. В тепловом насосе необходимо установить для последовательно включенных по хладагенту газоохладителя: один для подогрева прямой сетевой воды отапливаемого здания, а второй для подогрева наружного воздуха, поступающего к испарителю теплового насоса.
3. Для поддержания требуемого значения температуры хладагента для подогрева наружного воздуха перед испарителем, рационально использование САУ с ПИД-регулятором и статической компенсацией температуры наружного воздуха.

ЛИТЕРАТУРА (REFERENCES)

[1] Wang, Z., Han, F., & Sundén, B. (2018). Parametric evaluation and performance comparison of a modified CO 2 transcritical refrigeration cycle in air-conditioning applications. Chemical Engineering Research and Design, 131, 617–625. doi:10.1016/j.cherd.2017.08.003

[2] Qi, P.-C., He, Y.-L., Wang, X.-L., & Meng, X.-Z. (2013). *Experimental investigation of the optimal heat rejection pressure for a transcritical CO2 heat pump water heater. Applied Thermal Engineering, 56(1-2), 120–125.* doi:10.1016/j.applthermaleng.2013.03.045

[3] Louis D. Albright, & Mathew L. Behle. (1984). *An Air-Liquid-Air Heat Exchanger for Greenhouse Humidity Control. Transactions of the ASAE, 27(5), 1524–1530.* doi:10.13031/2013.32998

[4] Prokhorenkov A.M. Modelirovanie protsessov teploobmena, protekaiuschih plastinchatyh teploobmennih apparatah. [Modeling of heat exchange processes in lamellar heat exchange devices]. Vestnik MGTU [Bulletin of MSTU], V. 17, № 1, 2014. pp. 92-101 (in Russian).

[5] Sanchez, J. A., Kulkarni, D., Tang, X., & Winkel, C. (2018). *Experimental and Numerical Investigation of Liquid-to-Air Heat Exchangers. 2018*

17th IEEE Intersociety Conference on Thermal and Thermomechanical Phenomena in Electronic Systems. doi:10.1109/itherm.2018.8419653.

[6] Al-Dawery, S. K., Alrahawi, A. M., & Al-Zobai, K. M. (2012). *Dynamic modeling and control of plate heat exchanger. International Journal of Heat and Mass Transfer, 55(23-24), 6873–6880.* doi: 0.1016/j.ijheatmasstransfer.2012.06.094.

[7] Lavrov N.A. Mnogourovnevaia Sistema modelirovania nestatsionarnih I meniauschihsia rejimov raboti nizkotemperaturnih ustanovok. [Multilevel system of modeling nonstationary and variable operating modes of low-temperature installations]. Moscow, 2013. Doctor thesys.https://www.google.com/url?sa=t&rct=j&q=&esrc=s&source=web&cd=3&cad=rja&uact=8&ved=2ahUKEwjh9rD26p7fAhXH2KQKHeTPDfEQFjACegQIA-BAC&url=http%3A%2F%2Fwww.bmstu.ru%2Fps%2F~lavrov%2Ffileman%2Fdownload%2F%25D0%259B%25D0%25B0%25D0%25B2%25D1%2580%25D0%25BE%25D0%25B2-%25D0%25B4%25D0%25B8%25D1%2581%25D1%2581.pdf&usg=AOvVaw0RUNk_0AuFo6c2en0a7Lg0 (accessed 5.12.2020).

[8] Zhang, W.-J., & Zhang, C.-L. (2011). *A correlation-free on-line optimal control method of heat rejection pressures in CO2 transcritical systems. International Journal of Refrigeration, 34(4), 844–850.* doi:10.1016/j.ijrefrig.2011.01.014.

[9] Maidi, A., & Corriou, J.-P. (2020). *PDE control of heat exchangers by input-output linearization approach. Advanced Analytic and Control Techniques for Thermal Systems with Heat Exchangers, 367–386.* doi:10.1016/b978-0-12-819422-5.00.

[10] Stermole F.G. The Dynamic response of Flow Forced Hear Exchangers. Iowa State University, (1963). *Retrospective Theses and Dissertations*. 2948.

[11] Golinko I.M. [Dynamichna modeli tepl omasoobminu dlia vodianogo oholodjuvacha promyslovogo kondytsionera], Dynamic model of heat and mass transfer for water cooler of industrial conditioner. [Naukovi visti "NTUU KHPI"], Scientific news of NTUU of Ukraine,

[12] Shao, L.-L., Zhang, Z.-Y., & Zhang, C.-L. (2018). *Constrained optimal high pressure equation of CO 2 transcritical cycle. Applied Thermal Engineering, 128, 173–178.* doi:10.1016/j.applthermaleng.2017.

[13] Kravaris, C., & Kantor, J. C. (1990). *Geometric methods for nonlinear process control. 2. Controller synthesis. Industrial & Engineering Chemistry Research, 29(12), 2310–2323.* doi:10.1021/ie00108a002

[14] Padhee, S., Khare, Y. B., & Singh, Y. (2011). *Internal model based PID control of shell and tube heat exchanger system. IEEE Technology Students' Symposium.* doi:10.1109/techsym.2011.5783833.

[15] Dudnikov E.G. Avtomaticheskoe upravlenie v himicheskoi promishlennosti. [Automatic control in chemical industry]. Mashinostroenie, 1987. 368 p.

[16] Automatic control of a heat exchanger with changing operation conditions. http://www.mathematik.tudortmund.de/papers/BayazitBicerKulaliMueminogluTorres2008.pdf (accessed 12.12.2020).

[17] Applying heat exchanger control strategies. https://www.controleng.com/articles/applying-heat-exchanger-control-strategies/ (accessed 12.12.2020).

[18] Khan, A. R., Baker, N. S., & Wardle, A. P. (1988). *The dynamic characteristics of a countercurrent plate heat exchanger. International Journal of Heat and Mass Transfer, 31(6), 1269–1278.* doi:10.1016/0017-9310(88)90069-5002.

[19] Kanellakopoulos I., Kokotovic P. V., and Morse A. S., "Systematic design of adaptive controllers for feedback linearizable systems," *IEEE Transactions on Automatic Control*, vol. 36, no. 11, pp. 1241–1253, 1991.

[20] The future of heat pumps. World Energy Outlook Special Report. IEA, 2022.

[21] https://iea.blob.core.windows.net/assets/536f38a4-2624-476a-a048-21b6b4df12b6/TheFutureofHeatPumps.pdf

[22] https://www.rehva.eu/rehva-journal/chapter/application-of-heat-pumps-in-existing-district-heating-system (accsessed 25.04.2023).

[23] Span R. and Wagner W., A New Equation of State for Carbon Dioxide Covering the Fluid Region from Triple-Point Temperature to 1100 K at Pressures up to 800 MPa, J. Phys. Chem. Ref. Data, 25, 6, (1996), pp.1509-1597.

[24] Ommen, T., Markussen, W.B., Elmegaard B. Heat pumps in combined heat and power systems. Energy 2014; 76:989–1000. doi:10.1016/j.energy. 2014.09.016.28

[25] Maidia A., Corriou J.-P. PDE control of heat exchangers by input-output linearization approach. In Advanced Analytic and Control Techniques for Thermal Systems with Heat Exchangers # 2020 Elsevier Inc. All rights reserved., pp.367-386, https://doi.org/10.1016/B978-0-12-819422-5.00017-7 (accessed 08.04.2023).

[26] Malleswararao, Y. S. N., & Chidambaram, M. (1992). *Non-linear controllers for a heat exchanger. Journal of Process Control, 2(1), 17–21.* doi:10.1016/0959-1524(92)80014-o.

[27] Togashi, E. Development of heat pump model based on outlet temperature of heat medium. *Jpn Archit Rev*. 2018; 1: 129- 139. https://doi.org/10.1002/2475-8876.1006 (accessed 08.04.2023).

[28] Ferrarini, L., Rastegarpour, S., Caseri, L., Watanabe, T., & Choi, Y. (2020). *Predictive control-oriented models of a domestic air-to-water heat pump under variable conditions. IEEE Robotics and Automation Letters, 1–1.* doi:10.1109/lra.2020.3007474.

[29] Sahoo A., Radhakrishnan T.K., Sankar Rao C. Modeling and control of a real time shell and tube heat exchanger. Resource-Efficient Technologies 3 (2017) 124–132, http://dx.doi.org/10.1016/j.reffit.2016.12.001 (accessed 08.04.2023).

[30] Skorospeshkin M. V., Sukhodoev M.S., Skorospeshkin V.N., Rymashevskiy P. O. An adaptive control system for a shell-and-tube heatexchanger. IOP Conf. Series: Journal of Physics: Conf. Series 803 (2017) 012153 doi:10.1088/1742-6596/803/1/012153 (accsessed 08.11.2022).

[31] Chitra. V. S, Manimaran. M, Petchithai. V. Non-linear Block-Box Modelling and Control a Shell and Tube Heat Exchanger Using Generalized predictive Controller. International Journal of ChemTech Research Vol.7, No.4, pp 1843-1848, 2014-2015.

[32] AlsopA.W. & Edgar T.W. (1989) nonlinear heat exchanger control through the use of partially linearized control variables, Chemical Engineering Communications, 75:1, 155-170. DOI: 10.1080/00986448908940674 (accessed 08.04.2023).

Результаты были получены в рамках проекта Госпрограммы с номером 20.80009.7007.18: «Эко-инновационные технические решения по снижению энергопотребления зданий и разработка опций по развитию интеллектуальных сетей с высокой интеграцией ВИЭ в Молдове»

Сведения об авторах.

Шит Михаил Львович – к.т.н., доцент-исследователь. Область научных интересов: тепловые насосы, автоматическое управление технологическими процессами.
E-mail: mihail_sit@mail.ru

Журавлев Анатолий Александрович – к. т. н. Область научных интересов: микропроцессорные системы управления, промышленная автоматика.
E-mail: AZhur5249@mail.ru

Тыршу Михаил Степанович, Институт энергетики, кандидат технических наук. Научные интересы связаны с диагностикой высоковольтного оборудования и силовой электроникой.
tirsu.mihai@gmail.com.

Лупу Михаил Леонидович Институт энергетики. Научные интересы связаны с энергоэффективностью, развитием возобновляемых источников энергии, уменьшением выбросов и защитой окружающей среды.
mihu.lupu@gmail.com

Тимченко Дмитрий Викторович – ведущий инженер – программист Института энергетики АН Молдовы. Область научных интересов: программирование микропроцессоров.
E-mail: dimmy@bk.ru

Дауд Василий Петрович к.т.н., научные интересы связаны с энергоэффективностью, развитием возобновляемых источников энергии, уменьшением выбросов и защитой окружающей среды.
E-mail:
caporalprim@yahoo.com

Experimental Study of Gas Entrainment by Free Jets of Water-Slurry Suspensions into Tubes of Shell-and-Tube Jet-Injection Apparatus

Malakhov Y.L., Kuznetsov A.Yu. Novoselov A.G., Chebotar A.V., Baranov I.V., Rumyantseva O.N., Mironova D.Yu.
ITMO University
Saint-Petersburg, Russian Federation

Abstract. In industries, the task of intensifying the process of dissolving gases in liquid media is relevant, since the time of the technological cycle depends on its course. Absorption processes affect the quality of the finished product and energy costs. In the food industry shell-and-tube jet injectors (SJT) are widespread, in which the mechanical injection of a free-falling jet of liquid surrounding its gas is applied. The aim of this work is to investigate the process of gas entrainment by free jets of water-malt slurry (WSS) in the pipes of the SJT. The set goal was achieved by solving the tasks: creating an experimental stand to study the process of atmospheric air injection by water-salt suspensions in the tubes of the SJT; developing a methodology for experimental studies; conducting research on the processes of gas injection by free liquid jets depending on the flow rate and liquid concentration. The most important result of the work is the establishment of graphical and mathematical dependences for the investigated WSS hydromodules, which allow calculating the flow rate carried away by the jet depending on the nozzle diameter. It is found that the gas phase entrainment by free suspension jets is influenced by the viscosity of the suspension, which depends on a number of technological parameters. The practical significance of the obtained results consists in the proposed methodology for calculating the design characteristics of SISA, providing the highest efficiency of its operation taking into account the properties of working environments and parameters of technological processes.
Keywords**:** shell-and-tube jet injector, injection, shell-and-tube heat exchanger, heat and mass exchange, gas-liquid jet, water-malt slurry, hydromodulus.

DOI: https://doi.org/10.52254/1857-0070.2023.2-58-10
UDC: 637.143

Cercetarea experimentală al antrenării gazelor prin jeturi libere de suspensii apă-malț în tuburile unui aparat de injecție cu jet cu carcasă și tub

Malahov Y.L., Kuznețov A.Iu. Novoselov A.G., Cebotar A.V., Baranov I.V., Rumeanțseva O.N., Mironova D.Iu.
Universitatea ITMO, Sanct-Petersburg, Federația Rusă

Rezumat. În diverse industrii, sarcinile de intensificare a procesului de dizolvare a gazelor în medii lichide sunt relevante, deoarece timpul ciclului tehnologic depinde în mod semnificativ de cursul acestuia. Procesele de absorbție afectează atât calitatea produsului finit, cât și costurile energetice în producția acestuia. În industria alimentară s-au răspândit aparatele de injecție cu jet cu carcasă și tub (AIJCT), în care este utilizat fenomenul de injecție mecanică printr-un jet de lichid în cădere liberă a gazului din jur. În ciuda numărului mare de studii în acest domeniu, problema unei abordări teoretice a estimării cantității de antrenare a gazului prin jeturi libere de lichid nu a fost complet rezolvată până acum. Scopul lucrării este de a studia procesul de antrenare a gazelor prin jeturi libere de suspensii apă-malț (SAM) în conductele AIJCT. Scopul stabilit a fost atins prin rezolvarea următoarelor sarcini: realizarea unui stand experimental pentru studierea procesului de injectare a aerului atmosferic prin suspensii apă-malț în conductele AIJCT; elaborarea metodologiei de cercetare experimentală; efectuarea cercetărilor asupra proceselor de injectare a gazelor prin jeturi libere de lichid în funcție de debitul de ieșire și concentrația lichidului. Standul experimental elaborate a fost folosit pentru a studia antrenarea gazului de către un jet de suspensie liberă care curge dintr-o duză cilindrică. Cel mai important rezultat al lucrării este stabilirea unor dependențe grafice și matematice pentru modulele hidraulice studiate ale SAM care permit calcularea debitului de aer transportat de jet, în funcție de diametrul duzei. Semnificația practică a rezultatelor obținute constă în metoda propusă de calcul a caracteristicilor structurale ale AIJCT, care asigură cea mai mare eficiență a funcționării acestuia, ținând cont de proprietățile mediilor de lucru și parametrii procesului.
Cuvinte-cheie**:** aparat de injecție cu jet cu carcasă și tub, injecție, schimbător de căldură cu carcasă și tub, transfer de căldură și masă, jet gaz-lichid, suspensie apă-malț, hidromodul.

Экспериментальное исследование уноса газа свободными струями водно-солодовых суспензий в трубы кожухотрубного струйно-инжекционного аппарата

Малахов Ю.Л., Кузнецов А.Ю. Новоселов А.Г., Чеботарь А.В.,
Баранов И.В., Румянцева О.Н., Миронова Д.Ю.
Университет ИТМО, Санкт-Петербург, Россия

***Аннотация*.** В различных отраслях промышленности актуальны задачи интенсификации процесса растворения газов в жидких средах, поскольку от его протекания существенно зависит время проведения технологического цикла. Абсорбционные процессы влияют как на качество готовой продукции, так и на энергетические затраты при её производстве. В пищевой промышленности получили распространение кожухотрубные струйно-инжекционные аппараты (КСИА), в которых применяется явление механической инжекции свободно падающей струей жидкости окружающего её газа. Несмотря на большое число исследований в данной области, проблема теоретического подхода к оценке количества уноса газа свободными струями жидкости до настоящего времени полностью не решена. Целью работы является исследование процесса уноса газа свободными струями водно-солодовых суспензий (ВСС) в трубы КСИА. Поставленная цель достигнута за счет решения следующих задач: создание экспериментального стенда для исследований процесса инжекции атмосферного воздуха водно-солодовыми суспензиями в трубах КСИА; разработка методики экспериментальных исследований; проведение исследований процессов инжекции газа свободными струями жидкости в зависимости от скорости истечения и концентрации жидкости. На разработанном экспериментальном стенде проводилось изучение уноса газа свободной суспензионной струей, вытекающей из цилиндрического сопла. Наиболее важным результатом работы является установление для исследуемых гидромодулей ВСС графических и математических зависимостей, позволяющих рассчитывать расход воздуха, уносимого струей, в зависимости от диаметра сопла. Установлено, что на унос газовой фазы свободными суспензионными струями оказывает влияние вязкость суспензии, которая зависит от ряда технологических параметров (степень измельчения зерна, его химический состав и т.п.). Практическая значимость, полученных результатов, состоит в предложенной методике расчета конструктивных характеристик КСИА, обеспечивающей наибольшую эффективность его работы с учётом свойств рабочих сред и параметров технологических процессов.

Ключевые слова: кожухотрубный струйно-инжекционный аппарат, инжекция, кожухотрубный теплообменник, тепломассообмен, газожидкостная струя, водно-солодовая суспензия, гидромодуль.

ВВЕДЕНИЕ

На сегодняшний день вопросы повышения эффективности тепло- и массообменных процессов в пищевых технологиях являются крайне актуальными.

Для применения в пищевой промышленности одними из перспективных тепло-массообменных аппаратов являются кожухотрубные струйно-инжекционные аппараты (КСИА).

Данный тип устройств представляет собой универсальный аппарат для проведения тепло-массообменных процессов в пищевых технологиях, поскольку позволяет проводить одновременно тепло-массообменные процессы между газом и жидкостью. Различные модификации конструкции КСИА были апробированы на пищевых производствах, в том числе для технологий получения газированных напитков на основе воды, молочной сыворотки, фруктовых и овощных соков (сатурация напитков), хлебопекарных дрожжей (культивирование биомассы), пива (на стадиях культивирования биомассы и сбраживания сусла), этанола (на стадиях проведения водно-тепловой обработки зернового сырья, осахаривания и сбраживания), олифы (на стадиях оксидирования растительного масла) [1,2,3,4,5].

Во всех вышеприведенных случаях КСИА показал свою работоспособность и эффективность. Однако, промышленное производство КСИА требует научно-обоснованной методики их расчетов, основанной на системном анализе всех происходящих явлений в рабочем объёме аппарата.

В работах [6,7,8,9,10] показано, что, несмотря на достаточно большое число опубликованных исследований, проблема теоретического подхода к оценке количества уноса газа свободными струями жидкости до настоящего времени не имеет решения.

В основе механизма подачи газовой фазы в КСИА лежит явление механической инжекции свободно падающей струей жидкости окружающего её газа. Именно этот эффект, в совокупности с конструкцией вертикального кожухотрубного

теплообменника (КТО), позволяет проводить одновременно тепло-массообменные процессы между газом и жидкостью. Простота конструкции КСИА и возможность регулировки подачи газовой фазы в реакционный объем, без установки газонагнетательного оборудования сделала этот аппарат одним их перспективных для получения пивного сусла из солодовых суспензий при проведении водно-тепловой обработки - одной из важнейших технологических стадий в пивоварении.

Большинство исследований КСИА носит экспериментальный характер, а полученные уравнения являются эмпирическими, с той или иной степенью точности, описывающими объемный унос количества газовой фазы в пределах рабочих режимов проведенных экспериментов. Кроме того, подавляющая часть экспериментов была проведена на воде, что не позволяет судить о влиянии физических свойств других рабочих сред на этот процесс [3,6,11,12,13,14]. Несмотря на то, что газовая фаза не несет в себе определенных функций, влияющих на качество пивного сусла, она определяет энергетическую составляющую проводимого процесса. Учитывая, что солодовые суспензии обладают значительной вязкостью, то присутствие газовой фазы в виде мелких пузырей снижает гидравлические потери энергии на трение. Кроме того, предполагается, что наличие мелких пузырей приводит к турбулизации жидкостной фазы, стимулируя более интенсивное растворение крахмальных зерен солода.

МЕТОДЫ ИССЛЕДОВАНИЯ

Экспериментальное изучение уноса газа свободной суспензионной струей, вытекающей из цилиндрического сопла, выполнялось на экспериментальной установке, представленной на рис. 1.

Экспериментальная установка состояла из трехтрубной модели струйно-инжекционного аппарата (СИА) I, емкости-накопителя (Е-Н) II, циркуляционного насоса III.

Модель СИА I представляла собой вертикальный КТО без теплообменной рубашки и была выполнена из прозрачных материалов для возможности визуальных наблюдений за гидродинамической обстановкой. Аппарат состоял из вертикальных труб (опускная труба 1, подъемная труба 2, сливная труба 3). Эти трубы закреплены в трубных решетках 4 и 6. К нижней трубной решетке 6 прикреплялось днище аппарата с переходным каналом 11 и сливным отверстием, равным внутреннему диаметру труб 36 мм. Над верхней трубной решеткой 4 была размещена верхняя газовая камера, образованная прозрачными стенками, верхней трубной решеткой 4 и верхней крышкой 5. Верхняя газовая камера была разделена перегородкой 7 на две части: приемную камеру 9 и верхнюю циркуляционную камеру 10. Трубы 1, 2 и 3 с внутренним диаметром 36 мм и длиной 0,8 м были изготовлены из стекла, а соединительные фланцы и стенки верхней газовой камеры аппарата из оргстекла.

В аппарат подавался приготовленный объем суспензии заданного гидромодуля. Затем включался насос III и при не полностью открытом кране 14 производилось заполнение исследуемой суспензией циркуляционного жидкостного трубопровода модели КСИА. Затем полностью открывался кран 14 и фиксировался расход суспензии электромагнитным расходомером 13 марки «Proline Promag 55». Суспензия под напором, создаваемым насосом III, вытекала из сопла 8 в виде свободной жидкостной струи. Она инжектировала окружающий её воздух, и далее полученная смесь поступала в опускную трубу 1. Затем, образовавшаяся газо-суспензионная смесь двигалась в виде нисходящего потока к нижнему концу опускной трубы 1, перетекала через переходной канал 11 и поступала в подъемную трубу 2. В подъемной трубе 2, газо-суспензионная смесь двигалась восходящим потоком и поступала в верхнюю циркуляционную камеру 10, из которой сливалась по сливной трубе 3 в емкость-накопитель II. Поток воздуха поступал в приемную камеру 9 через газовый счетчик 12 по газовой коммуникации 20 за счет разности между атмосферным и абсолютным давлениями в приемной камере 9. Перепад давлений возникает в результате уноса свободной суспензионной струей газовой фазы, из приемной камеры 9 в трубу 1.

Эксперименты по изучению уноса газа свободными суспензионными струями в вертикальные трубы КСИА выполнялись по методике, разработанной авторами.

Суть данной методики заключается в следующем. Предварительно устанавливалось сопло заданного диаметра.

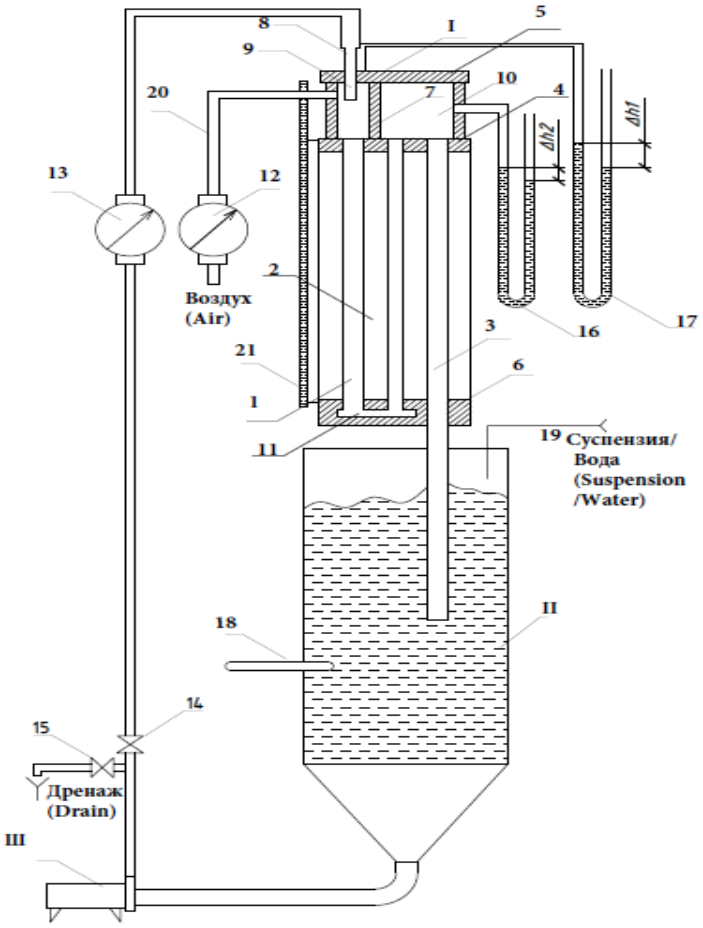

I – модель струйно-инжекционного аппарата; II – емкость-накопитель; III – циркуляционный насос; 1 – опускная труба, 2 – подъемная труба; 3 – сливная труба; 4 – верхняя трубная решетка; 5 – верхняя крышка; 6 – нижняя трубная решетка; 7 – перегородка; 8 – съемное сопло; 9 – приемная камера; 10 – верхняя циркуляционная камера; 11 – переходной канал; 12 – газовый счетчик; 13 – электромагнитный жидкостной расходомер; 14 – регулирующий вентиль, 15 – сливной кран; 16, 17 – дифференциальные жидкостные манометры; 18 – термометр; 19 – линия подачи суспензии; 20 – воздушная магистраль, 21 – миллиметровая линейка.

Рис. 1. Схематическое изображение экспериментальной установки по исследованию гидродинамики.[1]

Подготовленные к исследованию массы измельченного солода и воды тщательно взвешивались, смешивались в предварительно оттарированной емкости. Полученная ВСС заданного гидромодуля переносилась в емкость-накопитель II. После внесения заданного объема суспензии, включался насос III, суспензия заполняла установку и циркулировала в течение 3 минут. Затем измерялись: 1) расход суспензии с помощью электромагнитного расходомера 13; 2) расход воздуха, уносимого свободной суспензионной струей, при помощи барабанного газового счетчика «ГСБ-400»; 3) давление в камерах 9 и 10 с помощью дифференциальных жидкостных манометров 16 и 17; 4) температуры суспензии с помощью спиртового термометра; 5) уровень суспензии в опускной трубе 1 при помощи миллиметровой линейки 21. В процессе опытов фиксировались структуры потоков в трубах.

Исследование начинали с максимального расхода суспензии. По окончании измерений меняли исследованное сопло на другое, с меньшим диаметром проходного сечения. Затем изменялся гидромодуль суспензии, и цикл измерений проводился по вышеизложенной последовательности.

[1] Appendix 1

Из данных измерений рассчитывали расход воздуха через аппарат по уравнению:

$$Q_g = \frac{V_g}{t}, \quad (1)$$

где V_g - объём воздуха, прошедший через счетчик газа, за время *t*.

Зная Q_g, определяли приведенную скорость газа в трубах по уравнению:

$$\omega_g = \frac{Q_g}{S_{Pi}} = \frac{4 \cdot Q_g}{\pi \cdot d_{Pi}^2}. \quad (2)$$

По результатам измерений расхода суспензии Q_S, рассчитывали скорость истечения суспензии из сопла ν_0:

$$\nu_0 = \frac{Q_S}{S_0} = \frac{4 \cdot Q_S}{\pi \cdot d_0^2}, \quad (3)$$

и приведенную скорость суспензии в трубах:

$$\omega_S = \frac{Q_S}{S_{Pi}} = \frac{4 \cdot Q_S}{\pi \cdot d^2_{Pi}}. \quad (4)$$

По величине уровня газо-суспензионной смеси в опускной трубе H_{S_1} с учётом фиксированного расположения сопла 8 и толщины фланца 4, определялась длина свободной суспензионной струи:

$$L_S = H_{g_1} - H_{S_1}, \quad (5)$$

где H_{g_1} - расстояние от верхней поверхности фланца 4 до среза сопла 8, равное 0,915 м.

Температура суспензии определялась с помощью спиртового термометра, установленного на выходе солодовой суспензии из сливной трубы.

Для обработки опытных данных необходимо было связать отраслевое понятие «гидромодуль» с физическим понятием «концентрация» твердой фазы (измельченный солод) в воде. Для этого был сделан пересчёт, который представлен в таблице 1.

Таблица 1.[2]

Сопоставление величин гидромодуля и концентрации твердой фазы в воде[3]

Гидромодуль, кг зерна/кг воды (Hydromodulus, seeds kg/water kg)	Концентрация кг солода/кг смеси (Concentration, malt kg/ blend kg)
1:6	0,142
1:4	0,2
1:3,5	0,222
1:3	0,25
1:2,5	0,286

РЕЗУЛЬТАТЫ И ОБСУЖДЕНИЕ

Рассмотрение механизма уноса газа в трубы КСИА необходимо проводить с учетом влияния конструктивных особенностей аппарата на состояние структуры струи в точке ее входа в жидкостную фазу.

Структура струи в первую очередь будет определяться геометрическими размерами и формой проходного сечения сопла, но также очевидно, что на развитие этой структуры будут оказывать влияние и физические свойства протекающей через него жидкости, а именно, плотность, вязкость и поверхностное натяжение [17].

На рис. 2 показано развитие формы свободной струи, начиная от капельного истечения при очень малых расходах жидкости, до полного разрушения струи при очень больших расходах.

Как видно из рисунка 2, при фиксированном расстоянии от среза сопла до свободной поверхности жидкости, структура струи сильно зависит от скорости истечения. При этом можно выделить 9 состояний.

[2,3]Appendix 1

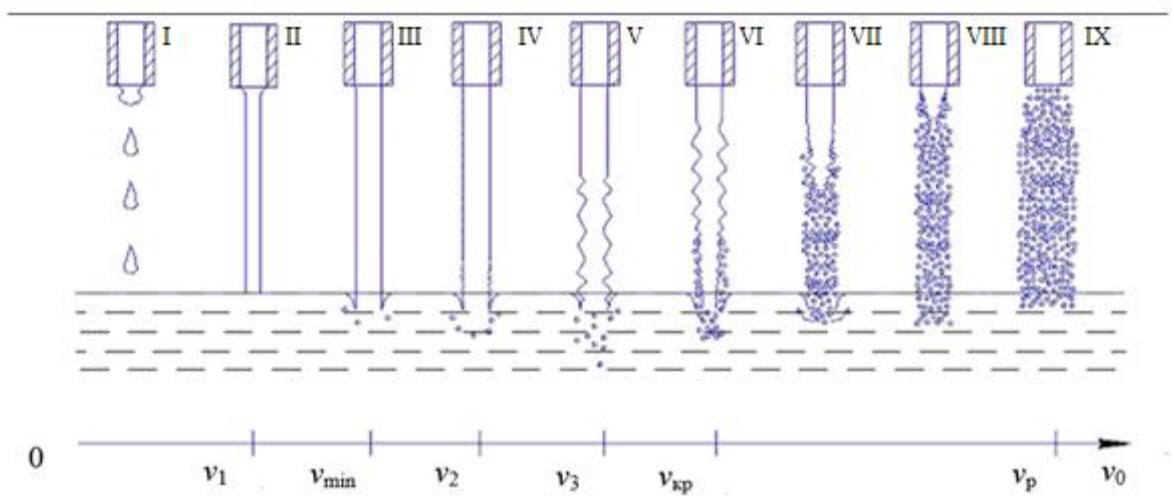

Рис. 2. Изменение состояния свободной поверхности струи при ее постоянной длине (условно) в зависимости от скорости истечения v_0.[4]

Состояние I характерно для очень малых расходов жидкости. Оно определяет капельное истечение жидкости в диапазоне скоростей от $v \geq 0$ до v_1.

В пределах этого диапазона происходит образование капель, но по достижении некой скорости v_1, начинается непрерывное истечение жидкости из сопла. С этого момента появляется свободная непрерывная струя жидкости, состояние II.

Очевидно, что на состояние поверхности свободной струи будет оказывать влияние, так называемая предыстория потока жидкости на входе в сопло.

В частности, её начальная турбулентность, зависящая, в свою очередь, от гидравлических сопротивлений подводящего трубопровода. Наличие только этого фактора, приводит к тому, что значение скорости v_1 в различных случаях подведения жидкости к соплу будет различным. Тем не менее, если гидравлические сопротивления трубопровода постоянны и зависят только от средней скорости потока в нем, то значения v_1 для жидкости постоянных физических свойств будет близко к постоянному значению.

С момента образования свободной струи жидкости при скорости v_1 она имеет гладкую поверхность по всей длине, но при этом значении скорости диаметр струи на выходе из сопла несколько больше, чем на входе в свободный объем жидкости, на расстоянии *L*. Это обусловлено тем, что под действием сил земного притяжения частицы жидкости ускоряются, а подача жидкости к соплу ограничена силами трения жидкости о стенки сопла.

Действующие силы поверхностного натяжения стремятся сжать струю, и поэтому на каком-то расстоянии от среза сопла диаметр струи d_J начинает уменьшаться. С увеличением скорости истечения, т. е. с увеличением расхода жидкости, этот эффект вырождается и диаметр струи остается постоянным по всей длине при этом свободная поверхность струи остается гладкой. При этом, следует отметить, что унос газа такими свободными струями не происходит. Этот эффект использовался рядом исследователей для разработки метода определения коэффициентов молекулярной диффузии (так называемый метод ламинарной струи) [17,18,19]. Однако даже при незначительном увеличении скорости истечения свободной струи v_1 до значения v_{min} начинается унос окружающего струю газа (состояние III).

В первую очередь унос газа свободной струей жидкости обусловлен разностью скоростей самой струи и скоростью частиц жидкости находящейся в объёме жидкости, в который она поступает. В результате происходит торможение струи в точке входа её в объём жидкости и на поверхности возникают возмущения в виде осесимметричных колебаний [20,21].

Осесимметричные колебания поверхности возникают, в первую очередь, из-за небольших колебаний гидростатического давления внутри струи. Появление колебаний гидростатического давления связано с частичным переходом кинетической энергии струи в потенциальную энергию давления.

[4] Appendix 1

Этот переход вызывает появление внутри сечения струи силы F_y, действующей в радиальном направлении.

Противодействующая им сила F_σ поверхностного натяжения стремится вернуть поверхность в первоначальное положение. В результате их взаимодействия и возникают осесимметричные колебания.

По мере увеличения скорости истечения струи от значения $v_{\min}$ точка зарождения колебаний поверхности струи смещается вверх по длине струи и все большая длина струи становится подверженной возмущениям (состояния IV, V).

Величина колебаний поверхности струи определяется значением скорости струи, поступающей в объём неподвижной жидкости и её вязкостью.

При достижении скорости движения свободной струи v_{cr} в результате появления радиальной силы F_y большей силы F_σ, начинается отрыв капель от поверхности струи, т.е. наблюдается ее разрушение (состояния VI и VII). Начало этого разрушения происходит в непосредственной близости от точки входа.

По мере увеличения скорости истечения сечение начала разрушения струи сдвигается вверх в сторону среза сопла.

С этого момента струя качественно меняет свою структуру и становится газожидкостной. Для человеческого глаза она представляет собой единое целое в виде слабо расширяющегося потока жидкости. Но это противоречит закону неразрывности жидкостного потока.

Расширение струи возможно только с уменьшением плотности жидкости, а такого явления при напорном истечении жидкости в атмосферу при нормальной температуре не происходит.

Это возможно увидеть только при условии срыва частиц жидкости с возмущенной поверхности струи.

В этом случае речь должна идти о газожидкостной струе с видимым диаметром d_J.

Это предположение нашло подтверждение в работах Дужего А.Б. и Тишина В.Б. [5; 15], которые исследовали структуру газожидкостной свободной струи электроконтактным методом.

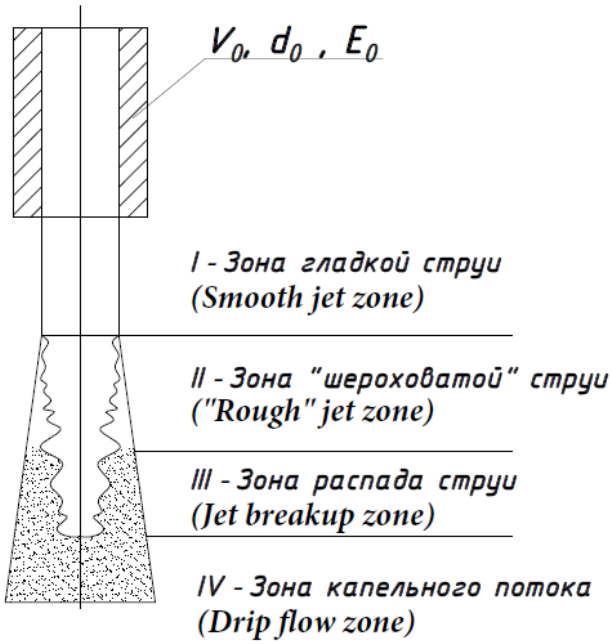

Рис. 3. Структура и форма свободной поверхности струи на бесконечно-большой длине, *v* = const [1][5].

[5] Appendix 1

На основании проведенных авторами экспериментов по изучению структуры свободных газожидкостных струй было установлено, что в состоянии VI структура струи представляет собой следующую модель: по оси газожидкостной струи движется основной поток жидкости, представляющий собой усеченный перевернутый конус. На каком-то расстоянии от среза сопла начинается отрыв капель от нее, которые движутся под некоторым углом к вертикальной оси. Вокруг жидкостного потока образуется, окружающий его газожидкостной слой, плавно расширяющийся по ходу движения.

Таким образом, жидкостная область газожидкостной струи плавно уменьшается в диаметре, по мере удаления рассматриваемого сечения от среза сопла, а газожидкостная область расширяется за счёт увеличения количества оторвавшихся капель и наличия радиальной составляющей скорости, а также уменьшения диаметра области чистой жидкости. Именно эта область, в основном, определяет количество газа, уносимого струей.

Дальнейшее увеличение скорости свободной газожидкостной струи приводит к смещению начала отрыва капель от струи в сторону среза сопла (состояния VII и VIII) заканчивающееся полным разрушением основного жидкостного потока на капли. Следует отметить, что кинетическая энергия капельного потока, пусть и компактного, существенно меньше энергии газожидкостной струи, что с точки зрения струйного уноса газа становится не практичным.

Эволюцию свободной поверхности струи бесконечно большой длины, можно проследить на примере истечения жидкости из сопла круглого поперечного сечения, представленного на рис. 3.

По состоянию поверхности струя может быть разбита на 4 характерные зоны по мере удаления потока от среза сопла:

- зона гладкой струи или зона ламинарной струи;
- зона шероховатой струи;
- зона разрушающейся струи;
- зона капельного потока.

Протяженность каждой из зон во многом зависит от скорости истечения жидкости из сопла. Чем больше скорость истечения, тем выше располагаются начала каждой из зон по отношению к срезу сопла. Более того, эти зоны последовательно исчезают по мере увеличения скорости истечения, сначала зона гладкой струи, затем зона шероховатой струи и распад струй на капли начинается сразу, после выхода жидкости из сопла. Таким образом, следует ожидать, что в зависимости от скорости истечения жидкости из сопла, скорость уноса газа или расход газа, инжектируемого в трубы КСИА, будет следующим: сначала, при увеличении расхода жидкости через сопло от $\nu = 0$ до $\nu = \nu_{\min}$, уноса газа не происходит по вышеупомянутым причинам.

Далее, при увеличении $\nu > \nu_{\min}$ начинается неравномерный унос малых количеств газа, переходящий к равномерному уносу газа, постоянно возрастающему с увеличением расхода жидкости Q_{Li}. Затем унос газа достигает своего максимального значения $Q_{g\max}$ и при дальнейшем увеличении Q_{Li} начинается уменьшение расхода Q_g.

Предполагается, что унос газа будет происходить в определенном диапазоне расходов жидкости, а именно, в диапазоне расходов от $Q_{Li} = Q_{Li\min}$ до $Q_{Li} = Q_{Li\max}$.

Количественные значения Q_g будут зависеть от диаметра проходного сечения сопла d_0, определяющего скорость истечения жидкости из сопла.

Таким образом, можно предположить, как будет происходить унос газа жидкостными струями в верхней газовой камере КСИА. Очевидно, что унос газа будет начинаться не сразу после образования свободной струи, а при достижении ею скорости $\nu \geq \nu_{\min}$.

В отличие от уноса газа в неподвижный объём жидкости, в рассматриваемом случае свободная струя будет входить в объём жидкости, заполняющий опускную трубу.

Таким образом, можно предположить, что возмущения поверхности свободной струи будут меньше, чем в случае поступления её в неподвижный объем, а, следовательно, значение скорости струи $\nu_{\min}$ будет несколько меньше. С другой стороны, унесенный свободной струей газ будет раздроблен на отдельные пузырьки, которые будут всплывать. Возникнет циркуляция газовой фазы в верхней части опускной трубы. Унесенный газ входит в объём жидкости, но

затем всплывает в виде газовых пузырьков и возвращается в газовую камеру. Этот процесс показан на рис. 4.

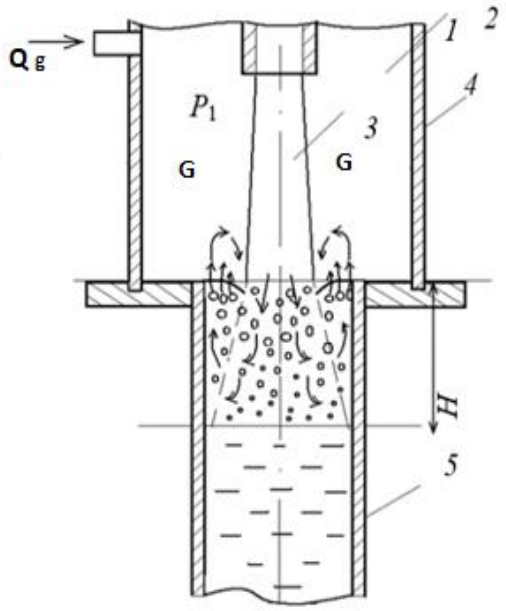

Рис. 4. Схематическое изображение верхней газовой камеры: 1- сопло, 2- верхняя (основная) газовая камера, 3- свободная струя, 4 - перегородка, 5 – опускная труба, G - газовая фаза[6].

Отсюда следует ожидать, что показания приборов, фиксирующих расход подачи газовой фазы в верхнюю газовую камеру, будут нулевыми. Фиксация расхода газа начнется только тогда, когда пузырьки газа будут уноситься нисходящим потоком жидкости в подъемную трубу. Унос пузырьков газа будет возможен только в том случае, когда скорость всплывания пузырьков ω_b будет меньше приведенной скорости жидкости в опускной трубе ω_{Li}, которая в свою очередь, зависит от расхода жидкости через сопло. Связь между скоростью истечения v_0 и приведенной скоростью жидкости ω_{Li} в опускной трубе будет определяться соотношением, полученным из уравнения расхода для несжимаемой жидкости:

$$Q_{Li} = v_0 \cdot S_0 = \omega_{Li} \cdot S_{Pi} = const \qquad (6)$$

Откуда:

$$\omega_{Li} = \frac{v_0 \cdot S_0}{S_{Pi}} = \frac{v_0 \cdot d_0^2}{d_{Pi}^2} \quad . \qquad (7)$$

Скорость подъема одиночного пузыря во многом зависит от его размеров, физических свойств окружающей его жидкости и гидродинамической обстановки в рассматриваемом объёме жидкости.

Применительно к рассматриваемой задаче, определение размеров одиночных пузырей в условиях неинтенсивной работы аппарата, не имеет практического смысла.

Совокупное влияние размеров пузырей, их скорости всплывания и физических свойств жидкости на унос газа в условиях интенсивной работы КСИА отразится на уровне газосуспензионной смеси в опускной трубе КСИА, который определяется экспериментальным путем [9,22,23,24,25].

В свою очередь уровень газосуспензионной смеси будет определять длину свободной струи жидкости, которая влияет на унос газа [9,26,27]. Обработка результатов экспериментов по определению расхода воздуха Q_g, уносимого струей, в зависимости от диаметра сопел (d_0) выполнялась с помощью специализированных компьютерных программ. Результаты, проведенных экспериментов, в виде графических зависимостей представлены на рис. 5-8.

На рисунке 9 представлена зависимость уноса газа от концентрации измельченного солода.

Математическая обработка данных представлена на примере обработки результатов, полученных при истечении свободной суспензионной струи из всех исследованных сопел в опускную трубу.

В процессе эксперимента неизбежно происходило нагревание суспензии, за счет диссипации механической энергии и перехода ее в тепловую энергию [28,29]. Во всех экспериментах с различными гидромодулями этот нагрев фиксировался термометром 18 и составлял не более 5 °С.

[6] Appendix 1

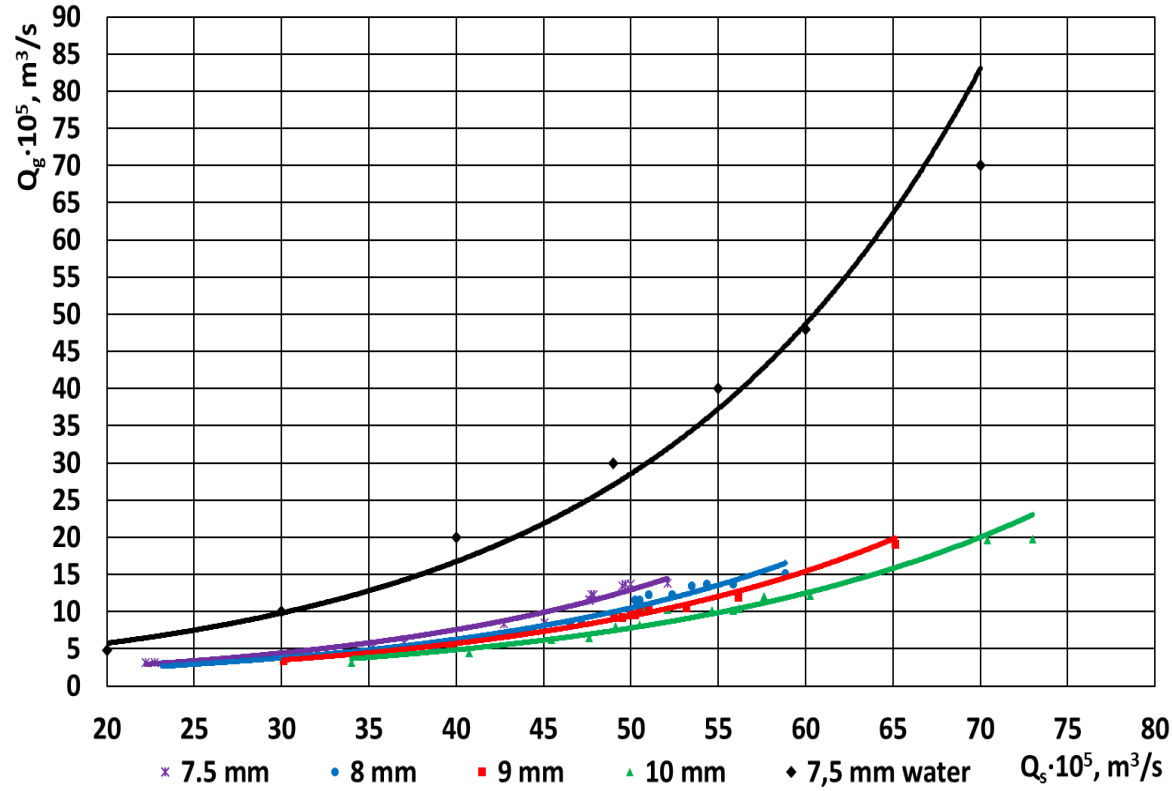

Рис. 5. Зависимость изменения $Q_г$ от $Q_с$ для различных диаметров сопел (гидромодуль 1:2,5)[7]

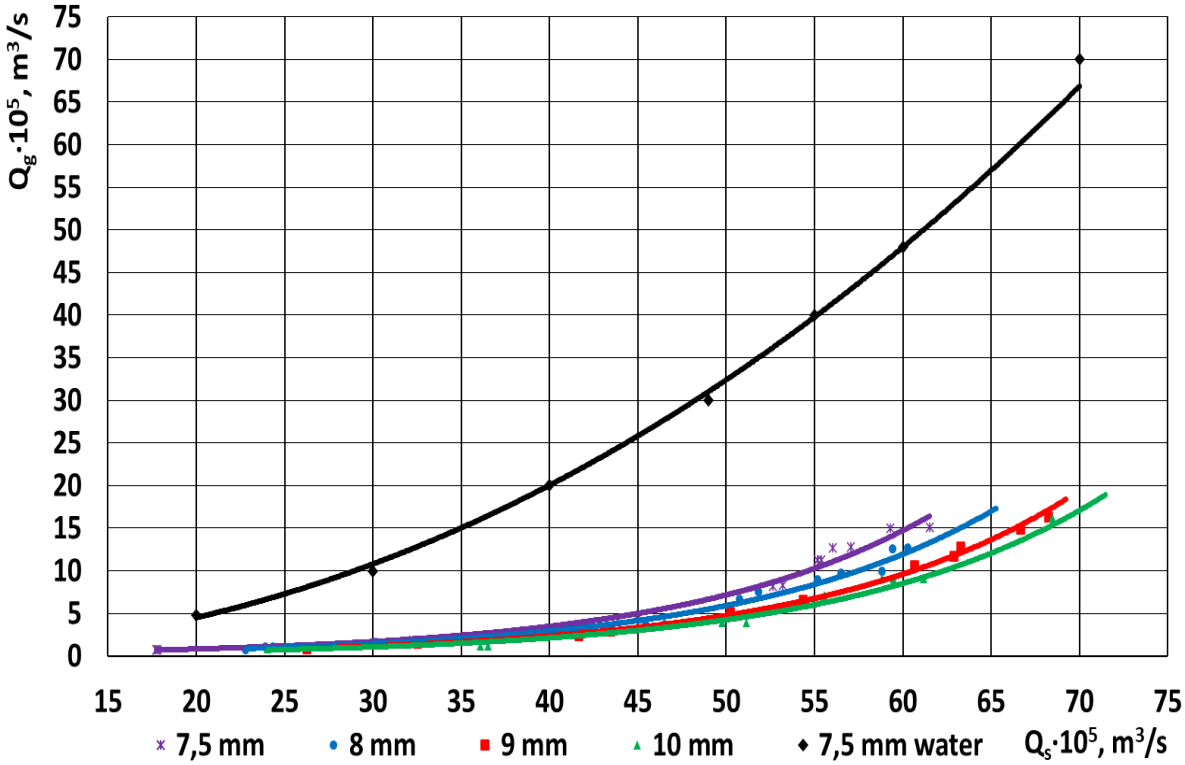

Рис. 6. Зависимость изменения $Q_г$ от $Q_с$ для различных диаметров сопел (гидромодуль 1:3).[8]

[7,8] Appendix 1

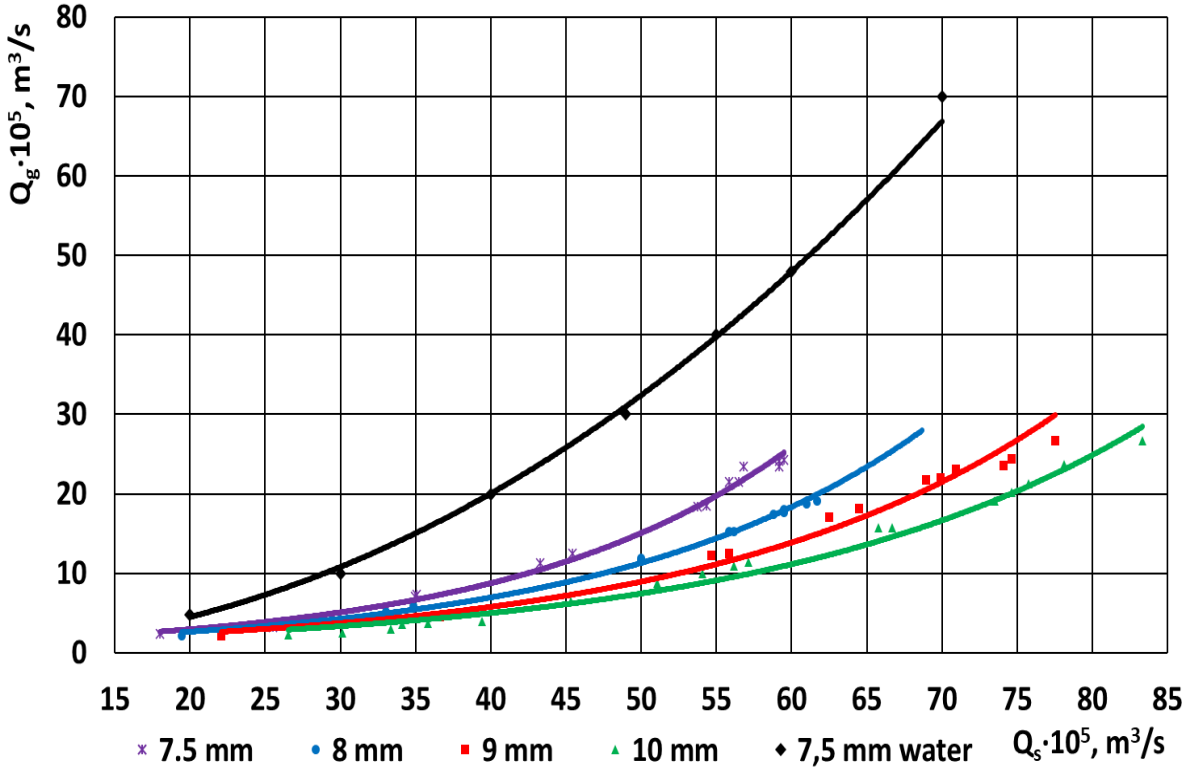

Рис. 7. Зависимость изменения $Q_г$ от $Q_с$ для различных диаметров сопел (гидромодуль 1:4)[9]

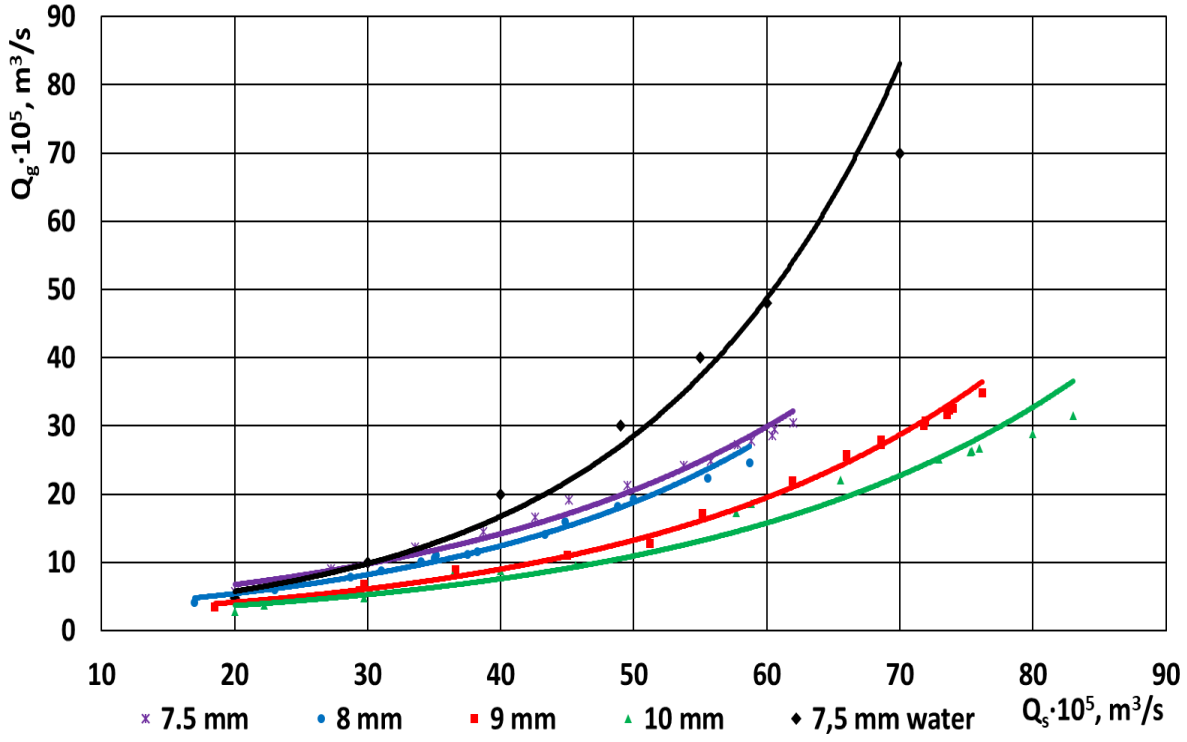

Рис.8. Зависимость изменения $Q_г$ от $Q_с$ для различных диаметров сопел (гидромодуль 1:6).[10]

[9,10] Appendix 1

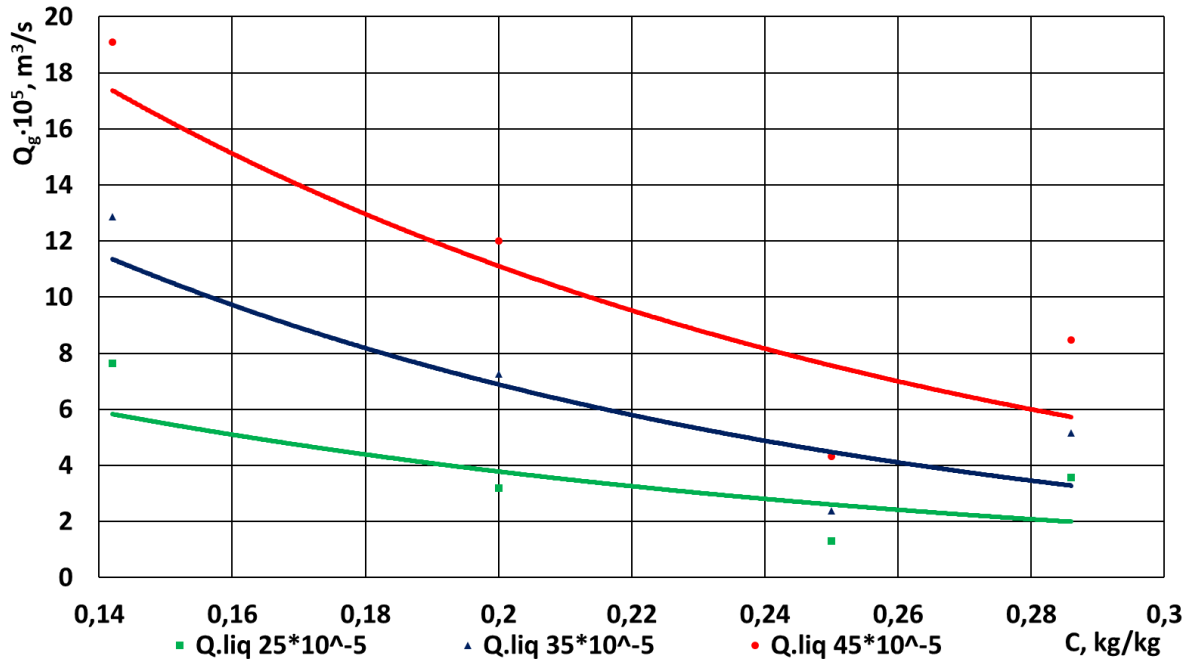

Рис. 9. Зависимость уноса газа свободной суспензионной струей от концентрации измельченного солода.[11]

Значения коэффициентов динамической вязкости суспензионной смеси заданного гидромодуля в зависимости от температуры были получены в результате дополнительных реологических исследований. В таблице 2 представлена зависимость уноса газа от диаметра сопел.

Таблица 2[12]

Результаты обработки экспериментальных данных по уносу газовой фазы свободными струями солодовых суспензий при t= 25 °C.[13]

d_0, mm	Гидромодуль (Hydromodulus)			
	1:2,5	1:3	1:4	1:6
7,5	$Q_g = 0,895 \cdot e^{0,05 \cdot Q_S}$	$Q_g = 0,195 \cdot e^{0,07 \cdot Q_S}$	$Q_g = 0,896 \cdot e^{0,056 \cdot Q_S}$	$Q_g = 3,20 \cdot e^{0,037 \cdot Q_S}$
8	$Q_g = 0,814 \cdot e^{0,05 \cdot Q_S}$	$Q_g = 0,175 \cdot e^{0,07 \cdot Q_S}$	$Q_g = 0,924 \cdot e^{0,05 \cdot Q_S}$	$Q_g = 2,360 \cdot e^{0,042 \cdot Q_S}$
9	$Q_g = 0,790 \cdot e^{0,05 \cdot Q_S}$	$Q_g = 0,142 \cdot e^{0,07 \cdot Q_S}$	$Q_g = 0,931 \cdot e^{0,045 \cdot Q_S}$	$Q_g = 1,916 \cdot e^{0,039 \cdot Q_S}$
10	$Q_g = 0,741 \cdot e^{0,05 \cdot Q_S}$	$Q_g = 0,132 \cdot e^{0,07 \cdot Q_S}$	$Q_g = 0,747 \cdot e^{0,045 \cdot Q_S}$	$Q_g = 1,760 \cdot e^{0,037 \cdot Q_S}$

ВЫВОДЫ

В данной работе представлено описание экспериментального стенда, позволяющего проводить исследования процесса инжекции газа струями водно-солодовых суспензий различной концентрации в зависимости от скорости их истечения.

Разработана методика измерения расхода воздуха, поступающего в КСИА за счет его инжектирования свободной струей водно-солодовой суспензии.

Предложенный экспериментальный стенд и описанная методика позволяют проводить исследования процесса инжекции газов для различных сред. Проведены

[11,12,13] Appendix 1

исследования по определению расхода воздуха, уносимого свободной струей, для нескольких гидромодулей водно-солодовых суспензий. В результате исследований установлены аналитические выражения для расчётов расхода воздуха, поступающего в КСИА, в зависимости от диаметра сопла, определяющего скорость истечения, и концентрации (вязкости) ВСС. Результаты исследований могут быть использованы при проектировании КСИА для различных отраслей промышленности.

Также следует отметить, что указанный экспериментальный стенд позволяет провести исследования процессов диффузии различных газов в жидкости с различной концентрацией.

APPENDIX 1 (ПРИЛОЖЕНИЕ 1)

[1]Fig.1. Schematic representation of the experimental setup for the study of hydrodynamics (I – model of the jet–injection apparatus; II storage vessel; III – circulation pump; 1 downpipe, 2 – upper pipe; 3 – drain pipe; 4 – upper tube grid; 5 – top cover; 6 – lower tube grid; 7 – partition; 8 – quick connection nozzle; 9 – receiving chamber; 10 – upper circulation chamber; 11 – transitional channel; 12 gas meter; 13 – electromagnetic liquid flowmeter; 14 – control valve, 15 – drain valve; 16, 17 – differential liquid manometers; 18 – thermometer; 19 suspension supply line; 20 – air line, 21 – mm ruler.)

[2,3]Table 1. Comparison of the values of the hydromodulus and the concentration of the solid phase in water

[4]Fig. 2. Change in the state of the free surface of the jet at its constant length as a function of the flow velocity v_0.

[5]Fig. 3. Structure and shape of the free surface of the jet at infinitely long length, v = const

[6]Fig. 4. Schematic representation of the upper gas chamber: 1 - nozzle, 2 - upper (main) gas chamber, 3 - free jet, 4 - baffle, 5 - downpipe, G - gas phase

[7]Fig. 5. Dependence of change in *Qr* on *Qc* for different nozzle diameters (hydromodulus 1:2.5)

[8]Fig. 6. Dependence of change in *Qr* on *Qc* for different nozzle diameters (hydromodulus 1:3)

[9]Fig. 7. Dependence of change in *Qr* on *Qc* for different nozzle diameters (hydromodulus1:4)

[10]Fig. 8. Dependence of change in *Qr* on *Qc* for different nozzle diameters (hydromodulus 1:6)

[11]Fig. 9. Dependence of gas entrainment by the free suspension jet on the concentration of crushed malt

[12,13]Table 2. Results of processing experimental data on gas phase entrainment by free jets of malt suspensions at t = 25 °C.

Литература (References)

[1] Gulyaeva Y.N. *Issledovanie protsessa kul'tivirovaniya khlebopekarnykh drozhzhey pri usloviyakh vysokoy kontsentratsii biomassy v kozhukhotrubnom struyno-inzhektsionnom fermentatore (KSIF).* Diss. kand. tech. nauk. [Study of the cultivation process of baking yeast under conditions of high concentration of biomass in shell-and-tube jet-injection fermenter (KSIF). Ph.D. techn. sci. diss.]. Saint-Petersburg, 1998. 153 p.

[2] Darkov G.M. *Issledovanie kinetiki rosta chistoy kul'tury pivnykh drozhzhey v kozhukhotrubnom struyno-inzhektsionnom apparate.* Diss. kand. techn. nauk. [The study of the growth kinetics of pure culture of beer yeast in shell-and-tube jet-injection fermenter. Ph.D. techn. sci. diss.]. Saint-Petersburg, 2002. 124 p.(in Russian).

[3] Ibragimov T.S. *Sovershenstvovanie mashinno-apparaturnoy skhemmy proizvodstva etilovogo spirta.* Diss. kand. tech. nauk. [Perfection of the machine-apparatus scheme of ethyl alcohol production. Ph.D. techn. sci. diss.]. Saint-Petersburg, 2014. 94 p.

[4] Selevtsov A.L. *Izuchenie zakonomernostey oksidirovaniya rastitel'nych masel v struynych techeniyach.* Diss. kand. tech. nauk. [Study of patterns of oxidation of vegetable oils in jet streams. Ph.D. techn. sci. diss.]. Saint-Petersburg, 2000. 139 p.

[5] Duzhiy A.B. *Issledovanie protsessa inzhektsii gaza svobodnymi zhidkimi struyami v kozhukhotrubnom struyno-inzhektsionnom absorbere dlya proizvodstva pishevykh produktov.* Diss. kand. tech. nauk. [Research of gas injection by free liquid jets in a shell-and-tube jet absorber for food production. Ph.D. techn. sci. diss.]. Saint-Petersburg, 2001. 136 p.

[6] Pranit M. Patil, Amol P. Yadav, Dr. P. A. Patil. [Comparative Study between Heat Transfer through Laminar Flow and Turbulent Flow]. *International Journal of Innovative Research in Science, Engineering and Technology*, 2015, no. 4. Available at: http://www.ijirset.com/upload/2015/april/76_Comparative-1.pdf. (Accessed 15.04.2023).

[7] Molana, M., Banooni, S. [Investigation of Heat Transfer Processes Involved Liquid Impingement Jets: A Review]. *Brazilian Journal of Chemical Engineering*, 2013, no. 03, pp. 413-435. Available at: https://www.scielo.br/j/bjce/a/JjxLF3TjD5X3Qrr8TsQTmZb/?format=pdf&lang=en. (Accessed 15.04.2023).

[8] Xu, Q., Liu, W., Li, W., Yao, T., Chu, X., Guo, L. [Numerical investigation on thermal hydraulic characteristics of steam jet condensation in subcooled water flow in pipes]. *International Journal of Heat and Mass*

Transfer, 2022, vol. 184. doi: 10.1016/j.ijheatmasstransfer.2021.122277.

[9] Agaev K.E. *Sovershenstvovanie gidrodinamicheskikh protsessov obrabotki pishevogo cyr'ya v kozhotrubnom struyno-inzhektsionnom apparate.* Diss. kand. tech. nauk. [Perfection of hydrodynamic processes of food raw materials processing in shell-and-tube jet-injection apparatuses. Ph.D. techn. sci. diss.].Saint-Petersburg, 2012. 148 p.

[10] Blaznov A.N. *Issledovanie i razrabotka absorbentov na osnove zhidkostno-gazovykh struynykh apparatov s udlinennoy kameroy smesheniya*. Abstract Diss. kand. tech. nauk. [Research and development of absorbers based on liquid-gas jet apparatuses with an elongated mixing chamber. Abstract Ph.D. techn. sci. diss.]. Biysk, 2001, 24 p.

[11] Sivenkov A.V. *Intensifikatsiya gidrodinamicheskikh protsessov v struynykh apparatakh pishevoy promyshlennosti.* Diss. kand. tech. nauk. [Intensification of hydrodynamic processes in jet apparatuses of food industry. Ph.D. techn. sci. diss.]. Saint-Petersburg, 2011.148 p.

[12] Shakouchi, T., Kito, M., Tsuda, M., Tsujimoto, K., Ando, T. Flow and Heat Transfer of Impinging Jet from Notched-Orifice Nozzle. *Journal of Fluid Science and Technology*, 2011, vol. 6, pp. 453–464. doi: 10.1299/jfst.6.453.

[13] A.M. Cervantes-Alvarez, Y.Y. Escobar Ortega, A. Sauret, F. Pacheco-Vazquez. Air entrainment and granular bubbles generated by a jet of grains entering water. *Journal of Colloid and Interface Science.* 2020, vol. 574, pp. 285-292. doi: 10.1016/j.jcis.2020.04.009.

[14] L.-S Fan, R Lau, C Zhu, K Vuong, W Warsito, X Wang, G Liu Evaporative liquid jets in gas–liquid–solid flow system. *Chemical Engineering Science.* 2001, vol. 56, pp. 5871-5891. doi: 10.1016/S0009-2509(01)00283-4.

[15] Tishin V.B. *Intensifikatsiya protsessov v gazozhidkostnykh plastinchatykh i kozhukhotrubnykh apparatakh pishevoy i milrobiologicheskoy promyshlennosti.* Diss. dokt. techn. nauk. [Intensification of processes in gas-liquid plate and shell-and-tube apparatuses of food and microbiological industries. Dr. techn. sci.]. Saint-Petersburg, 1998. 412 p.

[16] Blenke H. Loop reactors. *Advances in biochemical engineering.* 2006, vol. 13, pp. 121-214. doi: 10.1007/3540094687_8.

[17] Novoselov A.G., Sorokin S.A., Baranov I.V., Martyushev N.V., Rumiantceva O.N., Fedorov A.A. Comprehensive Studies of the Processes of the Molecular Transfer of the Momentum, Thermal Energy and Mass in the Nutrient Media of Biotechnological Industries. *Bioengineering*, 2022, vol. 9, no. 1, pp. 18. doi: 10.3390/bioengineering9010018.

[18] Mc Keogh E.j, Elsawy E.M. Measurements of air entrainment by vertical plunging liquid jets. *Experiments in Fluids*, 2002, vol. 32, no. 6, pp. 624-638. doi: 10.1007/s00348-001-0388-1.

[19] Mc Keogh E.J., Ervine D.A. Air entrainment rate and diffusion pattern of plunging liquid jets. *Chemical Engineering Science*, 1981, vol. 36, no. 7, pp. 1161-1172. doi: 10.1016/0009-2509(81)85064-6.

[20] Mc Carthy M.J., Molloy N.A. Review of stability of liquid jets and the influence of nozzle design. *The Chemical Engineering Journal*, 1974, vol. 7, pp. 1-20. doi: 10.1016/0300-9467(74)80021-3.

[21] Ohkawa A., Kusabaraki D., Kawai I., Sakai N., Endoh K. Some flow characteristics of a vertical liquid jet system having downcomers. *Chemical Engineering Science*, 1986, vol. .41, no. 9, pp. 2347-2361. doi: 10.1016/0009-2509(86)85085-0.

[22] Ohkawa A., Kusabaraki D., Sakai N. [Effect of nozzle length on gas entrainment characteristics of vertical liquid jet]. *Chemical Engineering Science*, 1987, vol. 20, no. 3, pp. 295-299. Available at: https://www.jstage.jst.go.jp/article/jcej1968/20/3/20_3_295/_pdf/-char/en. (Accessed 15.04.2023).

[23] Bin A.K. Minimum air entrainment velocity of vertical plunging liquid jets. *Chemical Engineering Science*, 1988, vol. 43, no. 2, pp. 379-389. doi: 10.1016/0009-2509(88)85051-6.

[24] Liang Hu, Hanghang Xu, Mingbo Li, Weiting Liu, Wenyu Chen, Haibo Xie, Xin Fu. Liquid jet formation during a suspended liquid suction process. *Experimental Thermal and Fluid Science*, 2020, vol. 114, doi: 10.1016/j.expthermflusci.2019.109952.

[25] Shuichiro Miwa, Takahiro Moribe, Kohei Tsutstumi, Takashi Hibiki. Experimental investigation of air entrainment by vertical plunging liquid jet. *Chemical Engineering Science*, 2018, vol. 181, pp. 251-263, doi: 10.1016/j.ces.2018.01.037.

[26] Henry Z. Kister, Garry Jacobs, Abraham A. Kister. Gas entrainment by liquid jets and cascades can unsettle towers. *Chemical Engineering Research and Design*, 2023, vol. 191, pp. 313-318, doi: 10.1016/j.cherd.2023.01.039.

[27] Bongliba T Sangtam, Subrata Kumar Majumder. Entrainment characteristic of liquid–liquid dispersion in a jet-driven mixing column: Substantial for process intensification in liquid–liquid extraction. *Chemical Engineering and Processing - Process Intensification*, 2020, vol. 153, doi: 10.1016/j.cep.2020.107927.

[28] Bharath Kumar Goshika, Subrata Kumar Majumder. Entrainment and holdup of gas-liquid-liquid dispersion in a downflow gas-liquid-liquid contactor. *Chemical Engineering and Processing - Process Intensification*, 2018, vol. 125, pp. 112-123, doi: 10.1016/j.cep.2018.01.011.

[29] Bharath Kumar Goshika, Subrata Kumar Majumder. Dispersion of liquid–liquid phase by a jet-induced gas–liquid–liquid mixing column developed for separation of organic pollutants. *Separation Science and Technology*, 2019, vol. 54. doi: 10.1080/01496395.2018.1504796.

[30] M. Opletal, P. Novotny, V. Linek, T. Moucha, M. Kordac. Gas suction and mass transfer in gas-liquid up-flow ejector loop reactors. Effect of nozzle and ejector geometry. *Chemical Engineering Journal*, 2018, vol. 353, pp. 436-452, doi: 10.1016/j.cej.2018.07.079.

[31] Tong Li, A-Man Zhang, Shi-Ping Wang, Shuai Li, and Wen-Tao Liu. Bubble interactions and bursting behaviors near a free surface. *Physics of Fluids*, 2019, vol. 31, doi: 10.1063/1.5088528

Сведения об авторах.

Малахов Юрий Леонидович
Университет ИТМО, аспирант
E-mail: yuri.malakhov@kersia-group.com
Область научных интересов: пищевая безопасность, процессы и аппараты пищевых производств

Кузнецов Александр Юрьевич
Университет ИТМО, аспирант
E-mail: sasha_2731@mail.ru
Область научных интересов: процессы тепло-массообмена

Баранов Игорь Владимирович
Университет ИТМО, профессор, д.т.н.
E-mail: barigor@mail.ru
Область научных интересов: теплофизические свойства продуктов

Миронова Дарья Юрьевна
Университет ИТМО, доцент, к.э.н.
E-mail: mironova@itmo.ru
Области научных интересов: промышленный симбиоз, управление инновациями

Новоселов Александр Геннадьевич.
Университет ИТМО, профессор, д.т.н.
E-mail: agnovoselov@itmo.ru
Область научных интересов: процессы тепло-массообмена

Чеботарь Анастасия Викторовна
Университет ИТМО, к.т.н.
E-mail: avchebotar@itmo.ru
Область научных интересов: процессы и аппараты пищевых производств

Румянцева Ольга Николаевна
Университет ИТМО, доцент к.т.н.
Область научных интересов: холодильная технология пищевых продуктов
E-mail: rumiantseva@itmo.ru

Electrodynamic Technologies in the Eco-industry of Food and Pharmaceutical Production

Burdo O.G.[1], Levitsky A.P.[1], Trishyn F.A.[1], Terziev S. G.[2], Sirotyuk I.V.[1], Burdo A.K.[1], Lapinska A.P.[1], Molchanov M.Yu.[1]

[1]Odesa National University of Technology, Odesa, Ukraine
[2]PRJSC "ENNI FOODS", Odesa, Ukraine

***Abstract*.** The growing interest in the world for research on microwave processing technologies of raw materials is shown. It has been established that information in available sources is only about laboratory-scale equipment, and theoretical information (models, mechanisms, calculation methods) is practically absent. The aim of the work is to conduct systematic studies in the "extractor — dehydrator — plant material" scheme. To achieve the goal, these electrodynamical systems are presented with parametric, mathematical, and experimental models. The most significant result of the work is that the concept of a "hybrid" process is introduced to explain the mechanism of interaction between the electromagnetic field and the raw material. Using the first law of thermodynamics, it is shown that the "hybrid" process performs work to move the solution from the volume of the material to its surface. As a result, sluggish diffusion processes are accompanied by powerful flows, the driving force of which is the pressure difference in the capillary of the material and the environment. The importance of the work is that new effects are established: mechanodiffusional and vapordynamical. Mechanodiffusional allows obtaining polyextracts in one extractor, and vapordynamical allows the dehydration of the solid phase in the form of two parallel streams — vapor and juice. Experiments were conducted with rosehip fruits, soybeans, tomato squeezes, and sunflower meal. It is shown that electrodynamical dehydrators are characterized by stable performance indicators of vapor generation up to concentrations of 85°brix, at low levels of energy consumption. The results of chemical studies of the obtained samples in electrodynamical devices are presented.

***Keywords*:** electrodymanic apparatuses, energy technologies, extraction, evaporation, drying, mathematical and experimental modeling, food and medicinal plant raw material.

DOI: https://doi.org/10.52254/1857-0070.2023.2-58-11
UDC: 621.31: 67.03-035[615:664]:66.048:519.87

Tehnologii electrodinamice în eco-industria alimentară și farmaceutică

Burdo O.G.[1], Levițkii A.P.[1], Trișîn F.A.[1], Terziev S. G.[2], Sirotiuk I.V.[1], Burdo A.K.[1], Lapinskaia A.P.[1], Molceanov M.Iu.[1]

[1] Universitatrea Națională Tehnologică din Odesa, Odesa, Ucraina
[2]SA «ENNI FOODS», Odesa, Ucraina

Rezumat. Este fundamentată relevanța problemei eficienței resurselor energetice în tehnologiile alimentare și farmaceutice. Se arată creșterea interesului în lume pentru cercetarea tehnologiilor cu microunde pentru prelucrarea materiilor prime. Sunt date exemple de utilizare cu succes a extractoarelor și evaporatoarelor cu microunde în prelucrarea materialelor vegetale medicinale și alimentare. S-a stabilit că sursele disponibile conțin informații doar despre dispozitivele la scară de laborator, în timp ce informațiile teoretice (modele, mecanisme, metode de calcul) sunt practic absente. Scopul lucrării este de a efectua cercetări sistematice în schema „extractor – deshidrator – materii prime vegetale". Pentru atingerea acestui scop, aceste sisteme electrodinamice sunt reprezentate prin modele parametrice, matematice și experimentale. Se propune o clasificare a sistemelor electrodinamice. Cel mai semnificativ rezultat al lucrării este că conceptul de proces „hibrid" este introdus pentru a explica mecanismul de interacțiune dintre câmpul electromagnetic și materiile prime. Acest proces este inițiat de un câmp electromagnetic, bazat pe specificul materialelor vegetale. Folosind prima lege a termodinamicii, se arată că procesul „hibrid" funcționează pentru a muta soluția din cea mai mare parte a materiei prime la suprafața sa. Ca urmare, procesele de difuzie lente sunt însoțite de fluxuri puternice, a căror forță motrice este diferența de presiune în capilarul materiei prime și a mediului. Semnificația lucrării este că au fost stabilite efecte noi: mecanodifuziune și parodinamică. Metoda mecanodifuziei face posibilă obținerea de poliextracte într-un singur extractor, iar metoda dinamică cu abur permite deshidratarea fazei solide sub forma a

două fluxuri paralele - abur și suc. Și acestea sunt toate premisele pentru o reducere semnificativă a resurselor energetice în prelucrarea industrială a materialelor vegetale.
Cuvinte-cheie: aparate electrodinamice, tehnologii energetice, extracție, evaporare, uscare, modelare matematică și experimentală, materie primă alimentară și plante medicinale.

Электродинамические технологии в экоиндустрии пищевых и фармацевтических производств

Бурдо О.Г.[1], Левицкий А.П.[1], Тришин Ф.А.[1], Терзиев С.Г.[2], Сиротюк И.В.[1], Бурдо А.К.[1], Лапинская А.П.[1], Молчанов М.Ю.[1]

[1] Одесский национальный технологический университет, Одесса, Украина

[2]ЧАО «ENNI FOODS», г. Одесса, Украина

***Аннотация*.** Обоснована актуальность проблемы ресурсо-энергоэффективности в пищевых и фармацевтических технологиях. Показан рост интереса в мире к исследованиям микроволновых технологий переработки сырья. Приведены примеры успешного применения микроволновых экстракторов и выпарных аппаратов при переработке лекарственного и пищевого растительного сырья. Установлено, что в доступных источниках есть информация только об аппаратах лабораторного масштаба, сведения теоретического характера (модели, механизмы, методы расчета) практически отсутствуют. В работе поставлена цель: провести системные исследования в схеме «экстрактор — дегидратор — растительное сырье». Для достижения поставленной цели эти электродинамические системы представлены параметрической, математической и экспериментальными моделями. Предложена классификация электродинамических систем. Наиболее существенным результатом работы является то, что для объяснения механизма взаимодействия электромагнитного поля и сырья введено понятие «гибридный» процесс. Этот процесс инициируется электромагнитным полем, базируется на специфике растительного сырья. С привлечением первого закона термодинамики показано, что «гибридный» процесс совершает работу по перемещению раствора из объема сырья на его поверхность. В результате вялые диффузионные процессы сопровождаются мощными потоками, движущей силой которых являются разность давлений в капилляре сырья и среды. Значимость работы в том, что установлены новые эффекты: механодиффузионный и пародинамический. Механодиффузионный позволяет получать в одном экстракторе полиэкстракты, а пародинамический — осуществлять дегидратацию твердой фазы в виде параллельных двух потоков — пара и сока. А это все предпосылки существенного сокращения энергетических ресурсов при промышленной переработке растительного сырья. Выдвинутые положения подтверждены экспериментом. Опыты проводились с плодами шиповника, соей, томатными выжимками и шротом подсолнечника. Показано, что электродинамические дегидраторы характеризуются стабильными показателями паропроизводительности вплоть до концентраций 85°brix, при низких уровнях энергетических затрат. Приведены результаты химических исследований, полученных в электродинамических аппаратах образцов.
***Ключевые слова*:** электродинамические аппараты, энерготехнологии, экстрагирование, выпарка, сушка, математическое и экспериментальное моделирование, пищевое и лекарственное растительное сырье.

INTRODUCTION

During the processing of plant material, the key processes in food and pharmaceutical production are extraction, evaporation, and drying. Traditional equipment for these processes has a number of common drawbacks, such as long processing times, insufficient process intensity, use of expensive agents, damage to the final product, high energy costs, and high labor intensity. Moreover, some traditional equipment does not allow for the preservation of ecological safety of the production [1—2]. Dirty heat carriers, gasoline, and other environmentally unfriendly solvents are used as extractants. There are often cases of significant losses of the product itself, raw materials, and wasteful use of energy resources [3—6]. All of these determine the relevance of searching for new approaches to creating modern equipment.

Currently, one of the innovative ways to improve heat and mass exchange equipment in the world is considered to be the use of electromagnetically dynamic systems, which are characterized by high specific power effects on biomass placed in the reactor chamber. Thus, the power of microwaves decisively affects the drying rate, effective moisture diffusion, and drying time. As the power of microwaves increases, the drying rate and effective moisture diffusion capacity increase, and the drying time is reduced. Positive results of using microwave have been obtained in the drying of oil camellia seeds [7], as well as in the drying of corn and apple slices [8]. Energy costs for microwave drying are much lower than for electric thermal

drying with the same load. The issues of modeling drying lines in a periodic microwave regime have been studied in [9], and a good agreement with the experiment has been obtained.

During the drying of kivano seeds (African cucumber), the influence of microwave drying and sublimation drying methods on the chemical composition, organoleptic, textural, and antioxidant properties of kivano seeds, as well as the potential of microwave drying as an alternative to sublimation drying, was studied. For this purpose, kivano seeds were dried using a lyophilizer and a microwave dryer. The protein, ash, fat, fiber, vitamin C, beta-carotene, total phenolic content, antioxidant, textural, and organoleptic properties of the dried seeds were compared. Microwave drying increased the total phenolic content in kivano seeds and reduced the drying time. This study showed that the microwave drying could become a promising innovative alternative for the rapid production of freeze-dried fruit materials while maintaining product quality [10]. Optimization of drying conditions for the production of high-quality dried pineapples was carried out using microwave pre-treatment before the conventional hot-air drying. It was demonstrated that the microwave pre-treatment should be considered as a stage of the industrial pineapple and other products processing to reduce drying time and obtain higher quality products [11].

For the first time, the kinetics of drying and dehydration of sliced bitter melon was investigated using low-temperature microwave drying. The power density of the microwaves played a crucial role in the dehydration characteristics of the dried bitter melon during microwave drying [12]. In the study of microwave drying of green turnip, the adjustable microwave falling power was preferred for improving product quality and reducing energy consumption. A power control strategy for microwave drying of green turnip cylindrical roots was proposed by comparing continuous and intermittent microwave drying with gradually decreasing microwave power based on experimentally determined dielectric properties and changes in the electric field intensity with respect to the temporary moisture content. The experiments showed that such power regulation leads to a higher dehydration coefficient of the dried green turnip and a significant reduction in energy consumption compared to continuous and intermittent microwave drying. Additionally, this power control strategy can maintain the material temperature within specified values with small fluctuations [13]. The effect of microwave power, vacuum degree, and loading weight on the moisture content of seedless white grapes during microwave vacuum drying was studied. It was found that during microwave vacuum drying, the effective moisture diffusion coefficient of seedless white grapes varied from 1.0232×10^{-9} to 4.6354×10^{-9} m^2/s [14].

During the study of the evaporation process, cherry nectar and apple juice were concentrated using traditional thermal methods and intermittent microwave concentration under vacuum conditions (at 250 mbar). The total phenol content in the apple juice and cherry nectar samples varied within the range of 209.87—216.67 mg/L and 571—588.57 mg/L, respectively [15]. Barberry juice was concentrated using two different methods (indirect heating and microwave evaporation at pressures of 100 and 30 kPa) until reaching 60 Brix degrees. The results showed that the microwave evaporation rate was 49% higher than that of indirect heating. In addition, the use of this method can better preserve the anthocyanin content, antioxidant activity, and total phenol content in barberry juice compared to the traditional method [16]. During the concentration of orange juice using microwave vacuum evaporation (MVE) and rotary evaporation (RE), the kinetics of vitamin C degradation, total phenolic content (TPC), total carotenoid content (TCC), and color values were investigated. MVE significantly increased the evaporation rate. Results showed that the degradation rate constants of vitamin C, TPC, and TCC in orange juices concentrated using RE were significantly higher than those using MVE [17]. The use of microwaves as an alternative to traditional evaporation methods was investigated for concentrating sugar solutions. Moreover, dielectric spectroscopy can be an effective tool to help use MVE for obtaining high-quality sugars [18]. It was found that microwave heating can be used for pineapple juice concentration with minimal impact on quality characteristics [19]. Positive results were obtained from the use of microwaves in drying and extraction during processing of alfalfa. The method was optimized with regard both to drying and extraction, and modes of minimal energy consumption were recommended [20].

Thus, the key processes in the processing of plant raw materials are extraction and

dehydration. Mass transfer processes are multifactorial (Fig. 1) and require priority resolution.

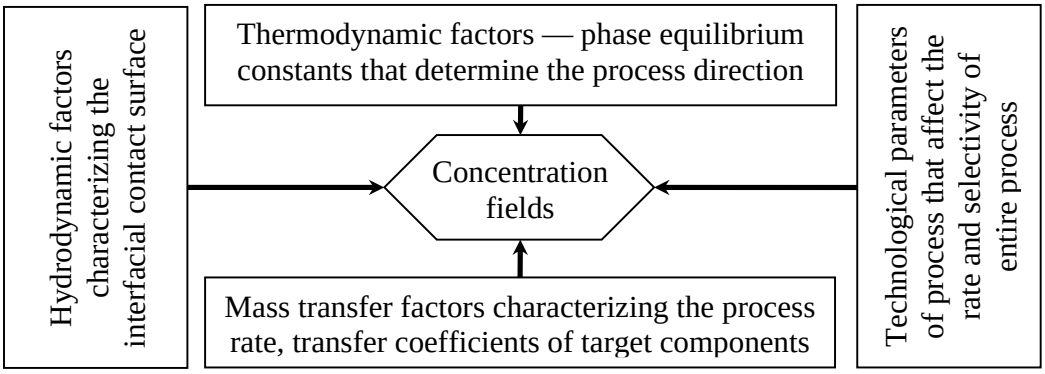

Fig. 1. Factors determining mass transfer process.

The literature review conducted allows us to draw two conclusions. The first one is that there are scientific and technical contradictions for traditional technologies of plant raw material processing [21]. As the temperature increases, the intensity of the mass transfer process increases, however, the rate of degradation of thermolabile elements also increases. Therefore, the level of thermal exposure should be chosen based on both physical and chemical research.

The second conclusion is that the use of microwave technologies allows for a significant increase in the efficiency of the process even at room temperatures, to increase the mass transfer characteristics of equipment, to sharply reduce energy costs, and to make some processes more environmentally friendly. However, all known studies are limited to laboratory scale.

The task of the work is to solve the formulated problems by using developed electrodynamical systems in ONUT (Odesa National University of Technology) [21]. The solution is based on two hypotheses.

1. "The use of substances with polar molecules as extractants and the transition to electromagnetic principles of energy supply will allow for the extraction of target components from raw materials in the form of two streams: traditional diffusion and additional hydrodynamic, with the power of the latter being able to exceed the former by orders of magnitude."
2. "The inclusion of hydrodynamic driving force in the transport process will ensure the extraction of a wider range of target components from the raw material, as it will be possible to extract not only components soluble in this extractant, which will solve the problem of polyextracts."

CLASSIFICATION AND DEVELOPMENT OF SCIENTIFIC FOUNDATIONS OF ELECTRODYNAMIC TECHNOLOGIES

Let's consider the classification of electrodynamic technologies developed at ONUT (Fig. 2).

Regarding the object of research — food and medicinal plant raw materials — let us develop the scientific basis of electrodynamic technologies at the level of static and kinetic models.

In this work, when developing static models of electrodynamic systems, two consecutive processes are considered: extraction and dehydration of the extract, for example, by evaporation (Fig. 3). By mixing the plant raw material G_r and the solvent G_{ex}, the necessary hydrodynamic modulus is achieved. The extractor outputs a stream of extract, the amount of which is G_e, and the concentration of target components is X_e. It is possible to obtain a more concentrated product in the amount of G_p and at the concentration of X_p by evaporating the solvent from the extract. The solvent vapor, in the amount of G_{ex}, is directed to the mixer or condensed.

In the process of extraction, as a rule, the characteristics of the raw material (G_R, C_R) are known. The objectives of the calculations may be: the concentration of the target components X_S and the amount of the resulting sludge G_S (Fig. 3), or the content of extractive substances in the solution. Equations of material balance

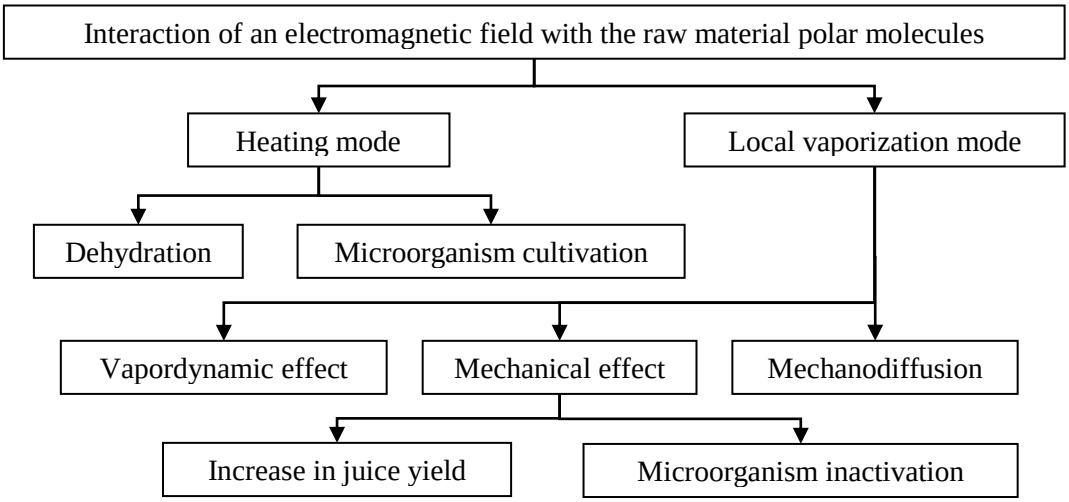

Fig. 2. Classification of specific effects in the electrodynamic systems.

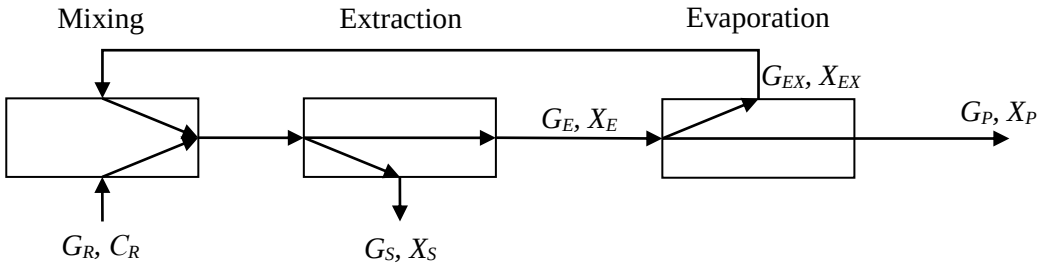

Fig. 3. Material flows scheme. [1]

$$\left.\begin{aligned} G_{EX} + G_R &= G_E + G_S \\ G_{EX} X_{EX} + G_R C_R &= G_E X_E + G_S X_S \end{aligned}\right\} \quad (1)$$

are found from the values of:

$$X_S = X_E - \frac{G_{EX} X_{EX} + G_R C_R - G_E X_E}{G_{EX} + G_R - G_E} \quad (2)$$

$$X_{EX} = \frac{G_E X_E - G_P C_P}{G_E - G_P} \quad (3)$$

The analytical studies of the kinetics of the extraction process include a thermophysical model of the extraction stages, a model of a heterogeneous cell consisting of a solid phase, an extractant, and a boundary layer at the phase contact boundaries. The mathematical description is based on the idea of A.V. Lykov's drying model, P.A. Rehbinder's concepts of moisture bonding forms, and mass transfer mechanisms developed by the authors of [21].

Then, the differential equation of heat and mass transfer will have the form

In (4): K_{ij} — are the phenomenological coefficients; P — is the pressure; t — is temperature; C — are the concentrations of target components; subscripts: $_P$ — is at the surface; $_M$ — is in the intercellular space; $_K$ — is in the cellular structure of the raw material.

The mathematical model (4) is complex in practical implementation due to an uncertainty in calculating the phenomenological coefficients.

Let's simplify the task of modeling the mass transfer process. The physical scheme of the process (Fig. 4) is represented by a channel located in the solid phase of the raw material and filled with an extractant.

The following assumptions were made in formulating the modeling problem:

— all target components of the raw material are expressed as a common complex;
— following the moisture binding model of Rehbinder, the complex is considered on the surface and in the volume (in capillaries and cells);
— for each time interval (zone), the transfer coefficients are assumed to be constant;

[1] Appendix 1

— the solid body has a poly-capillary structure whose transfer of target components occurs by diffusion;

— the structure of the solid body remains unchanged during the mass transfer process.

$$\left.\begin{aligned}
\frac{\partial U_P}{\partial \tau} &= K_{11}\nabla^2 U_P + K_{12}\nabla^2 U_K + K_{13}\nabla^2 U_A + K_{14}\nabla^2 t + K_{15}\nabla^2 P \\
\frac{\partial U_K}{\partial \tau} &= K_{21}\nabla^2 U_P + K_{22}\nabla^2 U_M + K_{23}\nabla^2 U_K + K_{24}\nabla^2 t + K_{25}\nabla^2 P \\
\frac{\partial U_A}{\partial \tau} &= K_{31}\nabla^2 U_P + K_{32}\nabla^2 U_M + K_{33}\nabla^2 U_K + K_{34}\nabla^2 t + K_{35}\nabla^2 P \\
\frac{\partial t}{\partial \tau} &= K_{41}\nabla^2 U_P + K_{42}\nabla^2 U_M + K_{43}\nabla^2 U_K + K_{44}\nabla^2 t + K_{45}\nabla^2 P \\
\frac{\partial P}{\partial \tau} &= K_{51}\nabla^2 U_P + K_{52}\nabla^2 U_K + K_{53}\nabla^2 U_A + K_{54}\nabla^2 t + K_{55}\nabla^2 P
\end{aligned}\right\} \quad (4)$$

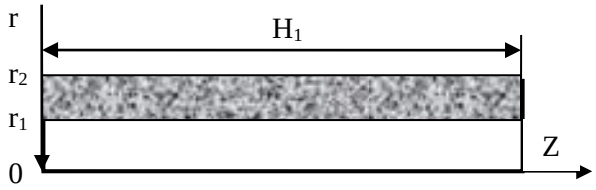

r_1 – internal radius of channel;
r_2 – external radius of solid phase;
H_1 – channel length

Fig. 4. Physical scheme of mass transfer process.

The mathematical model presented in the article reflects the coupled processes of hydrodynamics, heat transfer, and mass transfer, i.e. it contains the Navier—Stokes equations, continuity and energy equations with corresponding uniqueness conditions. Electromagnetic energy is volumetrically supplied, with power N and boundary conditions of the second kind $(N = const)$. The analytical model of the axisymmetric scheme is written in cylindrical coordinates [21]. The mathematical model for the heating stage and the stage of vapor phase formation includes energy equations, a one-dimensional Fick's equation establishing a non-stationary concentration field in the system. It is shown [21] that in addition to the traditional diffusive mass transfer, Fick's equation also allows for the possibility of convective transport of the target elements. The authors attempted to use this possibility to intensify the mass transfer processes.

This is precisely the basis for the second hypothesis formulated above. In the depth of the solid phase capillary, a vapor bubble is formed using the microwaves. As a result, the pressure in the capillary sharply increases, and a hydrodynamic driving force arises, which "ejects" the contents of the capillary at a speed corresponding to the main hydrodynamic equation [21].

The task set in the work is to organize the output of the solution from the capillary channel at a speed of w. To do this, an auxiliary process is carried out, which the authors referred to as "hybrid". The concept of forming the hybrid process is based on the difference in temperature and moisture content gradients in the raw material in traditional and electromagnetically assisted technologies (Fig. 5).

Let's write the first law of thermodynamics for the schemes (Fig. 5).

For the traditional scheme, the supplied energy (Q)is spent only for an increase in the internal energy (ΔU_T),and no work is done $A_T = 0$.

$$Q = \Delta U_T + A_T \quad (5)$$

From the heat balance equation, the change in the internal energy is proportional to the product volume (V), its density (ρ) and the difference in enthalpies at the end (i_K) and beginning of the process (i_H).

$$\Delta U_T = V \times \rho \times (i_K - i_H) \quad (6)$$

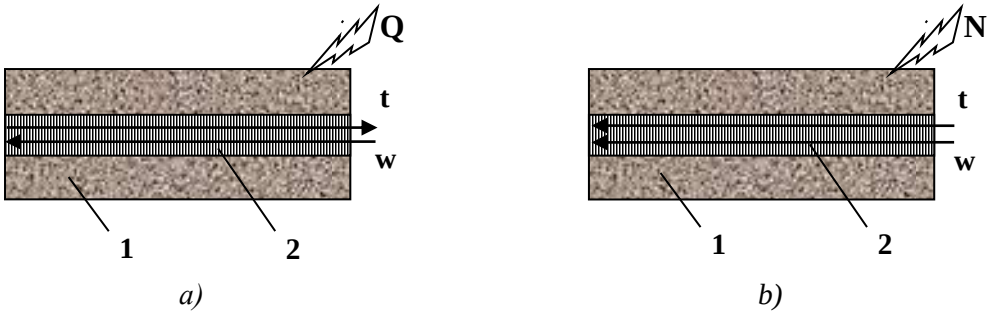

Fig. 5. Temperature (t) and moisture contents (w) gradients during traditional drying (a) and hybrid processes (b).

In the case of the innovative, hybrid process (index i)

$$Q = \Delta U_I + A_I \tag{7}$$

there are differences both in the nature of the energy source, the power of the magnetron (N_E), and its efficiency (η): $Q = \eta \times N_E$, as well as in the distribution of energy flow. Part of it goes to increase the internal energy

$$\Delta U_I = V \times \rho \times (i_K - i_H) \tag{8}$$

and part of it goes to perform the work

$$A_I = F \times L = \frac{\Delta P}{S} \times L \tag{9}$$

The value of work is proportional to the force acting on the liquid (F) and the length of its transportation (L). The force (F) is determined by the increase in the capillary pressure (ΔP), which is determined by the main hydrodynamic equation [21]. Thus, a portion of the liquid in the capillary, whose volume (V) is displaced to the open end of the capillary due to the work of the pressure forces (ΔP). The work of the hybrid process determines the formation of barodiffusion, mechanodiffusion, or vapordynamic flow. Moreover, the power of microwaves can easily be used to regulate the development of the hybrid process. It becomes possible to form polyextracts in a microwave extractor [21].

Thus, the use of technology for targeted delivery of energy to individual phases of the raw material can radically change the hydrodynamic situation and significantly intensify the mass transfer process. In processes of combined effects on the cell, various known and unexpected effects are possible.

The hybrid process is approximately represented by a model of the functioning of a point source. The model is universal, however, like all models of this class, it is extremely difficult to be implemented in practice.

Analytical solution of the model presented is impossible, despite the serious assumptions made in setting the problem.

The complexity of the solution is associated with problems in implementing the Navier—Stokes equation and calculating the radial and axial components of velocity.

Using similarity theory methods, it is possible to significantly simplify the model and pass to the relationships that describe quasi-stationary transport processes within a limited range.

For this purpose, a parametric model of the extractor with the organization of the hybrid process and microwave dryer will be developed (Fig. 6).

In general, the effective mass transfer coefficient $\beta_э$ is influenced by the height of the raw material layer H, the density ρ and viscosity μ of the extractant, the velocity of its movement w, and the diffusion coefficient D. This group of parameters characterizes the inertial properties of the flow. The hydrodynamic situation during the formation of the boundary layer in the channel is expressed by the ratio of layer height H to the length (diameter) of layer L.

The contribution of natural convection is established by the concentration difference in the flow ΔX and the gravitational field. The action of barodiffusion due to the microwave field is determined by the pressure difference in the channel zones.

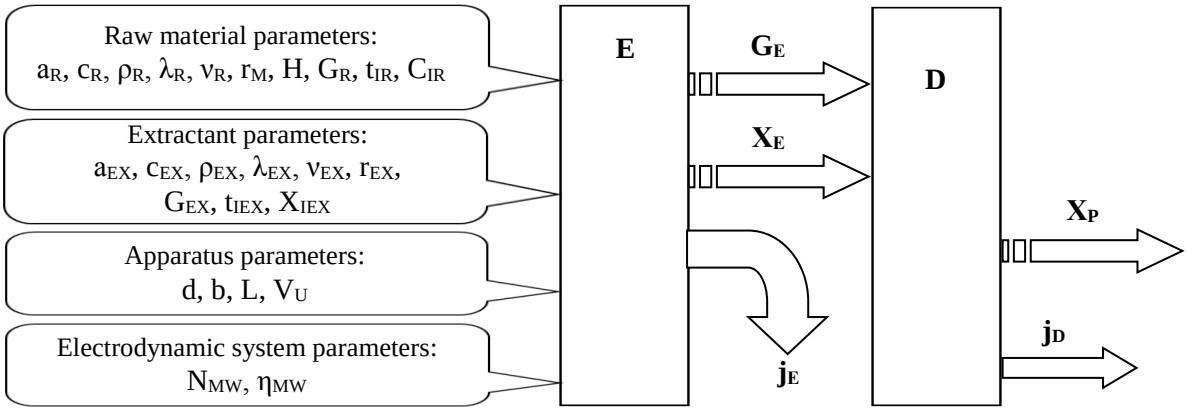

Fig. 6. Parametrical model of "Extractor — Dehydrator" system. [2]

The magnitude of this difference is proportional to the radiation energy and the energy required for vaporization. That is, to the specific heat of vaporization r and the power of the field N.

Then the initial functional dependence of the general form for the effective mass transfer coefficient will be $\beta_{\Im}=f\left(H, L, r, m, w, D, r, N, k, \Delta X, g\right)$. Using similarity theory methods, the following criterial dependence is obtained:

$$St_m = A\times\left(Re\right)^m\times\left(Gr_{\partial}\right)^g\times\left(Sc\right)^n\times\left(Bu\right)^p\times\left(L/H\right)^q\times\left(\Pi\right)^k \quad (10)$$

For the conditions of the analyzed problem, we can neglect the parameter complex Π, which is a measure of the turbulence of the hydrodynamic boundary layer in the inlet zone and is characteristic for short channels, as well as the Grashof number $\left(Gr_{\partial}\right)$, since the contribution of natural convection is small in the inertial flow regime. Finally, the structure of the criterial equation will be:

$$St_m = A\times\left(Re\right)^m\times\left(Sc\right)^n\times\left(Bu\right)^p\times\left(L/H\right)^q \quad (11)$$

Similarly, for vacuum microwave extractors with a reverse refrigerator, the following is obtained:

$$Nu_m = B\times\left(Sc\right)^n\times\left(Bu\right)^p\times\left(L/H\right)^q \quad (12)$$

The task of experimental modeling is to determine the constants *A, m, n, p,* and *q* in the equation (11).

Extraction experiments were conducted using [illegible] fruits in the pressure range of 0.01—0.1 [illegible]es up to 50°C, and hydraulic ratios of 1:1—1:4.

Four different extraction methods were investigated on four stands. Stand #1 contained a thermostat with traditional extraction methods being investigated on it. Stand #2 was assembled based on a microwave chamber. The raw material layer was located in the extractant volume. Stand #3 (ONUT design) consisted of a microwave extractor, a refrigeration unit, and a circulation pump for pumping the extractant through the raw material layer. Stand #4 was developed based on a vacuum microwave extractor and a reverse refrigerator.

During the experiments, the following parameters were periodically measured: temperatures (using a FLIR TG165 thermal imager and thermocouples) — t; extractant flow rate (by weight method) — V_{EX}; microwave field duration — τ_{MW}; magnetron power $\left(N_{MW}\right)$; optical density of the solution (using Spekol) — $Д$; extract concentration X (using the digital refractometer HI 96801); registration time of the parameters — τ. The initial parameters of the experiments are calculated: extract concentration $\left(X_E\right)$ (based on calibration dependence); hydro module $\left(\Gamma\right)$; microwave energy flow rate $\left(E_{MW}\right)$.

The obtained data allowed us to calculate the mass of substances transferred into the solution

[2] Appendix 1

(13) and the concentrations of target components in the fruits (14).

$$m = X_E \times V_E \times \rho_E \quad (13)$$

$$C_i = C_{in} - X_E / \Gamma \quad (14)$$

where C_{in} is the initial content of target components in the fruits.

The following relationship was used to calculate the mass transfer coefficient:

$$\beta = V_E / (C_{in} - C_i) \times F \quad (15)$$

The independent effects of the type of energy, processing time, and temperature on the intensity of mass transfer were sequentially studied. The type of energy input had the greatest impact (Fig. 7).

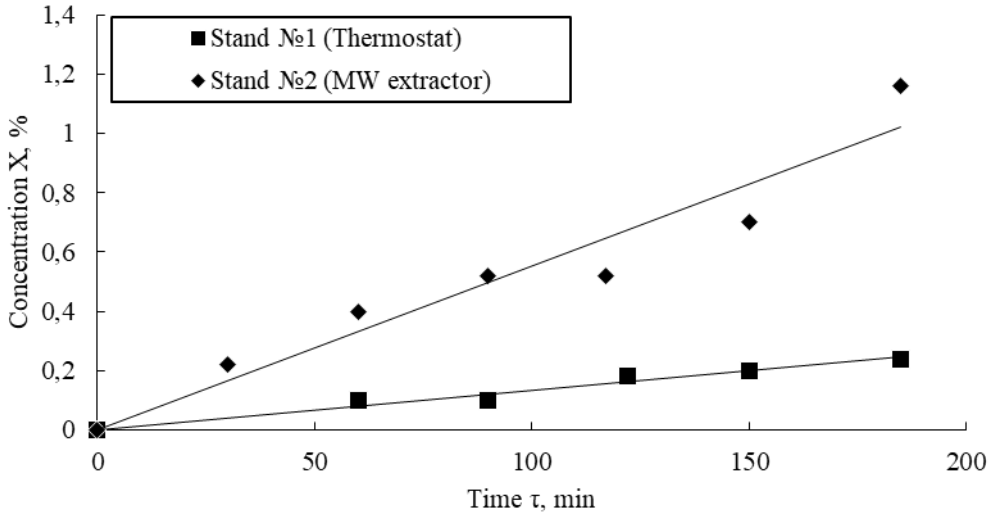

Fig. 7. Extraction kinetics in a fixed bed.

It can be seen (Fig. 7) that when processed in a microwave field, the yield of extractive substances was 5 times higher than that in thermal extraction. The influence of the degree of grinding of the fruits was determined (Fig. 8).

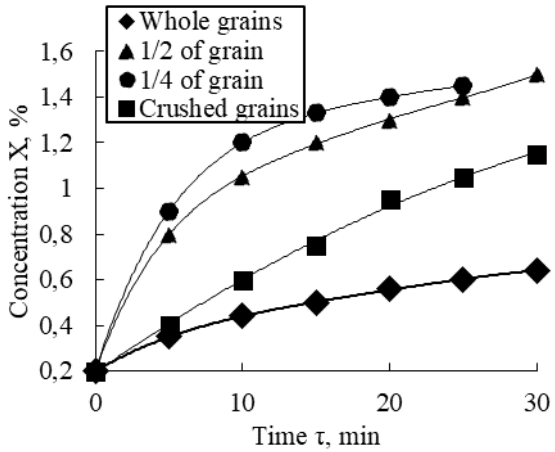

Fig. 8. Effect of grinding degree.

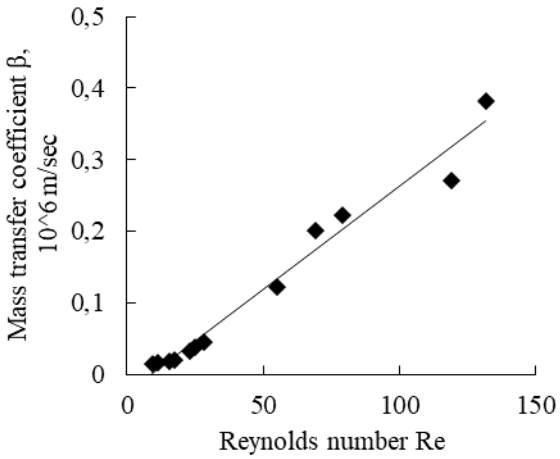

Fig. 9. Effect of extractant flow.

In terms of technological factors, preference should be given to berry halves. Therefore, further research was carried out specifically with berry halves. The second stage of the study is dedicated to working on stand #3. The main task was to establish the effect of extractant flow rate (Fig. 8). It was found that with a fivefold increase in flow rate, the intensity of extraction increases by 10 times. Processing the experimental results established the dependence of the mass transfer coefficient on the Reynolds number (Fig. 9).

The third stage of experimental research was carried out on stand #4. In the microwave chamber 1 (Fig. 10), a reactor 2 made of radio-transparent material was placed. The reactor was

filled with raw materials and extractant 3. The vapor outlet from 2 was directed to the reverse refrigerator 4. The stability of pressure and temperature was achieved by matching the microwave power with the vacuum system 6 and the flow rate of cold water from the refrigeration machine 5. A special attention was paid to the reliability of sealing the "reactor—reverse refrigerator" nodes. Therefore, the vacuum pump was usually turned on only when the stand was started.

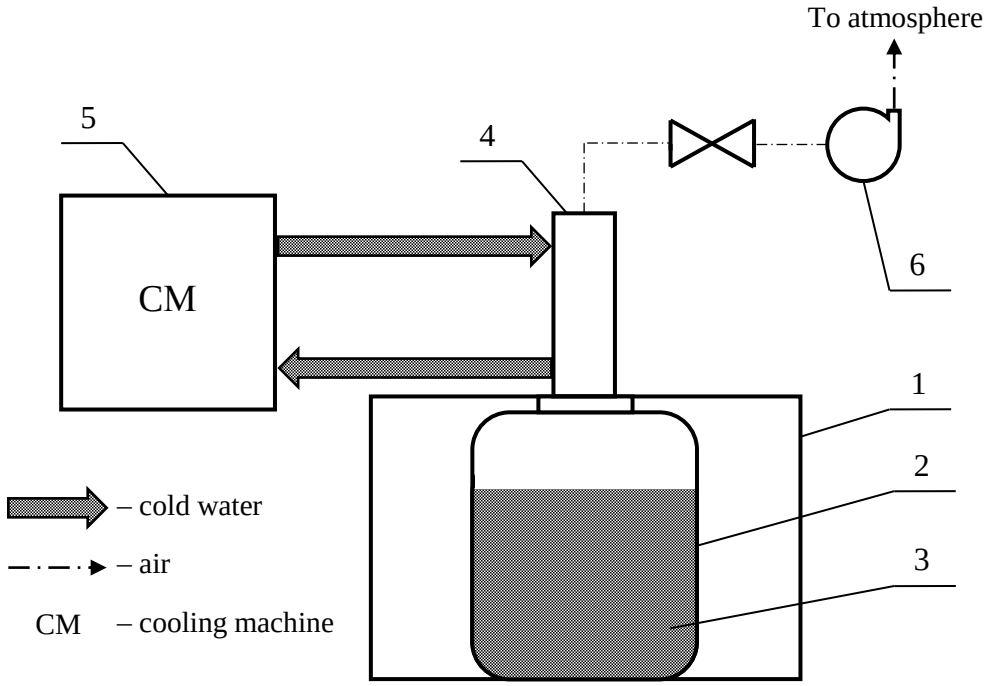

Fig. 5. Stand (№4) with microwave vacuum plant.

At the first stage, a comparison was made of the efficiency of extraction in a flow without a microwave field, with a microwave field, and with a vacuum microwave extractor. Experiments were carried out with halves of rosehip fruits under the same temperature conditions. The results are shown in Fig. 11.

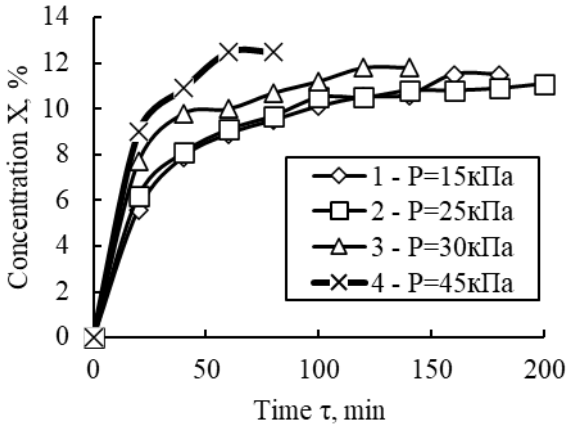

Fig. 11. Extraction kinetics for plants №3 and №4.

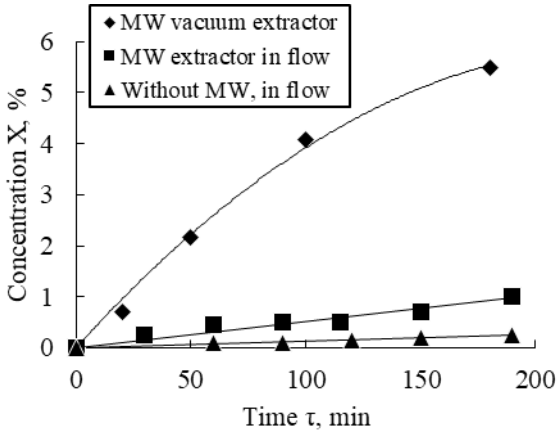

Fig. 12. Pressure effect on extraction kinetics.

As seen in Fig. 11, the effect of vacuum is apparent. The influence of pressure in the chamber on the intensity of extraction was determined (Fig. 12). With an increase in pressure from 15 kPa to 45 kPa, the extract concentration increased by 25%. However, at the same time, the extraction temperature also increased, which could have a negative impact on the content of ascorbic acid.

Thus, the contradiction between the intensity of extraction and the preservation of vitamin C should be resolved based on chemical analysis of the extract samples. The determining factor that affects the kinetics of extraction is the power of the microwave field (Fig. 13).

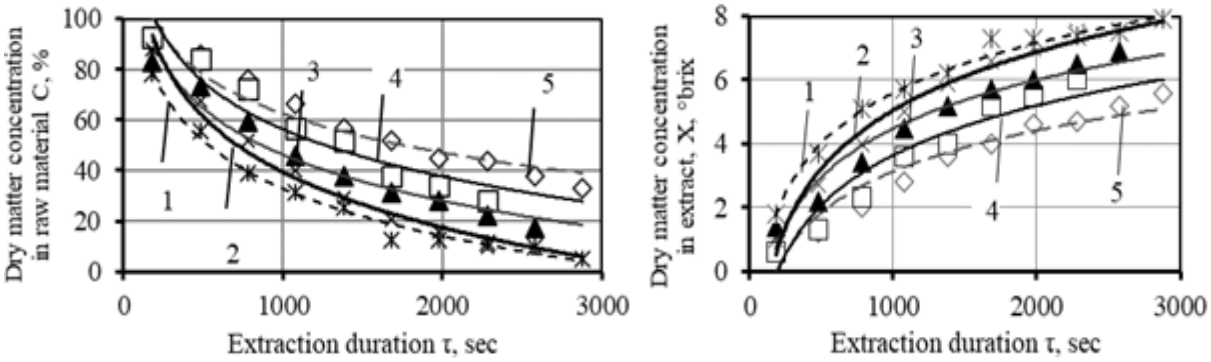

(1 — 1024 W, 2 — 682 W, 3 — 512 W, 4 — 273 W, 5 — 136 W)

Fig. 13. Radiation power effect on extraction kinetics.

With increasing power, the intensity of mass transfer increased, but so did the temperature of the process. The experimental data was processed, and a dependence of the mass transfer coefficient on the main parameter — the radiation power — was obtained (Fig. 14).

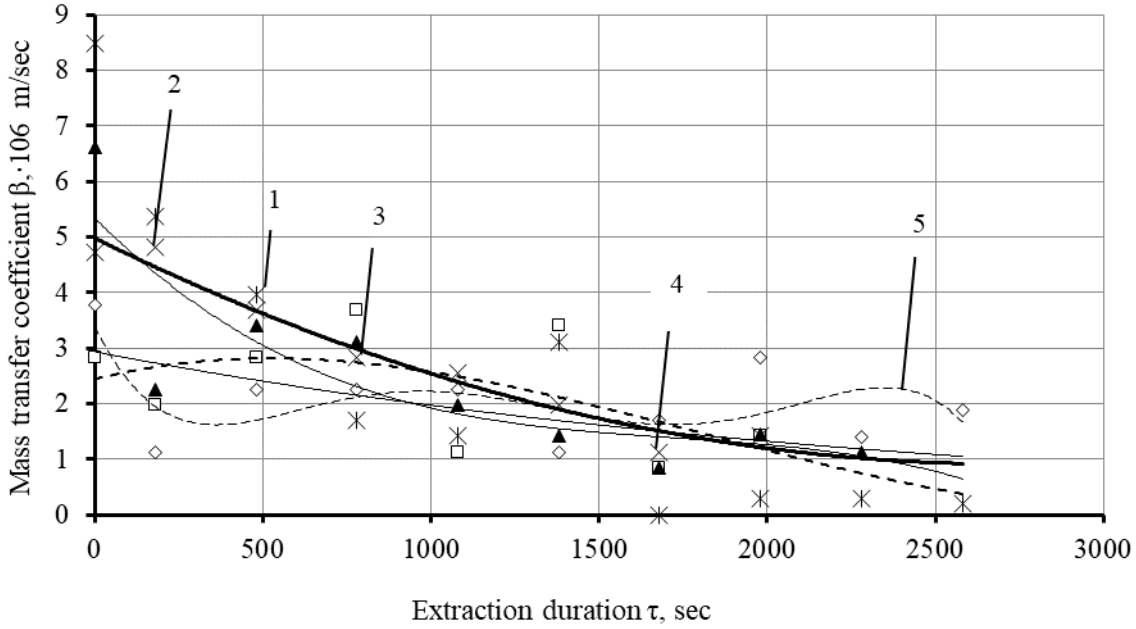

Fig. 14. Coefficient β values.

The values of β were used to calculate the corresponding Nusselt numbers. Constants in the dimensionless model (12) were determined by the methods of similarity theory. The power—law exponents for the Schmidt numbers (Sc) and the dimensionless parameter (L/H) were accepted as traditional.

The information in Fig. 14 was processed as a dependence of the mass transfer rate on the current extract concentration:

$$Nu_m = 0{,}17 \times (Sc)^{0{,}33} \times (Bu)^{1{,}6} \times (L/H)^{0{,}8} \quad (16)$$

In equation (16), the energy action number is calculated as $Bu = \left(rwd^2\rho\right)^{-1}$. This relationship is a key to the algorithm for calculating the vacuum microwave extractor.

Samples of extracts and their concentrates obtained by the proposed technology underwent sensory and chemical studies. The concentrates were obtained both in a microwave vacuum evaporator and in a block-type cryo-concentrator

developed at ONTU. The results of chemical analysis are presented in Table 1.

Table 1.

Extracts and concentrates characteristics.

Sample	Dry matter concentration %	Vitamin C content, mg/100 sm^3	Vitamin C content relative to dry matter %
Extract	4,2	430…550	10,2…13
Concentrate №1	24	3640…4050	9,2…10,2
Cryoconcentrate №2	14	2120…2310	11,2…12,5

The obtained samples had a saturated, characteristic aroma of rosehip, a bright reddish-orange color, a taste without any hints of cooking, with a pronounced sour aftertaste, and a homogeneous consistency. The cryo-concentrate (No. 2) had a better aroma, color, and taste.

MICROWAVE EVAPORATION

Experiments were carried out at the installation described in [21]. New results on the dehydration of extracts over a wide range were obtained (Table 2).

Table 2.

The studies range during extracts evaporation.

№	Solid phase	Extractant	Pressures, MPa	Tempera-tures °C	Concentra-tions, %	Power, W	Vapor flow, g/min
1	Rosehip	Water	0,01—0,12	30—50	10—54	136	1,08
2	Rosehip	Water	0,01—0,12	30—50	17—80	512	4,64
3	Rosehip	Water	0,01—0,12	30—50	4,5—50	682	5,4
4	Sunflower oil cake	Ethanol	0,02—0,03	25—50	3—44	512	16,7— 14
5	Tomato pomace	Water	0,02—0,03	60—70	10—68	1024	11,7
6	Soybeans	Water	0,02—0,06	60—85	0,8—59	512	4,2

The information was processed as a dependence of the moisture removal rate on the current extract concentration (Fig. 15).

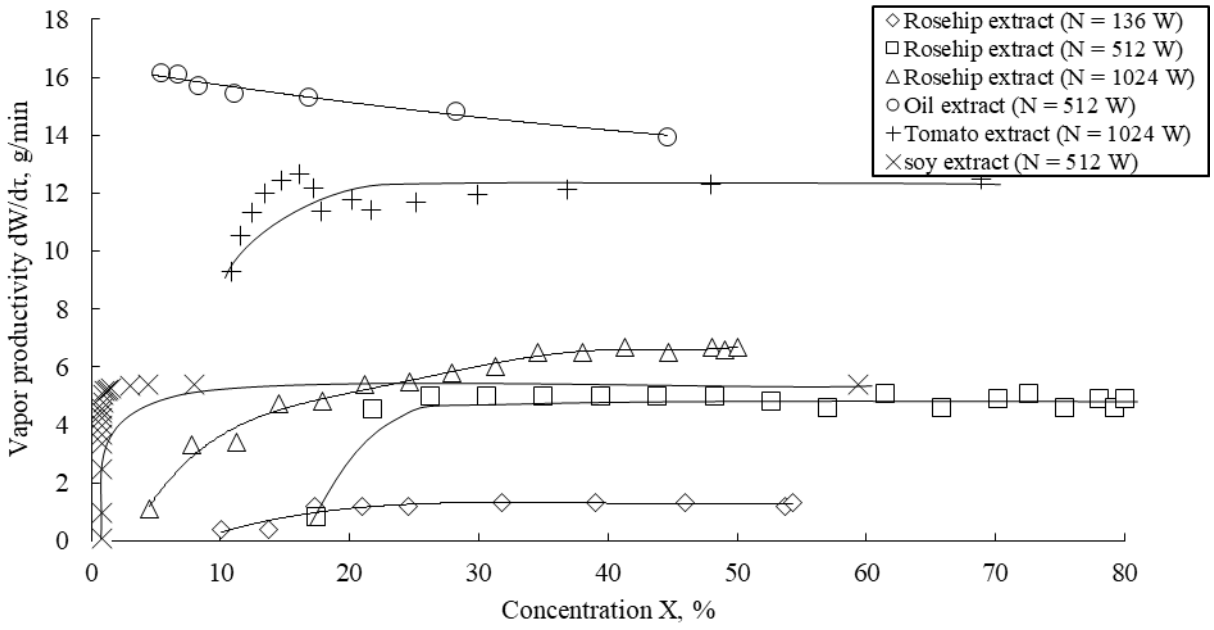

Fig. 15. Dependence of vapor productivity on the current concentration of extract.

The main conclusion based on the experimental results is that the amount of removed vapor depends on the solvent type and is closely correlated with the applied microwave power.

A feature of hybrid processes initiated by electromechanical systems is that their energy is weakly dependent on the solution concentration (Fig. 16).

ENERGY OF HYBRID PROCESSES

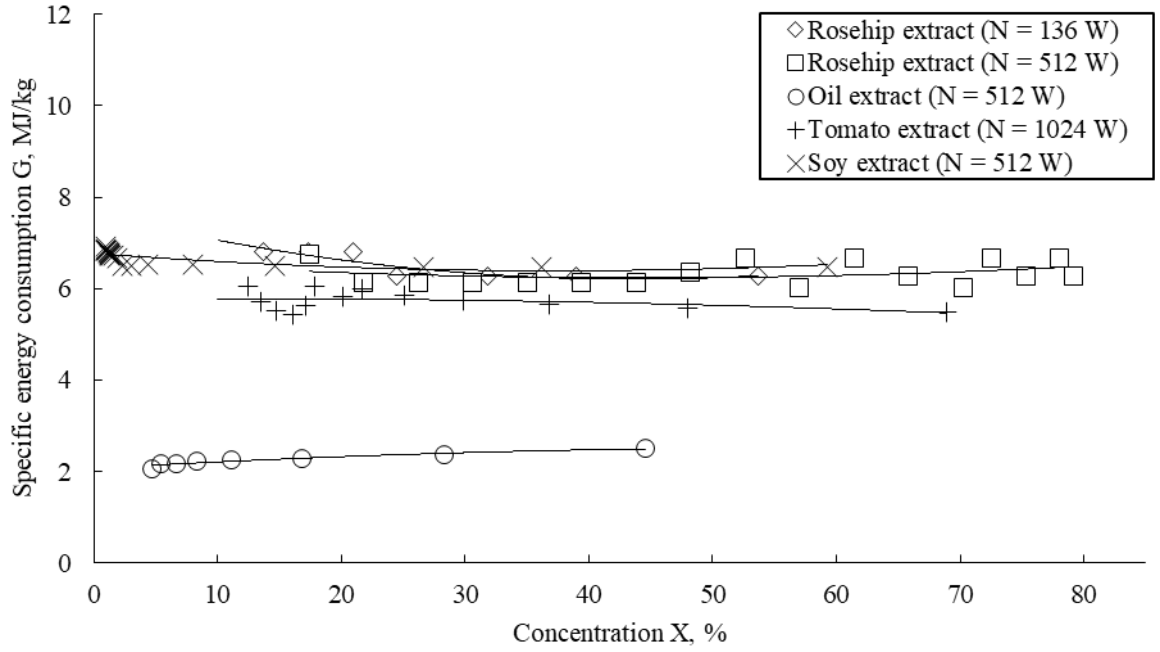

Fig. 16. Dependence of energy consumption on the concentration during various extracts evaporation.

The solvent and its phase transition heat play a decisive role in determining the specific energy consumption in microwave evaporation devices. Therefore, aqueous extracts require three times more energy than alcohol extracts (Fig. 16). It is noteworthy that stable energy consumption is maintained even at high concentrations, where traditional evaporation devices are not effective, in the area of energy-intensive drying technologies.

Gas chromatographic analysis was used to determine the fatty acid composition of tomato pomace oil obtained using a microwave evaporation apparatus (Fig. 17).

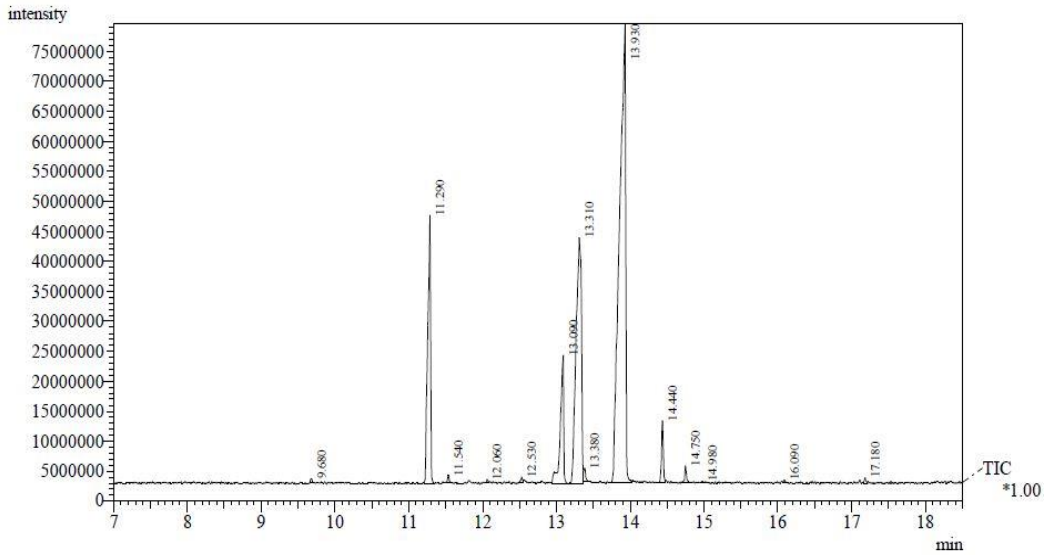

Fig. 17. Chromatogram of tomato pomace oil.

Table 3.

The content of fatty acids in tomato pomace oil.

№	Name of acid	Content, %
1	Myristic	0,14
2	Palmitic	13,70
3	Palmitolinic	0,20
4	Heptadecanoic	0,09
5	Heptadecenoic	0,18
6	Stearic	7,49
7	Oleic	24,04
8	Vacecenoic	0,53
9	Linoleic	50,74
10	Linolenic	2,06
11	Arachidic	0,53
12	Eicosadiene	0,05
13	Behenic	0,06
14	Lignoceric	0,19

As can be seen from the obtained data (Table 3), the oil from tomato extracts obtained using a microwave vacuum evaporation apparatus belongs to the linoleic type (with a linoleic acid content of 50.74%), similar to most traditional vegetable oils (sunflower, soybean). However, it should be noted that the oil from tomato extracts has a significantly higher biological value due to its much higher content of alpha-linolenic acid (2.06%) compared to sunflower oil, in which this indicator is up to 0.4%. Alpha-linolenic acid belongs to ω-3 fatty acids, which play an important role in maintaining healthy human body function, and the search for sources of supply in the diet is a relevant problem. The oil from tomato extracts also contains a higher percent of palmitic acid (13.7%), which promotes better absorption. The high biological value of oil from tomato extracts is also due to the presence of lycopene, which is a powerful antioxidant and a unique natural agent for the prevention of cardiovascular and oncological diseases.

CONCLUSIONS

The hypothesis that the use of substances with polar molecules as extractants and the transition to electromagnetic principles of energy supply would allow the output of target components from plant materials in the form of two streams, the traditional diffusion and additional hydrodynamic, with the power of the latter being orders of magnitude higher than diffusion, has been formulated and proven in this work.

Experimental setups and corresponding methodologies have been developed to compare traditional and proposed extraction principles in an electromagnetic field. Traditional modes were simulated in a thermostat. Microwave-assisted extraction was performed on stationary layer setups, in the mode of extractant circulation, and under vacuum conditions with a reverse refrigerator.

Comprehensive experimental studies of the kinetics of extraction in an electromagnetic field have established that the use of a microwave generator intensifies the mass transfer process several times over. Using the methods of similarity theory, the obtained database of experimental data was generalized as a dimensional model, which was used as a key element in the developed engineering methodology for the calculation of microwave extractors.

The extractor is distinguished by the ability to transfer target components from the raw material at temperatures of up to 40°C with high intensity. The operating time of the apparatus is by 5—8 times less than the traditional methods, while the values of the final concentration of the product are correspondingly higher. The vapor productivity and specific energy costs of the evaporator remain practically unchanged over the entire range of working concentrations (from 0.5 to 85°Brix).

APPENDIX 1

[1]**Fig. 3.** Material flows scheme. (G_R — raw material mass, C_R — concentration of target components in raw material, G_S — sludge mass, X_S — concentration of target components in sludge, G_E — extract mass, X_E — extract concentration, G_{EX} — extractant mass, X_{EX} — extractant concentration, G_P — product mass, X_P — product concentration).

[1]**Fig. 6.** Parametrical model of "Extractor — Dehydrator" system. (a_R — thermal diffusivity coefficient of raw material, c_R — heat capacity of raw material, ρ_R — density of raw material, λ_R — thermal conductivity of raw material, ν_R — kinematic viscosity of raw material, r_M — phase transition heat of moisture, H — raw material layer height, t_{IR} — initial temperature of raw material, C_{IR} — initial concentration of target components in raw material, a_{EX} — thermal diffusivity coefficient

of extractant, c_{EX} — heat capacity of extractant, ρ_{EX} — density of extractant, λ_{EX} — thermal conductivity of extractant, ν_{EX} — kinematic viscosity of extractant, r_{EX} — phase transition heat of moisture, t_{IEX} — initial temperature of raw material, X_{IEX} — initial concentration of target components in raw material, d, b, L — height, width and length of apparatus, V_U — useful volume of apparatus, N_{MW} — magnetron power, η_{MW} — magnetron efficiency, E — extractor, j_E — extractor specific energy consumption, D — dehydrator, j_D — dehydrator specific energy consumption).

References

[1] Goodman E.M., Redmond J., Elia D., Harris S.R., Augustine M.B., Hand R.K. Practice Roles and Characteristics of Integrative and Functional Nutrition Registered Dietitian Nutritionists. *Journal of the Academy of Nutrition and Dietetics*, 2018, vol. 118, no. 12, pp. 2356—2369. doi: 10.1016/j.jand.2018.03.027

[2] Gryshova I., Nikoliuk O., Shestakovska T. The Organic Production In The Context Of Improving The Ecological Safety Of Production Of The Food Industry. *Journal Of Food Science And Technology-Ukraine*, 2017, vol. 11, no. 4, pp. 103— 112. doi: 10.15673/fst.v1li4736

[3] Bazhenov A.A., Mizikovsky, I.E., Garina, E.P., Kuznetsov, V.P., Gavrilov, A.I. Normal Flow of Resources as a Basis for Improving the Quality of Final Financial Information. *Conference on Future of the Global Financial System — Downfall or Harmony, April 13-14 2018*, vol. 57, pp. 309— 315. doi: 10.1007/978-3-030-00102-5_32

[4] Trojahn S. Logistics Strategies For Resource Supply Chains. *Transport And Telecommunication Journal*, 2018, vol. 19, no. 3, pp. 244—252. doi: 10.2478/ttj-2018-0021

[5] Landgrebe D., Kräusel V., Bergmann M., Werner, M., Rautenstrauch A. Conserving Resources in Production — Breaking New Ground. *Procedia Manufacturing*, 2017, vol. 8, pp. 619—626. doi: 10.1016/j.promfg.2017.02.079

[6] Irmak S. Biomass as Raw Material for Production of High Value Products. *Biomass Volume Estimation and Valorization for Energy*, 2017, pp. 201—225. doi:10.5772/65507

[7] Zhang DY., Huang D., Zhang XY., Zhao HY., Gong GL., Tang XH., Li LJ. Drying Performance and Energy Consumption of Camellia Oleifera Seeds Under Microwave—Vacuum Drying. *Food Science and Biotechnology*. Early Access JAN 2023. doi: 10.1007/s10068-022-01239-0

[8] Liu HL., Liu HY., Liu HY., Zhang X., Hong QC., Chen W., Zeng X. Microwave Drying Characteristics and Drying Quality Analysis of Corn in China. *Processes*, 2021, vol. 9, no. 9. Article number 1511. doi: 10.3390/pr9091511

[9] Tepe T.K., Tepe B. The Comparison of Drying and Rehydration Characteristics of Intermittent—Microwave and Hot-Air Dried-Apple Slices. *Heat and Mass Transfer*, 2020, vol. 56, no. 11, pp. 3047—3057. doi: 10.1007/s00231-020-02907-9

[10] Bolek, S (Bolek, Sibel). Potential of Energy Saving by Microwave Drying for Waste Cucumis Metuliferus Seeds as Alternative to Freeze Drying. *Environmental Engineering and Management Journal*, 2021, vol. 20, no. 9, pp. 1583—1589. doi: 10.30638/eemj.2021.146

[11] Abano EE. Microwave Assisted Convective air Drying of Sugarloaf Pineapples (ananas comosus). *Applied Engineering in Agriculture*, 2021, vol. 37, no. 5, pp. 763—774. doi: 10.13031/aea.14380

[12] Nguyen TVL., Nguyen PBD., Tran TTV., Tran B.L., Huynh TP. Low-Temperature Microwave-Assisted Drying of Sliced Bitter Melon: Drying Kinetics and Rehydration Characteristics. *Journal of Food Process Engineering*, 2022, vol. 45, no. 12. doi: 10.1111/jfpe.14177

[13] Wang RF., Zhao D.H., Gao YP., Xu Q., Wu L., Li ZY. Power Control in Microwave Drying of Green Turnip. *Drying Technology*, 2022, vol. 40, no. 10, pp. 2153—2163. doi: 10.1080/07373937.2021.1927073

[14] Lei YD., Chen JL., Zhang ZH., Deng XR. Influence of Microwave Vacuum Drying on the Effective Moisture Diffusivity of Seedless White Grapes. Volume 42. Article number e37020. DOI10.1590/fst.37020. Published 2022

[15] Dincer C. Effect of Intermittent Microwave Vacuum Concentration on Quality Parameters of Apple Juice and Sour Cherry Nectar and Mathematical Modeling of Concentration. *Food Science and Technology*, 2021, vol. 55, no. 3, pp. 175—196.
doi: 10.1080/08327823.2021.1952837

[16] Nejad S.L., Shahedi M., Fathi M. Comparative Study of Microwave-Assisted Vacuum Evaporation, Microwave-Assisted Evaporation, and Conventional Evaporation Methods on Physicochemical Properties of Barberry Juice. *Journal of Agricultural Science and Technology*, 2021, vol. 23, no. 2, pp. 307—317.

[17] Bozkir H., Tekgul Y. Production of Orange Juice Concentrate Using Conventional and Microwave Vacuum Evaporation: Thermal Degradation

Kinetics of Bioactive Compounds and Color Values. *Journal of Food Processing and Preservation*, 2022, vol. 46, no. 6. Article number 15902. doi: 10.1111/jfpp.15902

[18] Tao Y., Yan BW., Zhang N.N., Wang M.F., Zhao JX., Zhang H., Chen W., Fan DM. Microwave Vacuum Evaporation as a Potential Technology to Concentrate Sugar Solutions: A Study Based on Dielectric Spectroscopy. *Journal of Food Engineering*, 2021, vol. 294. Article number 110414. doi: 10.1016/j.jfoodeng.2020.110414

[19] Chua LS., Leong C.Y. Effects of Microwave Heating on Quality Attributes of Pineapple Juice. *Journal of Food Processing and Preservation*, 2020, vol. 44, no. 10. Article number 14786. doi: 10.1111/jfpp.14786

[20] Khan M.K.I., Ghauri Y.M., Alvi T., Amin U., Khan M.I., Nazir A., Saeed F., Aadil R.M., Nadeem M.T., Babu I. Microwave Assisted Drying and Extraction Technique; Kinetic Modeling, Energy Consumption and Influence on Antioxidant Compounds of Fenugreek Leaves. *Food Science and Technology*, 2022, vol. 42. Article number e56020. doi: 10.1590/fst.56020

Information about the authors.

Burdo Oleg
Doctor of Technical Sciences, Professor.
Area of scientific interests: heat and mass transfer processes, nanotechnology in food industry, energy efficiency.
Odesa, Ukraine
E-mail: poem.ontu@gmail.com

Levitsky Anatoly
Doctor of Biological Sciences, Professor.
Area of scientific interests: biotechnology of food products, biochemistry of nutrition.
Odesa, Ukraine
E-mail: dirbiochemtech@gmail.com

Trishyn Fedir
PhD, Associate Professor.
Area of scientific interests: automation, energy efficiency, management.
Odesa, Ukraine
E-mail: poem.ontu@gmail.com

Terziev Sergey
Doctor of Technical Sciences, Associate Professor.
Area of scientific interests: heat and mass transfer processes, eco-industry in agricultural sector
Odesa, Ukraine
E-mail: poem.ontu@gmail.com

Sirotyuk Ilya
PhD, Assistant Professor.
Area of scientific interests: heat and mass transfer processes, extraction, dehydration of food products, energy efficiency.
Odesa, Ukraine
E-mail: ilyxin09@gmail.com

Burdo Alla
PhD, Associate Professor.
Area of scientific interests: technologies for producing concentrated extracts from plant materials.
Odesa, Ukraine
E-mail: poem.ontu@gmail.com

Lapinska Alla
PhD, Associate Professor.
Area of scientific interests: food technologies, nutrition biochemistry
Odesa, Ukraine
E-mail: alocnka.onaft@gmail.com

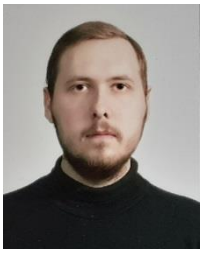

Molchanov Mikhail
graduate student.
Area of scientific interests: heat and mass transfer processes, extraction, evaporation.
Odesa, Ukraine
E-mail: Mihatapok3@gmail.com

Improvement of the Burden Column Structure by Controlling the Multicomponent Burden Loading Mode into the Blast Furnace

Myrav'yova I.G., Ivancha N.G., Shcherbachov V.R., Vishnyakov V.I., Ermolina E.P.
Iron and Steel Institute of Z.I. Nekrasov National Academy of Sciences of Ukraine, Dnipro, Ukraine

Abstract. The purpose of this work was to study the possibility of correcting the shape and position of the plastic zone, as the main element of the structure of the burden column in a blast furnace, by controlling its loading mode. To achieve this goal, a new method has been developed for determining the coordinates of the lines of softening and melting of the burden based on information about the gas temperature above the surface of the charge and the characteristics of the distribution of burden materials, a criterion for the technological assessment of the cohesive zone has been proposed, and the relationship between its thickness and the distribution of the burden has been studied. Important results are the established connections between the coordinates of the softening and melting lines with the gas temperature above the surface of the charge and the characteristics of the distribution of burden materials, as well as the development of a criterion for the technological assessment of the formed cohesive zone and the justification for the possibility of adjusting its parameters by changing the distribution of charge components with the calculation determination of the composition and prediction of high-temperature properties of their mixtures in different zones of the furnace. The significance of the obtained results lies in the justification of the possibility and solution of the problem of improving the parameters of the cohesive zone by adjusting the charge loading regime to ensure the energy efficiency of the blast furnace process.
***Keywords*:** blast furnace, multicomponent burden, mixtures, high temperature characteristics, cohesive zone, melting and softening lines, criterion, control.

DOI: https://doi.org/10.52254/1857-0070.2023.2-58-12
UDC: 669.162.21.27.012.3

Îmbunătățirea structurii coloanei de încărcare prin controlul modului de încărcare a încărcăturii cu mai multe componente în furnal

Muraviova I., Ivancia N., Scerbachov V., Vișniakov V., Ermolina E.
Institutul de Fier și Oțel al Z.I. Academia Națională de Științe Nekrasov a Ucrainei, Dnipro, Ucraina

Rezumat. Scopul acestei lucrări a cercetarea posibilității de îmbunătățire a parametrilor zonei de coeziune, elementul principal al structurii de încărcare a furnalului, prin controlul regimului de încărcare. Pentru a atinge acest obiectiv, a fost elaborată o nouă metodă de determinare a parametrilor zonei de coeziune bazată pe informații despre temperatura gazului deasupra suprafeței de încărcare și compoziția încărcăturii în diferite zone ale furnalului, un criteriu de raționalitate pentru zona de coeziune, a fost propusă și a fost studiată relația dintre grosimea zonei de coeziune și distribuția sarcinii. Rezultatele importante includ stabilirea conexiunii dintre coordonatele liniilor de înmuiere și topire cu temperatura gazului deasupra suprafeței de încărcare și caracteristicile distribuției componentelor de încărcare. Dezvoltarea criteriului de raționalitate pentru zona de coeziune și justificarea posibilității de ajustare a parametrilor acesteia prin modificarea distribuției materialelor de încărcare cu calculul preliminar al compoziției amestecului componentelor de sarcină în diferite zone ale cuptorului și prezicerea temperaturii lor ridicate proprietățile sunt, de asemenea, rezultate semnificative. Semnificația rezultatelor obținute constă în justificarea posibilității și soluționării problemei îmbunătățirii parametrilor zonei de coeziune prin ajustarea regimului de încărcare a sarcinii pentru a asigura eficiența energetică a procesului de furnal. Se arată că corectarea parametrilor zonei plastice, alegerea direcției și mărimii acțiunii de control în fiecare caz specific ar trebui să se bazeze pe rezultatele modelării matematice a distribuției materialelor de sarcină de-a lungul razei vârfului, determinând compoziția amestecurilor de componente de sarcină în diferite zone ale cuptorului și prezicerea proprietăților lor la temperatură ridicată, precum și tendințele de modificare a acestor proprietăți la modificarea compoziției componentelor amestecului.
***Cuvinte-cheie**:* furnal, sarcină multicomponentă, amestecuri, caracteristici de temperatură ridicată, zonă de coeziune, linii de topire și dedurizare, criteriu, control.

Усовершенствование структуры столба шихты путем управления режимом загрузки многокомпонентной шихты в доменную печь

Муравьева И.Г., Иванча Н.Г., Щербачев В.Р., Вишняков В.И., Ермолина Е.П.
Институт черной металлургии им. З.И. Некрасова Национальной академии наук Украины, г. Днепр, Украина

Аннотация. Целью настоящей работы являлось исследование возможности корректировки формы и положения пластичной зоны, как основного элемента структуры столба шихты в доменной печи, путем управления режимом ее загрузки. Для достижения поставленной цели разработан новый метод определения координат линий размягчения и плавления шихты на основании информации о температуре газа над поверхностью засыпи (температуре поверхности засыпи) и характеристиках распределения шихтовых материалов в сочетании с использованием ряда математических моделей, предложен критерий для технологической оценки сформировавшейся пластичной зоны, исследована связь ее толщины с содержанием компонентов шихты в различных зонах доменной печи. Важным результатом выполненных расчетно – аналитических исследований являются корреляционные связи координат линии плавления с температурой газа над поверхностью засыпи в соответствующих зонах колошника, температур размягчения - плавления и толщины пластичной зоны в рабочем пространстве печи с распределением основных железосодержащих шихтовых материалов по радиусу колошника. К важным результатам следует отнести также разработку критерия для технологической оценки пластичной зоны и оценка возможности корректировки ее параметров путем изменения распределения рудных нагрузок и компонентов шихты. Показано, что корректировка параметров пластичной зоны, выбор направления и величины управляющего воздействия в каждом конкретном случае должны основываться на результатах математического моделирования распределения шихтовых материалов по радиусу колошника, определении состава смесей компонентов шихты в различных зонах печи и прогнозировании их высокотемпературных свойств, а также тенденций изменения этих свойств при изменении компонентного состава смеси. Значимость полученных результатов заключается в обосновании возможности и решении задачи улучшения параметров пластичной зоны путем корректировки режима загрузки шихты в доменную печь для обеспечения энергоэффективности доменной плавки.

Ключевые слова: доменная печь, многокомпонентная шихта, смеси, высокотемпературные характеристики, пластичная зона, линии размягчения и плавления, критерий, управление.

INTRODUCTION AND FORMULATION OF THE PROBLEM

The efficiency of blast furnace smelting and the quality of cast iron are largely determined by the characteristics of the burden column formed in the furnace. The current level of knowledge of blast furnace smelting processes, summarizing the results of the work of leading researchers in this field, suggests the development of methods for controlling the parameters of the cohesive zone in the furnace as one of the main tasks. It is known that the cohesive zone, being the most important structural element of the burden column, which is mainly formed as a result of the implementation of a given mode of loading a blast furnace, determines the distribution of the gas flow and the main melting indicators. As a rule, the choice of parameters of the blast furnace loading mode is carried out on the basis of an assessment of the distribution of burden materials using calculation methods (mathematical models, calculation methods, etc.) and subsequent analysis of the results and their compliance with the specified parameters and indicators of blast furnace smelting.

It should be noted that earlier, when considering the relationship between the loading mode and the configuration (shape) of the cohesive zone, the main attention was paid to the influence of the distribution of ore loads on the furnace top [1]. Such an approach could be considered correct for the conditions of loading a mono-charge into a blast furnace, which would cause the invariance of the high temperature properties of burden materials and their melts in various sections of the furnace. At the same time, the blast furnace charge in modern conditions is multicomponent. Until recently, it was not possible to predict the high temperature properties of mixtures of iron-containing burden materials in various zones of the furnace, since there are no tools for determining the distribution of individual charge components. However, with the advent of appropriate mathematical models, refinements can be made to the solution of the problem of determining the configuration of the cohesive zone, taking into account the distribution of high temperature characteristics of the charge layer in the working space of a blast furnace. In this work, we used a complex model for the distribution of

burden materials, developed at the Iron and Steel Institute of Z.I. Nekrasov of National Academy of Sciences (NAS) of Ukraine (ISI), which has been repeatedly used with positive results in blast furnaces to determine the distribution of charge components and predict the properties of the resulting melts in industrial conditions in order to correct the applied technological regimes and increase the efficiency of melting. The availability of data on the composition of mixtures of burden materials in various zones of the blast furnace makes it possible to determine the temperatures of the onset of softening and melting in these zones as points of the corresponding lines.

The main characteristics of the cohesive zone are considered to be its shape, position in the furnace and thickness, which significantly affect the productivity and other performance indicators of the blast furnace. To date, generally accepted analytical, sufficiently substantiated methods for determining the shape of the cohesive zone have not been developed. The ISI has developed a method for determining the parameters of the cohesive zone, based on information about the distribution of the temperature of the gas flow or the surface of the charge along the radius of the top [Method of determining the position and shape of the cohezive zone in a blast furnace using gas flow temperature distribution indicators] / Muravyova I.H., Ivancha M.H., Shcherbachov V.R. and etc. // Fundamental and applied problems of ferrous metallurgy. 2022. Collection 36. P. 95 - 108. [In Ukrainian]. DOI: 10.52150/2522 – 9117 – 2022 – 36 - 95 - 108.]. The method is based on a systematic set of mathematical models, including those developed by the authors, and also includes a new method for determining softening and melting lines in a blast furnace. The method is implemented using a complex mathematical model for calculating the distribution characteristics of the charge components in the annular zones of the top.

An analysis of the published results of earlier studies showed that the bulk of the work on studying the features of the formation of a cohesive zone in a blast furnace was carried out in the 70s of the last century [2]. Their focus was determined by the unique studies of Japanese scientists carried out on frozen blast furnaces, as a result of which it was found that the burden column in a blast furnace is a combination of structural elements, the main of which is the cohesive zone. In subsequent years, studies of the formation of a cohesive zone in a blast furnace using mathematical models were actively continued in Germany, China and Japan.

Publications of recent years indicate the further development of research on the development of mathematical models for determining the parameters of the cohesive zone, including models that take into account non-stationary processes in the furnace. Nippon Steel Corp. continues research in this direction; its employees have developed a method for determining and visualizing the position of the cohesive zone root under the assumption that the root abuts against the centers of gravity of the figures determined by the results of evaluating the change in a number of controlled parameters over time [3]. In [4], a method was proposed for determining the position of the root of the cohesive zone based on an analysis of the nature of changes in the temperatures of the refractory lining of the mine and cooling water, as well as the degree of CO utilization along the height of the furnace, and a number of other parameters. In [5], a method for determining the characteristics of the cohesive zone in a blast furnace is described, which is based on the mass conservation equations and the heat conservation equations, which, according to the authors, govern the chemical reactions occurring in the furnace. Based on this assumption, dividing the blast furnace into a number of concentric circles, the authors determine the temperature fields of the furnace, and then, depending on the fusibility of iron-containing burden materials, the shape and position of the cohesive zone are predicted.

In [6], the results of the development of a mathematical model describing the flow of liquid, heat and mass transfer, as well as chemical reactions in a blast furnace are presented. Unlike the previous models, the proposed one considers three variants of the structure of the layers of the cohesive zone - layered, isotropic non-layered and anisotropic. The authors have studied the influence of these three options on the processes of distribution of the gas flow in the furnace. It is shown that the calculated estimate of the parameters of the cohesive zone, which is alternating layers of iron-containing materials and coke, which corresponds to the layer-by-layer loading of the charge, makes it possible to predict (simulate) the passage of the gas flow through the "coke windows".

To determine the shape of the cohesive zone in [7], mass and heat transfer in three separate furnace zones is considered. As the initial information, the readings of the probe that

measures the composition and temperature of the gas and is located below the level of the charge. Calculated as isotherms, the lines of the beginning of softening and melting determine the location of the cohesive zone in the furnace.

Also known is the approach to determining the shape and position of the cohesive zone in a blast furnace, proposed by the researchers of Tata Steel Ltd. (India) [8, 9], who use a combined approach to determine the shape and position of the cohesive zone, which involves the use of a mathematical model in the form of differential equations, in combination with furnace operation indicators, and information from various probing devices.

To estimate the shape and position of the cohesive zone in a blast furnace, researchers actively use computational fluid dynamics (CFD) models. In [10], the results of improving the blast furnace smelting model, which was previously developed by Nippon Steel Corp., are presented. In addition to the existing private models (mass transfer, reactions and heat transfer in the dry and cohesive zones of the furnace), models have been developed to assess the distribution of ore loads on the top, a model of the tuyere hearth, as well as a model to estimate the porosity of the zone of low-mobility materials. All these models describing the flow processes in the blast furnace are integrated into the model used to calculate the parameters of the cohesive zone. A similar mathematical apparatus is used in the works of a number of other researchers [11 - 14]. In [11], the model describes in detail the layered structure of the cohesive zone. It was shown in [12] that the upper boundary of the cohesive zone is set as a constant temperature, and the lower boundary, the melting line, is defined as the liquidus temperature. Moreover, the liquidus temperature is established as a function of the chemical composition of the slag. To obtain such a function, the authors performed a regression analysis based on the data given in published sources, and obtained a third-order polynomial dependence for calculating the liquidus temperature.

In [13], a model developed by the authors is presented, which includes a description of the dynamics of the gas flow, the movement of the burden, chemical reactions, heat and mass transfer between the gas phase and the burden. The burden in the blast furnace is presented in the form of alternating layers of iron ore and coke. The multilayer CFD model, according to the authors, quite accurately estimates the shape and location of the cohesive zone, which are determined by the iterative method based on the distribution of the melting temperature of the ore part of the charge. Of the works that also use CFD modeling methods to determine the shape and position of the cohesive zone in a blast furnace, it should be noted [15], where the influence of the charge loading program on the position of the cohesive zone - its root and top. In this case, the position of the root of the cohesive zone is determined by changes in the temperature of the cooling water in the lower part of the furnace shaft.

There is also a work on predicting the position and configuration of a cohesive zone, in which the computational fluid dynamics model (CFD) and the support vector method (SVM) are combined to solve this problem [16]. The authors have created an axisymmetric two-dimensional stationary CFD model for describing the processes of fluid flow, heat and mass transfer in a blast furnace shaft. Prediction of the position of the cohesive zone is carried out using SVM.

In the development of models for determining the position of the cohesive zone in a blast furnace, the discrete element method (DEM) is also used [17]. A feature of the application of this method for the conditions of blast furnace smelting is the discretization of the charge in the volume of the furnace into its individual elements, which involves the use of many assumptions about their interaction.

In recent years, when developing mathematical models of blast furnace melting, in particular, a model for determining the cohesive zone, researchers combine continual and discrete models. The model combined in this way received the terminology «DEM - CFD model» [18 - 20]. The CFD-DEM model is suitable for modeling fluid-solid or fluid-particle systems. In a typical CFD - DEM model, the phase motion of discrete solids or particles is described using the discrete element method (DEM), which involves the application of Newton's laws to the motion of each particle, and the flow of a continuous fluid is described by the local averaged Navier - Stokes equation, which is solved using the methods traditional computational fluid dynamics DEM - CFD. In the studies reported in [19], the melting characteristics of iron ore and the structure of the layers during the operation of the furnace with low coke consumption were entered into the DEM - CFD model, and then the gas and moving bed behavior in the blast furnace was modeled. As a result of the calculation, the influence of the

thickness of "coke windows" in the cohesive zone on the gas flow rate is demonstrated.

An analysis of the above results shows that only one of the considered works studied the effect of the charge loading program on the position of the cohesive zone - its root and top [15], but the studies were limited to taking into account the effect of the ore and fuel components of the charge as a whole. Features of the distribution of the components of the iron ore part of the charge, as well as the relationship of its characteristics with the parameters of the cohesive zone, were not considered in the known models, which reduces the reliability of the calculation results and limits the ability to control the process of formation of the cohesive zone.

The results of previous work also allow us to conclude that researchers agree on the approach to controlling the parameters of the cohesive zone: the main influence on the formation of the cohesive zone is exerted by the mode of loading burden materials, which determines the size of the melting surface area of iron-containing materials (the lower surface of the cohesive zone) and the thickness of the "coke windows", providing gas permeability of the burden column in the furnace. At the same time, according to V.M. Parshakov, whose works are closest to solving the problem of improving the technology of blast furnace smelting by adjusting the parameters of the cohesive zone, the results of studies of a quantitative assessment of the relationship between the parameters of the cohesive zone and melting indicators are practically absent at the moment.

This work differs from previous studies by providing a justification and solution for improving the parameters of the cohesive zone in the blast furnace by adjusting the charging regime, taking into account the distribution of components within the charge along the radius of the furnace, as well as the composition and high-temperature properties of their mixtures formed in different zones of the blast furnace.

The aim of this study was to develop a method for the prompt determination of cohesive zone parameters (its configuration, position in the furnace, and thickness) based on information about gas temperature (surface temperature of the charge) and the content of components in the charge in different zones of the furnace, identifying their interconnections, as well as developing a criterion for the technological assessment of the cohesive zone and justifying the possibility of adjusting its parameters by changing the distribution of ore loads and charge components along the radius of the furnace, combined with a computational and analytical prediction of the high-temperature properties of burden mixtures in different zones of the blast furnace.

II. SOLUTION METHODS AND RESULTS

To establish the relationship between the parameters of the cohesive zone and the characteristics of the distribution of burden materials along the radius of the top, using the proposed method for several options for industrial operating conditions of a blast furnace, the coordinates of the points of softening and melting surfaces were determined. The indicated coordinates are determined using the calculation of the melting surface area according to the Goodenau method [21], the composition of mixtures of iron-containing charge components in various zones of the top, determined using a complex mathematical model of burden distribution [Ivancha N.G., Murav'yova I.G., Shumel'chik E.I., Vishnyakov V.I., Semenov Yu.S. / Complex Mathematical Model of the Distribution of Multicomponent Charge in a Blast Furnace. Metallurgist, №5, 2018, v. 62, is. 1 – 2, pp. 95 – 100], as well as a predictive calculation estimate of the high temperature characteristics of these mixtures and the melts formed from them [22]. An example of the resulting cohesive zone configuration is shown in fig. 1, where the difference in the vertical coordinates of the corresponding points of the surfaces in the annular zones characterizes the thickness of the cohesive zone, and the points of intersection of the softening and melting lines with the top wall characterize the position of the root. The validity of the approach to constructing the cohesive zone configuration using information on the temperature of the gas flow above the surface of the charge is confirmed by experimental data on the presence of a fairly close relationship between the vertical coordinates of the points of the melting line and the gas temperature above the surface of the charge (Fig. 2). Based on the results of mathematical modeling of the distribution of burden materials, a relationship was also established between the vertical coordinates of the melting line and ore loads in the annular furnace zones of equal area (Fig. 3). In fig. 2 and fig. 3 shown the results indicate the possibility of using data on the distribution of gas temperatures above the grist charge (or charge surface temperature) to develop methods for controlling the position and

shape of the cohesive zone, and also confirm the possibility of adjusting the parameters of this zone by changing the distribution of ore burden along the radius of the blast furnace top. The connection of the vertical coordinates of the points of the melting line *Z* in the annular zones with the corresponding ore burden is characterized by a rather high value of the coefficient of reliability of approximation by a power function of more than 0.80.

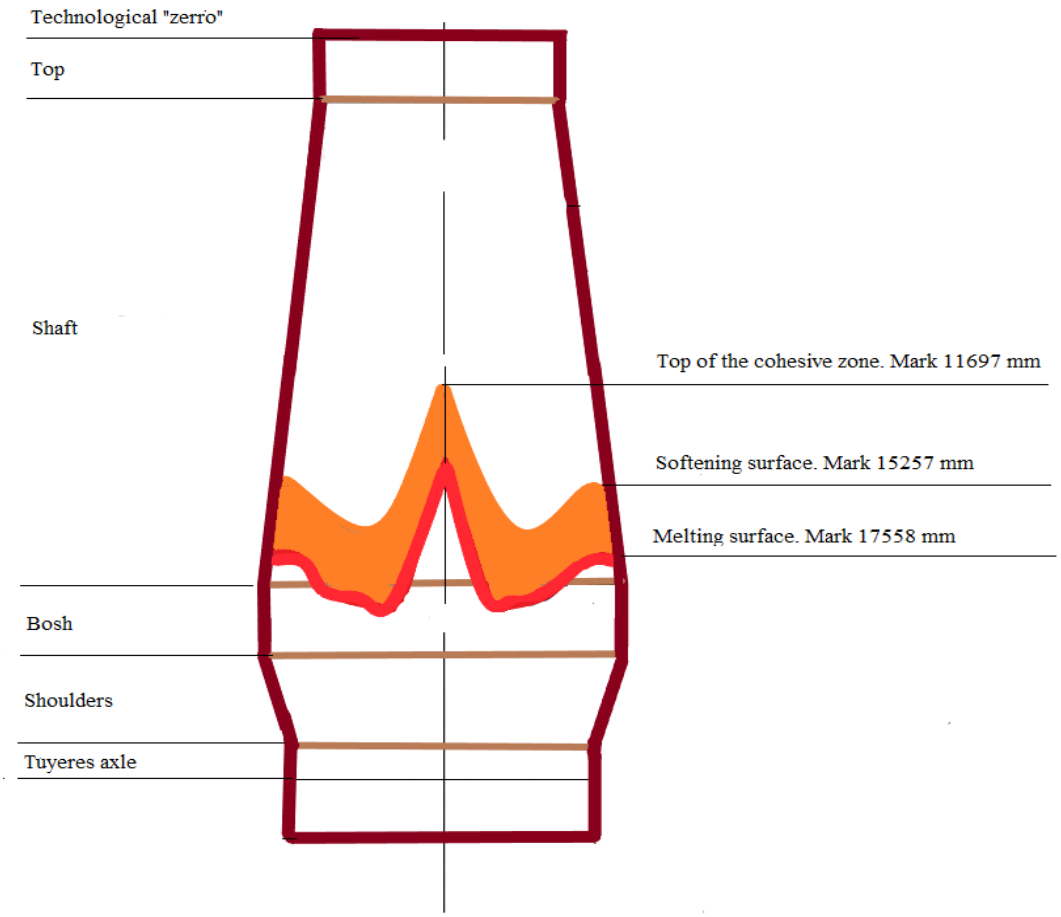

Fig. 1. The configuration of the cohesive zone obtained by the proposed method.

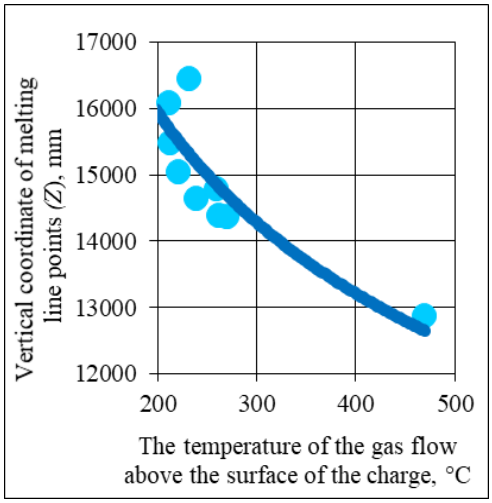

Fig. 2. Linkage of vertical coordinates of the points of the melting line (*Z*) in the annular zones of the blast furnace with the gas temperature above the surface of the charge in these zones.

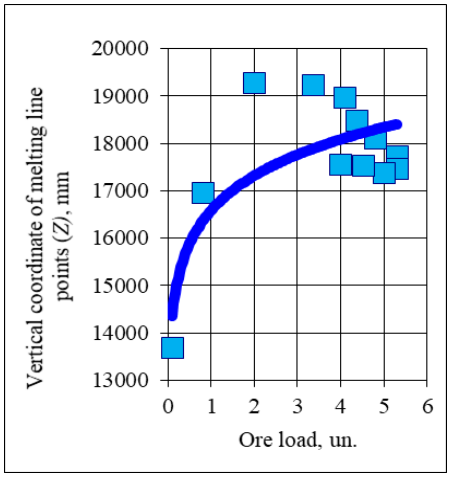

Fig. 3. Connection of vertical coordinates of the point of the melting line (*Z*) near the annular zones of the blast furnace with the ore burden in these zones.

The possibility of calculating the content of the charge components and the mixtures formed from them in the annular zones of the furnace using a complex mathematical model developed earlier in the ISI made it possible to formulate a new approach to the selection of control parameters for correcting the characteristics of the cohesive zone.

Under the conditions of loading a blast furnace with a multicomponent burden, the lines of softening and melting (the boundaries of the cohesive zone) are determined by the composition of mixtures of burden materials formed in different zones of the working space of the furnace, and their individual high temperature properties. As shown by numerous laboratory studies performed in the ISI, the softening and melting temperatures of mixtures of iron ore materials and additives are not a simple additive consequence of the high temperature properties of the components that make up the mixture. The interaction of components during high temperature processing and during the development of reduction processes leads to the fact that a mixture of charge components with known high temperature properties manifests itself as a new type of burden material with properties that differ significantly from the properties of the mixture components.

An indirect indicator of the thickness of the cohesive zone, a parameter characterizing its gas permeability, is the difference in melting and softening temperatures. It is believed that to ensure the gas permeability of the cohesive zone, this value should not exceed 300 ºC. The established relationship between the ratio of pellets and agglomerate in a mixture with the difference in melting and softening temperatures of this mixture allows us to conclude that this ratio can be used as a control parameter when adjusting the thickness of the cohesive zone. The basis for this conclusion is the high coefficient of reliability of the approximation of the relationship between the difference in softening and melting temperatures with the indicated ratio, which is 0.99 (Fig. 4).

Geometrically, the thickness of the cohesive zone can also be defined as the difference in the coordinates of the points of intersection of the softening and melting lines with the average lines of this zone at the corresponding level.

On fig. 5 shows the results of studying the relationship between the ratio of the content of pellets and the content of sinter with the difference in the vertical coordinates (thickness) of the cohesive zone (Z) in the annular zones of the furnace. The coefficient of reliability of the approximation of the revealed connection is 0.62, which indicates the possibility of using a change in the ratio of the main iron-containing components in the annular zone to correct the geometric parameters of the cohesive zone.

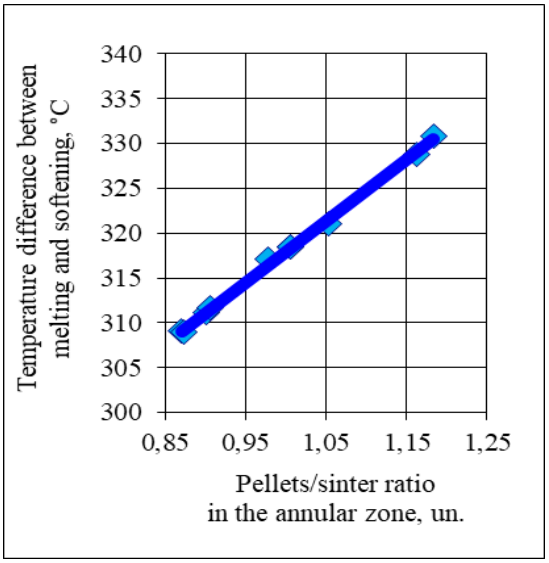

Fig. 4. Relationship between the difference in melting and softening temperatures of mixtures of iron-containing burden materials in the annular zone of the top with the ratio of the number of pellets and sinter in this zone.

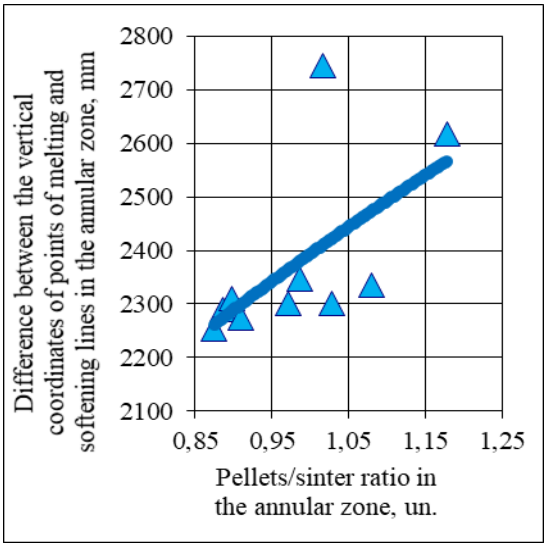

Fig. 5. Connection of the difference in the vertical coordinates of the points of the melting and softening lines (thickness of the cohesive zone (ΔH_{czi})) in the annular zones of the blast furnace and the ratio of the amount of pellets and sinter in these zones.

The necessary correction of the parameters of the cohesive zone within certain limits can also be implemented by changing the distribution of additives in combination with a change in the distribution of the main components of the charge, or exclusively by redistributing additives.

From the above statement about the significant difference in the high temperature properties of mixtures of iron-containing burden materials and similar properties of the initial components of the mixture, it follows that the control of the parameters of the cohesive zone by changing the distribution of burden materials, the choice of the direction and magnitude of the corrective influence in each specific case should be based on the results of mathematical modeling of the distribution of components burden along the radius of the top, determining the composition of mixtures of burden components in various zones of the furnace, predicting their high temperature properties and tendencies of changes in these properties with a change in the component composition of the mixture. The ISI has developed a technology for loading a multicomponent charge into a blast furnace, from the main provisions of which it follows that in order to control the distribution of a specific component of the mixed iron ore portion along the radius of the top, a change in the location of the dose of this component in the volume of the portion (feed) can be used as a control parameter (see our article in the same journal for 2022). In everyday practice, technologists, in the presence of appropriate control systems and mathematical models on a blast furnace, in assessing the rationality of the shape of the cohesive zone, are guided by the results of visual observations, which are interpreted on the basis of their own body of knowledge and technological experience. It is generally accepted that it is rational to consider the L-shaped form of the cohesive zone, however, as technological practice shows, this provision cannot be extended to many options for the technological conditions of blast furnace operation. This is confirmed by the results of previous and own studies: cases of highly efficient operation of blast furnaces with a cohesive zone shape that differs significantly from the L-shaped one have been repeatedly noted. From this we can make a platoon that the shape of the cohesive zone itself, without taking into account other indicators, cannot be used to assess the level of rationality and compliance with the melting regime.

For a comprehensive assessment of the level of rationality of the cohesive zone and the correspondence of its parameters to the technological conditions of melting, a criterion has been developed for assessing the shape and position of the cohesive zone in a blast furnace. As arguments of the criterion (K_{cz}), the main parameters characterizing the cohesive zone, i.e., its configuration, thickness, and position in the furnace, are taken. These parameters can be determined using a new method proposed by the authors, based on information about the temperatures of the gas flow (surface of the charge) at various points in the furnace section, obtained using the following tools:

- thermal measuring probes installed above the surface of the level of charge;
- systems based on the determination of gas flow temperatures based on the results of measuring the speed of sound in a gaseous medium and its change depending on the gas temperature;
- systems for measuring temperatures of the grist charge.

Based on the well-known ideas about the parameters that determine the shape and position of the cohesive zone, as well as the results of the correlation analysis of the relationships between these parameters and the technological indicators of melting, complexes are compiled that are arguments for the criterion for evaluating the cohesive zone.

The first argument of criterion X_1 includes the sum of the ratios of the thickness of the cohesive zone in adjacent annular zones (ΔH_{czi} and ΔH_{czi+1}, m, where i is the number of the annular zone), estimated from the difference in melting and softening temperatures of iron-containing materials in these zones, and the ratio of the maximum value thickness of the cohesive zone to the minimum. Thus, the argument reflects the configuration of softening and melting lines in the controlled sections and along their entire length as a whole.

The argument can be represented by the expression:

$$X_1 = \sum_{i=1}^{n} \frac{\Delta H_{czi+1}}{\Delta H_{czi}} + \frac{\max\left(\Delta H_{czi}\right)}{\min\left(\Delta H_{czi}\right)}, \qquad (1)$$

where ΔH_{czi} – cohesive zone thickness in the i-th annular zone of the blast furnace, m;

n – the number of annular zones.

The second argument of the criterion characterizes the relative position of the root of

the cohesive zone, the location of which is assumed to be in the zone of the maximum level of readings of thermocouples of the refractory lining of the furnace shaft:

$$X_2 = T_{sh\ max}, \quad (2)$$

where $T_{sh\ max}$ – maximum temperature of the refractory lining of the mine, °C.

The third argument of the criterion is the effective melting surface area [21]:

$$X_3 = A_{ef}. \quad (3)$$

After the normalization procedures, the study to the normal distribution law logit - the transformation of each argument of the criterion of the plastic situation takes the form:

$$K_{cz} = \left(F\left(X_1\right) \cdot F\left(X_2\right) \cdot F\left(X_3\right)\right)^{\frac{1}{3}}. \quad (4)$$

The possibility of using the K_{cz} criterion for

a qualitative assessment of the conformity of the shape and position of the cohesive zone in the blast furnace to the prevailing technological conditions is confirmed by the presence of its connection with the main technological indicators of melting – the level of iron production and the consumption of standard fuel (the coefficient of reliability of the approximation is 0,55 – 0,60).

The need to adjust the cohesive zone parameters (shape, thickness and/or position) by changing the charge loading mode to achieve the specified target functions (maximum iron production, minimum coke consumption) can be determined by comparing the current value of the criterion with the range of its rational values for the technological operating conditions of a particular object.

Based on the established relationships between the characteristics of the burden distribution along the radius of the top (ore loads, the content of the burden components in different zones of the top) with the parameters of the cohesive zone, the main provisions for adjusting the parameters of the charge loading mode, which improves the parameters of the cohesive zone, are substantiated and developed.

The main provisions and the sequence of solving problems for their implementation are given below.

1. Determination of the characteristics of the distribution of the components of the burden in the annular zones along the radius of the top.

2. Calculation - analytical forecast of softening and melting temperatures of mixtures of iron-containing components in the annular zones.

3. Calculation - analytical and graphical modeling of the cohesive zone using the means of controlling the temperature of the gas flow and the surface of the charge based on the proposed method.

4. Determination of rational values of the criterion for evaluating the shape and position of the cohesive zone in a blast furnace under the current technological conditions of blast furnace smelting and the allowable ranges of its change. Evaluation of the level of rationality of the formed cohesive zone and its compliance with the current parameters (indicators) of the melting process using the developed criterion.

5. Expert assessment of the necessary changes in the shape, location and thickness of the cohesive zone, based on the results of calculations using the proposed method, and taking into account the objective technological parameters of the melting process, as well as the readings of the means of controlling the distribution of the burden and gas flow.

6. Choice of a possible direction for correcting the loading mode, depending on the required change in the parameters of the cohesive zone.

The choice of corrective action is carried out depending on the need to solve a specific problem, the main of which are given below.

6.1. Changing the position of the “root” and/or top of the cohesive zone in the axis of the furnace.

6.1.1. Changing the position of the “root” and/or top of the cohesive zone in the furnace axis with a change in the shape of the cohesive zone.

6.1.2. Changing the position of the “root” and/or top of the cohesive zone in the axis of the furnace without changing the shape of the cohesive zone.

6.2. Change in the volumetric location of the cohesive zone.

6.3. Change in the temperature interval ("thickness") of the cohesive zone.

The tasks according to clause 6.1 are solved by changing the ore loads and/or by changing the distribution of components along the radius of the top. Clause 6.2 is implemented mainly by changing the total ore load in the charge. The task according to clause 6.3 is solved solely by changing the distribution of components.

The choice of control parameters for adjusting the loading mode in each particular case is determined by the degree of technological significance of possible influences, among which

the distribution of ore loads is predominant in relation to the content of the charge components in the annular zones along the radius of the top. However, the optimization of the distribution of components in conjunction with the rational distribution of ore loads is also one of the significant reserves for increasing the efficiency of smelting. In this regard, the development of a rational regime for loading a blast furnace should be carried out in two, and if necessary, in three stages.

The first stage is the development of a loading program, which is carried out on the basis of an analysis and selection of a rational distribution of ore loads along the radius of the top. At the second stage, the choice of a rational distribution of the components of portions of burden materials should be made with minimization of deviations in the distribution of ore loads from that adopted at the first stage. If, according to the results of the computational and analytical prediction of the high temperature properties of the mixture of components in the furnace zones, it is not possible to achieve the specified softening and melting temperatures, it is necessary to change the composition of the burden materials, taking into account technological limitations regarding the distribution of components, their mixtures and melts formed from them (third stage).

III. THE DISCUSSION OF THE RESULTS

The applicability of the proposed method for determining the shape and position of the cohesive zone in a blast furnace using information on the distribution of gas temperature over the surface of the charge or the temperature of this surface is confirmed by the analysis of the features of the formation of the cohesive zone under various technological melting conditions. The study of the influence of various melting conditions, characterized by the corresponding technological parameters, on the position of the cohesive zone in the furnace is a multifactorial task. Multivariate comparative analysis was used to identify the most informative and significant indicators. The results of assessing the influence of technological parameters on the position of the cohesive zone in the furnace, determined by the coordinates of the softening and melting lines, allow us to conclude that the existing relationships of the studied values, characterized by the obtained factor loads, confirm the validity and reliability of determining the position of the cohesive zone in the blast furnace using the proposed method, which can be used online during the operation of the blast furnace.

The proposed method of justified adjustment of the parameters of the cohesive zone expands the technological possibilities of smelting control by using the distribution of charge components along the radius of the top as a control parameter in addition to the traditionally used distribution of ore loads. Accounting for the characteristics of the distribution of charge components makes it possible to determine the composition of mixtures of iron-containing materials, as well as the calculated prediction of their high temperature characteristics and properties of melts in various zones of the blast furnace, thereby contributing to an increase in the accuracy of determining the coordinates of softening and melting lines that limit the cohesive zone.

IV. CONCLUSIONS

A new method is proposed for determining the parameters of the cohesive zone (shape, position and thickness) in a blast furnace equipped with means to control the temperature of the gas flow or the level of charge. The method is based on a systematized set of mathematical models, including those developed by the authors, as well as on a new method for determining the coordinates of softening and melting lines in a blast furnace using information obtained by means of monitoring the distribution of gas temperature over the charge surface (or charge surface temperature) , as well as on the calculated determination of the characteristics of the distribution of charge components in various annular zones along the radius of the top using a complex mathematical model. Relationships between the coordinates of the melting line points and the gas temperature above the charge surface, the softening and melting temperatures and the thickness of the cohesive zone in various zones of the blast furnace with the ratio of the amount of sinter and pellets in these zones are established. The relationship between the coordinates of the points of the melting line and the ore load in the annular zones of the blast furnace has been confirmed. A criterion for evaluating the rationality of the formed cohesive zone has been developed and the possibilities of adjusting its parameters by changing the distribution of ore loads and charge components have been shown. It is shown that the correction of the parameters of the cohesive zone, the choice of the direction and magnitude of the control action in each specific case should be based on the results of

mathematical modeling of the distribution of burden materials along the radius of the top, determining the composition of mixtures of charge components in various zones of the furnace and predicting their high temperature properties, as well as trends in change these properties when changing the component composition of the mixture.

References

[1] Parshakov V.M., Polinov A.A., Pavlov A.V. and etc. Poryadok provedeniya operatsiy po dosti-zheniyu optimal'nykh znacheniy parametrov zonyu plavleniya I nailuchshikh pokazateley plavki. *Sbornik trudov mezhdunarodnogo soyuza domen-shchikov, 2017, V.1, pp. 69 – 75. (In Russian).*

[2] Ueda S., Miki T., Murakami T., Nogami H., & Sato T.(2013). Agenda for low reducing agent operation of blast furnace - Reduction and melting phenomena of iron ore. *Tetsu-To-Hagane Journal of the Iron and Steel Institute of Japan, 99(1),11.* https://doi.org/10.2355/tetsutohagane.99-1.

[3] Masahiro Ito, Shinroku Matsuzaki, Kazumoto Kakiuchi, Makoto Isobe. Development of Visual Evaluation and Numerical Analysis System of Blast Furnace «Development of Visual Information Technique of Blast Furnace Process Data». *Nippon Steel Technical Report January 2004. No. 89. UDC 669.162.26 : 681.3. P. 38–45.*

[4] Method for determining position of root of blast furnace cohesive zone through multi-source information fusion. *Patent China CN 103593540A. Publication 19.02.2014.*

[5] S.Z. Li, Jian Cheng, W.Q. Ma "A Method to Forecast the Cohesive Zone of Blast Furnace." *Materials Science Forum, vol. 471–472, Trans Tech Publications, Ltd., Dec. 2004, pp. 358–361.*

[6] X.F. Dong, A.B. Yu, S.J. Cew, and P. Zulli. Modeling of Blast Furnace with Layered Cohesive Zone. *The Minerals, Metals & Materials Society and ASM International 2009. Metallurgical and materials transactions b, volume 41b, April 2010— 331.*

[7] Mikolaj Bernasowski, Arkadiusz Klimczyk and Ryszard Stachura. Calculation of Coke Layers Situation in the Cohesive Zone of Blast Furnace. *Materials 2021, 14, 192.*

[8] Mriganshu Guha. Revealing cohesive zone shape and location inside blast furnace. June, 2017. *Ironmaking & Steelmaking 45(6):1-6.*

[9] Mriganshu Guha, Shailendra Rai, M.K. Agarwal, Ramna, R.V. Model for real-time prediction of cohesive zone shape and location inside blast furnace. *Iron and Steel Technology Conference Proceedings 2013/01/01, pp. 657-664.*

[10] Shinroku Matsuzaki, Akihiko Shinotake, Masaaki Naito, Tsunehisa Nishimura, Kazuya Kunitomo, Takashi Sugiyama. Development of Mathematical Model of Blast Furnace. *Nippon Steel Technical Report No. 94 JULY 2006. UDC 699.162.26 : 681.3. pp. 87 – 95.*

[11] Lulu Jiao, Shibo Kuang, Aibing Yu, Yuntao Li, Xiaoming Mao, Hui Xu. Three-dimensional modeling of an ironmaking blast furnace with a layered cohesive zone. *Metallurgical and Materials Transactions B: Process Metallurgy and Materials Processing Science. Feb 2020. pp. 258-275.*

[12] Dong Fu and Chenn Q. Zhou, Yongfu Zhao, John D'Alessio, Kyle J. Ferron. Numerical simulation of blast furnace shaft process. *Proceedings of 4th International Conference on Modeling and Simulation of Metallurgical Processes in Steelmaking. Dusseldorf, 27 June – 1 July 2011. pp. 1 – 10.*

[13] Dong Fu, Yan Chen, Yongfu Zhao, John D'Alessio, Kyle J. Ferron, Chenn Q. Zhou. CFD modeling of multiphase reacting flow in blast furnace shaft with layered burden. *Applied Thermal Engineering, V. 66, May 2014, pp. 298 – 308.*

[14] Dong Fu, John Dalessio. Prediction of the cohesive zone in a blast furnace. *AISTech 2011 Proceedings, v.1, p. 695 – 708.*

[15] Ping Zhou, Li Jia-ling, Wen Qi-quan, Zu En-xue, Gui Wei-hua, Chenn Q Zhou. Soft-sensing method of cohesive zone shape and position in blast furnace shaft. *IFAC PapersOnLine 51-21 (2018), pp. 48–52, https://doi.org/10.1016/j.ifacol.2018.09.391*

[16] Jialing Li, Rongjia Zhu, Ping Zhou, Yan-po Song & Chenn Q. Zhou. Prediction of the cohesive zone in a blast furnace by integrating CFD and SVM modeling. *Ironmaking & Steelmaking, 48(3): June 2020, pp. 284-291. DOI:10.1080/03019233.2020.1771893.*

[17] Zhengyun Fan, Shungo Natsui, Shigeru Ueda, Tianjun Yang, Junya Kano, Ryo Inoue and Tatsuro Ariyama. Transient Behavior of Burden Descending and Influence of Cohesive Zone Shape on Solid Flow and Stress Distribution in Blast Furnace by Discrete Element Method. *ISIJ International, V. 50 (2010), N 7, p. 946 – 953.*

[18] Shibo Kuang, Zhaoyang Li and Aibing Yu. Review on modeling and simulation of blast furnace. *Steel research int. 89 (2018) No. 1.*

[19] Shigeru Ueda, Tatsuya Kon, Hiroyuki Kurosawa, Shungo Natsui, Tatsuro Ariyama and Hiroshi Nogami. Influence of Shape of Cohesive Zone on Gas Flow and Permeability in the Blast Furnace Analyzed by DEM-CFD Model. *ISIJ International, Vol. 55 (2015), No. 6, pp. 1232–1236.*

[20] Tatsuya Kon, Shungo Natsui, Shohei Matsuhashi, Shigeru Ueda, Ryo Inoue and Tatsuro Ariyama. Influence of Cohesive Zone Thickness on Gas Flow in Blast Furnace Analyzed by DEM-CFD Model Considering Low Coke Operation. *Steel research int. 84 (2013) No. 11, pp. 1146 – 1156.*

[21] Gudenau G. V., Stendish N., Gerlah V. Fizicheskie usloviya v oblasti plasticheskoy zonyi domennoy pechi. Chast 1. Osnovnyie printsipyi modeli. *Chernyie metallyi, 1992. – №8. – pp. 34–41.*

[22] Prikhod'ko E.V., Togobitskaya D.N., Khamkhotko A.F., Stepanenko D.A. Prognozirovanie fiziko-khimicheskikh svoystv oksidnykh system. *Porogi, 2013, 339 p.*

Information about authors.

Myrav'yova Irina Gennadievna, doctor of technical sciences, senior researcher, department of iron metallurgy, Iron and Steel Institute of Z.I. Nekrasov National Academy of Sciences of Ukraine, Dnipro, Ukraine
E-mail:
irinamuravyova@gmail.com

Ivancha Nikolay Grigor'evich, senior researcher, department of iron metallurgy, Iron and Steel Institute of Z.I. Nekrasov National Academy of Sciences of Ukraine, Dnipro, Ukraine
E-mail: ing.witc@gmail.com

Ermolina Ekaterina Petrovna, lead engineer, department of iron metallurgy, Iron and Steel Institute of Z.I. Nekrasov National Academy of Sciences of Ukraine, Dnipro, Ukraine
E-mail: ketrinerm11@gmail.com

Shcherbachov Vadim Rodionovich, lead engineer, отдела department of iron metallurgy, Iron and Steel Institute of Z.I. Nekrasov National Academy of Sciences of Ukraine, Dnipro, Ukraine
E-mail:
vadim0072vadim@gmail.com

Vishnyakov Valeriy Ivanovich, researcher, department of iron metallurgy, Iron and Steel Institute of Z.I. Nekrasov National Academy of Sciences of Ukraine, Dnipro, Ukraine
E-mail:
vishnyakov.v.i.0705@gmail.com

Cryogenic Thermomechanical Compressor

Simonenko Iu.M.[1], Chygrin A.A.[2], and Kostenko Ye.V.[1]

[1]National University of Technology, Odessa, Ukraine; [2]Cryoin Engineering Ltd., Odessa, Ukraine

Abstract. The purpose of this work is to create a compact supercharger to provide circulation of protective gas medium in a closed circuit. It was proposed to use a thermomechanical compressor to achieve this purpose. The operating principle of such devices is to change cyclically the temperature of the working medium in contact with warm and cold sources. Heating and cooling are carried out sequentially, pushing a part of gas through the regenerator by means of a displacer. The energy consumption for piston displacement is lower by an order of magnitude than that in conventional compressors. This makes it possible to use a seamless displacer movement mechanism. There can be two designs, both with one of the heat carriers close to ambient temperature. In a high-temperature thermomechanical compressor, the temperature is usually does not exceed 800 K. In the second type compressor, by reducing the absolute temperature of the cold "source" it is possible to achieve a high degree of compression at a relatively small temperature difference. The most significant result of the work is the design of the small-sized thermos-compressor that ensures a moderate degree of gas compression. The significance of the achieved results is shown in the compactness and tightness of the prototype for the use as an alternative to traditional machines in the field of inert gases production. The proposed technical solutions were tested during bench tests of the thermomechanical compressor. The experimental dependences were obtained of the flow rate characteristics on temperature mode, discharge pressure and cycle period.

Keywords: thermomechanical compressor, regenerator, inert gases, heat transfer, refrigerant.

DOI: https://doi.org/10.52254/1857-0070.2023.2-58.13
UDC: 621.56

Compresor termomecanic criogenic

[1]Simonenko Iu.M., [2]Cigrin A.A., [1]Kostenko Ye.V.
[1]Universitatea Națională tehnologică din Odesa, [2]Cryoin Engineering Ltd.
Odesa, Ucraina

Rezumat. Scopul lucrării este de a crea o schemă a unui compresor compact care să asigure circulația unui mediu gazos protector într-un circuit închis. Echipamentul criogenic se caracterizează prin condiții specifice de funcționare: presiune mare de funcționare de 10 ... 15 MPa, raport de compresie moderat de 1,2 ... 1,4 și productivitate relativ scăzută (mai puțin de 1 m3/h în condiții de aspirație). Prin urmare, utilizarea mașinilor voluminoase cu piston și diafragmă de tip tradițional pentru circulație nu este întotdeauna rațională. Pentru atingerea acestui scop au fost rezolvate următoarele sarcini: 1) a fost dezvoltat și testat un termocompresor; 2) se propune utilizarea unui drive magnetic; 3) a fost selectat un agent frigorific intermediar; 4) aplicarea procesului intern de recuperare a căldurii. Într-un termocompresor cu temperatură înaltă, temperatura este limitată de proprietățile de rezistență ale materialelor de construcție și, de obicei, nu depășește 800 K. Cel mai semnificativ rezultat al lucrării este dezvoltarea unui termocompresor de dimensiuni mici, care asigură un grad moderat de compresie a gazului ca alternativă la mașinile tradiționale din domeniul producției de gaze inerte. Semnificația rezultatelor obținute se manifestă prin faptul că au făcut posibilă realizarea unui prototip compact și etanș al unui termocompresor cu recuperare internă a căldurii, în care ansamblul pressepul a fost înlocuit cu un antrenament pe bază de magneți permanenți; utilizarea unui agent frigorific intermediar sigur - cripton - vă permite să excludeți tranziția de fază (condensare sau înghețare) a componentelor amestecului pompat. Soluțiile tehnice propuse au fost testate în procesul de teste pe banc.

***Cuvinte-cheie*:** compressor termomecanic, regenerator, gaze inerte, transfer termic, agent frigorific.

Криогенный термомеханический компрессор

[1]Симоненко Ю.М., [2]Чигрин А.А., [1]Костенко Е.В.
[1]Одесский национальный технологический университет; [2]ООО «Криоин Инжиниринг»
Одесса, Украина

***Аннотация*.** Цель работы – создание схемы компактного нагнетателя для обеспечения циркуляции защитной газовой среды в замкнутом контуре. Для криогенной техники характерны специфические условия эксплуатации: высокое рабочее давление 10…15 МПа, умеренная степень сжатия 1,2…1,4 и относительно небольшая производительность (менее 1м^3/ч при условиях всасывания). Поэтому использование для циркуляции громоздких поршневых и диафрагменных машин традиционного типа не всегда рационально. Для достижения поставленной цели были решены следующие задачи: 1) разработан и испытан термокомпрессор; 2) предложено использовать магнитный привод; 3) осуществлен выбор промежуточного хладагента; 4) применение процесса внутренней регенерации тепла. Принцип работы таких устройств заключается в цикличном изменении температуры рабочего тела при контакте с теплым и холодным источниками. Для повышения экономичности нагрев и охлаждение осуществляют последовательно, переталкивая порцию газа через регенератор при помощи вытеснителя. Затраты энергии на перемещение поршня на порядок меньше, чем в компрессорах традиционного типа. Возможны две конструкции, в каждой из которых один из теплоносителей близок к температуре окружающей среды. В высокотемпературном термокомпрессоре температура ограничивается прочностными свойствами материалов конструкции и обычно не превышает 800 К. В компрессоре второго типа за счет уменьшения абсолютной температуры холодного «источника» можно реализовать высокую степень сжатия при относительно небольшой разности температур. Наиболее существенным результатом работы является разработка малогабаритного термокомпрессора, обеспечивающего умеренную степень сжатия газа, в качестве альтернативы машинам традиционного типа в области производства инертных газов. Значимость достигнутых результатов проявляется том, что они позволили создать компактный и герметичный прототип термокомпрессора с внутренней регенерацией тепла, в котором узел сальника заменен приводом на основе постоянных магнитов; использование безопасного промежуточного хладагента – криптона – позволяет исключить фазовый переход (конденсация или замерзание) компонентов перекачиваемой смеси. Предложенные технические решения апробированы в процессе стендовых испытаний.

Ключевые слова: термомеханический компрессор, регенератор, инертные газы, теплообмен, хладагент.

INTRODUCTION

It is known that gas pressure can be increased either by reducing its volume or by increasing its temperature. The latter option is implemented in so-called thermos-compressors. The simplest thermal pumps appeared several centuries ago and were practically displaced as piston engines improved.

More efficient compressors with thermal drives have appeared over the past few decades. This is achieved by removing heat input and output locations and introducing internal regeneration. These gas displacement processes were first implemented by V. Bush in 1939 [1].

A natural step in the improvement of thermos-compressors was the separation of the hot and cold parts of the working volume, which alternately came into contact with a portion of gas due to a movable displacer. The counter-pressure acting on the displacer was determined only by the hydraulic resistance of the system. As for the displacer, only a small amount of power was required to drive it. However, even after such modernization, thermos-compressors remained highly inertial and low-productivity devices [5-20].

The peculiarity of real devices is the consumption of thermal energy for gas compression and mechanical energy for driving the thermomechanical compressor [2-4]. Moreover, this work requires significantly less energy for gas compression.

Such devices are mainly used in gasifiers and autoclaves.

Their main drawbacks were their inertia and significant heat losses. In addition to changing the parameters of the gas itself, the heat-intensive walls of the working chamber were also forced to heat up and cool down.

As previously noted, the acceleration of heat exchange processes and the increase in cycle dynamics were achieved through internal heat regeneration. Simplified diagrams of the main layout options for the compressor are shown in Fig. 1.

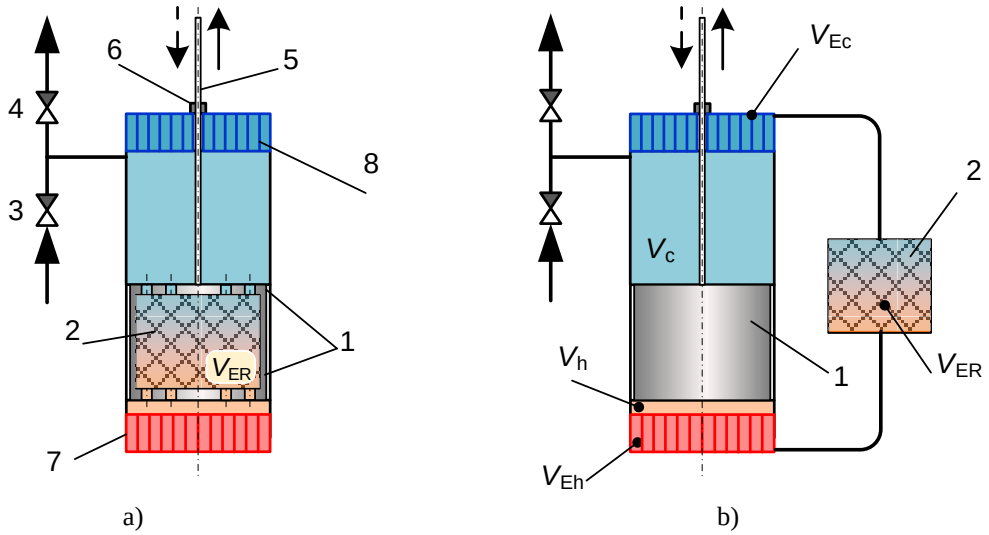

Figure 1. Schemes of thermocompressors: (a) – with the built-in regenerator in the displacer; (b) – with the external regenerator; 1 – the displacer; 2 – the regenerator; 3, 4 – the suction and discharge valves; 5 – the displacer rod; 6 – the gasket; 7 – the heater; 8 – the cooler; V_h and V_c – the operating cylinder warm and cold cavities' volumes; V_{Eh} and V_{Ec} – dead volumes of the heater and the cooler.

I. PRINCIPLE OF OPERATION AND ENERGY SUPPLY OPTIONS

The sequence of individual phases of the cycle is shown in Fig. 2, which illustrates the processes in the cold and hot chambers on the "volume-pressure" diagrams. As the displacer moves, the volumes of the cold V_c and hot V_h chambers cyclically change from the maximum value V_W to 0. At the same time, the sum of the volumes V_h and V_c remains constant throughout the cycle. The values V_{Ec} and V_{Eh} indicate the volumes of the heat exchange devices associated with the working chamber. The sum of the volumes of the cooler, heater, and regenerator forms the dead volume, as shown in formula

$$V_E = V_{Ec} + V_{Eh} + V_{ER} = \text{const.} \quad (1).$$

When designing heat exchangers, it is important to work for minimizing the dead volumes, as increasing the gas volumes of the heat exchangers in relation to the cylinder's working volume V_W reduces the compressor's productivity.

Depending on the position of the displacer, one cycle of the thermos-compressor can be divided into four separate processes [2, 3].

I-II - Pressure increase process. Displacer 1 is in the extreme lower position, and the volume of the hot chamber is zero. As the plunger moves, gas begins to be pushed from volume V_c to volume V_h through the regenerator, and its temperature increases. As a result, the pressure in the working cylinder begins to rise. One of the intermediate states is denoted by point x. Thermal compression continues until at point II the pressure reaches the value of the compression pressure P_D (Fig. 3).

II-III - Discharge process. The displacer continues to move up. Part of the gas, as before, flows into the hot chamber. The second part, through the open valve 4, enters the compressor line at pressure P_D.

III-IV – Pressure reduction process. At the beginning of the reverse (downward) stroke of the displacer, at point III, the compressor valve 4 closes. The compressed gas remaining in the hot space is pushed back through the regenerator to the cold space V_c. As a result of this cooling, the pressure in the cylinder drops to P_S (Fig. 3).

IV-I – Suction process. When the pressure is P_S, the suction valve 3 opens. As a result of the pressure drop and cooling of the gas, the cylinder begins to fill with a fresh portion of gas. Suction ends when the displacer reaches the lowest point (fragment I). The cycle then repeats. In the

second option (Fig. 4a), temperature of the hot chamber T_h is ensured by a flow of air or flowing water, while the temperature level T_c is lowered to cryogenic temperatures. The θ value depends more on T_c. For example, if the θ value in a low-temperature compressor needs to be increased from 1.5 to 2.5, temperature T_c needs to be changed from 200 to 125 K, then for the same θ increase in a high-temperature compressor, an increase in T_h from 450 to 750 K is required. Naturally, the energy consumption for cryostatization of a low-temperature compressor exceeds the energy consumption for driving a high-temperature one. However, in some advanced technologies, there are waste streams of cryogenic liquid vapors, which can be used to activate low-temperature compressors designed for circulating high-pressure gas media. In this case, with the availability of cold streams, energy supply issues for cryogenic compressors become secondary.

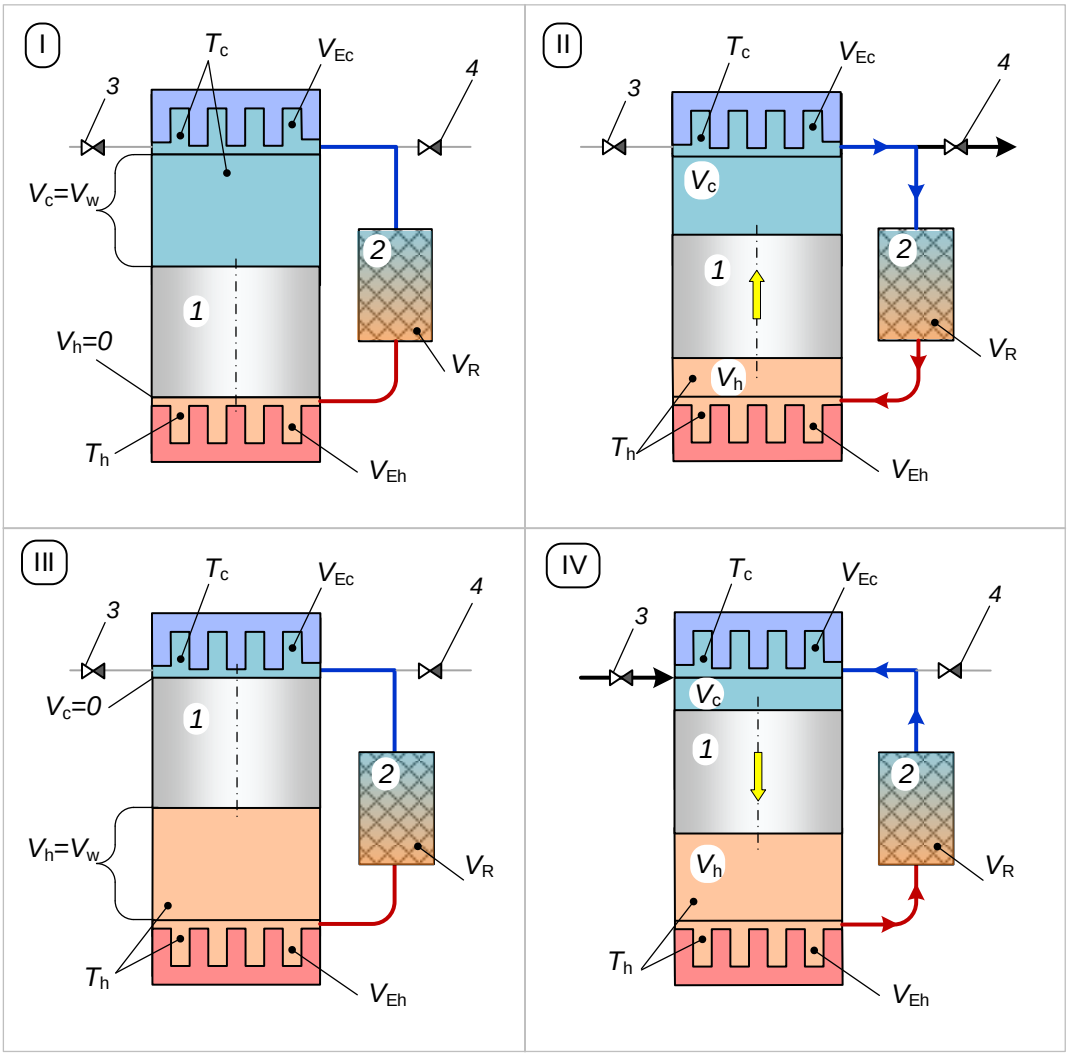

Fig. 2. The operation principle of the thermocompressor with an external location of the regenerator: 1…4 correspond to Fig. 1; V_W – the working volume of the cylinder, equal to the multiplication of the displacer motion 1 and its cross-sectional area; V_R, V_{Ec} and V_{Eh} –the hydraulic volumes of the regenerator, cooler and heater; V_c and V_h – the current volumes of the working cavity; T_c and T_h – the average gas temperatures in cold and warm cavities.

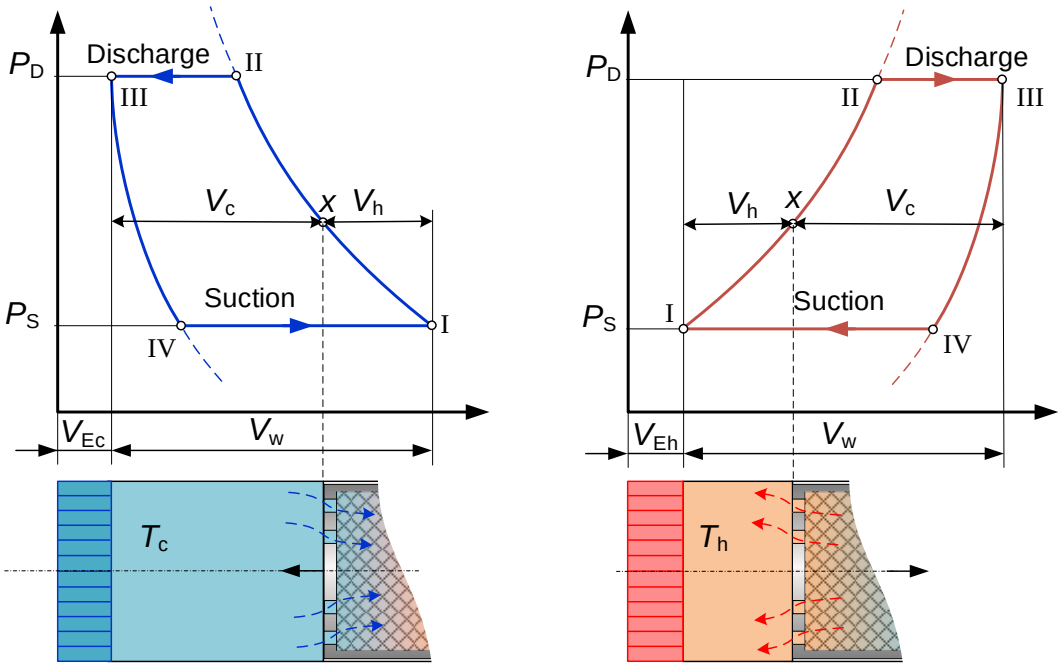

a) b)

Fig. 3. The operating cycle in the diagram *P-V*: cold (a) and (b) warm cavities.

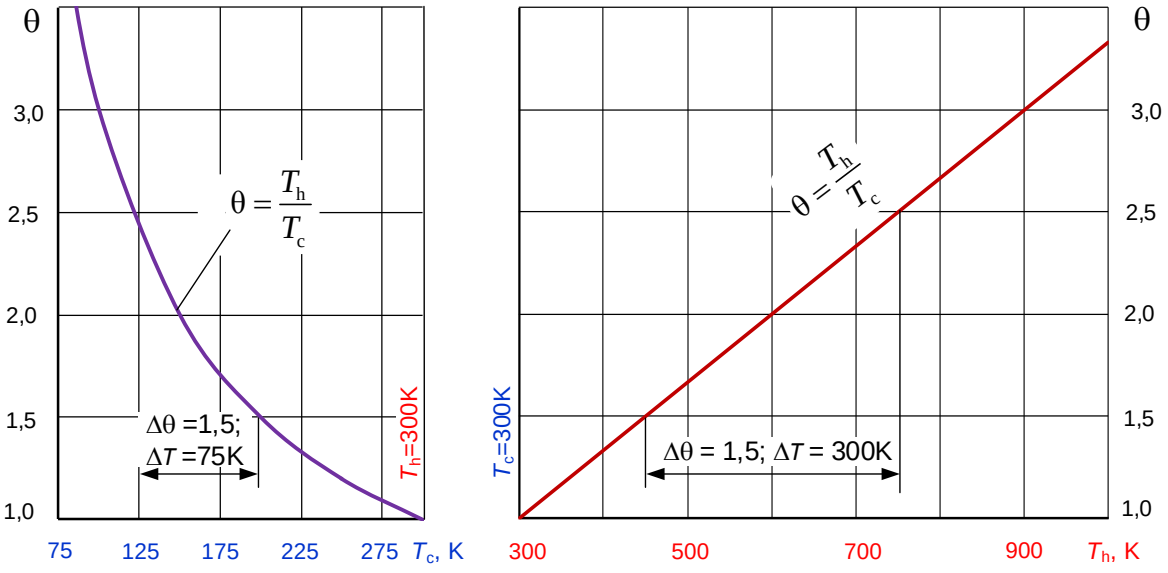

a) b)

Fig. 4. The dependence between the ratio of operating temperatures θ for the low-temperature (a) and high-temperature (b) compressor at the temperature of one of the sources, close to ambient conditions (*T* = 300 K).

The presence of remaining gas in the heat exchange apparatus volumes V_{Ec}, V_{Eh}, and V_{ER} adversely affects the compressor's performance.

$$a = \frac{V_{Ec} + V_{Eh} + V_{ER}}{V_W}. \qquad (2)$$

However, excessive reduction of this parameter leads to a reduction in the heat exchange surface areas. Therefore, in real models, the relative dead

When designing the heat exchangers, one should strive to minimize the total dead volume relative to the cylinder's working volume, as shown in formula (2).

volume usually fluctuates in the range of a = 0.5...1.0. The most important operating parameter of a thermo-mechanical compressor is the ratio of absolute temperatures of the working fluid in the hot and cold chambers.

$$\theta = \frac{T_h}{T_c}. \qquad (3)$$

Two temperature level options are possible, both assuming the use of one of the heat carriers close to the level of the ambient environment. In a high-temperature thermo-compressor, an electric heater is usually used as the second heat source. In this case, temperature T_h is limited by the strength properties of the structural materials and usually does not exceed 800…1000K (Fig. 4b).

II. FEATURES OF OPERATION OF A CRYOGENIC THERMOCOMPRESSOR IN THE PRESENCE OF HIGH-BOILING COMPONENTS IN THE PRODUCT

When pumping substances with a relatively high phase transition temperature, it is necessary to limit the temperature of the cold chamber T_c. Condensation or freezing of a component in a low-temperature thermos-compressor will block the regeneration process and lead to a change in the composition of the pumped mixture. The probability of this phenomenon increases at high pressures. Let's consider an example of pumping a mixture based on helium containing $y = 2\%$ tetrafluoromethane (CF_4; R14). The temperature of condensation of the high-boiling component is determined by its partial pressure in the mixture. In accordance with Dalton's law:

$$P_{R14} = P_{\Sigma} \cdot y_{R14} \approx P_D \cdot y_{R14}, \qquad (4)$$

where P_{Σ} - is the maximum pressure of the mixture in the cylinder determined by the pumping conditions P_D. The dependence of the condensation temperature of R14 on the specified concentration is presented in Table 1.

The calculated temperature in the cold cavity (last row in table 1) is chosen several degrees higher than the possible level of R14 condensation in the mixture. Such a step is justified in ensuring the prevention of phase transition in case of deviations from operational parameters, for example, an increase in the concentration $y_{R14} > 2\%$ or a decrease in the load on heat exchangers due to the reduced performance.

Table 1.

Condensation temperature of tetrafluoromethane at different pressures of He-R14 mixture.

Maximum mixture pressure (discharge pressure) $P_{\Sigma} \approx P_D$, MPa	5	10	15	20
Partial pressure of tetrafluoromethane in a 2% mixture P_{R14}, MPa (4)	0,1	0,2	0,3	0,4
The temperature of tetrafluoromethane condensation at T_{R14}, K.	44,9	55,6	62,6	168,1
Allowable temperature in the cold box (with margin) T_c, K	50	61	68	173

When using nitrogen vapor as an external refrigerant, stabilizing the temperature T_c becomes relevant. Due to the significant temperature difference between N_2 and the mixture in the working chamber, local cooling of the heat exchanger sections is possible. Technical solutions based on regulating the refrigerant flow consumption depending on temperature T_c are fairly inertial. They do not prevent the occurrence of R14 refrigerant condensation and even its freezing at T < 90 K.

We have implemented a heat removal scheme using an intermediate substance (Fig. 5a). In the example under consideration, krypton and methane are suitable as intermediate refrigerants (Fig. 5b). As can be seen from the graphs, at allowable temperatures in the cold chamber T_c = 145...168 K, krypton is preferred because it is safe and at the same temperatures its boiling pressure is by 30...40% lower than in the case of CH_4.

III. IMPLEMENTATION OF THE ENGINEERING SOLUTION

A prototype of a low-temperature thermo-mechanical compressor was manufactured and tested. A mechanism without a seal was used to drive the displacer (Fig. 6).

The transmission of motion through the hermetic wall was achieved using a balanced pair of neodymium Nd magnets. The total static force of the linear transmission was more than 100 N.

This value guaranteed the displacement of the displacer at a frequency of $\upsilon < 2\ c^{-1}$, taking into account its mass, inertial forces, and piston ring

friction. The movable support 3, which contains 12 magnets, surrounds the external wall of the stationary hermetic channel 1. In the photo (Fig. 6c), the cover of the support is removed, and only six magnets are visible.

The same number of magnets is symmetrically located on the other side of the cylindrical channel (Fig. 6b).

External magnets are in contact with the magnets 5 of the internal block. Assembly 2-3-4 performs reciprocating motion due to a pneumatic cylinder attached to links 8 of the support and controlled by a solenoid valve SV (Fig. 7). The characteristics of the model and the results of experimental studies are presented in table 2.

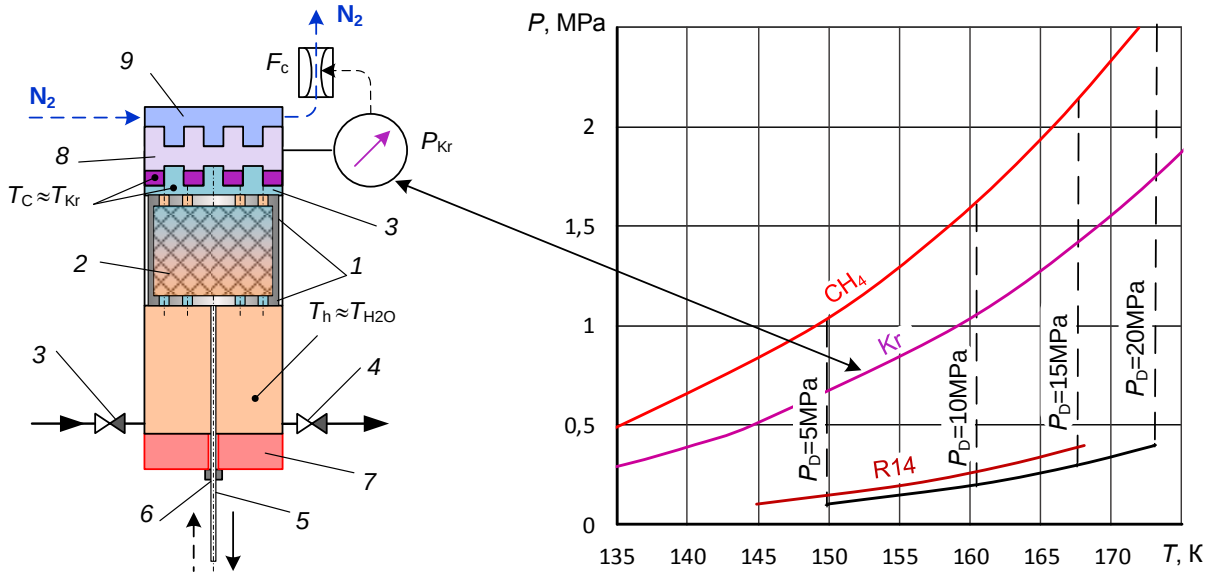

Figure 5. Scheme of low-temperature thermocompressor with heat exhaustion by means of the intermediate refrigerant (krypton). Designations 1...6 - correspond to Fig. 1; 7 – water "heater"; 8 – cooler filled with two-phase krypton; 9 – external refrigerant (N_2); P_{Kr} – pressure in the intermediate refrigerant cavity; F_c – external refrigerant flow regulator; recommended pressure (b) in the cavity of the intermediate refrigerant, depending on the discharge pressure, at which the phase transition of R14 is excluded at its concentration in the mixture $y_{R14} = 2\%$ (table 1).

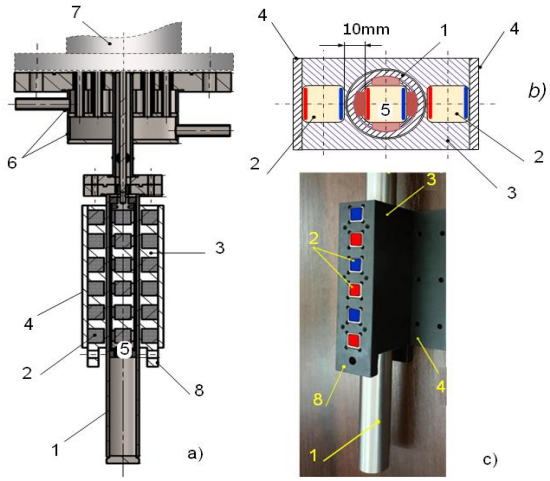

Fig. 6. Magnetic-mechanical drive device: a) – longitudinal section; b) – cross section; c) – view with the caliper cover removed; 1 – stationary sealed wall connected to the volume of the working chamber; 2 – magnets of the external unit; 3 – movable support for the external unit magnets; 4 – caliper cover; 5 – magnets of the internal unit; 6 – cooling water collectors; 7 – working cylinder; 8 – mechanical drive rods.

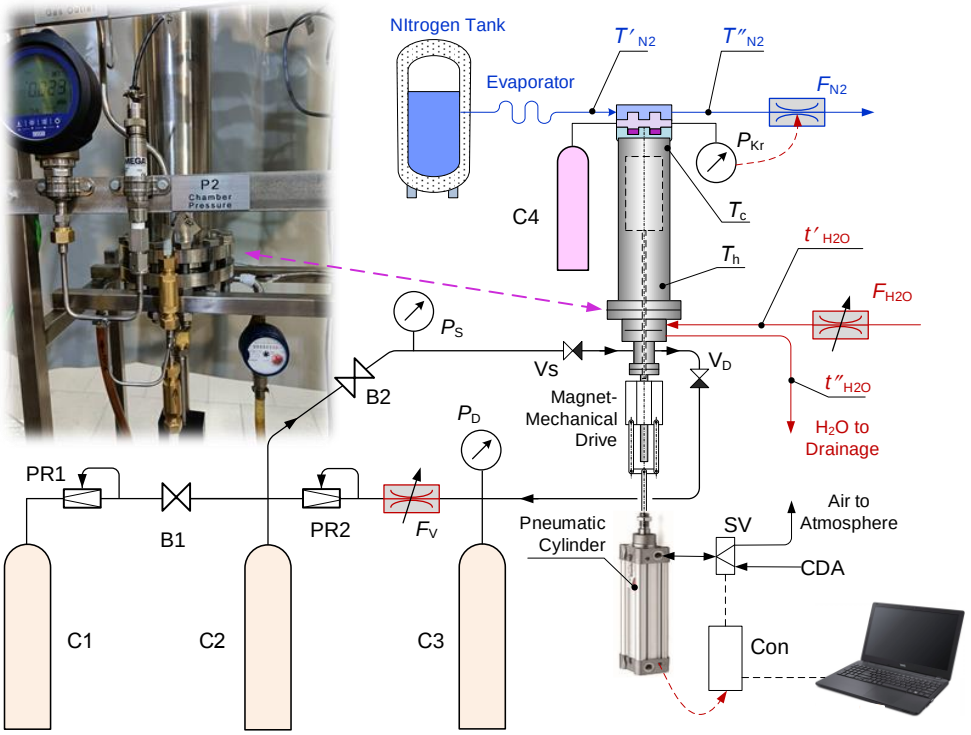

Figure 7. Simplified scheme of the test bench: C1 – cylinder with pumped mixture; C2 and C3 – buffers on the suction and discharge lines; C4 – cylinder with the intermediate refrigerant (Kr); PR1 – pressure regulators "AFTER itself"; PR2 – pressure regulator "BEFORE itself"; B1, B2 – valves; SV - solenoid pneumatic valve; Con – controller; CDA – pneumatic network; VS and VD – suction and discharge valves; FV – circulating flow meter; FH2O – "heating" water flow meter; FN2 – external refrigerant flow regulator (N2); PS and PD – suction and discharge manometers; PKr – pressure in the intermediate refrigerant cavity; t and T – temperature sensors.

Table 2.

Geometric parameters of the thermo-mechanical compressor and the results of the tests carried out using pure helium.

№	Name, unit	Symbol	Value
1.	Cylinder diameter, mm	D_C	106
2.	Displacement stroke, mm	L_C	96
3.	Dead volume, dm^3	V_E	0,78
4.	Relative dead volume, %	V_E / V_C	92
5.	One cycle period, s	τ_c	1,5…4,0
6.	Helium inlet pressure, MPa	P_S	7,45
7.	Heating water temperature at the inlet, K (°C)	t'_{H_2O}	302,6; (29,4)
8.	Average heater temperature, K (°C)	T_h	294,2; (21,1)
9.	Average cooler temperature, K (°C)	T_c	156,8; (-116,4)
10	Relative temperature	θ	1,88
11	Compression ratio	$\sigma = P_D / P_S$	1,2…1,3
12	Volumetric flow rate per 1 cycle at suction conditions, dm^3 per 1 cycle at P_0 = 0,1013 MPa, T_0 = 293 K, std. dm^3 per 1 cycle at P_0 = 0,1013 MPa, T_0 = 293 K, std. m^3/h	 f_S f_{0S} F_0	 0,078…0,183 10,0…23,5 9,0…56,4

CONCLUSIONS

The use of Internal heat regeneration processes in thermal compression systems allows the creation of sufficiently effective installations for the production of compressed gas - thermomechanical compressors.

The feature of the work performed is that two qualitatively different types of energy are consumed in installations for the production of compressed gas: thermal energy, directly used for gas compression, and mechanical energy, necessary to compensate for losses due to friction in seals, as well as to overcome hydraulic resistance of heat exchangers and gas pipelines. The principle of operation of such devices is based on cyclic changes in the temperature of the working fluid when in contact with warm and cold sources.

The most important result of the work is the development of a small-sized thermos-compressor with heat exchange processes provided by the introduction of the internal heat regeneration process between the heater and cooler through the built-in regenerator in the displacer.

In addition, the created low-temperature thermos-compressor differs from machines of the traditional type in several design and operational advantages. The drive based on permanent magnets eliminates the seal node and ensures the tightness of the working volume, preventing the penetration of oil and other by-products into the technological process, which is very significant for the inert gases production.

If there are high-boiling components in the pumped mixture, the minimum coolant temperature should be limited to avoid phase transitions (condensation or freezing). A promising option for this is a heat removal scheme using an intermediate coolant - krypton. Krypton is more preferable because it is safe and, at the same temperatures, its boiling pressure is 30...40% lower than, for example, that of methane.

This thermo-compressor can operate at pressures of P > 10 MPa and at a moderate compression ratio of 1.2...1.4, and also use the exergy of cryogenic product vapors, such as N_2, for driving.

At moderate coolant temperatures of T_c > 150 K, the maximum compression ratio is σ_{max} < 1.4.

In the case of compressing pure gases, such as helium, the coolant temperature can be reduced to T_c = 90 K. At the same time, the maximum compression ratio increases to σ_{max} < 1.8, and the performance under otherwise equal conditions increases by at least two times.

References

[1] Bush V. Apparatus for Compressing Gases. US Patent 2,157,229, 1939.

[2] Suslov A.D., Gorokhovsky G.A., Poltaraus V.B., Gorshkov A.M. *Kriogennye Gazovye Mashiny* [Cryogenic Gas Machines]. Moskva: Mashinostroenie, 1982. 213 p. (in Russian).

[3] Karabulut H. Thermodynamic Analysis of Bush Engine. *G.U. Journal of Science*, 2003, pp. 135-144.

[4] Blagin E., Dovgyallo A., Uglanov D. Numerical Modeling of Non-stationary Processes in Cryogenic Mechanical Thermo-Compressor. *International Journal of Mechanical Engineering and Robotics Research*, 2017, vol. 6, no. 4, pp. 258-262.

[5] Wu S.S., Wang J., Zhang H.C., Huang C.J. Thermodynamic Analysis of Ideal Thermo-Compressor Based on Euler View. *IOP Conference Series Materials Science and Engineering*, 2022, 1240(1):012035.

[6] Blagin E., Dovgyallo A., Uglanov D. Study of Different Factors Influence on Thermocompressor Performance. *International Conference on Mechanical, Aeronautical and Automotive Engineering*, 2017, vol. 108, 04001.

[7] Fischer F., Kuehl H.-D. Generation of CompressedAir by Cascaded Thermo-Compressors – Project Status. *19th International Stirling Engine Conference*, 2021, vol. 313, 04003.

[8] Sharifi N., Boroomand M., Kouhikamali R. Wet Steam Flow Energy Analysis Within Thermo-Compressors. *Energy*, 2012, vol. 47, is. 1, pp. 609-619.

[9] Ahmad K. Sleiti, Wahib A. Al-Ammari, Mohammed Al-Khawaja, Ahmad T. Saker. Experimental Investigation on the Performance of a Novel Thermo-Mechanical Refrigeration System Driven by an Expander-Compressor Unit. *Applied Thermal Engineering*, 2022, vol. 212, 118635.

[10] Fischer F., Kuehl H.-D. Analytical Model for an Overdriven Free-Displacer Thermo-Compressor. *Applied Thermal Engineering*, 2021, vol.185, 116251.

[11] Lin W.Y., Wu X.H., Yang J.L., Yang L.W. Experimental Study and Numerical Analysis of Thermo-Compressors with Annular Regenerators. *International Journal of Refrigeration*, 2013, vol. 36, is. 4, pp. 1376-1387.

[12] Ji W., Xue X., Wang J., Zhou Y., Chen L., Zhu W. Coupling Study of a Novel Thermo-Compressor Driven Pulse Tube Refrigerator. *Applied Thermal Engineering*, 2013, vol. 51, is. 1-2, pp. 630-634.
[13] Seth T., Eric J. Barth. Active Stirling Thermo-Compressor: Modelling and Effects of Controlled Displacer Motion Profile on Work Output. *Applied Energy*, 2022, vol. 327, 120084.
[14] Ahmad K. Sleiti, Mohammed Al-Khawaja, Wahib A. Al-Ammari. A Combined Thermo-Mechanical Refrigeration System with Isobaric Expander-Compressor Unit Powered by Low Grade Heat – Design and Analysis. *International Journal of Refrigeration*, 2020, vol.120, pp. 39-49.
[15] Sharifi N., Boroomand M. An Investigation of Thermo-Compressor Design by Analysis and Experiment: Part 1. Validation of the Numerical Method. *Energy Conversion and Management*, 2013, vol. 69, pp. 217-227.
[16] Sharifi N., Boroomand M. An Investigation of Thermo-Compressor Design by Analysis and Experiment: Part 2. Development of Design Method by Using Comprehensive Characteristic Curves. *Energy Conversion and Management*, 2013, vol. 69, pp. 228-237.
[17] Aristides M. Bonanos. Physical Modeling of Thermo-Compressor for Desalination Applications. *Desalination*, 2017, vol. 412, pp. 13-19.
[18] Kouhikamali R., Sharifi N. Experience of Modification of Thermo-Compressors in Multiple Effects Desalination Plants in Assaluyeh in IRAN. *Applied Thermal Engineering*, 2012, vol. 40, pp. 174-180.
[19] Noori Rahim Abadi S.M.A., Kouhikamali R., Atashkari K. Non-Equilibrium Condensation of Wet Steam Flow Within High-Pressure Thermo-Compressor. *Applied Thermal Engineering*, 2015, vol. 81, pp. 74-82.
[20] Wang J., Pan C., Luo K., Chen L., Wang J., Zhou Y. Thermal Analysis of Stirling Thermo-Compressor and Its Prospect to Drive Refrigerator by Using Natural Working Fluid. *Energy Conversion and Management*, 2018, vol. 177, pp. 280-291.

Information about the authors.

Simonenko Yury Mikhailovich. Doctor of Technical Sciences. Area of scientific interests: low-temperature systems for separation of multicomponent gas mixtures. E-mail: ysimonenko@cryoin.com

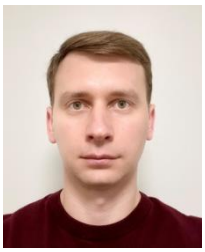

Chygrin Artem Aleksandrovich. Engineer-technologist. Area of scientific interests: low-temperature systems for separation of multicomponent gas mixtures. E-mail: achigrin@cryoin.com

Kostenko Evgeny Vladimirovich. Graduate student. Area of scientific interests: low-temperature systems for separation of multicomponent gas mixtures. E-mail: kostenko-zheka@hotmail.com